

1 **The Sensitivity to Oscillation Parameters**
2 **from a Simultaneous Beam and**
3 **Atmospheric Neutrino Analysis that**
4 **combines the T2K and SK Experiments**



6 Daniel Robert Clement Barrow
7 Magdalen College
8 University of Oxford

9 A thesis submitted for the degree of
10 *Doctor of Philosophy*
11 Michaelmas 2022

Abstract

12

13 Lorem ipsum dolor sit amet, consectetur adipiscing elit. Pellentesque sit amet
14 nibh volutpat, scelerisque nibh a, vehicula neque. Integer placerat nulla massa,
15 et vestibulum velit dignissim id. Ut eget nisi elementum, consectetur nibh in,
16 condimentum velit. Quisque sodales dui ut tempus mattis. Duis malesuada arcu
17 at ligula egestas egestas. Phasellus interdum odio at sapien fringilla scelerisque.
18 Mauris sagittis eleifend sapien, sit amet laoreet felis mollis quis. Pellentesque
19 dui ante, finibus eget blandit sit amet, tincidunt eu neque. Vivamus rutrum
20 dapibus ligula, ut imperdiet lectus tincidunt ac. Pellentesque ac lorem sed
21 diam egestas lobortis.

22 Suspendisse leo purus, efficitur mattis urna a, maximus molestie nisl. Aenean
23 porta semper tortor a vestibulum. Suspendisse viverra facilisis lorem, non
24 pretium erat lacinia a. Vestibulum tempus, quam vitae placerat porta, magna
25 risus euismod purus, in viverra lorem dui at metus. Sed ac sollicitudin nunc.
26 In maximus ipsum nunc, placerat maximus tortor gravida varius. Suspendisse
27 pretium, lorem at porttitor rhoncus, nulla urna condimentum tortor, sed suscipit
28 nisi metus ac risus.

29 Aenean sit amet enim quis lorem tristique commodo vitae ut lorem. Duis
30 vel tincidunt lacus. Sed massa velit, lacinia sed posuere vitae, malesuada vel
31 ante. Praesent a rhoncus leo. Etiam sed rutrum enim. Pellentesque lobortis
32 elementum augue, at suscipit justo malesuada at. Lorem ipsum dolor sit amet,
33 consectetur adipiscing elit. Praesent rhoncus convallis ex. Etiam commodo nunc
34 ex, non consequat diam consectetur ut. Pellentesque vitae est nec enim interdum
35 dapibus. Donec dapibus purus ipsum, eget tincidunt ex gravida eget. Donec
36 luctus nisi eu fringilla mollis. Donec eget lobortis diam.

37 Suspendisse finibus placerat dolor. Etiam ornare elementum ex ut vehicula.
38 Donec accumsan mattis erat. Quisque cursus fringilla diam, eget placerat neque
39 bibendum eu. Ut faucibus dui vitae dolor porta, at elementum ipsum semper.
40 Sed ultrices dui non arcu pellentesque placerat. Etiam posuere malesuada turpis,
41 nec malesuada tellus malesuada.

Acknowledgements

⁴³ Personal

⁴⁴ This is where you thank your advisor, colleagues, and family and friends.

⁴⁵ Lorem ipsum dolor sit amet, consectetur adipiscing elit. Vestibulum feugiat
⁴⁶ et est at accumsan. Praesent sed elit mattis, congue mi sed, porta ipsum. In
⁴⁷ non ullamcorper lacus. Quisque volutpat tempus ligula ac ultricies. Nam sed
⁴⁸ erat feugiat, elementum dolor sed, elementum neque. Aliquam eu iaculis est,
⁴⁹ a sollicitudin augue. Cras id lorem vel purus posuere tempor. Proin tincidunt,
⁵⁰ sapien non dictum aliquam, ex odio ornare mauris, ultrices viverra nisi magna
⁵¹ in lacus. Fusce aliquet molestie massa, ut fringilla purus rutrum consectetur.
⁵² Nam non nunc tincidunt, rutrum dui sit amet, ornare nunc. Donec cursus
⁵³ tortor vel odio molestie dignissim. Vivamus id mi erat. Duis porttitor diam
⁵⁴ tempor rutrum porttitor. Lorem ipsum dolor sit amet, consectetur adipiscing
⁵⁵ elit. Sed condimentum venenatis consectetur. Lorem ipsum dolor sit amet,
⁵⁶ consectetur adipiscing elit.

⁵⁷ Aenean sit amet lectus nec tellus viverra ultrices vitae commodo nunc. Mauris
⁵⁸ at maximus arcu. Aliquam varius congue orci et ultrices. In non ipsum vel
⁵⁹ est scelerisque efficitur in at augue. Nullam rhoncus orci velit. Duis ultricies
⁶⁰ accumsan feugiat. Etiam consectetur ornare velit et eleifend.

⁶¹ Suspendisse sed enim lacinia, pharetra neque ac, ultricies urna. Phasellus sit
⁶² amet cursus purus. Quisque non odio libero. Etiam iaculis odio a ex volutpat, eget
⁶³ pulvinar augue mollis. Mauris nibh lorem, mollis quis semper quis, consequat
⁶⁴ nec metus. Etiam dolor mi, cursus a ipsum aliquam, eleifend venenatis ipsum.
⁶⁵ Maecenas tempus, nibh eget scelerisque feugiat, leo nibh lobortis diam, id laoreet
⁶⁶ purus dolor eu mauris. Pellentesque habitant morbi tristique senectus et netus
⁶⁷ et malesuada fames ac turpis egestas. Nulla eget tortor eu arcu sagittis euismod
⁶⁸ fermentum id neque. In sit amet justo ligula. Donec rutrum ex a aliquet egestas.

⁶⁹ Institutional

⁷⁰ If you want to separate out your thanks for funding and institutional support,
⁷¹ I don't think there's any rule against it. Of course, you could also just remove
⁷² the subsections and do one big traditional acknowledgement section.

⁷³ Lorem ipsum dolor sit amet, consectetur adipiscing elit. Ut luctus tempor ex at
⁷⁴ pretium. Sed varius, mauris at dapibus lobortis, elit purus tempor neque, facilisis
⁷⁵ sollicitudin felis nunc a urna. Morbi mattis ante non augue blandit pulvinar.
⁷⁶ Quisque nec euismod mauris. Nulla et tellus eu nibh auctor malesuada quis
⁷⁷ imperdiet quam. Sed eget tincidunt velit. Cras molestie sem ipsum, at faucibus
⁷⁸ quam mattis vel. Quisque vel placerat orci, id tempor urna. Vivamus mollis,
⁷⁹ neque in aliquam consequat, dui sem volutpat lorem, sit amet tempor ipsum felis
⁸⁰ eget ante. Integer lacinia nulla vitae felis vulputate, at tincidunt ligula maximus.
⁸¹ Aenean venenatis dolor ante, euismod ultrices nibh mollis ac. Ut malesuada
⁸² aliquam urna, ac interdum magna malesuada posuere.

Contents

83

84	1 Introduction	1
85	2 Neutrino Oscillation Physics	2
86	2.1 Discovery of Neutrinos	3
87	2.2 Theory of Neutrino Oscillation	4
88	2.3 Neutrino Oscillation Measurements	8
89	2.4 Summary Of Oscillation Parameter Measurements	18
90	2.5 Overview of Oscillation Effects	19
91	3 T2K and SK Experiment Overview	27
92	3.1 The Super-Kamiokande Experiment	27
93	3.2 The Tokai to Kamioka Experiment	38
94	4 Bayesian Statistics and Markov Chain Monte Carlo Techniques	53
95	4.1 Bayesian Statistics	54
96	4.2 Monte Carlo Simulation	56
97	4.3 Understanding the MCMC Results	64
98	5 Simulation, Reconstruction, and Event Reduction	69
99	5.1 Simulation	69
100	5.2 Event Reconstruction at SK	75
101	5.3 Event Reduction at SK	86
102	6 Sample Selections and Systematics	91
103	6.1 Atmospheric Samples	93
104	6.2 Near Detector Beam Samples	101
105	6.3 Far Detector Beam Samples	103
106	6.4 Systematic Uncertainties	109
107	6.5 Likelihood Calculation	129
108	7 Oscillation Probability Calculation	133
109	7.1 Treatment of Fast Oscillations	134
110	7.2 Calculation Engine	141
111	7.3 Matter Density Profile	145
112	7.4 Production Height Averaging	150

¹¹³	8 Oscillation Analysis	153
¹¹⁴	8.1 Monte Carlo Prediction	154
¹¹⁵	8.2 Sensitivities	167
¹¹⁶	9 Conclusions and Outlook	219

1

117

118

Introduction

2

119

120

Neutrino Oscillation Physics

121 When first proposed, neutrinos were expected to be approximately massless
122 fermions that only interact through weak and gravitational forces. This meant
123 they were very difficult to detect as they can pass through significant amounts
124 of matter without interacting. Despite this, experimental neutrino physics has
125 developed many different detection techniques and observed neutrinos from
126 both natural and artificial sources. In direct tension with Standard Model physics,
127 neutrinos have been determined to oscillate between different lepton flavours,
128 requiring them to have mass.

129 The observation techniques which led to the discovery of the neutrino are doc-
130 umented in section 2.1. The theory underpinning neutrino oscillation is described
131 in section 2.2 and includes the approximations which can be made to simplify
132 the understanding of neutrino oscillation in the two-flavour approximation. Past,
133 current, and future neutrino experiments are detailed in section 2.3, including the
134 reactor, atmospheric, and long-baseline accelerator neutrino sources that have
135 been used to successfully constrain oscillation parameters. Finally, the current
136 state of oscillation parameter measurements are summarised in section 2.4.

2.1 Discovery of Neutrinos

¹³⁷ At the start of the 20th century, the electrons emitted from the β -decay of the nucleus were found to have a continuous energy spectrum [1, 2]. This observation seemingly broke the energy conservation invoked within that period's nuclear models. In 1930, Pauli provided a solution to this problem in the form of a new particle, the neutrino (originally termed "neutron"). It was theorized to be an electrically neutral spin-1/2 fermion with a mass smaller than that of the electron [3]. This neutrino was emitted with the electron in β -decay to alleviate the apparent breaking of energy conservation. As a predecessor of today's weak interaction model, Fermi's theory of β -decay developed the understanding by coupling the four constituent particles: electron, proton, neutron, and neutrino, into a quantitative model [4].

¹⁴⁹ Whilst Pauli was not convinced of the ability to detect neutrinos, the first observations of the particle were made in the mid-1950s when neutrinos from a reactor were observed via the inverse β -decay (IBD) process, $\bar{\nu}_e + p \rightarrow n + e^+$ [5, 6]. The detector consisted of two parts: a neutrino interaction medium and a liquid scintillator. The interaction medium was built from two water tanks, loaded with cadmium chloride to allow for increased efficiency in the detection of neutron capture. The positron emitted from IBD annihilates, $e^+ + e^- \rightarrow 2\gamma$, generating a prompt signal and the neutron is captured on the cadmium via $n + {}^{108}Cd \rightarrow {}^{109*}Cd \rightarrow {}^{109}Cd + \gamma$, producing a delayed signal. An increase in the coincidence rate was observed when the reactor was operating which was interpreted as interactions from neutrinos generated in the reactor.

¹⁶⁰ After the discovery of the ν_e , the question of how many flavours of neutrino exist was asked. In 1962, a measurement of the ν_μ was conducted at the Brookhaven National Laboratory [7]. A proton beam was directed at a beryllium target, generating pions which then decayed via $\pi^\pm \rightarrow \mu^\pm + (\nu_\mu, \bar{\nu}_\mu)$, and the subsequent interactions of the ν_μ were observed. As the subsequent interaction of the neutrino generated muons rather than electrons, it was determined that

the ν_μ was fundamentally different from ν_e . The final observation to be made was that of the ν_τ from the DONUT experiment [8]. Three neutrinos seem the obvious solution as it mirrors the known number of charged leptons (as they form weak isospin doublets) but there could be evidence of more. Several neutrino experiments have found anomalous results [9, 10] which could be attributed to “sterile” neutrinos. These hypothesised particles are not affected by gauge interactions in the Standard Model so their presence can only be inferred through the observation of non-standard oscillation modes. However, cosmological observations indicate the number of neutrino species $N_{eff} = 2.99 \pm 0.17$ [11], as measured from the cosmic microwave background power spectrum. LEP also measured the number of active neutrino flavours to be $N_\nu = 2.9840 \pm 0.0082$ [12] from measurements of the Z-decay width, but this does not strongly constrain the number of sterile neutrinos.

2.2 Theory of Neutrino Oscillation

A neutrino generated with lepton flavour α can change into a different lepton flavour β after propagating some distance. This phenomenon is called neutrino oscillation and requires that neutrinos must have a non-zero mass. This behaviour has been characterised by the Pontecorvo-Maki-Nakagawa-Sakata (PMNS) [13–15] mixing matrix which describes how the flavour and mass of neutrinos are associated. This is analogous to the Cabibbo-Kobayashi-Maskawa (CKM) [16] matrix measured in quark physics.

2.2.1 Three Flavour Oscillations

The PMNS parameterisation defines three flavour eigenstates, ν_e , ν_μ and ν_τ (indexed ν_α), which are eigenstates of the weak interaction and three mass eigenstates, ν_1 , ν_2 and ν_3 (indexed ν_i). Each mass eigenstate is the superposition

¹⁹¹ of all three flavour states,

$$|\nu_i\rangle = \sum_{\alpha} U_{\alpha i} |\nu_{\alpha}\rangle. \quad (2.1)$$

¹⁹² Where U is the 3×3 PMNS matrix which is unitary and connects the mass
¹⁹³ and flavour eigenstates.

¹⁹⁴ The weak interaction, when interacting via a W^{\pm} boson, couples to flavour
¹⁹⁵ eigenstates so neutrinos interact with leptons of the same flavour. The prop-
¹⁹⁶ agation of a neutrino flavour eigenstate, in a vacuum, can be re-written as a
¹⁹⁷ plane-wave solution to the time-dependent Schrödinger equation,

$$|\nu_{\alpha}(t)\rangle = \sum_i U_{\alpha i}^{*} |\nu_i\rangle e^{-i\phi_i}. \quad (2.2)$$

¹⁹⁸ The ϕ_i term can be expressed in terms of the energy, E_i , and magnitude of the
¹⁹⁹ three momenta, p_i , of the neutrino, $\phi_i = E_i t - p_i x$ (t and x being time and position
²⁰⁰ coordinates). The probability of observing a neutrino of flavour eigenstate β from
²⁰¹ one which originated as flavour α can be calculated as,

$$P(\nu_{\alpha} \rightarrow \nu_{\beta}) = |\langle \nu_{\beta} | \nu_{\alpha}(t) \rangle|^2 = \sum_{i,j} U_{\alpha i}^{*} U_{\beta i} U_{\alpha j} U_{\beta j}^{*} e^{-i(\phi_j - \phi_i)}. \quad (2.3)$$

²⁰² The term within the exponential can be represented as,

$$\phi_j - \phi_i = E_j t - E_i t - p_j x + p_i x. \quad (2.4)$$

²⁰³ For a relativistic particle, $E_i \gg m_i$, a Taylor series expansion means,

$$p_i = \sqrt{E_i^2 - m_i^2} \approx E_i - \frac{m_i^2}{2E_i}. \quad (2.5)$$

²⁰⁴ Making the approximations that neutrinos are relativistic, the mass eigenstates
²⁰⁵ were created with the same energy and that $x = L$, where L is the distance
²⁰⁶ travelled by the neutrino, Equation 2.4 then becomes

$$\phi_j - \phi_i = \frac{\Delta m_{ij}^2 L}{2E}, \quad (2.6)$$

207 where $\Delta m_{ij}^2 = m_i^2 - m_j^2$. This, combined with further use of unitarity relations
 208 results in Equation 2.3 becoming

$$\begin{aligned} P(\nu_\alpha \rightarrow \nu_\beta) &= \delta_{\alpha\beta} - 4 \sum_{i>j} \Re \left(U_{\alpha i}^* U_{\beta i} U_{\alpha j} U_{\beta j}^* \right) \sin^2 \left(\frac{\Delta m_{ij}^2 L}{4E} \right) \\ &\quad + (-) 2 \sum_{i>j} \Im \left(U_{\alpha i}^* U_{\beta i} U_{\alpha j} U_{\beta j}^* \right) \sin \left(\frac{\Delta m_{ij}^2 L}{2E} \right). \end{aligned} \quad (2.7)$$

209 Where $\delta_{\alpha\beta}$ is the Kronecker delta function and the negative sign on the last
 210 term is included for the oscillation probability of antineutrinos. As an important
 211 point to note, the observation of oscillation probability requires a non-zero value
 212 of Δm_{ij}^2 , which in turn requires that neutrinos have differing masses.

213 Typically, the PMNS matrix is parameterised into three mixing angles, a
 214 charge parity (CP) violating phase δ_{CP} , and two Majorana phases $\alpha_{1,2}$,

$$U = \underbrace{\begin{pmatrix} 1 & 0 & 0 \\ 0 & c_{23} & s_{23} \\ 0 & -s_{23} & c_{23} \end{pmatrix}}_{\text{Atmospheric, Accelerator}} \underbrace{\begin{pmatrix} c_{13} & 0 & s_{13}e^{-i\delta_{CP}} \\ 0 & 1 & 0 \\ -s_{13}e^{-i\delta_{CP}} & 0 & c_{13} \end{pmatrix}}_{\text{Reactor, Accelerator}} \times \underbrace{\begin{pmatrix} c_{12} & s_{12} & 0 \\ -s_{12} & c_{12} & 0 \\ 0 & 0 & 1 \end{pmatrix}}_{\text{Reactor, Solar}} \underbrace{\begin{pmatrix} e^{i\alpha_1/2} & 0 & 0 \\ 0 & e^{i\alpha_2/2} & 0 \\ 0 & 0 & 1 \end{pmatrix}}_{\text{Majorana}}. \quad (2.8)$$

215 Where $s_{ij} = \sin(\theta_{ij})$ and $c_{ij} = \cos(\theta_{ij})$. The oscillation parameters are often
 216 grouped: (1,2) as “solar”, (2,3) as “atmospheric” and (1,3) as “reactor”. Many
 217 neutrino experiments aim to measure the PMNS parameters from a wide array
 218 of origins, as is the purpose of this thesis.

219 The Majorana phase, $\alpha_{1,2}$, included within the fourth matrix in Equation 2.8
 220 is only included for completeness. For an oscillation analysis experiment, any
 221 terms containing this phase disappear due to taking the expectation value of the
 222 PMNS matrix. Measurements of these phases can be performed by experiments
 223 searching for neutrino-less double β -decay [17].

224 A two-flavour approximation can be obtained when one assumes the third
225 mass eigenstate is degenerate with another. This results in the two-flavour
226 approximation being reasonable for understanding the features of the oscillation.
227 In this two-flavour case, the mixing matrix becomes,

$$U_{\text{2 Flav.}} = \begin{pmatrix} \cos(\theta) & \sin(\theta) \\ -\sin(\theta) & \cos(\theta) \end{pmatrix}. \quad (2.9)$$

228 This culminates in the oscillation probability,

$$\begin{aligned} P(\nu_\alpha \rightarrow \nu_\alpha) &= 1 - \sin^2(2\theta) \sin^2\left(\frac{\Delta m^2 L}{4E}\right), \\ P(\nu_\alpha \rightarrow \nu_\beta) &= \sin^2(2\theta) \sin^2\left(\frac{\Delta m^2 L}{4E}\right). \end{aligned} \quad (2.10)$$

229 Where $\alpha \neq \beta$. For a fixed neutrino energy, the oscillation probability is
230 a sinusoidal function depending upon the distance over which the neutrino
231 propagates. The frequency and amplitude of oscillation are dependent upon
232 $\Delta m^2 / 4E$ and $\sin^2 2\theta$, respectively. The oscillation probabilities presented thus far
233 assume $c = 1$, where c is the speed of light in a vacuum. In more familiar units, the
234 maximum oscillation probability for a fixed value of θ is given at $L[\text{km}] / E[\text{GeV}] \sim$
235 $1.27 / \Delta m^2$. It is this calculation that determines the best L/E value for a given
236 experiment to be designed around for measurements of a specific value of Δm^2 .

237 2.2.2 The MSW Effect

238 The theory of neutrino oscillation in a vacuum has been described in subsec-
239 tion 2.2.1. However, the beam neutrinos and atmospheric neutrinos originating
240 from below the horizon propagate through the matter in the Earth. The coherent
241 scattering of neutrinos from a material target modifies the Hamiltonian of the
242 system which results in a change in the oscillation probability. This modification
243 is termed the Mikheyev-Smirnov-Wolfenstein (MSW) effect [18–20]. This occurs
244 because charged current scattering ($\nu_e + e^- \rightarrow \nu_e + e^-$, propagated by a W boson)
245 only affects electron neutrinos whereas the neutral current scattering ($\nu_l + l^- \rightarrow$

- ²⁴⁶ $\nu_l + l^-$, propagated by a Z^0 boson) interacts through all neutrino flavours equally.
²⁴⁷ In the two-flavour approximation, the effective mixing parameter becomes

$$\sin^2(2\theta) \rightarrow \sin^2(2\theta_m) = \frac{\sin^2(2\theta)}{(A/\Delta m^2 - \cos(2\theta))^2 + \sin^2(2\theta)}, \quad (2.11)$$

²⁴⁸ where $A = 2\sqrt{2}G_F N_e E$, N_e is the electron density of the medium and G_F
²⁴⁹ is Fermi's constant. It is clear that there exists a value of $A = \Delta m^2 \cos(2\theta)$ for
²⁵⁰ $\Delta m^2 > 0$, which results in a divergent mixing parameter, colloquially called the
²⁵¹ matter resonance. This resonance regenerates the electron neutrino component of
²⁵² the neutrino flux [18–20]. The density at which the resonance occurs is given by

$$N_e = \frac{\Delta m^2 \cos(2\theta)}{2\sqrt{2}G_F E}. \quad (2.12)$$

²⁵³ At densities lower than this critical value, the oscillation probability will
²⁵⁴ be much closer to that of vacuum oscillation. For antineutrinos, $N_e \rightarrow -N_e$
²⁵⁵ [21]. The resonance occurring from the MSW effect depends on the sign of Δm^2 .
²⁵⁶ Therefore, any neutrino oscillation experiment which observes neutrinos and
²⁵⁷ antineutrinos which have propagated through matter can have some sensitivity
²⁵⁸ to the ordering of the neutrino mass eigenstates.

²⁵⁹ 2.3 Neutrino Oscillation Measurements

²⁶⁰ As evidence of beyond Standard Model physics, the 2015 Nobel Prize in Physics
²⁶¹ was awarded to the Super-Kamiokande (SK) [22] and Sudbury Neutrino Ob-
²⁶² servatory (SNO) [23] collaborations for the first definitive observation of solar
²⁶³ and atmospheric neutrino oscillation [24]. Since then, the field has seen a wide
²⁶⁴ array of oscillation measurements from a variety of neutrino sources. As seen
²⁶⁵ in subsection 2.2.1, the neutrino oscillation probability is dependent on the ratio
²⁶⁶ of the propagation baseline, L , to the neutrino energy, E . It is this ratio that
²⁶⁷ determines the type of neutrino oscillation a particular experiment is sensitive to.

²⁶⁸ As illustrated in Figure 2.1, there are many neutrino sources that span a
²⁶⁹ wide range of energies. The least energetic neutrinos are from reactor and

²⁷⁰ terrestrial sources at $O(1)$ MeV whereas the most energetic neutrinos originate
²⁷¹ from atmospheric and galactic neutrinos of $> O(1)$ TeV.



Figure 2.1: The electro-weak cross-section for $\bar{\nu}_e + e^- \rightarrow \bar{\nu}_e + e^-$ scattering on free electrons from various natural and man-made neutrino sources, as a function of neutrino energy. Taken from [25]

²⁷² 2.3.1 Solar Neutrinos

²⁷³ Solar neutrinos are emitted from fusion reaction chains at the centre of the Sun.
²⁷⁴ The solar neutrino flux, given as a function of neutrino energy for different
²⁷⁵ fusion and decay chains, is illustrated in Figure 2.2. Whilst proton-proton fusion
²⁷⁶ generates the largest flux of neutrinos, the neutrinos are low energy and are
²⁷⁷ difficult to reconstruct due to the IBD interaction threshold of 1.8MeV [26].
²⁷⁸ Consequently, most experiments focus on the neutrinos from the decay of 8B
²⁷⁹ (via $^8B \rightarrow ^8Be^* + e^+ + \nu_e$), which are higher energy.

²⁸⁰ The first measurements of solar neutrinos observed a significant reduction in
²⁸¹ the event rate compared to predictions from the Standard Solar Model [28, 29]. A
²⁸² proposed solution to this “solar neutrino problem” was $\nu_e \leftrightarrow \nu_\mu$ oscillations in a



Figure 2.2: The solar neutrino flux as a function of neutrino energy for various fusion reactions and decay chains as predicted by the Standard Solar Model. Taken from [27].

283 precursory version of the PMNS model [30]. The Kamiokande [31], Gallex [32]
 284 and Sage [33] experiments confirmed the ~ 0.5 factor deficit of solar neutrinos.

285 The conclusive solution to this problem was determined by the SNO col-
 286 laboration [23]. Using a deuterium water target to observe 8B neutrinos, the
 287 event rate of charged current (CC), neutral current (NC), and elastic scattering
 288 (ES) interactions (Given in Equation 2.13) was simultaneously measured. CC
 289 events can only occur for electron neutrinos, whereas the NC channel is agnostic
 290 to neutrino flavour, and the ES reaction has a small excess sensitivity for the
 291 detection of electron neutrino interactions. This meant that there were direct
 292 measurements of the ν_e and ν_x neutrino flux. It was concluded that the CC and
 293 ES interaction rates were consistent with the deficit previously observed. Most
 294 importantly, the NC reaction rate was only consistent with the others under the

295 hypothesis of flavour transformation.

$$\begin{aligned} \nu_e + d &\rightarrow p + p + e^- & (CC) \\ \nu_x + d &\rightarrow p + n + \nu_x & (NC) \\ \nu_x + e^- &\rightarrow \nu_x + e^- & (ES) \end{aligned} \quad (2.13)$$

296 Since the SNO measurement, many experiments have since measured the
297 neutrino flux of different interaction chains within the sun [34–36]. The most
298 recent measurement was that of CNO-cycle neutrinos which were recently
299 observed with 5σ significance by the Borexino collaboration [34].

300 2.3.2 Accelerator Neutrinos

301 The concept of using an artificial “neutrino beam” was first realised in 1962 [7].
302 Since then, many experiments have adopted the same fundamental concepts.
303 Typically, a proton beam is aimed at a target producing charged mesons that
304 decay to neutrinos. The mesons can be sign-selected by the use of magnetic
305 focusing horns to generate a neutrino or antineutrino beam. Pions are the primary
306 mesons that decay and depending on the orientation of the magnetic field, a
307 muon (anti-)neutrino beam is generated via $\pi^+ \rightarrow \mu^+ + \nu_\mu$ or $\pi^- \rightarrow \mu^- + \bar{\nu}_\mu$.
308 The decay of muons and kaons results in an irreducible intrinsic electron neutrino
309 background. In T2K, this background contamination is $O(< 1\%)$ [37]. There is
310 also an approximately $\sim 5\%$ “wrong-sign” neutrino background of $\bar{\nu}_\mu$ generated
311 via the same decays. As the beam is generated by proton interactions (rather
312 than anti-proton interactions), the wrong-sign component in the antineutrino
313 beam is larger when operating in neutrino mode.

314 Tuning the proton energy in the beam and using beam focusing techniques
315 allows the neutrino energy to be set to a value that maximises the disappear-
316 ance oscillation probability in the L/E term in Equation 2.10. This means that
317 accelerator experiments are typically more sensitive to the mixing parameters as
318 compared to a natural neutrino source. However, the disadvantage compared
319 to atmospheric neutrino experiments is the cost of building a facility to provide

320 high-energy neutrinos, with a high flux, which is required for longer baselines.
 321 Consequently, there is typically less sensitivity to matter effects and the ordering
 322 of the neutrino mass eigenstates.

323 A neutrino experiment measures

$$R(\vec{x}) = \Phi(E_\nu) \times \sigma(E_\nu) \times \epsilon(\vec{x}) \times P(\nu_\alpha \rightarrow \nu_\beta), \quad (2.14)$$

324 where $R(\vec{x})$ is the event rate of neutrinos at position \vec{x} , $\Phi(E_\nu)$ is the flux of
 325 neutrinos with energy E_ν , $\sigma(E_\nu)$ is the cross-section of the neutrino interaction and
 326 $\epsilon(\vec{x})$ is the efficiency and resolution of the detector. In order to leverage the most
 327 out of an accelerator neutrino experiment, the flux and cross-section systematics
 328 need to be constrained. This is typically done via the use of a “near detector”,
 329 situated at a baseline of $O(1)$ km. This detector observes the unoscillated neutrino
 330 flux and constrains the parameters used within the flux and cross-section model.

331 The first accelerator experiments to precisely measure oscillation parameters
 332 were MINOS [38] and K2K [39]. These experiments confirmed the ν_μ disappear-
 333 ance seen in atmospheric neutrino experiments by finding consistent parameter
 334 values for $\sin^2(\theta_{23})$ and Δm_{32}^2 . The current generation of accelerator neutrino
 335 experiments, T2K and NO ν A extended this field by observing $\bar{\nu}_\mu \rightarrow \bar{\nu}_e$ and lead
 336 the sensitivity to atmospheric mixing parameters as seen in Figure 2.6 [40]. The
 337 two experiments differ in their peak neutrino energy, baseline, and detection tech-
 338 nique. The NO ν A experiment is situated at a baseline of 810km from the NuMI
 339 beamline which delivers 2GeV neutrinos. The T2K neutrino beam is peaked
 340 around 0.6GeV and propagates 295km [41]. Additionally, the NO ν A experiment
 341 uses functionally identical detectors (near and far) whereas T2K uses a plastic
 342 scintillator technique at the near detector and a water Cherenkov far detector.
 343 The future generation experiments DUNE [42] and Hyper-Kamiokande [43]
 344 will succeed these experiments as the high-precision era of neutrino oscillation
 345 parameter measurements develops.

346 Several anomalous results have been observed in the LSND [9] and Mini-
 347 BooNE [10] detectors which were designed with purposefully short baselines.

348 Parts of the neutrino community attributed these results to oscillations induced
349 by a fourth “sterile” neutrino [44] but several searches in other experiments,
350 MicroBooNE [45] and KARMEN [46], found no hints of additional neutrino
351 species. The solution to the anomalous results is still being determined.

352 2.3.3 Atmospheric Neutrinos

353 The interactions of primary cosmic ray protons in the Earth’s upper atmosphere
354 generate showers of energetic hadrons. These are mostly pions and kaons that
355 decay to produce a natural source of neutrinos spanning energies of MeV to
356 TeV [47]. The main decay is via,

$$\begin{aligned} \pi^\pm &\rightarrow \mu^\pm + (\nu_\mu, \bar{\nu}_\mu), \\ \mu^\pm &\rightarrow e^\pm + (\nu_e, \bar{\nu}_e) + (\nu_\mu, \bar{\nu}_\mu), \end{aligned} \tag{2.15}$$

357 such that for a single pion decay, three neutrinos can be produced. The
358 atmospheric neutrino flux energy spectra as predicted by the Bartol [48], Honda
359 [49–51], and FLUKA [52] models are illustrated in Figure 2.3. The flux distribution
360 peaks at an energy of $O(10)$ GeV. The uncertainties associated with these models
361 are dominated by the hadronic production of kaon and pions as well as the
362 primary cosmic flux.

363 Unlike long-baseline experiments which have a fixed baseline, the distance
364 atmospheric neutrinos propagate is dependent upon the zenith angle at which
365 they interact. This is illustrated in Figure 2.4. Neutrinos that are generated
366 directly above the detector ($\cos(\theta) = 1.0$) have a baseline equivalent to the
367 height of the atmosphere, whereas neutrinos that interact directly below the
368 detector ($\cos(\theta) = -1.0$) have to travel a length equal to the diameter of the Earth.
369 This means atmospheric neutrinos have a baseline that varies from $O(20)$ km to
370 $O(6 \times 10^3)$ km. Any neutrino generated at or below the horizon will be subject
371 to MSW matter resonance as they propagate through the Earth.

372 Figure 2.5 highlights the neutrino flux as a function of the zenith angle for
373 different slices of neutrino energy. For medium to high-energy neutrinos (and to

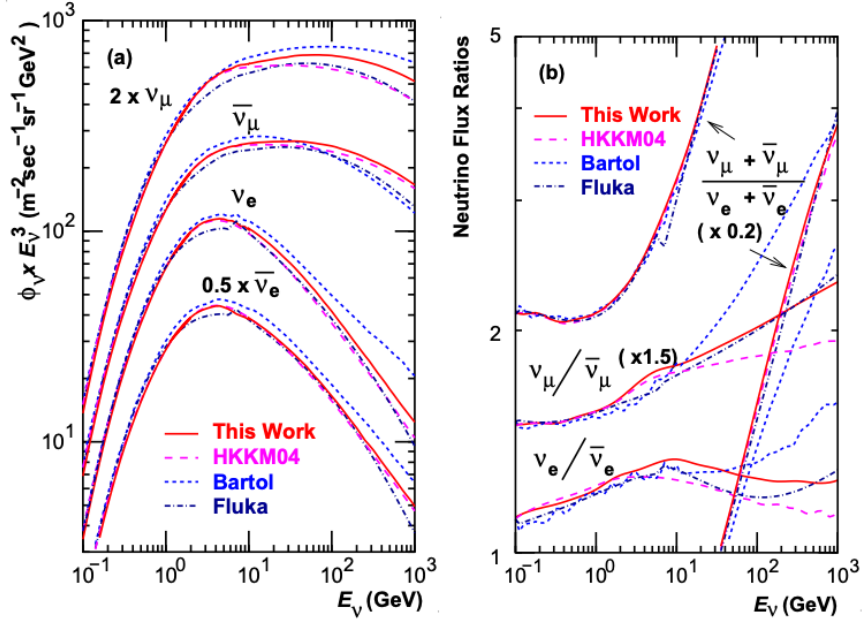


Figure 2.3: Left panel: The atmospheric neutrino flux for different neutrino flavours as a function of neutrino energy as predicted by the 2007 Honda model (“This work”) [49], the 2004 Honda model (“HKKM04”)[50], the Bartol model [48] and the FLUKA model [52]. Right panel: The ratio of the muon to electron neutrino flux as predicted by all the quoted models. Both figures taken from [49].



Figure 2.4: A diagram illustrating the definition of zenith angle as used in the Super Kamiokande experiment [53].

374 a lesser degree for low-energy neutrinos), the flux is approximately symmetric
 375 around $\cos(\theta) = 0$. To the accuracy of this approximation, the systematic
 376 uncertainties associated with atmospheric flux for comparing upward-going
 377 and down-going neutrino cancels. This allows the down-going events, which are

378 mostly insensitive to oscillation probabilities, to act as an unoscillated prediction
 379 (similar to a near detector in an accelerator neutrino experiment).



Figure 2.5: Prediction of $\nu_e, \bar{\nu}_e, \nu_\mu, \bar{\nu}_\mu$ fluxes as a function of zenith angle as calculated by the HKKM model [51]. The left, middle and right panels represent three values of neutrino energy, 0.32GeV, 1.0GeV and 3.2GeV respectively. Predictions for other models including Bartol [48], Honda [49] and FLUKA [52] are given in [53].

380 Precursory hints of atmospheric neutrinos were observed in the mid-1960s
 381 searching for $\nu_\mu + X \rightarrow X^* + \mu^\pm$ [54]. This was succeeded by the IMB-3 [55]
 382 and Kamiokande [56] experiments which measured the double ratio of muon
 383 to electron neutrinos in data to Monte Carlo, $R(\nu_\mu/\nu_e) = (\mu/e)_{Data}/(\mu/e)_{MC}$.
 384 Both experiments were found to have a consistent deficit of muon neutrinos,
 385 with $R(\nu_\mu/\nu_e) = 0.67 \pm 0.17$ and $R(\nu_\mu/\nu_e) = 0.658 \pm 0.016 \pm 0.035$, respectively.
 386 Super-Kamiokande (SK) [53] extended this analysis by fitting oscillation pa-
 387 rameters in $P(\nu_\mu \rightarrow \nu_\tau)$ which found best fit parameters $\sin^2(2\theta) > 0.92$ and
 388 $1.5 \times 10^{-3} < \Delta m^2 < 3.4 \times 10^{-3} \text{ eV}^2$.

389 Since then, atmospheric neutrino experiments have been making precision
 390 measurements of the $\sin^2(\theta_{23})$ and Δm^2_{32} oscillation parameters. Atmospheric
 391 neutrino oscillation is dominated by $P(\nu_\mu \rightarrow \nu_\tau)$, where SK observed a 4.6σ
 392 discovery of ν_τ appearance [57]. Figure 2.6 illustrates the current estimates on
 393 the atmospheric mixing parameters, from a wide range of atmospheric and
 394 accelerator neutrino observatories.

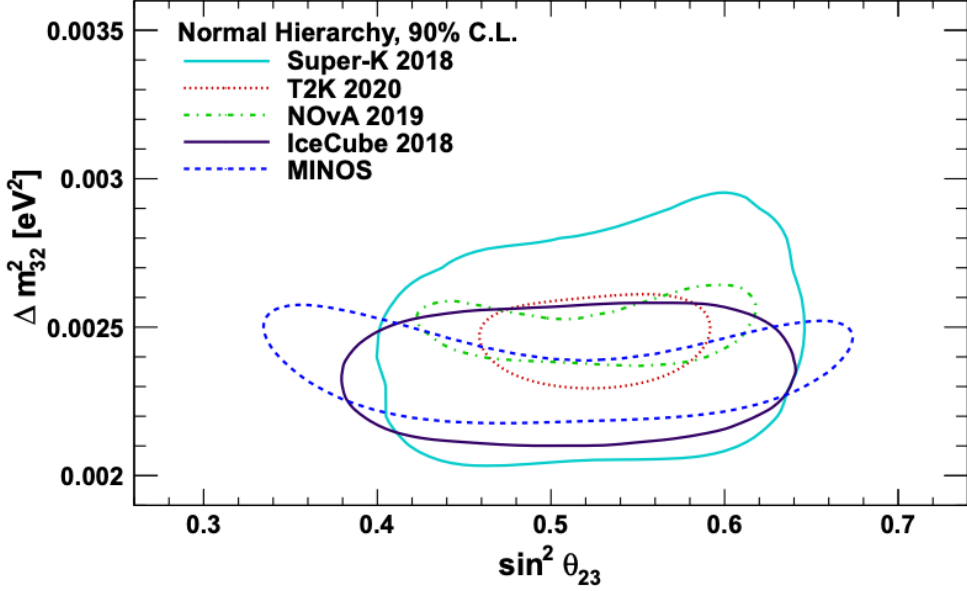


Figure 2.6: Constraints on the atmospheric oscillation parameters, $\sin^2(\theta_{23})$ and Δm_{32}^2 , from atmospheric and long-baseline experiments: SK [58], T2K [59], NOvA [60], IceCube [61] and MINOS [62]. Figure taken from [63].

395 2.3.4 Reactor Neutrinos

396 As illustrated in the first discovery of neutrinos (section 2.1), nuclear reactors
 397 are a very useful artificial source of electron antineutrinos. For reactors that use
 398 low-enriched uranium ^{235}U as fuel, the antineutrino flux is dominated by the
 399 β -decay fission of ^{235}U , ^{238}U , ^{239}Pu and ^{241}Pu [64] as illustrated in Figure 2.7.

400 Due to their low energy, reactor electron antineutrinos predominantly interact
 401 via the inverse β -decay (IBD) interaction. The typical signature contains two
 402 signals delayed by $O(200)\mu\text{s}$; firstly the prompt photons from positron annihila-
 403 tion, and secondly the photon emitted ($E_{tot}^\gamma = 2.2\text{MeV}$) from de-excitation after
 404 neutron capture on hydrogen. Searching for both signals improves the detector's
 405 ability to distinguish between background and signal events [65].

406 There are many short baseline experiments ($L \sim O(1)\text{km}$) that have measured
 407 the $\sin^2(\theta_{13})$ and Δm_{32}^2 oscillation parameters. Daya Bay [66], RENO [67] and
 408 Double Chooz [68] have all provided precise measurements, with the first discov-
 409 ery of a non-zero θ_{13} made by Daya Bay and RENO (and complemented by T2K
 410 [68]). The constraints on $\sin^2(\theta_{13})$ by the reactor experiments lead the field. They



Figure 2.7: Reactor electron antineutrino fluxes for ^{235}U (Black), ^{238}U (Green), ^{239}Pu (Purple), and ^{241}Pu (Orange) isotopes. The inverse β -decay cross-section (Blue) and corresponding measurable neutrino spectrum (Red) are also given. Top panel: Schematic of Inverse β -decay interaction including the eventual capture of the emitted neutron. This capture emits a γ -ray which provides a second signal of the event. Taken from [63].

are often used as external inputs to accelerator neutrino experiments to improve their sensitivity to δ_{CP} and mass hierarchy determination. JUNO-TAO [69], a small collaboration within the larger JUNO experiment, is a next-generation reactor experiment that aims to precisely measure the isotopic antineutrino yields from the different fission chains.

Kamland [70] is the only experiment to have observed reactor neutrinos using a long baseline (flux weighted averaged baseline of $L \sim 180\text{km}$) which allows it to have sensitivity to Δm_{21}^2 . Combined with the SK solar neutrino experiment, the combined analysis puts the most stringent constraint on Δm_{21}^2 [71].

2.4 Summary Of Oscillation Parameter Measurements

Since the first evidence of neutrino oscillations, numerous measurements of the mixing parameters have been made. Many experiments use neutrinos as a tool for the discovery of new physics (diffuse supernova background, neutrinoless double beta decay and others) so the PMNS parameters are summarised in the Particle Data Group (PDG) review tables. The analysis presented in this thesis focuses on the 2020 T2K oscillation analysis presented in [72] which the 2020 PDG constraints [73] were used. These constraints are outlined in Table 2.1.

Parameter	2020 Constraint
$\sin^2(\theta_{12})$	0.307 ± 0.013
Δm_{21}^2	$(7.53 \pm 0.18) \times 10^{-5} \text{ eV}^2$
$\sin^2(\theta_{13})$	$(2.18 \pm 0.07) \times 10^{-2}$
$\sin^2(\theta_{23})$ (I.H.)	0.547 ± 0.021
$\sin^2(\theta_{23})$ (N.H.)	0.545 ± 0.021
Δm_{32}^2 (I.H.)	$(-2.546^{+0.034}_{-0.040}) \times 10^{-3} \text{ eV}^2$
Δm_{32}^2 (N.H.)	$(2.453 \pm 0.034) \times 10^{-3} \text{ eV}^2$

Table 2.1: The 2020 Particle Data Group constraints of the oscillation parameters taken from [73]. The value of Δm_{32}^2 is given for both normal hierarchy (N.H.) and inverted hierarchy (I.H.) and $\sin^2(\theta_{23})$ is broken down by whether its value is below (Q1) or above (Q2) 0.5.

The $\sin^2(\theta_{13})$ measurement stems from the electron antineutrino disappearance, $P(\bar{\nu}_e \rightarrow \bar{\nu}_e)$, and is taken as the average best-fit from the combination of Daya Bay, Reno and Double Chooz. It is often used as a prior uncertainty within other neutrino oscillation experiments, typically termed the reactor constraint. The $\sin^2(\theta_{12})$ parameter is predominantly measured through electron neutrino disappearance, $P(\nu_e \rightarrow \nu_{\mu,\tau})$, in solar neutrino experiments. The long-baseline reactor neutrino experiment Kamland also has a sensitivity to this parameter and is used in a joint fit to solar data from SNO and SK, using the reactor constraint. Measurements of $\sin^2(\theta_{23})$ are made by long-baseline and atmospheric neutrino experiments. The PDG value is a joint fit of T2K, NO ν A, MINOS and IceCube DeepCore experiments. The latest T2K-only measurement, provided at Neutrino2020 and is the basis of this thesis, is given as $\sin^2(\theta_{23}) = 0.546^{+0.024}_{-0.046}$ [72].

440 The PDG constraint on Δm_{21}^2 is provided by the KamLAND experiment using
 441 solar and geoneutrino data. This measurement utilised a $\sin^2(\theta_{13})$ constraint
 442 from accelerator (T2K, MINOS) and reactor neutrino (Daya Bay, RENO, Double
 443 Chooz) experiments. Accelerator measurements make some of the most stringent
 444 constraints on Δm_{32}^2 although atmospheric experiments have more sensitivity to
 445 the mass hierarchy determination. The PDG performs a joint fit of accelerator
 446 and atmospheric data, in both normal and inverted hierarchies separately. The
 447 latest T2K-only result is $\Delta m_{32}^2 = 2.49^{+0.058}_{-0.082} \times 10^{-3} \text{ eV}^2$ favouring normal hierarchy
 448 [72]. The value of δ_{CP} is largely undetermined. CP-conserving values of 0 and π
 449 were rejected with $\sim 2\sigma$ intervals, as published in Nature, although more recent
 450 analyses have reduced the credible intervals to 90%. Since the 2020 PDG publi-
 451 cation, there has been a new measurement of $\sin^2(\theta_{13}) = (2.20 \pm 0.07) \times 10^{-2}$
 452 [74], alongside updated Δm_{32}^2 and $\sin^2(\theta_{23})$ measurements.

453 Throughout this thesis, several sample spectra predictions and contours
 454 are presented, which require oscillation parameters to be assumed. Table 2.2
 455 defines two sets of oscillation parameters, with “Asimov A” set being close to
 456 the preferred values from a previous T2K-only fit [75] and “Asimov B” being
 457 CP-conserving and further from maximal θ_{23} mixing.

Parameter	Asimov A	Asimov B
Δm_{12}^2	$7.53 \times 10^{-5} \text{ eV}^2$	
Δm_{32}^2	$2.509 \times 10^{-3} \text{ eV}^2$	
$\sin^2(\theta_{12})$	0.304	
$\sin^2(\theta_{13})$	0.0219	
$\sin^2(\theta_{23})$	0.528	0.45
δ_{CP}	-1.601	0.0

Table 2.2: Reference values of the neutrino oscillation parameters for two different oscillation parameter sets.

458 2.5 Overview of Oscillation Effects

459 The analysis presented within this thesis focuses on the determination of oscil-
 460 lation parameters from atmospheric and beam neutrinos. Whilst subject to the

461 same oscillation formalism, the way in which the two samples have sensitivity
462 to the different oscillation parameters differs significantly.

463 Atmospheric neutrinos have a varying baseline, or “path length” L , such that
464 the distance each neutrino travels before interacting is dependent upon the zenith
465 angle, θ_Z . As primary cosmic rays can interact anywhere between the Earth’s
466 surface and $\sim 50\text{km}$ above that, the height, h , in the atmosphere at which the
467 neutrino was generated also affects the path length,

$$L = \sqrt{(R_E + h)^2 - R_E^2 (1 - \cos^2(\theta_Z))} - R_E \cos(\theta_Z). \quad (2.16)$$

468 Where $R_E = 6,371\text{km}$ is the Earth’s radius. This assumes a spherically
469 symmetric Earth model. Therefore, the oscillation probability is dependent upon
470 two parameters, $\cos(\theta_Z)$ and E_ν .

471 The oscillation probability used within this analysis is based on [21]. The
472 neutrino wavefunction in the vacuum Hamiltonian evolves in each layer of
473 constant matter density via

$$i \frac{d\psi_j(t)}{dt} = \frac{m_j^2}{2E_\nu} \psi_j(t) - \sum_k \sqrt{2} G_F N_e U_{ej} U_{ke}^\dagger \psi_k(t), \quad (2.17)$$

474 where m_j^2 is the square of the j^{th} vacuum eigenstate mass, E_ν is the neutrino
475 energy, G_F is Fermi’s constant, N_e is the electron number density and U is the
476 PMNS matrix. The transformation $N_e \rightarrow -N_e$ and $\delta_{CP} \rightarrow -\delta_{CP}$ is applied for
477 antineutrino propagation. Thus, a model of the Earth’s density is required for
478 neutrino propagation. Following the official SK-only methodology [76], this
479 analysis uses the Preliminary Reference Earth Model (PREM) [77] which provides
480 piecewise cubic polynomials as a function of the Earth’s radius. This density
481 profile is illustrated in Figure 2.8. As the propagator requires layers of constant
482 density, the SK methodology approximates the PREM model by using four layers
483 of constant density [76], detailed in Table 2.3.

484 The atmospheric neutrino oscillation probabilities can be presented as two di-
485 mensional “oscillograms” as illustrated in Figure 2.9. The distinct discontinuities,
486 as a function of $\cos(\theta_Z)$, are due to the discontinuous density in the PREM model.



Figure 2.8: The density of the Earth given as a function of the radius, as given by the PREM model (Black), and the constant density four-layer approximation (Blue), as used in the official SK-only analysis.

Layer	Outer Radius [km]	Density [g/cm ³]	Chemical composition (Z/A)
Inner Core	1220	13	0.468 ± 0.029
Outer Core	3480	11.3	0.468 ± 0.029
Lower Mantle	5701	5.0	0.496
Transition Zone	6371	3.3	0.496

Table 2.3: Description of the four layers of the Earth invoked within the constant density approximation of the PREM model [77].

Atmospheric neutrinos have sensitivity to δ_{CP} through the overall event rate. Figure 2.10 illustrates the difference in oscillation probability between CP-conserving ($\delta_{CP} = 0.$) and a CP-violating ($\delta_{CP} = -1.601$) value taken from Asimov A oscillation parameter set (Table 2.2). The result is a complicated oscillation pattern in the appearance probability for sub-GeV upgoing neutrinos. The detector does not have sufficient resolution to resolve these individual patterns so the sensitivity to δ_{CP} for atmospheric neutrinos comes via the overall normalisation of these events.

The presence of matter means that the effect δ_{CP} has on the oscillation probability is not equal between neutrinos and antineutrinos. Furthermore, the interaction cross-section for neutrinos is larger than for antineutrinos so the two

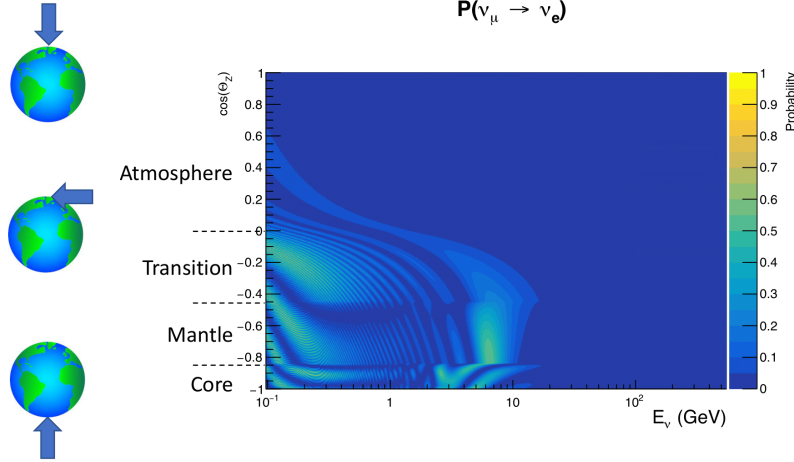


Figure 2.9: An “oscillogram” that depicts the $P(\nu_\mu \rightarrow \nu_e)$ oscillation probability as a function of neutrino energy and cosine of the zenith angle. The zenith angle is defined such that $\cos(\theta_Z) = 1.0$ represents neutrinos that travel from directly above the detector. The four-layer constant density PREM model approximation is used and Asimov A oscillation parameters are assumed (Table 2.2).

498 effects have to be disentangled. These effects are further convoluted by detector
 499 efficiencies as SK cannot distinguish neutrinos and antineutrinos well. All of
 500 these effects lead to a difference in the number of neutrinos detected compared
 501 to antineutrinos. This changes how the δ_{CP} normalisation term is observed,
 502 resulting in a very complex sensitivity to δ_{CP} .

503 The vacuum and matter oscillation probabilities for $P(\nu_e \rightarrow \nu_e)$ and $P(\bar{\nu}_e \rightarrow$
 504 $\bar{\nu}_e)$ are presented in Figure 2.11, where the PREM model has been assumed. The
 505 oscillation probability for both neutrinos and antineutrinos is affected in the
 506 presence of matter. However, the resonance effects around $O(5)\text{GeV}$ only occur
 507 for neutrinos in the normal mass hierarchy and antineutrinos in the inverse mass
 508 hierarchy. The exact position and amplitude of the resonance depend on $\sin^2(\theta_{23})$,
 509 further increasing the atmospheric neutrinos’ sensitivity to the parameter.

510 As the T2K beam flux is centered at the first oscillation maximum ($E_\nu =$
 511 0.6GeV) [41], the sensitivity to δ_{CP} is predominantly observed as a change in the
 512 event-rate of e-like samples in $\nu/\bar{\nu}$ modes. Figure 2.12 illustrates the $P(\nu_\mu \rightarrow \nu_e)$
 513 oscillation probability for a range of δ_{CP} values. A circular modulation of the

$$\mathbf{P}(\nu_\mu \rightarrow \nu_e; \delta_{CP} = -1.601) - \mathbf{P}(\nu_\mu \rightarrow \nu_e; \delta_{CP} = 0)$$

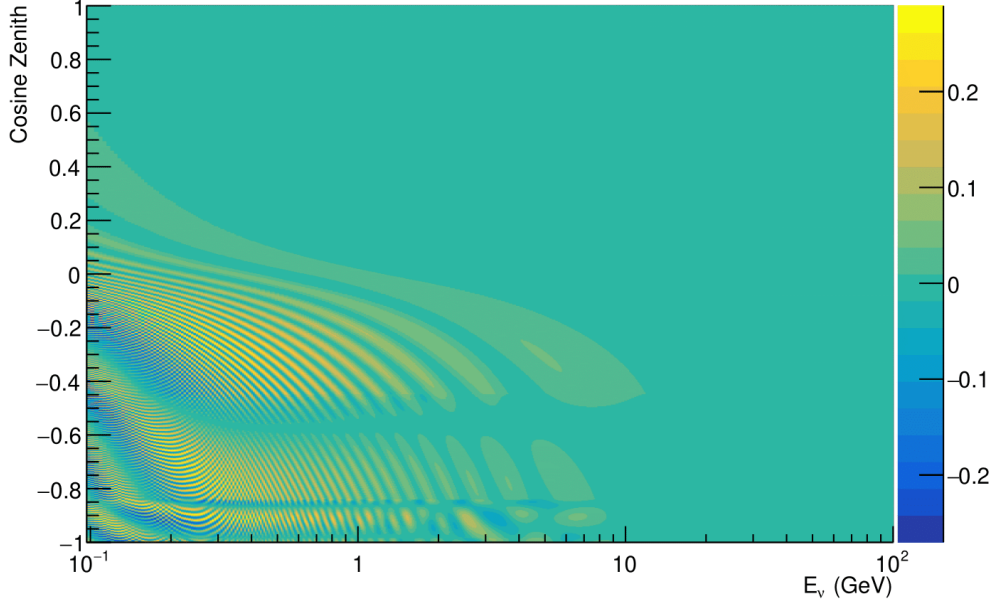


Figure 2.10: The effect of δ_{CP} for atmospheric neutrinos given in terms of the neutrino energy and zenith angle. This oscillogram compares the $P(\nu_\mu \rightarrow \nu_e)$ oscillation probability for a CP conserving ($\delta_{CP} = 0.0$) and a CP violating ($\delta_{CP} = -1.601$) value taken from the Asimov A parameter set. The other oscillation parameters assume the Asimov A oscillation parameter set given in Table 2.2.

514 first oscillation peak (in both magnitude and position) is observed when varying
 515 throughout the allowable values of δ_{CP} . The CP-conserving values of $\delta_{CP} = 0, \pi$
 516 have a lower(higher) oscillation maximum than the CP-violating values of $\delta_{CP} =$
 517 $-\pi/2$ ($\delta_{CP} = \pi/2$). A sub-dominant shift in the energy of the oscillation peak is
 518 also present, which aids in separating the two CP-conserving values of δ_{CP} .

519 T2K's sensitivity to $\sin^2(\theta_{23})$ and Δm_{32}^2 is observed as a shape-based variation
 520 of the muon-like samples, as illustrated in Figure 2.12. The value of Δm_{32}^2 laterally
 521 shifts the position of the oscillation dip (around $E_\nu \sim 0.6\text{GeV}$) in the $P(\nu_\mu \rightarrow \nu_\mu)$
 522 oscillation probability. A variation of $\sin^2(\theta_{23})$ is predominantly observed as
 523 a vertical shift of the oscillation dip with second-order horizontal shifts being
 524 due to matter effects. The beam neutrinos have limited sensitivity to matter
 525 effects due to the relatively shorter baseline as well as the Earth's mantle being
 526 a relatively low-density material (as compared to the Earth's core). For some



Figure 2.11: An illustration of the matter-induced effects on the oscillation probability, given as a function of neutrino energy and zenith angle. The top row of panels gives the $P(\nu_e \rightarrow \nu_e)$ oscillation probability and the bottom row illustrates the $P(\bar{\nu}_e \rightarrow \bar{\nu}_e)$ oscillation probability. The left column highlights the oscillation probability in a vacuum, whereas the middle and right column represents the oscillation probabilities when the four-layer fixed density PREM model is assumed. All oscillation probabilities assume the “Asimov A” set given in Table 2.2, but importantly, the right column sets an inverted mass hierarchy. The “matter resonance” effects at $E_\nu \sim 5\text{GeV}$ can be seen in the $P(\nu_e \rightarrow \nu_e)$ for normal mass hierarchy and $P(\bar{\nu}_e \rightarrow \bar{\nu}_e)$ for inverted hierarchy.

527 values of δ_{CP} , the degeneracy in the number of e-like events allows the mass
 528 hierarchy to be broken. This leads to a δ_{CP} -dependent mass hierarchy sensitivity
 529 which can be seen in Figure 2.13.

530 Whilst all oscillation channels should be included for completeness, the
 531 computational resources required to run a fit are limited and any reasonable
 532 approximations which reduce the number of oscillation probability calculations
 533 that need to be made should be applied. The $\nu_e \rightarrow \nu_{e,\mu,\tau}$ (and antineutrino

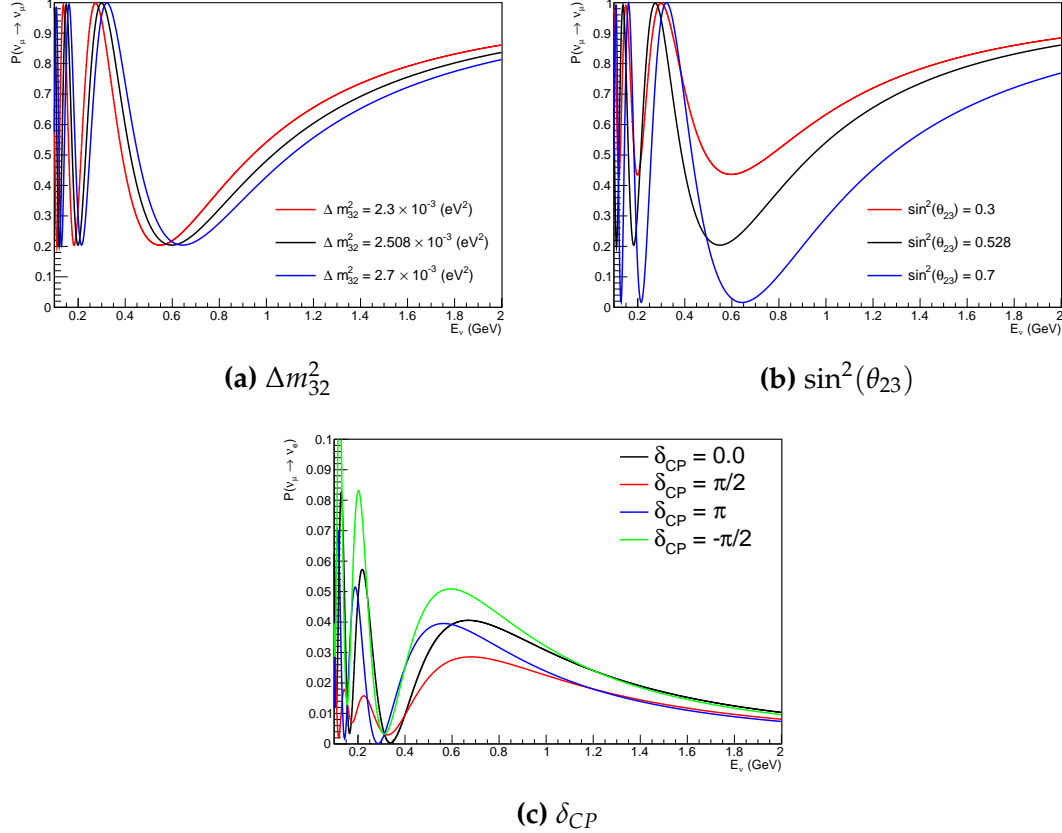


Figure 2.12: The oscillation probability for beam neutrino events given as a function of neutrino energy. All oscillation parameters assume the “Asimov A” set given in Table 2.2 unless otherwise stated. Each panel represents a change in one of the oscillation parameters whilst keeping the remaining parameters fixed.

equivalent) oscillations can be ignored for beam neutrinos as the $\nu_e/\bar{\nu}_e$ fluxes are approximately two orders of magnitude smaller than the corresponding $\nu_\mu/\bar{\nu}_\mu$ flux. Furthermore, as the peak neutrino energy of the beam is well below the threshold for charged current tau production ($E_\nu = 3.5\text{GeV}$ [57]), only a small proportion of the neutrinos produced in the beam have the required energy. For the few neutrinos that have sufficient energy, the oscillation probability is very small due to their energy being well above the oscillation maximum (small value of L/E). Whilst these approximations have been made for the beam neutrinos, the atmospheric flux of ν_e is of the same order of magnitude as the ν_μ flux and the energy distribution of atmospheric neutrinos extends well above the tau production threshold. These events can have non-negligible oscillation



Figure 2.13: The number of electron-like events in the FHC and RHC operating mode of the beam, as a function of the oscillation probabilities. Both normal hierarchy (Solid) and inverse hierarchy (Dashed) values of Δm_{32}^2 are given.

⁵⁴⁵ probabilities due to the further distance they travel.

3

546

547

T2K and SK Experiment Overview

548 As the successor of the Kamiokande experiment, the Super-Kamiokande (SK)
549 collaboration has been leading atmospheric neutrino oscillation analyses for
550 over two decades. The detector has provided some of the strongest constraints
551 on proton decay and the first precise measurements of the Δm_{32}^2 and $\sin^2(\theta_{23})$
552 neutrino oscillation parameters. The history, detection technique, and operation
553 of the SK detector is described in section 3.1.

554 The Tokai-to-Kamioka (T2K) experiment was one of the first long-baseline
555 experiments to use both neutrino and antineutrino beams to precisely measure
556 charge parity violation within the neutrino sector. The T2K experiment observed
557 the first hints of a non-zero $\sin^2(\theta_{13})$ measurement and continues to lead the
558 field with the constraints it provides on $\sin^2(\theta_{13})$, $\sin^2(\theta_{23})$, Δm_{32}^2 and δ_{CP} . In
559 section 3.2, the techniques that T2K use to generate the neutrino beam and
560 constrain systematic parameter through near detector constraints are described.

561 3.1 The Super-Kamiokande Experiment

562 The SK experiment began taking data in 1996 [78] and has had many modifi-
563 cations throughout its operation. There have been seven defined periods of
564 data taking as noted in Table 3.1. Data taking began in SK-I which ran for five

years. Between the SK-I and SK-II periods, approximately 55% of the PMTs were damaged during maintenance [79]. Those that survived were equally distributed throughout the detector in the SK-II era, which resulted in a reduced 19% photo-coverage. From SK-III onwards, repairs to the detector meant the full suite of PMTs was operational recovering the 40% photo-coverage. Before the start of SK-IV, the data acquisition and electronic systems were upgraded. Between SK-IV and SK-V, a significant effort was placed into tank open maintenance and repair/replacement of defective PMTs in preparation for the Gadolinium upgrade; a task for which the author of this thesis was required. Consequently, the detector conditions were significantly changed from this point. SK-VI marked the start of the SK-Gd era, with the detector being doped with gadolinium at a concentration of 0.01% by concentration. SK-VII, which started during the writing of this thesis, has increased the gadolinium concentration to 0.03% for continued operation [80].

The oscillation analysis presented within this thesis focuses on the SK-IV period of running and the data taken within it. This follows from the recent SK analysis presented in [81]. Therefore, the information presented within this section focuses on that period.

Period	Start Date	End Date	Live-time (days)
I	April 1996	July 2001	1489.19
II	October 2002	October 2005	798.59
III	July 2006	September 2008	518.08
IV	September 2008	May 2018	3244.4
V	January 2019	July 2020	461.02
VI	July 2020	May 2022	583.3
VII	May 2022	Ongoing	N/A

Table 3.1: The various SK periods and their respective live-time. The SK-VI live-time is calculated until 1st April 2022. SK-VII started during the writing of this thesis.

3.1.1 The SK Detector

The basic structure of the Super-Kamiokande (SK) detector is a cylindrical tank with a diameter 39.3m and height 41.1m filled with ultrapure water [79]. A diagram of the significant components of the SK detector is given in Figure 3.1.

586 The SK detector is situated in the Kamioka mine in Gifu, Japan. The mine is under-
 587 ground with roughly 1km rock overburden (2.7km water equivalent overburden)
 588 [82]. At this depth, the rate of cosmic ray muons is significantly decreased to a
 589 value of $\sim 2\text{Hz}$ (net rate). The top of the tank is covered with stainless steel which
 590 is designed as a working platform for maintenance, calibration, and location for
 591 high voltage and data acquisition electronics.



Figure 3.1: A schematic diagram of the Super-Kamiokande Detector. Taken from [83].

592 A smaller cylindrical structure (36.2m diameter, 33.8m height) is situated
 593 inside the tank, with an approximate 2m gap between this structure and the outer
 594 tank wall. The purpose of this structure is to support the photomultiplier tubes
 595 (PMTs). The volume inside and outside the support structure is referred to as the
 596 inner detector (ID) and outer detector (OD), respectively. In the SK-IV era, the
 597 ID and OD are instrumented by 11,129 50cm and 1,885 20cm PMTs respectively
 598 [79]. The ID contains a 32kton mass of water. Many analyses performed at SK
 599 use a “fiducial volume” defined by the volume of water inside the ID excluding
 600 some distance to the ID wall. This reduces the volume of the detector which is
 601 sensitive to neutrino events but reduces radioactive backgrounds and allows for

602 better reconstruction performance. The nominal fiducial volume is defined as the
603 area contained inside 2m from the ID wall for a total of 22.5kton water [84].

604 The two regions of the detector (ID and OD) are optically separated with
605 opaque black plastic hung from the support structure. The purpose of this is
606 to determine whether an event entered or exited the ID. This allows cosmic ray
607 muons and partially contained events to be tagged and separated from neutrino
608 events entirely contained within the ID. This black plastic is also used to cover
609 the area between the ID PMTs to reduce photon reflection from the ID walls.
610 Opposite to this, the OD is lined with a reflective material to allow photons to
611 reflect around inside the OD until collected by one of the PMTs. Furthermore,
612 each OD PMT is optically coupled with $50 \times 50\text{cm}$ plates of wavelength shifting
613 acrylic which increases the efficiency of light collection [82].

614 In the SK-IV data-taking period, the photocathode coverage of the detector, or
615 the fraction of the ID wall instrumented with PMTs, is $\sim 40\%$ [82]. The PMTs have
616 a quantum efficiency (the ratio of detected electrons to incident photons) of $\sim 21\%$
617 for photons with wavelengths of $360\text{nm} < \lambda < 390\text{nm}$ [85, 86]. The proportion
618 of photoelectrons that produce a signal in the dynode of a PMT, termed the
619 collection efficiency, is $> 70\%$ [82]. The PMTs used within SK are most sensitive
620 to photons with wavelength $300\text{nm} \leq \lambda \leq 600\text{nm}$ [82]. One disadvantage of
621 using PMTs as the detection media is that the Earth's geomagnetic field can
622 modify its response. Therefore, a set of compensation coils is built around the
623 inner surface of the detector to mitigate this effect [82].

624 The SK detector is filled with ultrapure water, which in a perfect world, con-
625 tains no impurities. However, bacteria and organic compounds can significantly
626 degrade the water quality. This decreases the attenuation length, which reduces
627 the total number of photons that hit a PMT. To combat this, a sophisticated water
628 treatment system has been developed [82, 87]. UV lights, mechanical filters, and
629 membrane degasifiers are used to reduce the bacteria, suspended particulates,
630 and radioactive materials from the water. The flow of water within the tank
631 is also critical as it can remove stagnant bacterial growth or build-up of dust

632 on the surfaces within the tank. Gravity drifts impurities in the water towards
633 the bottom of the tank which, if left uncontrolled, can create asymmetric water
634 conditions between the top and bottom of the tank. Typically, the water entering
635 the tank is cooled below the ambient temperature of the tank to control convection
636 and inhibit bacteria growth. Furthermore, the rate of dark noise hits within PMTs
637 is sensitive to the PMT temperature [88]. Therefore controlling the temperature
638 gradients within the tank is beneficial for stable measurements.

639 SK-VI is the first phase of the SK experiment to use gadolinium dopants
640 within the ultrapure water [80]. As such, the SK water system had to be replaced
641 to avoid removing the gadolinium concentrate from the ultrapure water [65]. For
642 an inverse β -decay (IBD) interaction on a water target, the emitted neutron is
643 thermally captured on hydrogen. This process releases a 2.2MeV γ ray which is
644 difficult to detect as the resulting Compton scattered electrons are very close to the
645 Cherenkov threshold, limiting detection capability. Thermal capture of neutrons
646 on gadolinium generates γ rays with higher energy (8MeV [65]) meaning they
647 are more easily detected and reconstructed. SK-VI has 0.01% Gd loading (0.02%
648 gadolinium sulphate by mass) which causes \approx 50% of neutrons emitted by IBD
649 to be captured on gadolinium[89]. Whilst predominantly useful for low energy
650 analyses, Gd loading allows better $\nu/\bar{\nu}$ separation for atmospheric neutrino
651 event selections [90]. Efforts are currently in place to increase the gadolinium
652 concentrate to 0.03% for \approx 75% neutron capture efficiency on gadolinium [91].
653 The final stage of loading targets 0.1% concentrate for \approx 90% neutron capture
654 efficiency on gadolinium.

655 3.1.2 Calibration

656 The calibration of the SK detector is documented in [79] and summarised below.
657 The analysis presented within this thesis is dependent upon ‘high energy events’
658 (Charged particles with $O(> 100)$ MeV momenta). These are events that are
659 expected to generate a larger number of photons such that each PMT will
660 be hit with multiple photons. The reconstruction of these events depends

upon the charge deposited within each PMT and the timing response of each individual PMT. Therefore, the most relevant calibration techniques to this thesis are outlined.

Before installation, 420 PMTs were calibrated to have identical charge responses and then distributed throughout the tank in a cross-shape pattern (As illustrated by Figure 3.2). These are used as a standardised measure for the rest of the PMTs installed at similar geometric positions within SK to be calibrated against. To perform this calibration, a xenon lamp is located at the center of the SK tank which flashes uniform light at 1Hz. This allows for geometrical effects, water quality variation, and timing effects to be measured in situ throughout normal data-taking periods.

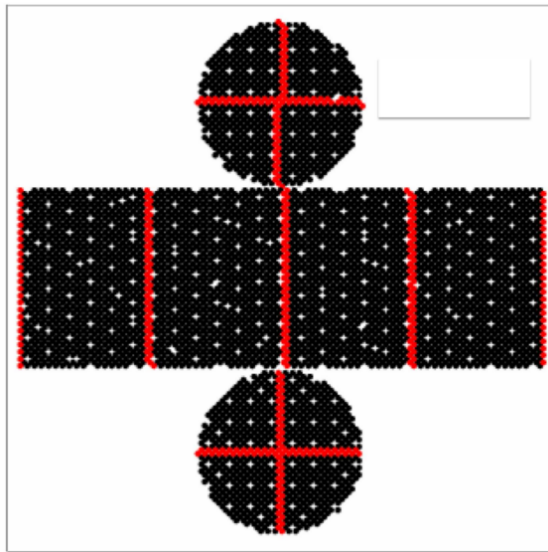


Figure 3.2: The location of “standard PMTs” (red) inside the SK detector. Taken from [79].

When specifically performing calibration of the detector (in out-of-data taking mode), the water in the tank was circulated to avoid top/bottom asymmetric water quality. Any non-uniformity within the tank significantly affects the PMT hit probability through scattering or absorption. This becomes a dominant effect for very low-intensity light sources that are designed such that only one photon is incident upon a given PMT.

678 The gain of a PMT is defined as the ratio of the total charge of the signal
 679 produced compared to the charge of photoelectrons emitted by the photocathodes
 680 within the PMT. To calibrate the signal of each PMT, the “relative” and “absolute”
 681 gain values are measured. The relative gain is the variation of gain among each
 682 of the PMTs whereas the absolute gain is the average gain of all PMTs.

683 The relative gain is calibrated as follows. A laser is used to generate two
 684 measurements: a high-intensity flash that illuminates every PMT with a sufficient
 685 number of photons, and a low-intensity flash in which only a small number
 686 of PMTs collect light. The first measurement creates an average charge, $Q_{obs}(i)$
 687 on PMT i , whereas the second measurement ensures that each hit PMT only
 688 generates a single photoelectron. For the low-intensity measurement, the number
 689 of times each PMT records a charge larger than 1/4 photoelectrons, $N_{obs}(i)$, is
 690 counted. The values measured can be expressed as

$$\begin{aligned} Q_{obs}(i) &\propto I_H \times f(i) \times \epsilon(i) \times G(i), \\ N_{obs}(i) &\propto I_L \times f(i) \times \epsilon(i). \end{aligned} \tag{3.1}$$

691 Where I_H and I_L is the intensity of the high and low flashes, $f(i)$ is the
 692 acceptance efficiency of the i^{th} PMT, $\epsilon(i)$ is the product of the quantum and
 693 collection efficiency of the i^{th} PMT and $G(i)$ is the gain of the i^{th} PMT. The relative
 694 gain for each PMT can be determined by taking the ratio of these quantities.

695 The absolute gain calibration is performed by observing fixed energy γ -rays
 696 of $E_\gamma \sim 9\text{MeV}$ emitted isotropically from neutron capture on a NiCf source
 697 situated at the center of the detector. This generates a photon yield of about 0.004
 698 photoelectrons/PMT/event, meaning that $> 99\%$ of PMT signals are generated
 699 from single photoelectrons. A charge distribution is generated by performing
 700 this calibration over all PMTs, and the average value of this distribution is taken
 701 to be the absolute gain value.

702 As mentioned in subsection 3.1.1, the average quantum and collection effi-
 703 ciency for the SK detector PMTs is $\sim 21\%$ and $> 70\%$ respectively. However,
 704 these values do differ between each PMT and need to be calibrated accordingly.

705 Consequently, the NiCf source is also used to calibrate the “quantum \times collection”
706 efficiency (denoted “QE”) value of each PMT. The NiCf low-intensity source is
707 used as the PMT hit probability is proportional to the QE ($N_{obs}(i) \propto \epsilon(i)$ in
708 Equation 3.1). A Monte Carlo prediction which includes photon absorption,
709 scattering, and reflection is made to estimate the number of photons incident on
710 each PMT and the ratio of the number of predicted to observed hits is calculated.
711 The difference is attributed to the QE efficiency of that PMT. This technique is
712 extended to calculate the relative QE efficiency by normalizing the average of
713 all PMTs which removes the dependence on the light intensity.

714 Due to differing cable lengths and readout electronics, the timing response
715 between a photon hitting the PMT and the signal being captured by the data
716 acquisition can be different between each PMT. Due to threshold triggers (De-
717 scribed in subsection 3.1.3), the time at which a pulse reaches a threshold is
718 dependent upon the size of the pulse. This is known as the ‘time-walk’ effect
719 and also needs to be accounted for in each PMT. To calibrate the timing response,
720 a pulse of light with width 0.2ns is emitted into the detector through a diffuser.
721 Two-dimensional distributions of time and pulse height (or charge) are made
722 for each PMT and are used to calibrate the timing response. This is performed
723 in-situ during data taking with the light source pulsing at 0.03Hz.

724 The top/bottom water quality asymmetry is measured using the NiCf calibra-
725 tion data and cross-referencing these results to the “standard PMTs”. The water
726 attenuation length is continuously measured by the rate of vertically-downgoing
727 cosmic-ray muons which enter via the top of the tank.

728 Dark noise is where a PMT registers a pulse that is consistent with a single
729 photoelectron emitted from photon detection despite the PMT being in complete
730 darkness. This is predominately caused by two processes. Firstly there is
731 intrinsic dark noise which is where photoelectrons gain enough thermal energy
732 to be emitted from the photocathode, and secondly, the radioactive decay of
733 contaminants inside the structure of the PMT. Typical dark noise rate for PMTs
734 used within SK are $O(3)\text{kHz}$ [82]. This is lower than the expected number of

735 photons generated for a ‘high energy event’ (As described in subsection 3.1.4)
736 but instability in this value can cause biases in reconstruction. Dark noise is
737 related to the gain of a PMT and is calibrated using hits inside a time window
738 recorded before an event trigger [92].

739 3.1.3 Data Acquisition and Triggering

740 As the analysis presented in this thesis will only use the SK-IV period of the
741 SK experiment so this subsection focuses on the relevant points of the data
742 acquisition and triggering systems to that SK period. The earlier data acquisition
743 and triggering systems are documented in [93, 94].

744 Before the SK-IV period started, the existing front-end electronics were re-
745 placed with “QTC-Based Electronics with Ethernet, QBEE” systems [95]. When
746 the QBEE observes a signal above a 1/4 photoelectron threshold, the charge-to-
747 time (QTC) converter generates a rectangular pulse. The start of the rectangular
748 pulse indicates the time at which the analog photoelectron signal was received
749 and the width of the pulse indicates the total charge integrated throughout the
750 signal. This is then digitized by time-to-digital converters and sent to the “front-
751 end” PCs. The digitized signal from every QBEE is then chronologically ordered
752 and sent to the “merger” PCs. It is the merger PCs that apply the software trigger.
753 Any triggered events are passed to the “organizer” PC. This sorts the data stream
754 of multiple merger PCs into chronologically ordered events, which are then saved
755 to disk. The schematic of data flow from PMTs to disk is illustrated in Figure 3.3.

756 The software trigger (described in [97]) operates by determining the number
757 of PMT hits within a 200ns sliding window, N_{200} . This window coincides with the
758 maximum time that a Cherenkov photon would take to traverse the length of the
759 SK tank [94]. For lower energy events that generate fewer photons, this technique
760 is useful for eliminating background processes like dark noise and radioactive
761 decay which would be expected to be separated in time. When the value of
762 N_{200} exceeds some pre-defined threshold, a software trigger is issued. There are
763 several trigger thresholds used within the SK-IV period which are detailed in

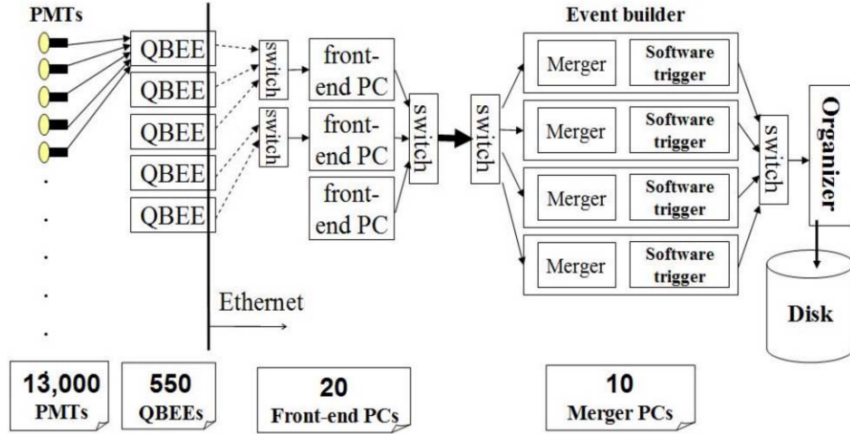


Figure 3.3: Schematic view of the data flow through the data acquisition and online system. Taken from [96].

764 Table 3.2. If one of these thresholds is met, the PMT hits within an extended time
 765 window are also read out and saved to disk. In the special case of an event that
 766 exceeds the SHE trigger but does not exceed the OD trigger, the AFT trigger looks
 767 for delayed coincidences of 2.2MeV gamma rays emitted from neutron capture in
 768 a $535\mu\text{s}$ window after the SHE trigger. A similar but more complex “Wideband
 769 Intelligent Trigger (WIT)” has been deployed and is described in [98].

Trigger	Acronym	Condition	Extended time window (μs)
Super Low Energy	SLE	>34/31 hits	1.3
Low Energy	LE	>47 hits	40
High Energy	HE	>50 hits	40
Super High Energy	SHE	>70/58 hits	40
Outer Detector	OD	>22 hits in OD	N/A

Table 3.2: The trigger thresholds and extended time windows saved around an event which were utilised throughout the SK-IV period. The exact thresholds can change and the values listed here represent the thresholds at the start and end of the SK-IV period.

770 3.1.4 Cherenkov Radiation

771 Cherenkov light is emitted from any highly energetic charged particle traveling
 772 with relativistic velocity, β , greater than the local speed of light in a medium [99].

⁷⁷³ Cherenkov light is formed at the surface of a cone with a characteristic pitch angle,

$$\cos(\theta) = \frac{1}{\beta n}. \quad (3.2)$$

⁷⁷⁴ Where n is the refractive index of the medium. Consequently, the Cherenkov
⁷⁷⁵ momentum threshold, P_{thres} , is dependent upon the mass, m , of the charged
⁷⁷⁶ particle moving through the medium,

$$P_{thres} = \frac{m}{\sqrt{n^2 - 1}}. \quad (3.3)$$

⁷⁷⁷ For water, where $n = 1.33$, the Cherenkov threshold momentum and energy
⁷⁷⁸ for various particles are given in Table 3.3. In contrast, γ -rays are detected
⁷⁷⁹ indirectly via the combination of photons generated by Compton scattering
⁷⁸⁰ and pair production. The threshold for detection in the SK detector is typically
⁷⁸¹ higher than the threshold for photon production. This is due to the fact that the
⁷⁸² attenuation of photons in the water means that typically $\sim 75\%$ of Cherenkov
⁷⁸³ photons reach the ID PMTs. Then the collection and quantum efficiencies
⁷⁸⁴ described in subsection 3.1.1 result in the number of detected photons being
⁷⁸⁵ lower than the number of photons which reach the PMTs.

Particle	Threshold Momentum (MeV)	Threshold Energy (MeV)
Electron	0.5828	0.7751
Muon	120.5	160.3
Pion	159.2	211.7
Proton	1070.0	1423.1

Table 3.3: The threshold momentum and total energy for a particle to generate Cherenkov light in ultrapure water, as calculated in Equation 3.2 in ultrapure water which has refractive index $n = 1.33$.

⁷⁸⁶ The Frank-Tamm equation [100] describes the relationship between the num-
⁷⁸⁷ ber of Cherenkov photons generated per unit length, dN/dx , the wavelength of
⁷⁸⁸ the photons generated, λ , and the relativistic velocity of the charged particle,

$$\frac{d^2N}{dxd\lambda} = 2\pi\alpha \left(1 - \frac{1}{n^2\beta^2}\right) \frac{1}{\lambda^2}. \quad (3.4)$$

789 where α is the fine structure constant. For a 100MeV momentum electron,
 790 approximately 330 photons will be produced per centimeter in the $300\text{nm} \leq \lambda \leq$
 791 700nm region which the ID PMTs are most sensitive to [82].

792 3.2 The Tokai to Kamioka Experiment

793 The Tokai to Kamioka (T2K) experiment is a long-baseline neutrino oscillation
 794 experiment located in Japan. Proposed in the early 2000s [83, 101] to replace
 795 K2K [102], T2K was designed to observe electron neutrino appearance whilst
 796 precisely measuring the oscillation parameters associated with muon neutrino
 797 disappearance [103]. The experiment consists of a neutrino beam generated
 798 at the Japan Proton Accelerator Research Complex (J-PARC), a suite of near
 799 detectors situated 280m from the beam target, and the Super Kamiokande far
 800 detector positioned at a 295km baseline. The cross-section view of the T2K
 801 experiment is drawn in Figure 3.4.

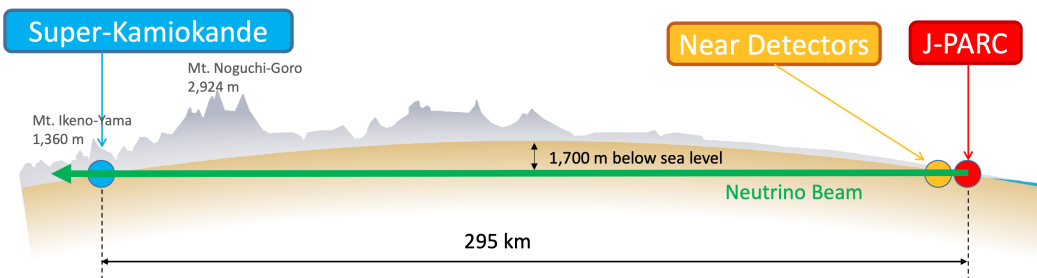


Figure 3.4: The cross-section view of the Tokai to Kamioka experiment illustrating the beam generation facility at J-PARC, the near detector situated at a baseline of 280m and the Super Kamiokande far detector situated 295km from the beam target.

802 The T2K collaboration makes world-leading measurements of the $\sin^2(\theta_{23})$,
 803 Δm_{32}^2 , and δ_{CP} oscillation parameters. Improvements in the precision and accu-
 804 racy of parameter estimates are still being made by including new data samples
 805 and developing the models which describe the neutrino interactions and detector
 806 responses [104]. Electron neutrino appearance was first observed at T2K in 2014
 807 [105] with 7.3σ significance.

808 The near detectors provide constraints on the beam flux and cross-section
 809 model parameters used within the oscillation analysis by observing the unoscil-
 810 lated neutrino beam. There are a host of detectors situated in the near detector hall
 811 (As illustrated in Figure 3.5): ND280 (subsection 3.2.3), INGRID (subsection 3.2.4),
 812 NINJA [106], WAGASCI [107], and Baby-MIND [108]. The latter three are not
 813 currently used within the oscillation analysis presented in this thesis.

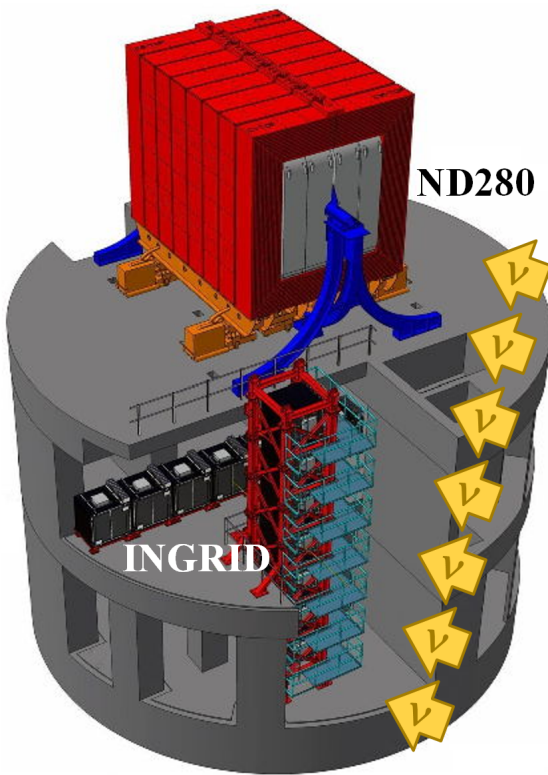


Figure 3.5: The near detector suite for the T2K experiment showing the ND280 and INGRID detectors. The distance between the detectors and the beam target is 280m.

814 Whilst this thesis presents the ND280 in terms of its purpose for the oscillation
 815 analysis, the detector can also make many cross-section measurements at neutrino
 816 energies of $O(1)$ GeV for the different targets within the detector [109, 110]. These
 817 measurements are of equal importance as they can lead the way in determining
 818 the model parameters used in the interaction models for the future high-precision
 819 era of neutrino physics.

3.2.1 Analysis Overview

There are two independent fitters, MaCh3 and BANFF, which perform the near detector fit. MaCh3 uses a bayesian Markov Chain Monte Carlo fitting technique, whereas BANFF uses a frequentist gradient descent technique. The output of each fitter is compared as a method of cross-checking the behaviour of the two fitters. This is done by comparing: the Monte Carlo predictions using various tunes, the likelihood that is calculated in each fitter and the post-fit constraint associated with every parameter used in the fit. Once validated, the output converted into a covariance matrix to describe the error and correlations between all the flux and cross-section parameters. This is then propagated to the far-detector oscillation analysis group.

The far detector group has three independent fitters: P-Theta, VALOR and MaCh3. The first two fitters use a hybrid frequentist fitting technique where the likelihood is minimised with respect to the parameters of interest and marginalised over all other parameters. These fitters use the covariance provided by the near detector fitters as a basis for implementing the near detector constraints. The MaCh3 fitter uses a simultaneous fit of all near and far detector samples. This removes any Gaussian assumptions when making the covariance matrix from the near detector results. The results for all three fitters are compares using a technique similar to the validation of the near detector fitters.

There are three particular tunes of the T2K flux and low energy cross section model typically considered. Firstly, the “generated” tune which is the set of dial values with which the Monte Carlo was generated. Secondly, the set of dial values which are taken from external data measurements and used as inputs. These are the “pre-fit” dial values. The reason these two sets of dial values are different is that the external data measurements are continually updated but it is very computationally intensive to regenerate a Monte Carlo prediction after each update. The final tune is the “post-fit”, “post-ND fit” or “post-BANFF” dial values. These are the values taken from the constraints provided by the near detector.

3.2.2 The Neutrino Beam

The neutrino beam used within the T2K experiment is described in [37, 41] and summarised below. The accelerator facility at J-PARC is composed of two sections; the primary and secondary beamlines. Figure 3.6 illustrates a schematic of the beamline, focusing mostly on the components of the secondary beamline. The primary beamline has three accelerators that progressively accelerate protons; a linear accelerator, a rapid-cycling synchrotron, and the main-ring (MR) synchrotron. Once fully accelerated by the MR, the protons have a kinetic energy of 30GeV. Eight bunches of these protons, separated by 500ns, are extracted per “spill” from the MR and directed towards a graphite target (a rod of length 91.4cm and diameter 2.6cm). Spills are extracted at 0.5Hz with $\sim 3 \times 10^{14}$ protons contained per spill.

The secondary beamline consists of three main components: the target station, the decay volume, and the beam dump. The target station is comprised of the target, beam monitors, and three magnetic focusing horns. The proton beam interacts with the graphite target to form a secondary beam of mostly pions and kaons. The secondary beam travels through a 96m long decay volume, generating neutrinos through the following decays [37],

$$\begin{array}{ll}
\pi^+ \rightarrow \mu^+ + \nu_\mu & \pi^- \rightarrow \mu^- + \bar{\nu}_\mu \\
K^+ \rightarrow \mu^+ + \nu_\mu & K^- \rightarrow \mu^- + \bar{\nu}_\mu \\
\rightarrow \pi^0 + e^+ + \nu_e & \rightarrow \pi^0 + e^- + \bar{\nu}_e \\
\rightarrow \pi^0 + \mu^+ + \nu_\mu & \rightarrow \pi^0 + \mu^- + \bar{\nu}_\mu \\
K_L^0 \rightarrow \pi^- + e^+ + \nu_e & K_L^0 \rightarrow \pi^+ + e^- + \bar{\nu}_e \\
\rightarrow \pi^- + \mu^+ + \nu_\mu & \rightarrow \pi^+ + \mu^- + \bar{\nu}_\mu \\
\mu^+ \rightarrow e^+ + \bar{\nu}_\mu + \nu_e & \mu^- \rightarrow e^- + \nu_\mu + \bar{\nu}_e.
\end{array}$$

The electrically charged component of the secondary beam is focused towards the far detector by the three magnetic horns. These horns direct charged particles of a particular polarity towards SK whilst defocusing the oppositely charged particles. This allows a mostly neutrino or mostly antineutrino beam to be used within the experiment, denoted as “forward horn current (FHC)” or “reverse horn current (RHC)” respectively.

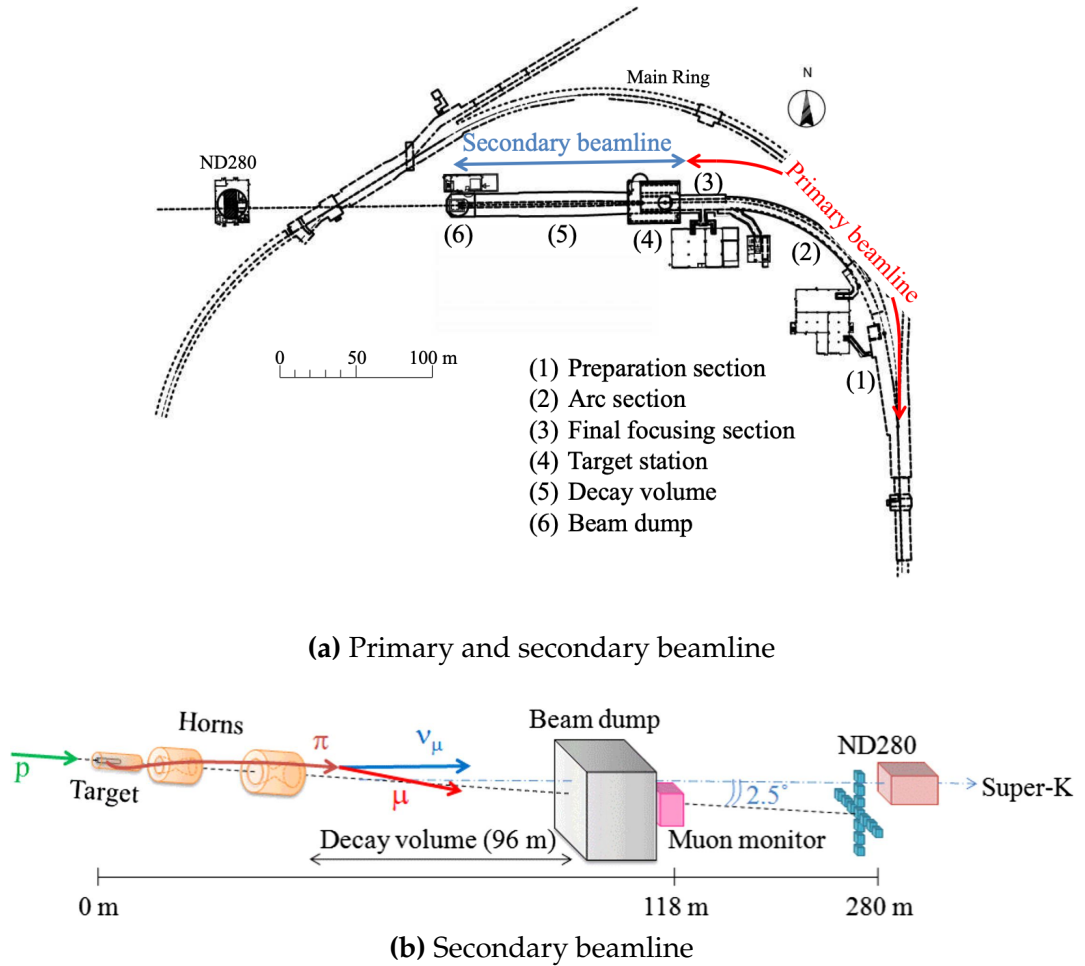


Figure 3.6: Top panel: Bird's eye view of the most relevant part of primary and secondary beamline used within the T2K experiment. The primary beamline is the main-ring proton synchrotron, kicker magnet, and graphite target. The secondary beamline consists of the three focusing horns, decay volume, and beam dump. Figure taken from [41]. Bottom panel: The side-view of the secondary beamline including the focusing horns, beam dump and neutrino detectors. Figure taken from [111].

Figure 3.7 illustrates the different contributions to the FHC and RHC neutrino flux. The low energy flux is dominated by the decay of pions whereas kaon decay becomes the dominant source of neutrinos for $E_\nu > 3\text{GeV}$. The “wrong-sign” component, which is the $\bar{\nu}_\mu$ background in a ν_μ beam, and the intrinsic irreducible ν_e background, are predominantly due to muon decay for $E_\nu < 2\text{GeV}$. As the antineutrino production cross-section is smaller than the neutrino cross-section, the wrong-sign component is more dominant in the RHC beam as compared to that in the FHC beam.



Figure 3.7: The Monte Carlo prediction of the energy spectrum for each flavour of neutrino (ν_e , $\bar{\nu}_e$, ν_μ and $\bar{\nu}_\mu$) in the neutrino dominated beam FHC mode (Left) and antineutrino dominated beam RHC mode (Right) expected at SK. Taken from [112].

883 The beam dump, situated at the end of the decay volume, stops all charged
 884 particles other than highly energetic muons ($p_\mu > 5\text{GeV}$). The MuMon detector
 885 monitors the penetrating muons to determine the beam direction and inten-
 886 sity which is used to constrain some of the beam flux systematics within the
 887 analysis [111, 113].

888 The T2K experiment uses an off-axis beam to narrow the neutrino energy
 889 distribution. This was the first implementation of this technique in a long-
 890 baseline neutrino oscillation experiment after its original proposal [114]. Pion
 891 decay, $\pi \rightarrow \mu + \nu_\mu$, is a two-body decay. Consequently, the neutrino energy,
 892 E_ν , can be determined based on the pion energy, E_π , and the angle at which
 893 the neutrino is emitted, θ ,

$$E_\nu = \frac{m_\pi^2 - m_\mu^2}{2(E_\pi - p_\pi \cos(\theta))}, \quad (3.5)$$

894 where m_π and m_μ are the mass of the pion and muon respectively. For a fixed
 895 energy pion, the neutrino energy distribution is dependent upon the angle at
 896 which the neutrinos are observed from the initial pion beam direction. For the
 897 295km baseline at T2K, $E_\nu = 0.6\text{GeV}$ maximises the electron neutrino appearance
 898 probability, $P(\nu_\mu \rightarrow \nu_e)$, whilst minimising the muon disappearance probability,

899 $P(\nu_\mu \rightarrow \nu_\mu)$. Figure 3.8 illustrates the neutrino energy distribution for a range of
 900 off-axis angles, as well as the oscillation probabilities most relevant to T2K.

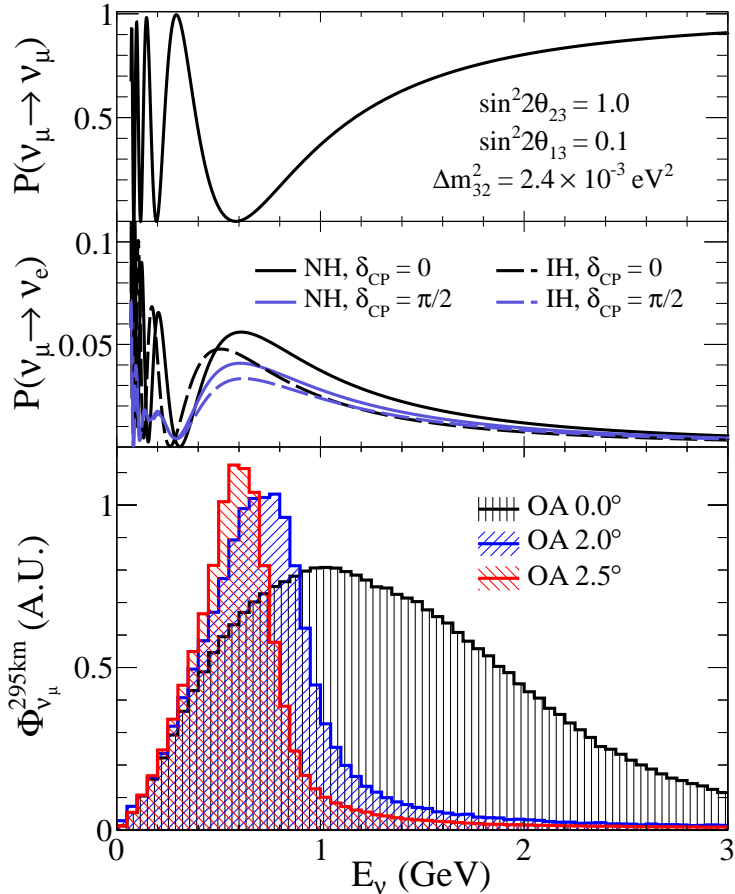


Figure 3.8: Top panel: T2K muon neutrino disappearance probability as a function of neutrino energy. Middle panel: T2K electron neutrino appearance probability as a function of neutrino energy. Bottom panel: The neutrino flux distribution for three different off-axis angles (Arbitrary units) as a function of neutrino energy.

901 3.2.3 The Near Detector at 280m

902 Whilst all the near detectors are situated in the same “pit” located at 280m from
 903 the beamline, the “ND280” detector is the off-axis detector which is situated at
 904 the same off-axis angle as the Super-Kamiokande far detector. It has two primary
 905 functions; firstly it measures the neutrino flux and secondly, it counts the event
 906 rates of different types of neutrino interactions. Both of these constrain the flux
 907 and cross-section systematics invoked within the model for a more accurate
 908 prediction of the expected event rate at the far detector.



Figure 3.9: The components of the ND280 detector. The neutrino beam travels from left to right. Taken from [41].

As illustrated in Figure 3.9, the ND280 detector consists of several sub-detectors. The most important part of the detector for this analysis is the tracker region. This is comprised of two-time projection chambers (TPCs) sandwiched between three fine grain detectors (FGDs). The FGDs contain both hydrocarbon plastics and water targets for neutrino interactions and provide track reconstruction near the interaction vertex. The emitted charged particles can then propagate into the TPCs which provide particle identification and momentum reconstruction. The FGDs and TPCs are further described in subsubsection 3.2.3.1 and subsubsection 3.2.3.2 respectively. The electromagnetic calorimeter (ECAL) encapsulates the tracker region alongside the π^0 detector (P0D). The ECAL measures the deposited energy from photons emitted from interactions within the FGD. The P0D constrains the cross-section of neutral current interactions which generate neutral pions, which is one of the largest backgrounds in the electron neutrino appearance oscillation channel. The P0D and ECAL detectors are detailed in subsubsection 3.2.3.3 and subsubsection 3.2.3.4 respectively. The entire detector is located within a large yoke magnet which produces a 0.2T magnetic field.

field. This design of the magnet also includes a scintillating detector called the side muon range detector (SMRD), which is used to track high-angle muons as well as acting as a cosmic veto. The SMRD is described in subsubsection 3.2.3.5.

3.2.3.1 Fine Grained Detectors

The T2K tracker region is comprised of two fine-grained detectors (FGD) and three Time Projection Chambers (TPC). A detailed description of the FGD design, construction, and assembly is found in [115] and summarised below. The FGDS are the primary target for neutrino interactions with a mass of 1.1 tonnes per FGD. Alongside this, the FGDS are designed to be able to track short-range particles which do not exit the FGD. Typically, short-range particles are low momentum and are observed as tracks that deposit a large amount of energy per unit length. This means the FGD needs good granularity to resolve these particles. The FGDS have the best timing resolution ($\sim 3\text{ns}$) of any of the sub-detectors of the ND280 detector. As such, the FGDS are used for time of flight measurements to distinguish forward-going positively charged particles from backward-going negatively charged particles. Finally, any tracks which pass through multiple sub-detectors are required to be track matched to the FGD.

Both FGDS are made from square scintillator planes of side length 186cm and width 2.02cm. Each plane consists of two layers of 192 scintillator bars in an X or Y orientation. A wavelength-shifting fiber is threaded through the center of each bar and is read out by a multi-pixel photon counter (MPPC). FGD1 is the most upstream of the two FGDS and contains 15 planes of carbon plastic scintillator which is a common target in external neutrino scattering data. As the far detector is a pure water target, 7 of the 15 scintillator planes in FGD2 have been replaced with a hybrid water-scintillator target. Due to the complexity of the nucleus, nuclear effects can not be extrapolated between different nuclei. Therefore having the ability to take data on one target which is the same as external data and another target which is the same as the far detector target is beneficial for reliable model parameter estimates.

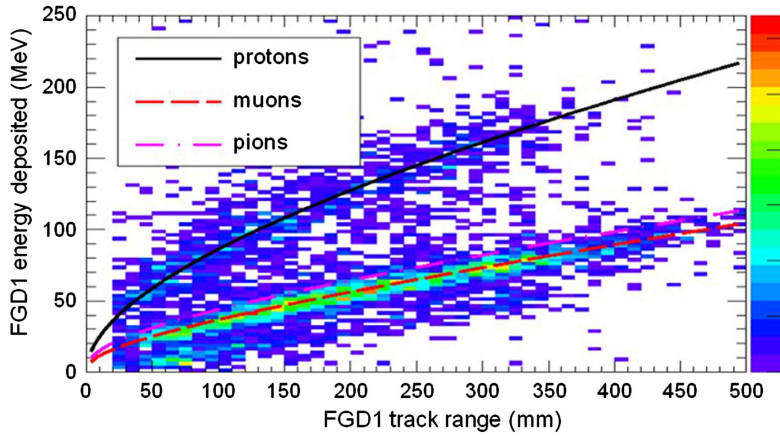


Figure 3.10: Comparison of data to Monte Carlo prediction of integrated deposited energy as a function of track length for particles that stopped in FGD1. Taken from [115].

954 The integrated deposited energy is used for particle identification. The FGD
955 can distinguish protons from other charged particles by comparing the integrated
956 deposited energy from data to Monte Carlo prediction as seen in Figure 3.10.

957 3.2.3.2 Time Projection Chambers

958 The majority of particle identification and momentum measurements within
959 ND280 are provided by three Time Projection Chambers (TPCs) [116]. The
960 TPCs are located on either side of the FGDs. They are located inside of the
961 magnetic field meaning the momentum of a charged particle can be determined
962 from the bending of the track.

963 Each TPC module consists of two gas-tight boxes, as shown in Figure 3.11,
964 which are made of non-magnetic material. The outer box is filled with CO₂ which
965 acts as an electrical insulator between the inner box and the ground. The inner box
966 forms the field cage which produces a uniform electric drift field of $\sim 275\text{V/cm}$
967 and is filled with an argon gas mixture. Charged particles moving through this
968 gas mixture ionize the gas and the ionised charge is drifted towards micromegas
969 detectors which measure the ionization charge. The time and position information
970 in the readout allows a three-dimensional image of the neutrino interaction.

971 The particle identification of tracks that pass through the TPCs is performed
972 using dE/dx measurements. Figure 3.12 illustrates the data to Monte Carlo



Figure 3.11: Schematic design of a Time Projection Chamber detector. Taken from [116].

distributions of the energy lost by a charged particle passing through the TPC as a function of the reconstructed particle momentum. The resolution is $7.8 \pm 0.2\%$ meaning that electrons and muons can be distinguished. This allows reliable measurements of the intrinsic ν_e component of the beam.

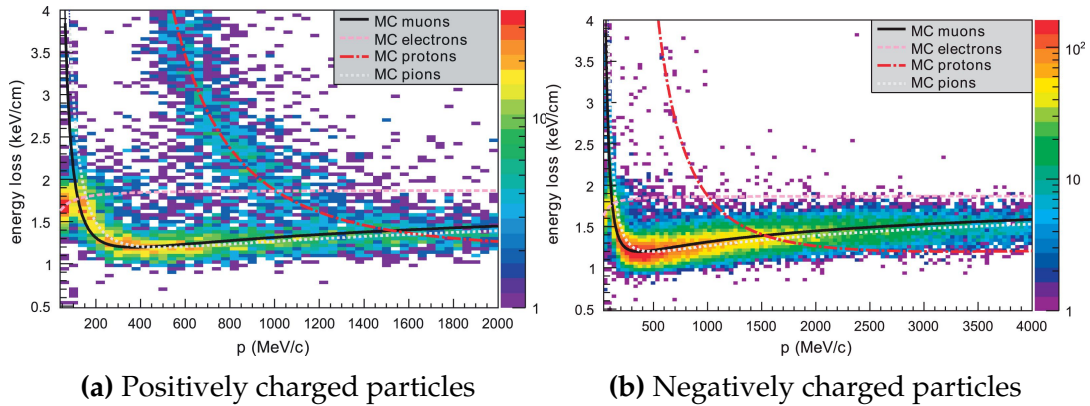


Figure 3.12: The distribution of energy loss as a function of reconstructed momentum for charged particles passing through the TPC, comparing data to Monte Carlo prediction. Taken from [116].

3.2.3.3 π^0 Detector

If one of the γ -rays from a $\pi^0 \rightarrow 2\gamma$ decay is missed at the far detector, the reconstruction will determine that event to be a charge current ν_e -like event. This is one of the main backgrounds hindering the electron neutrino appearance

981 searches. The π^0 detector (P0D) measures the cross-section of the neutral current
 982 induced neutral pion production on a water target to constrain this background.

983 The P0D is a cube of approximately 2.5m length consisting of layers of scin-
 984 tillating bars, brass and lead sheets, and water bags as illustrated in Figure 3.13.
 985 Two electromagnetic calorimeters are positioned at the most upstream and most
 986 downstream position in the sub-detector and the water target is situated in
 987 between them. The scintillator layers are built from two triangular bars orientated
 988 in opposite directions to form a rectangular layer. Each triangular scintillator bar
 989 is threaded with optical fiber which is read out by MPPCs. The high-Z brass and
 990 lead regions produce electron showers from the photons emitted in π^0 decay.

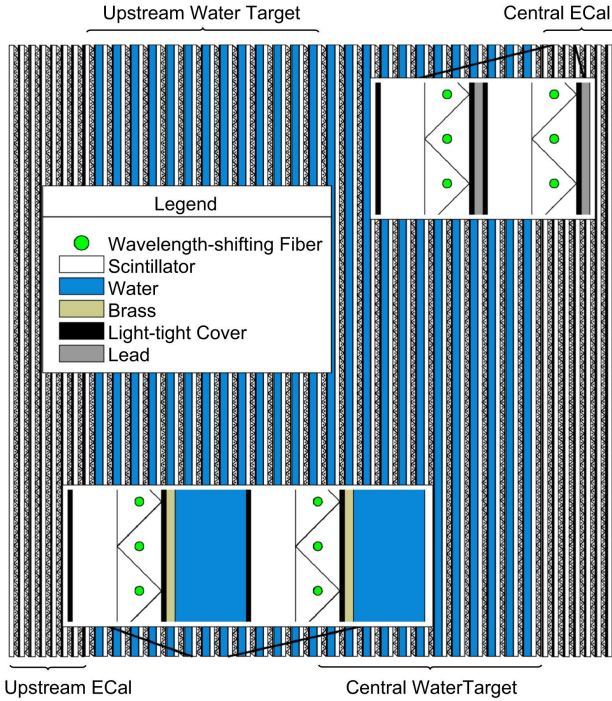


Figure 3.13: A schematic of the P0D side-view. Taken from [117].

991 The sub-detector can generate measurements of NC1 π^0 cross-sections on a
 992 water target by measuring the event rate both with and without the water target,
 993 with the cross-section on a water target being determined as the difference. The to-
 994 tal active mass is 16.1 tonnes when filled with water and 13.3 tonnes when empty.

995 3.2.3.4 Electromagnetic Calorimeter

996 The electromagnetic calorimeter [118] (ECal) encapsulates the P0D and tracking
997 sub-detectors. Its primary purpose is to aid π^0 reconstruction from any interac-
998 tion in the tracker. To do this, it measures the energy and direction of photon
999 showers from $\pi^0 \rightarrow 2\gamma$ decay. It can also distinguish pion and muon tracks
1000 depending on the shape of the photon shower deposited.

1001 The ECal is comprised of three sections; the P0D ECal which surrounds the
1002 P0D, the barrel ECal which encompasses the tracking region, and the downstream
1003 ECal which is situated downstream of the tracker region. The barrel and down-
1004 stream ECals are tracking calorimeters that focus on electromagnetic showers
1005 from high-angle particles emitted from the tracking sub-detectors. Particularly in
1006 the TPC, high-angle tracks (those which travel perpendicularly to the beam-axis)
1007 can travel along a single scintillator bar resulting in very few hits. The width of
1008 the barrel and downstream ECal corresponds to ~ 11 electron radiation lengths
1009 to ensure a significant amount of the π^0 energy is contained. As the P0D has
1010 its own calorimetry which reconstructs showers, the P0D ECal determines the
1011 energy which escapes the P0D.

1012 Each ECal is constructed of multiple layers of scintillating bars sandwiched
1013 between lead sheets. The scintillating bars are threaded with optical fiber and read
1014 out by MPPCs. Each sequential layer of the scintillator is orientated perpendicular
1015 to the previous which allows a three-dimensional event reconstruction. The
1016 target mass of the P0D ECal, barrel ECal, and downstream ECal are 1.50, 4.80,
1017 and 6.62 tonnes respectively.

1018 3.2.3.5 Side Muon Range Detector

1019 As illustrated in Figure 3.9, the ECal, FGDs, P0D, and TPCs are enclosed within
1020 the UA1 magnet. Reconditioned after use in the UA1 [119] and NOMAD [120]
1021 experiments, this magnet provides a uniform horizontal magnetic field of 0.2T
1022 with an uncertainty of 2×10^{-4} T.

1023 Built into the UA1 magnet, the side muon range detector (SMRD)[121] monitors
1024 high-energy muons which leave the tracking region and permeate through
1025 the ECal. It additionally acts as a cosmic muon veto and trigger.

1026 **3.2.4 The Interactive Neutrino GRID**

1027 The Interactive Neutrino GRID (INGRID) detector is situated within the same
1028 “pit” as the other near detectors. It is aligned with the beam in the “on-axis”
1029 position and measures the beam direction, spread, and intensity. The detector
1030 was originally designed with 16 identical modules [41] (two modules have since
1031 been decommissioned) and a “proton” module. The design of the detector is 14
1032 modules oriented in a cross with length and height 10m × 10m, as illustrated
1033 in Figure 3.14.

1034 Each module is composed of iron sheets interlaced with eleven tracking
1035 scintillator planes for a total target mass of 7.1 tonnes per module. The scintillator
1036 design is an X-Y pattern of 24 bars in both orientations, where each bar contains
1037 wave-length shifting fibers which are connected to multi-pixel photon counters
1038 (MPPCs). Each module is encapsulated inside veto planes to aid the rejection
1039 of charged particles entering the module.

1040 The proton module is different from the other modules in that it consists
1041 of entirely scintillator planes with no iron target. The scintillator bars are also
1042 smaller than those used in the other modules to increase the granularity of
1043 the detector and improve tracking capabilities. The module sits in the center
1044 of the beamline and is designed to give precise measurements of quasi-elastic
1045 charged current interactions to evaluate the performance of the Monte Carlo
1046 simulation of the beamline.

1047 The INGRID detector can measure the beam direction to an uncertainty of
1048 0.4mrad and the beam centre within a resolution of 10cm [41]. The beam direction
1049 in both the vertical and horizontal directions is discussed in [122] and it is found
1050 to be in good agreement with the MUMON monitor described in subsection 3.2.2.

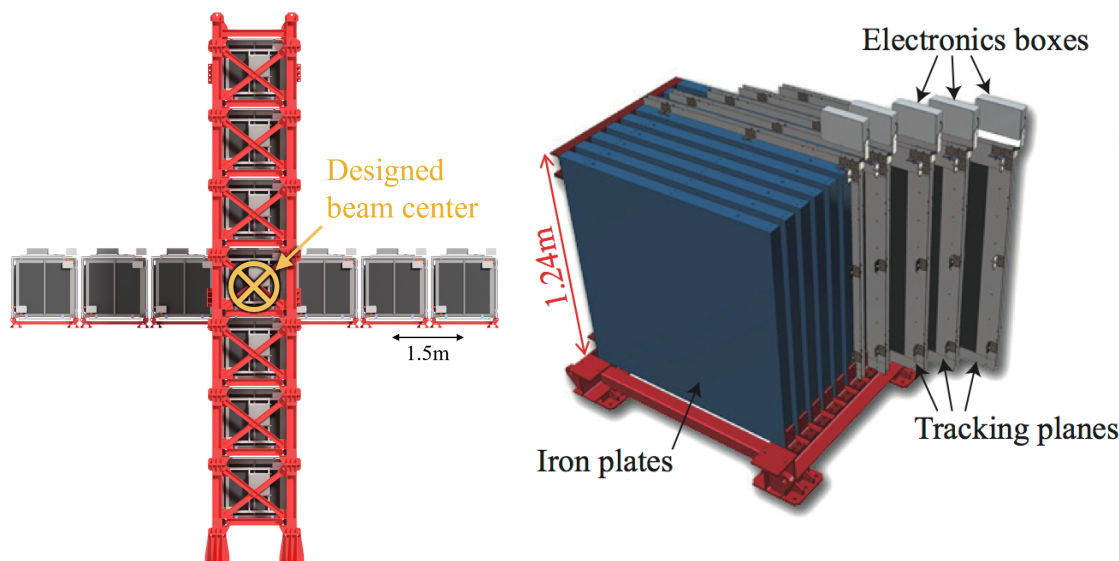


Figure 3.14: Left panel: The Interactive Neutrino GRID on-axis Detector. 14 modules are arranged in a cross-shape configuration, with the center modules being directly aligned with the on-axis beam. Right panel: The layout of a single module of the INGRID detector. Both figures are recreated from [41].

4

1051

1052

1053

Bayesian Statistics and Markov Chain Monte Carlo Techniques

1054 This thesis presents a Bayesian oscillation analysis. To extract the oscillation
1055 parameters, a Markov Chain Monte Carlo (MCMC) method is used. This chapter
1056 explains the theory of how parameter estimates can be determined using this
1057 technique and condenses the material found in the literature [123–126].

1058 The oscillation parameter determination presented here is built upon a si-
1059 multaneous fit to neutrino beam data in the near detector, beam data at SK, and
1060 atmospheric data at SK. In total, there are four oscillation parameters of interest
1061 ($\sin^2(\theta_{23})$, $\sin^2(\theta_{13})$, Δm_{32}^2 , and δ_{CP}), two oscillation parameters to which this
1062 study will not be sensitive ($\sin^2(\theta_{12})$, Δm_{21}^2) and many nuisance parameters that
1063 control the systematic uncertainty models.

1064 This analysis uses a Monte Carlo technique to generate a multi-dimensional
1065 probability distribution across all of the model parameters used in the fit. To
1066 determine an estimate for each parameter, this multi-dimensional object is in-
1067 tegrated over all other parameters. This process is called Marginalisation and
1068 is described in subsection 4.3.1. Monte Carlo techniques approximate the prob-
1069 ability distribution of each parameter within the limit of generating infinite
1070 samples. As ever, generating a large number of samples is time and resource-

1071 dependent. Therefore, an MCMC technique is utilised within this analysis to
1072 reduce the required number of steps to sufficiently sample the parameter space.
1073 This technique is described in further detail in subsection 4.2.1.

1074 The Bayesian analysis techniques used within this thesis are built within the
1075 MaCh3 framework [127]. This uses a custom MCMC library package exclusively
1076 supported and developed by the MaCh3 collaborators (which includes the author
1077 of this thesis).

1078 **4.1 Bayesian Statistics**

1079 Bayesian inference treats observable data, D , and model parameters, $\vec{\theta}$, on equal
1080 footing such that a probability model of both data and parameters is required.
1081 This is the joint probability distribution $P(D, \vec{\theta})$ and can be described by the
1082 prior distribution for model parameters $P(\vec{\theta})$ and the likelihood of the data given
1083 the model parameters $P(D|\vec{\theta})$,

$$P(D, \vec{\theta}) = P(D|\vec{\theta})P(\vec{\theta}). \quad (4.1)$$

1084 The prior distribution, $P(\vec{\theta})$, describes all previous knowledge about the
1085 parameters within the model. For example, if the risk of developing health
1086 problems is known to increase with age, the prior distribution would describe the
1087 increase. For the purpose of this analysis, the prior distribution is typically
1088 the best-fit values taken from external data measurements with a Gaussian
1089 uncertainty. The prior distribution can also contain correlations between model
1090 parameters. In an analysis using Monte Carlo techniques, the likelihood of
1091 measuring some data assuming some set of model parameters is calculated
1092 by comparing the Monte Carlo prediction generated at that particular set of
1093 model parameters to the data.

1094 It is parameter estimation that is important for this analysis and as such, Bayes'
1095 theorem [128] is applied to calculate the probability for each parameter to have a

1096 certain value given the observed data, $P(\vec{\theta}|D)$, which is known as the posterior
1097 distribution (often termed the posterior). This can be expressed as

$$P(\vec{\theta}|D) = \frac{P(D|\vec{\theta})P(\vec{\theta})}{\int P(D|\vec{\theta})P(\vec{\theta})d\vec{\theta}}. \quad (4.2)$$

1098 The denominator in Equation 4.2 is the integral of the joint probability distri-
1099 bution over all values of all parameters used within the fit. For brevity, the
1100 posterior distribution is

$$P(\vec{\theta}|D) \propto P(D|\vec{\theta})P(\vec{\theta}). \quad (4.3)$$

1101 For the purposes of this analysis, it is acceptable to neglect the normalisation
1102 term and focus on this proportional relationship.

1103 4.1.1 Application of Prior Knowledge

1104 The posterior distribution is proportional to the prior uncertainty applied to
1105 each parameter, as illustrated by Equation 4.3. This means that it is possible
1106 to change the prior after the posterior distribution has been determined. The
1107 prior uncertainty of a particular parameter can be ‘divided’ out of the posterior
1108 distribution and the resulting distribution can be reweighted using the new
1109 prior uncertainty that is to be applied. The methodology and implementation
1110 of changing the prior follows that described in [129].

1111 An example implementation that is useful for this analysis is the application
1112 of the “reactor constraint”. As discussed in section 2.4, an external constraint
1113 on $\sin^2(\theta_{13})$ is determined from measurements taken from reactor experiments.
1114 However, the sensitivities from just using the T2K and SK samples is equally
1115 as important. Without this technique, two fits would have to be run, doubling
1116 the required resources. Therefore, the key benefit for this analysis is the fact that
1117 only a single ‘fit’ has to be performed and can be used to build the two posterior
1118 distributions of the with and without reactor constraint applied.

1119 4.2 Monte Carlo Simulation

1120 Monte Carlo techniques are used to numerically solve a complex problem that
1121 does not necessarily have an analytical solution. These techniques rely on
1122 building a large ensemble of samples from an unknown distribution and then
1123 using the ensemble to approximate the properties of the distribution.

1124 An example that uses Monte Carlo techniques is to calculate the area under-
1125 neath a curve. For example, take the problem of calculating the area under a
1126 straight line with gradient $M = 0.4$ and intercept $C = 1.0$. Analytically, one can
1127 calculate the area under the line is equal to 30 units for $0 \leq x \leq 10$. Using Monte
1128 Carlo techniques, one can calculate the area under this line by throwing many
1129 random values for the x and y components of each sample and then calculating
1130 whether that point falls below the line. The area can then be calculated by the
1131 ratio of points below the line to the total number of samples thrown multiplied by
1132 the total area in which samples were scattered. The study is shown in Figure 4.1
1133 highlights this technique and finds the area under the curve to be 29.9 compared
1134 to an analytical solution of 30.0. The deviation of the numerical to analytical
1135 solution can be attributed to the number of samples used in the study. The
1136 accuracy of the approximation in which the properties of the Monte Carlo samples
1137 replicate those of the desired distribution is dependent on the number of samples
1138 used. Replicating this study with a differing number of Monte Carlo samples
1139 used in each study (As shown in Figure 4.2) highlights how the Monte Carlo
1140 techniques are only accurate within the limit of a high number of samples.

1141 Whilst the above example has an analytical solution, these techniques are just
1142 as applicable to complex solutions. Clearly, any numerical solution is only as
1143 useful as its efficiency. As discussed, the accuracy of the Monte Carlo technique is
1144 dependent upon the number of samples generated to approximate the properties
1145 of the distribution. Furthermore, if the positions at which the samples are
1146 evaluated are not ‘cleverly’ picked, the efficiency of the Monte Carlo technique
1147 significantly drops. Given the example in Figure 4.1, if the region in which the

1148 samples are scattered significantly extends passed the region of interest, many
1149 calculations will be calculated but do not add to the ability of the Monte Carlo
1150 technique to achieve the correct result. For instance, any sample evaluated at
1151 a $y \geq 5$ could be removed without affecting the final result. This does bring in
1152 an aspect of the ‘chicken and egg’ problem in that to achieve efficient sampling,
1153 one needs to know the distribution beforehand.

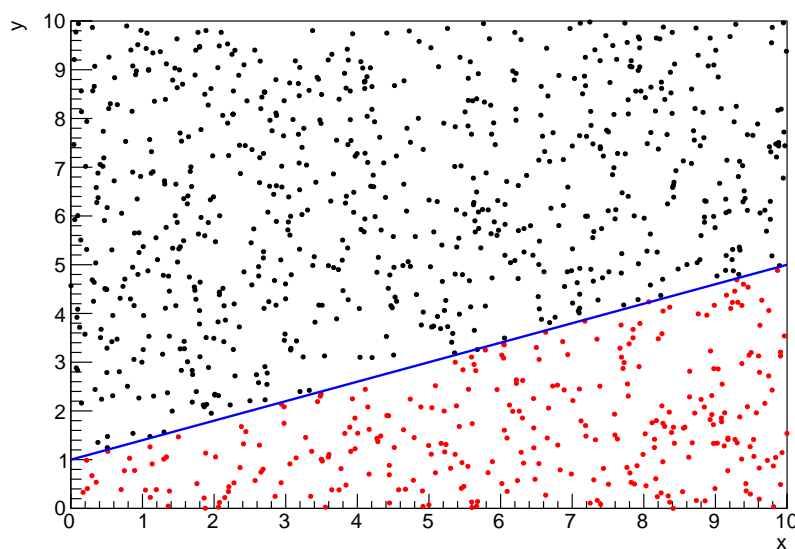


Figure 4.1: Example of using Monte Carlo techniques to find the area under the blue line. The gradient and intercept of the line are 0.4 and 1.0 respectively. The area found to be under the curve using one thousand samples is 29.9 units.

1154 4.2.1 Markov Chain Monte Carlo

1155 This analysis utilises a multi-dimensional probability distribution, with some
1156 dimensions being significantly more constrained than others. These constraints
1157 can be from prior knowledge of parameter distributions from external data or
1158 un-physical regions in which parameters can not exist. To maximise the efficiency
1159 of building the posterior distribution, a Markov Chain Monte Carlo (MCMC)
1160 technique is used. This employs a Markov chain to select the points at which
1161 to sample the posterior distribution. It performs a semi-random stochastic walk
1162 through the allowable parameter space. This builds a posterior distribution

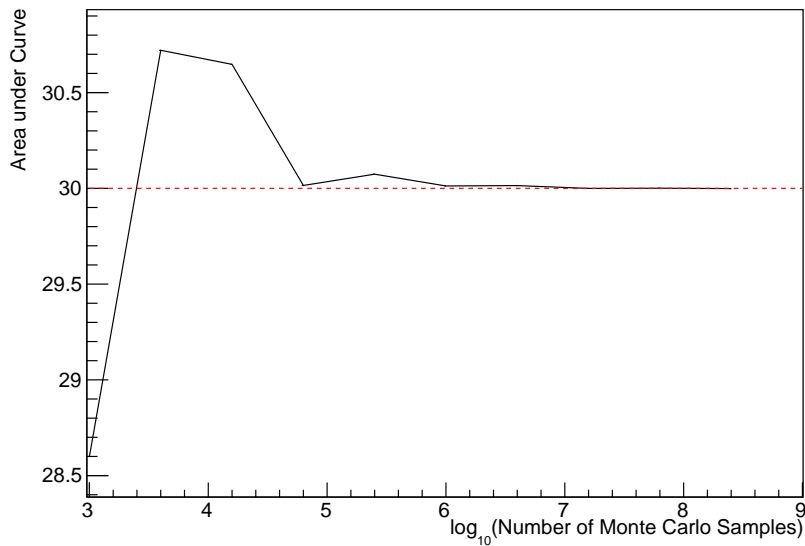


Figure 4.2: The area under a line of gradient 0.4 and intercept 1.0 for the range $0 \leq x \leq 10$ as calculated using Monte Carlo techniques as a function of the number of samples used in each repetition. The analytical solution to the area is 30 units as given by the red line.

1163 which has the property that the density of sampled points is proportional to the
 1164 probability density of that parameter. This means that the samples produced by
 1165 this technique are not statistically independent but they will cover the space
 1166 of the distribution.

1167 A Markov chain functions by selecting the position of step \vec{x}_{i+1} based on the
 1168 position of \vec{x}_i . The space in which the Markov chain selects samples is dependent
 1169 upon the total number of parameters utilised within the fit, where a discrete point
 1170 in this space is described by the N-dimensional space \vec{x} . In a perfectly operating
 1171 Markov chain, the position of the next step depends solely on the previous step
 1172 and not on the further history of the chain (\vec{x}_0, \vec{x}_1 , etc.). However, in solving
 1173 the multi-dimensionality of the fit used within this analysis, each step becomes
 1174 correlated with several of the steps preceding itself. Providing the MCMC chain is
 1175 well optimised, it will begin to converge towards a unique stationary distribution.
 1176 The period between the chain's initial starting point and the convergence to the
 1177 unique stationary distribution is colloquially known as the burn-in period. Once
 1178 the chain reaches the stationary distribution, all points sampled after that point

₁₁₇₉ will look like samples from that distribution.

₁₁₈₀ Further details of the theories underpinning MCMC techniques are discussed
₁₁₈₁ in [124] but can be summarised by the requirement that the chain satisfies the
₁₁₈₂ three ‘regularity conditions’:

- ₁₁₈₃ • Irreducibility: From every position in the parameter space \vec{x} , there must
₁₁₈₄ exist a non-zero probability for every other position in the parameter space
₁₁₈₅ to be reached.
- ₁₁₈₆ • Recurrence: Once the chain arrives at the stationary distribution, every step
₁₁₈₇ following from that position must be samples from the same stationary
₁₁₈₈ distribution.
- ₁₁₈₉ • Aperiodicity: The chain must not repeat the same sequence of steps at any
₁₁₉₀ point throughout the sampling period.

₁₁₉₁ The output of the chain after burn-in (i.e. the sampled points after the chain
₁₁₉₂ has reached the stationary distribution) can be used to approximate the posterior
₁₁₉₃ distribution and model parameters $\vec{\theta}$. To achieve the requirement that the unique
₁₁₉₄ stationary distribution found by the chain be the posterior distribution, one
₁₁₉₅ can use the Metropolis-Hastings algorithm. This guides the stochastic process
₁₁₉₆ depending on the likelihood of the current proposed step compared to that
₁₁₉₇ of the previous step.

₁₁₉₈ 4.2.2 Metropolis-Hastings Algorithm

₁₁₉₉ As a requirement for MCMCs, the Markov chain implemented in this technique
₁₂₀₀ must have a unique stationary distribution that is equivalent to the posterior
₁₂₀₁ distribution. To ensure this requirement and that the regularity conditions are
₁₂₀₂ met, this analysis utilises the Metropolis-Hastings (MH) algorithm [130, 131].
₁₂₀₃ For the i^{th} step in the chain, the MH algorithm determines the position in the
₁₂₀₄ parameter space to which the chain moves to based on the current step, \vec{x}_i , and
₁₂₀₅ the proposed step, \vec{y}_{i+1} . The proposed step is randomly selected from some

1206 proposal function $f(\vec{x}_{i+1}|\vec{x}_i)$, which depends solely on the current step (ie. not
1207 the further history of the chain). The next step in the chain \vec{x}_{i+1} can be either the
1208 current step or the proposed step determined by whether the proposed step is
1209 accepted or rejected. To decide if the proposed step is selected, the acceptance
1210 probability, $\alpha(\vec{x}_i, \vec{y}_i)$, is calculated as

$$\alpha(\vec{x}_i, \vec{y}_{i+1}) = \min\left(1, \frac{P(\vec{y}_{i+1}|D)f(\vec{x}_i|\vec{y}_{i+1})}{P(\vec{x}_i|D)f(\vec{y}_{i+1}|\vec{x}_i)}\right). \quad (4.4)$$

1211 Where $P(\vec{y}_{i+1}|D)$ is the posterior distribution as introduced in section 4.1. To
1212 simplify this calculation, the proposal function is required to be symmetric such
1213 that $f(\vec{x}_i|\vec{y}_{i+1}) = f(\vec{y}_{i+1}|\vec{x}_i)$. In practice, a multi-variate Gaussian distribution
1214 centered on \vec{x}_i is used to throw parameter proposals. This reduces Equation 4.4 to

$$\alpha(\vec{x}_i, \vec{y}_{i+1}) = \min\left(1, \frac{P(\vec{y}_{i+1}|D)}{P(\vec{x}_i|D)}\right). \quad (4.5)$$

1215 After calculating this quantity, a random number, β , is generated uniformly
1216 between 0 and 1. If $\beta \leq \alpha(\vec{x}_i, \vec{y}_{i+1})$, the proposed step is accepted. Otherwise,
1217 the chain sets the next step equal to the current step. This procedure is repeated
1218 for subsequent steps. This can be interpreted as if the posterior probability
1219 of the proposed step is greater than that of the current step, ($P(\vec{y}_{i+1}|D) \geq$
1220 $P(\vec{x}_i|D)$), the proposed step will always be accepted. If the opposite is true,
1221 ($P(\vec{y}_{i+1}|D) \leq P(\vec{x}_i|D)$), the proposed step will be accepted with probability
1222 $P(\vec{x}_i|D)/P(\vec{y}_{i+1}|D)$. This ensures that the Markov chain does not get trapped
1223 in any local minima in the potentially non-Gaussian posterior distribution. The
1224 outcome of this technique is that the density of steps taken in a discrete region
1225 is directly proportional to the probability density in that region.

1226 4.2.3 MCMC Optimisation

1227 As discussed in subsection 4.2.2, the proposal function invoked within the MH
1228 algorithm can take any form and the chain will still converge to the stationary
1229 distribution. At each set of proposed parameter values, a prediction of the same
1230 spectra has to be generated which requires significant computational resources.

1231 Therefore, the number of steps taken before the unique stationary distribution
1232 is found should be minimised as only steps after convergence add information
1233 to the oscillation analysis. Furthermore, the chain should entirely cover the
1234 allowable parameter space to ensure that all values have been considered. Tuning
1235 the distance that the proposal function jumps between steps on a parameter-by-
1236 parameter basis can both minimise the length of the burn-in period and ensure
1237 that the correlation between step \vec{x}_i and \vec{x}_j is sufficiently small.

1238 The effect of changing the width of the proposal function is highlighted in
1239 Figure 4.3. Three scenarios, each with the same underlying stationary distribution
1240 (A Gaussian of width 1.0 and mean 0.), are presented. The only difference between
1241 the three scenarios is the width of the proposal function, colloquially known as
1242 the ‘step size σ ’. Each scenario starts at an initial parameter value of 10.0 which
1243 would be considered an extreme variation. For the case where $\sigma = 0.1$, it is
1244 clear to see that the chain takes a long time to reach the expected region of the
1245 parameter. This indicates that this chain would have a large burn-in period and
1246 does not converge to the stationary distribution until step ~ 500 . Furthermore,
1247 whilst the chain does move towards the expected region, each step is significantly
1248 correlated with the previous. Considering the case where $\sigma = 5.0$, the chain
1249 approaches the expected parameter region almost instantly meaning that the
1250 burn-in period is not significant. However, there are clearly large regions of steps
1251 where the chain does not move. This is likely due to the chain proposing steps
1252 in the tails of the distribution which have a low probability of being accepted.
1253 Consequently, this chain would take a significant number of steps to fully span
1254 the allowable parameter region. For the final scenario, where $\sigma = 0.5$, you can
1255 see a relatively small burn-in period of approximately 100 steps. Once the chain
1256 reaches the stationary distribution, it moves throughout the expected region of
1257 parameter values many times, sufficiently sampling the full parameter region.
1258 This example is a single parameter varying across a continuous distribution and
1259 does not fully reflect the difficulties in the many-hundred multi-variate parameter

1260 distribution used within this analysis. However, it does give a conceptual idea of
1261 the importance of selecting the proposal function and associated step size.

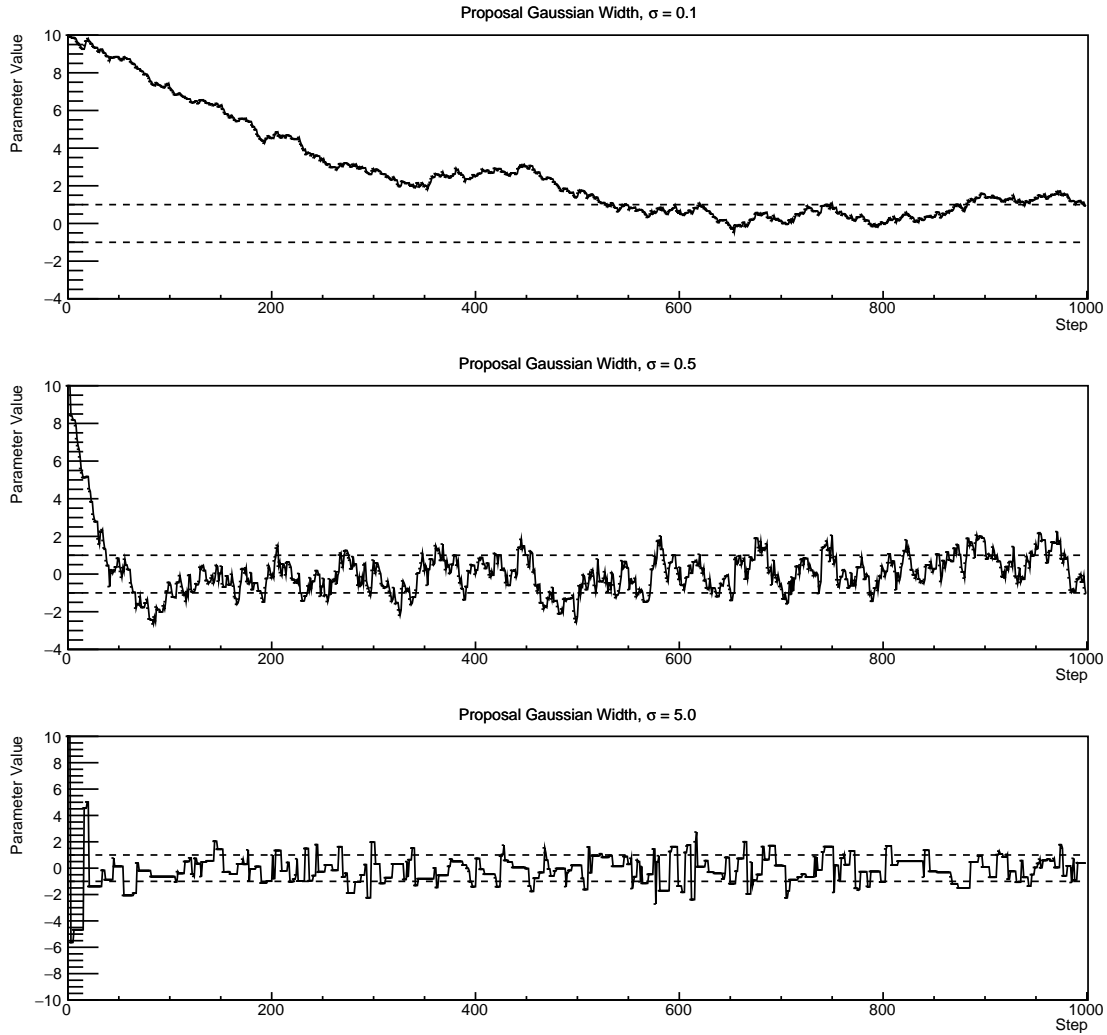


Figure 4.3: Three MCMC chains, each with a stationary distribution equal to a Gaussian centered at 0 and width 1 (As indicated by the black dotted lines). All of the chains use a Gaussian proposal function but have different widths (or ‘step size σ ’). The top panel has $\sigma = 0.1$, middle panel has $\sigma = 0.5$ and the bottom panel has $\sigma = 5.0$.

1262 As discussed, step size tuning directly correlates to the average step accep-
1263 tance rate. If the step size is too small, many steps will be accepted but the
1264 chain moves slowly. If the opposite is true, many steps will be rejected as the
1265 chain proposes steps in the tails of the distribution. Discussion in [132] suggests
1266 that the ‘ideal’ acceptance rate of a high dimension MCMC chain should be

₁₂₆₇ approximately $\sim 25\%$. An “ideal” step size [132] of

$$\sigma = \frac{2.4}{N_p}, \quad (4.6)$$

₁₂₆₈ where N_p is the number of parameters included in the MCMC fit. However,
₁₂₆₉ the complex correlations between systematics mean that some parameters have
₁₂₇₀ to be hand-tuned and many efforts have been taken to select a set of parameter-
₁₂₇₁ by-parameter step sizes to approximately reach the ideal acceptance rate.

₁₂₇₂ Figure 4.4 highlights the likelihood as calculated by the fit in subsection 8.2.4
₁₂₇₃ as a function of the number of steps in each chain. In practice, many independent
₁₂₇₄ MCMC chains are run simultaneously to parallelise the task of performing the
₁₂₇₅ fit. This figure overlays the distribution found in each chain. As seen, the
₁₂₇₆ likelihood decreases from its initial value and converges towards a stationary
₁₂₇₇ distribution after $\sim 1 \times 10^5$ steps.

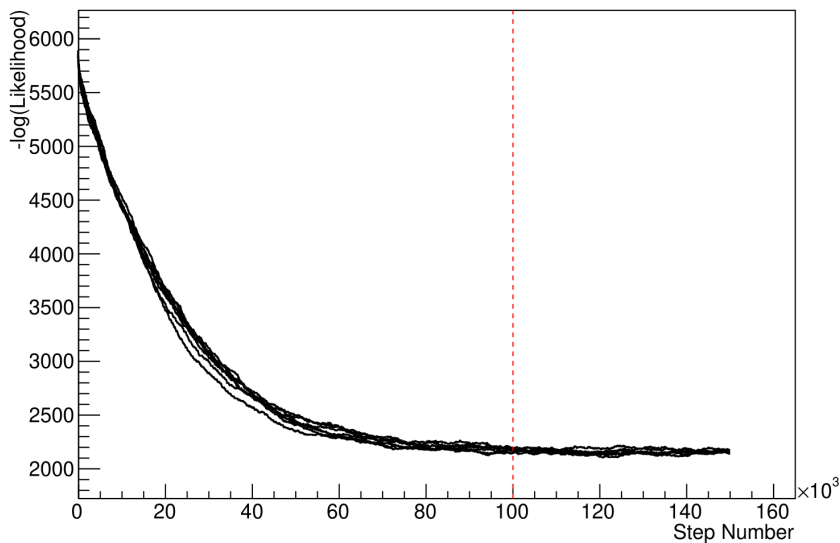


Figure 4.4: The log-likelihood from the fit detailed in subsection 8.2.4 as a function of the number of steps accumulated in each fit. Many independent MCMC chains were run in parallel and overlaid on this plot. The red line indicates the 1×10^5 step burn-in period after which the log-likelihood becomes stable.

₁₂₇₈ Multiple configurations of this analysis have been performed throughout this
₁₂₇₉ thesis where different samples or systematics have been used. For all of these con-
₁₂₈₀ figurations, it was found that a burnin period of 1×10^5 was sufficient in all cases.

1281 4.3 Understanding the MCMC Results

1282 The previous sections have described how to generate the posterior probability
1283 distribution using Bayesian MCMC techniques. However, this analysis focuses
1284 on oscillation parameter determination. The posterior distribution output from
1285 the chain is a high-dimension object, with as many dimensions as there are
1286 parameters included in the oscillation analysis. However, this multi-dimensional
1287 object is difficult to conceptualize so parameter estimations are often presented
1288 in one or two-dimensional projections of this probability distribution. To do
1289 this, marginalisation techniques are invoked.

1290 4.3.1 Marginalisation

1291 The output of the MCMC chain is a highly dimensional probability distribution
1292 which is very difficult to interpret. From the standpoint of an oscillation analysis
1293 experiment, the one or two-dimensional ‘projections’ of the oscillation parameters
1294 of interest are most relevant. Despite this, the best fit values and uncertainties on
1295 the oscillation parameters of interest should correctly encapsulate the correlations
1296 to the other systematic uncertainties (colloquially called ‘nuisance’ parameters).
1297 For this joint beam and atmospheric analysis, the oscillation parameters of
1298 interest are $\sin^2(\theta_{23})$, $\sin^2(\theta_{13})$, Δm_{32}^2 , and δ_{CP} . All other parameters (includ-
1299 ing the oscillation parameters this fit is insensitive to) are deemed nuisance
1300 parameters. To generate these projections, the posterior distribution is integrated
1301 over all nuisance parameters. This is called marginalisation. This technique
1302 also explains why it is acceptable to neglect the normalisation constant of the
1303 posterior distribution, which was discussed in section 4.1.

1304 A simple example of the marginalisation technique is to imagine the scenario
1305 where two coins are flipped. To determine the probability that the first coin
1306 returned a ‘head’, the exact result of the second coin flip is disregarded and
1307 simply integrated over. For the parameters of interest, $\vec{\theta}_i$, the marginalised

1308 posterior is calculated by integrating over the nuisance parameters, $\vec{\theta}_n$. In this
1309 case, Equation 4.2 becomes

$$P(\vec{\theta}_i|D) = \frac{\int P(D|\vec{\theta}_i, \vec{\theta}_n)P(\vec{\theta}_i, \vec{\theta}_n)d\vec{\theta}_n}{\int P(D|\vec{\theta})P(\vec{\theta})d\vec{\theta}}. \quad (4.7)$$

1310 Where $P(\vec{\theta}_i, \vec{\theta}_n)$ encodes the prior knowledge about the uncertainty and
1311 correlations between the parameters of interest and the nuisance parameters.
1312 In practice, this is simply taking the one or two-dimensional projection of the
1313 multi-dimensional probability distribution.

1314 While in principle an easy solution to a complex problem, correlations be-
1315 tween the interesting and nuisance parameters can bias the marginalised results.
1316 A similar effect is found when the parameters being marginalised over have
1317 non-Gaussian probability distributions. For example, Figure 4.5 highlights the
1318 marginalisation bias in the probability distribution found for a parameter when
1319 requiring a correlated parameter to have a positive parameter value. Due to
1320 the complex nature of the oscillation parameter fit presented in this thesis, there
1321 are correlations occurring between the oscillation parameters of interest and the
1322 other nuisance parameters included in the fit.



Figure 4.5: Left: The two-dimensional probability distribution for two correlated parameters x and y . The red distribution shows the two-dimensional probability distribution when $0 \leq x \leq 5$. Right: The marginalised probability distribution for the y parameter found when requiring the x to be bound between $-5 \leq x \leq 5$ and $0 \leq x \leq 5$ for the black and red distribution, respectively.

1323 4.3.2 Parameter Estimation and Credible Intervals

1324 The purpose of this analysis is to determine the best fit values for the oscillation
 1325 parameters that the beam and atmospheric samples are sensitive to: $\sin^2(\theta_{23})$,
 1326 $\sin^2(\theta_{13})$, Δm_{32}^2 , and δ_{CP} . The posterior probability density, taken from the output
 1327 MCMC chain, is binned in these parameters. The parameter best-fit point is then
 1328 taken to be the value that has the highest posterior probability. This is performed
 1329 in both one and two-dimensional projections.

1330 However, the single best-fit point in a given parameter is not of much use on its
 1331 own. The uncertainty on the best-fit point must also be presented using credible
 1332 intervals. The definition of the 1σ credible interval is that there is 68% belief
 1333 that the parameter is within those bounds. For a more generalised definition,
 1334 the credible interval is the region, R , of the posterior distribution that contains
 1335 a specific fraction of the total probability, such that

$$\int_R P(\theta|D)d\theta = \alpha. \quad (4.8)$$

1336 Where θ is the parameter being evaluated. This technique then calculates
 1337 the $\alpha \times 100\%$ credible interval.

1338 In practice, this analysis uses the highest posterior density (HPD) credible in-
 1339 tervals which are calculated through the following method. First, the probability
 1340 distribution is area-normalised such that it has an integrated area equal to 1.0.
 1341 The bins of probability are then summed from the highest to lowest until the sum
 1342 exceeds the 1σ level (0.68 in this example). This process is repeated for a range of
 1343 credible intervals, notably the 1σ , 2σ and 3σ along with other levels where the
 1344 critical values for each level can be found in [73]. This process can be repeated
 1345 for the two-dimensional probability distributions by creating two-dimensional
 1346 contours of credible intervals rather than a one-dimensional result.

¹³⁴⁷ 4.3.3 Bayesian Model Comparisons

¹³⁴⁸ Due to the matter resonance, this analysis has some sensitivity to the mass
¹³⁴⁹ hierarchy of neutrino states (whether Δm_{32}^2 is positive or negative) and the
¹³⁵⁰ octant of $\sin^2(\theta_{23})$. The Bayesian approach utilised within this analysis gives an
¹³⁵¹ intuitive method of model comparison by determining which hypothesis is most
¹³⁵² favourable. Taking the ratio of Equation 4.3 for the two hypotheses of normal
¹³⁵³ hierarchy, NH , and inverted hierarchy, IH , gives

$$\frac{P(\vec{\theta}_{NH}|D)}{P(\vec{\theta}_{IH}|D)} = \frac{P(D|\vec{\theta}_{NH})}{P(D|\vec{\theta}_{IH})} \times \frac{P(\vec{\theta}_{NH})}{P(\vec{\theta}_{IH})}. \quad (4.9)$$

¹³⁵⁴ The middle term defines the Bayes factor, $B(NH/IH)$, which is a data-driven
¹³⁵⁵ interpretation of how strong the data prefers one hierarchy to the other. For this
¹³⁵⁶ analysis, equal priors on both mass hierarchy hypotheses are chosen ($P(\vec{\theta}_{NH}) =$
¹³⁵⁷ $P(\vec{\theta}_{IH}) = 0.5$). In practice, the MCMC chain proposes a value of $|\Delta m_{32}^2|$ and
¹³⁵⁸ then applies a 50% probability that the value is sign flipped. Consequently,
¹³⁵⁹ the Bayes factor can be calculated from the ratio of the probability density in
¹³⁶⁰ either hypothesis. This equates to counting the number of steps taken in the
¹³⁶¹ normal and inverted hierarchies and taking the ratio. The same approach can be
¹³⁶² taken to compare the upper octant (UO) compared to the lower octant (LO)
¹³⁶³ hypothesis of $\sin^2(\theta_{23})$.

$\log_{10}(B_{AB})$	B_{AB}	Strength of Preference
< 0.0	< 1	No preference for hypothesis A (Supports hypothesis B)
0.0 – 0.5	1.0 – 3.16	Preference for hypothesis A is weak
0.5 – 1.0	3.16 – 10.0	Preference for hypothesis A is substantial
1.0 – 1.5	10.0 – 31.6	Preference for hypothesis A is strong
1.5 – 2.0	31.6 – 100.0	Preference for hypothesis A is very strong
> 2.0	> 100.0	Decisive preference for hypothesis A

Table 4.1: Jeffreys scale for strength of preference for two models A and B as a function of the calculated Bayes factor ($B_{AB} = B(A/B)$) between the two models [133]. The original scale is given in terms of $\log_{10}(B(A/B))$ but converted to linear scale for easy comparison throughout this thesis.

¹³⁶⁴ Whilst the value of the Bayes factor should always be shown, the Jeffreys scale
¹³⁶⁵ [133] (highlighted in Table 4.1) gives an indication of the strength of preference

1366 for one model compared to the other. Other interpretations of the strength of
1367 preference of a model exist, e.g. the Kass and Raferty Scale [134].

1368 4.3.4 Comparison of MCMC Output to Expectation

1369 To ensure the fit is performing well, a best-fit spectrum is produced using the
1370 posterior probability distribution and compared with the data, allowing easy
1371 by-eye comparisons to be made. A simple method of doing this is to perform a
1372 comparison in the fitting parameters (e.g. the reconstructed neutrino energy for
1373 T2K far detector beam samples) of the spectra generated by the MCMC chain to
1374 ‘data’. This ‘data’ could be true data or some variation of Monte Carlo prediction.
1375 This allows easy comparison of the MCMC probability distribution to the data. To
1376 perform this, N steps from the post-burnin MCMC chain are randomly selected.
1377 From these, the Monte Carlo prediction at each step is generated by reweighting
1378 the model parameters to the values specified at that step. Due to the probability
1379 density being directly correlated with the density of steps in a certain region,
1380 parameter values close to the best fit value are most likely to be selected.

1381 In practice, for each bin of the fitting parameters has a probability distribution
1382 of event rates, with one entry per sampled MCMC step. This distribution is
1383 binned where the bin with the highest probability is selected as the mean and an
1384 error on the width of this probability distribution is calculated using the approach
1385 highlighted in subsection 4.3.2. Consequently, the best fit distribution in the fit
1386 parameter is not necessarily that which would be attained by reweighting the
1387 Monte Carlo prediction to the most probable parameter values.

1388 A similar study can be performed to illustrate the freedom of the model
1389 parameter space prior to the fit. This can be done by throwing parameter values
1390 from the prior uncertainty of each parameter.

5

1391

1392

1393

Simulation, Reconstruction, and Event Reduction

1394 As a crucial part of the oscillation analysis, an accurate prediction of the expected
1395 neutrino spectrum at the far detector is required. This includes modeling the
1396 flux generation, neutrino interactions, and detector effects. All of the simulation
1397 packages required to do this are briefly described in section 5.1. The reconstruc-
1398 tion of neutrino events in the far detector, including the `fitQun` algorithm, is
1399 documented in section 5.2. This also includes data quality checks of the SK-V
1400 data which the author performed for the T2K oscillation analysis presented at the
1401 Neutrino 2020 conference [72]. Finally, section 5.3 describes the steps taken in the
1402 SK detector to trigger on events of interest whilst removing the comparatively
1403 large rate of cosmic ray muon events.

1404 5.1 Simulation

1405 In order to generate a Monte Carlo prediction of the expected event rate at
1406 the far detector, all the processes in the beam and atmospheric fluxes, neutrino
1407 interaction, and detector need to be modeled.

1408 5.1.1 Neutrino Flux

1409 The beamline simulation consists of three distinct parts: the initial hadron interac-
 1410 tion modeled by FLUKA [135], the target station geometry and particle tracking
 1411 performed by JNUBEAM, [37, 136] and any hadronic re-interactions simulated by
 1412 GCALOR [137]. The primary hadronic interactions are $O(10)$ GeV, where FLUKA
 1413 matches external cross-section data better than GCALOR [138]. However, FLUKA
 1414 is not very adaptable so a small simulation is built to model the interactions
 1415 in the target and the output is then passed to JNUBEAM and GCALOR for
 1416 propagation. The hadronic interactions are tuned to data from the NA61/SHINE
 1417 [139–141] and HARP [142] experiments. The tuning is done by reweighting the
 1418 FLUKA and GCALOR predictions to match the external data multiplicity and
 1419 cross-section measurements, based on final state particle kinematics [138]. The
 1420 culmination of this simulation package generates the predicted flux for neutrino
 1421 and antineutrino beam modes which are illustrated in Figure 3.7.

1422 The atmospheric neutrino flux is simulated by the HKKM model [49, 51]. The
 1423 primary cosmic ray flux is tuned to AMS [143] and BESS [144] data assuming
 1424 the US-standard atmosphere '76 [145] density profile and includes geomagnetic
 1425 field effects. The primary cosmic rays interact to generate pions and muons.
 1426 The interaction of these secondary particles to generate neutrinos is handled by
 1427 DPMJET-III [146] for energies above 32GeV and JAM [51, 147] for energies below
 1428 that value [47]. These hadronic interactions are tuned to BESS and L3 data [148,
 1429 149] using the same methodology as the tuning of the beamline simulation. The
 1430 energy and cosine zenith predictions of $\nu_e, \bar{\nu}_e, \nu_\mu, \bar{\nu}_\mu$ flux are given in Figure 2.3
 1431 and Figure 2.5, respectively. The flux is approximately symmetrical and peaked
 1432 around the horizon ($\cos(\theta_Z) = 0.0$). This is because horizontally-going pions
 1433 and kaons can travel further than their vertically-going counterparts resulting
 1434 in a larger probability of decaying to neutrinos. The symmetry is broken in
 1435 lower-energy neutrinos due to geomagnetic effects, which modify the track of the
 1436 primary cosmic rays. Updates to the HKKM model are currently ongoing [150].

5.1.2 Neutrino Interaction

Once a flux prediction has been made for all three detectors, NEUT 5.4.0 [151, 152] models the interactions of the neutrinos in the detectors. For the purposes of this analysis, quasi-elastic (QE), meson exchange (MEC), single meson production (PROD), coherent pion production (COH), and deep inelastic scattering (DIS) interactions are simulated. These interaction categories can be further broken down by whether they were propagated via a W^\pm boson in Charged Current (CC) interactions or via a Z^0 boson in Neutral Current (NC) interactions. CC interactions have a charged lepton in the final state, which can be flavour-tagged in reconstruction to determine the flavour of the neutrino. In contrast, NC interactions have a neutrino in the final state so no flavour information can be determined from the observables left in the detector after an interaction. This is the reason why neutrinos that interact through NC modes are assumed to not oscillate within this analysis. Both CC and NC interactions are modeled for all the above interaction categories, other than MEC interactions which are only modeled for CC events.

As illustrated in Figure 5.1, CCQE interactions dominate the cross-section of neutrino interactions around $E_\nu \sim 0.5\text{GeV}$. The NEUT implementation adopts the Llewellyn Smith [153] model for neutrino-nucleus interactions, where the nuclear ground state of any bound nucleons (neutrino-oxygen interactions) is approximated by a spectral-function [154] model that simulates the effects of Fermi momentum and Pauli blocking. The cross-section of QE interactions is controlled by vector and axial-vector form factors parameterised by the BBBA05 [155] model and a dipole form factor with $M_A^{QE} = 1.21\text{GeV}$ fit to external data [156], respectively. NEUT implements the Valencia [157] model to simulate MEC events, where two nucleons and two holes in the nuclear target are produced (often called 2p2h interactions).

For neutrinos of energy $O(1)\text{GeV}$, PROD interactions become dominant. These predominantly produce charged and neutral pions although γ , kaon,



Figure 5.1: The NEUT prediction of the ν_μ -H₂O cross-section overlaid on the T2K ν_μ flux. The charged current (black, solid) and neutral current (black, dashed) inclusive, charged current quasi-elastic (blue, solid), charged current 2p2h (blue, dashed), charged current single pion production (pink), and charged current multi- π and DIS (Purple) cross-sections are illustrated. Figure taken from [151].

and η production is also considered. To simulate these interactions, the Berger-Sehgal [158] model is implemented within NEUT. It simulates the excitation of a nucleon from a neutrino interaction, production of an intermediate baryon, and the subsequent decay to a single meson or γ . Pions can also be produced through COH interactions, which occur when the incoming neutrino interacts with the entire oxygen nucleus leaving a single pion outside of the nucleus. NEUT utilises the Berger-Sehgal [159] model to simulate these COH interactions.

DIS and multi- π producing interactions become the most dominant for energies $> O(5)\text{GeV}$. PYTHIA [160] is used to simulate any interaction with invariant mass $W > 2\text{GeV}/c^2$, which produces at least one meson. For any interaction which produces at least two mesons but has $W < 2\text{GeV}/c^2$, the

¹⁴⁷⁷ Bronner model is used [161]. Both of these models use Parton distribution
¹⁴⁷⁸ functions based on the Bodek-Yang model [162–164].

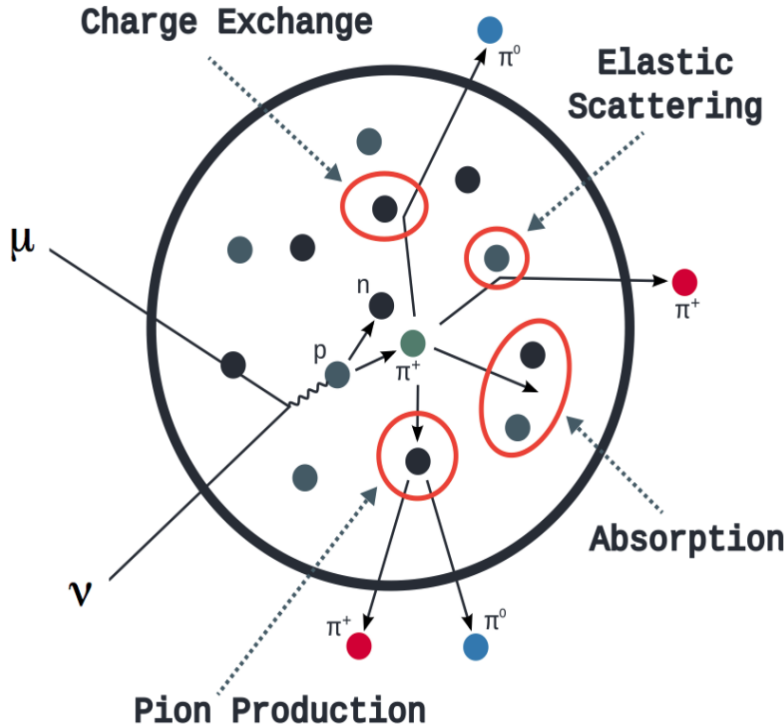


Figure 5.2: Illustration of the various processes which a pion can undergo before exiting the nucleus. Taken from [165].

¹⁴⁷⁹ Any pion that is produced within the nucleus can re-interact through final
¹⁴⁸⁰ state interactions before it exits, as illustrated by the scattering, absorption,
¹⁴⁸¹ production, and exchange interactions in Figure 5.2. These re-interactions alter
¹⁴⁸² the observable particles within the detector. For instance, if the charged pion
¹⁴⁸³ from a CC PROD interaction is absorbed, the observables would mimic a CC QE
¹⁴⁸⁴ interaction. To simulate these effects, NEUT uses a semi-classical intranuclear
¹⁴⁸⁵ cascade model [151]. This cascade functions by stepping the pion through the
¹⁴⁸⁶ nucleus in fixed-length steps equivalent to $dx = R_N/100$, where R_N is the radius
¹⁴⁸⁷ of the nucleus. At each step, the simulation allows the pion to interact through
¹⁴⁸⁸ scattering, charged exchange, absorption, or production with an interaction-
¹⁴⁸⁹ dependent probability calculated from a fit to external data [166]. This cascade
¹⁴⁹⁰ continues until the pion is absorbed or exits the nucleus.

1491 5.1.3 Detector

1492 Once the final state particle kinematics have been determined by NEUT, they
1493 are passed into the detector simulation. The near detectors, ND280 and INGRID,
1494 are simulated using a GEANT4 package [41, 167] to simulate the detector geom-
1495 etry, particle tracking, and energy deposition. The response of the detectors is
1496 simulated using the elecSim package [41].

1497 The far detector simulation is based upon the original Kamiokande experi-
1498 ment software which uses the GEANT3-based SKDETSIM [41, 168] package. This
1499 simulates the interactions of particles in the water as well as Cherenkov light
1500 production. The water quality and PMT calibration measurements detailed in
1501 subsection 3.1.2 are also used within this simulation to make accurate predictions
1502 of the detector response.

1503 Any event which generates optical photons that occurs in SK will be observed
1504 by the PMT array, where each PMT records the time and accumulated charge.
1505 This recorded information is shown in event displays similar to those illustrated
1506 in Figure 5.3 for simulated Monte Carlo events. To be useful for physics analyses,
1507 this series of PMT hit information needs to be reconstructed to determine the
1508 number and identity of particles and their kinematics (or track parameters): four-
1509 vertex, direction, and momentum. The reconstruction uses the fact that the charge
1510 and timing distribution of photons generated by a particular particle in an event is
1511 dependent upon its initial kinematics. Electron and muon rings are distinguished
1512 by their “fuzziness”. Muons are heavier and less affected by scattering or
1513 showering meaning they typically produce “crisp” rings. Electrons are more
1514 likely to interact via electromagnetic showering or scattering which results in
1515 larger variations of their direction from the initial direction. Consequently,
1516 electrons typically produce “fuzzier” rings compared to muons.



Figure 5.3: Event displays from Monte Carlo simulation at Super Kamiokande illustrating the “crisp” ring from a muon and the typically “fuzzy” electron ring. Each pixel represents a PMT and the color scheme denotes the accumulated charge deposited on that PMT. Figures taken from [169].

5.2 Event Reconstruction at SK

For the purposes of this analysis, the `fitQun` reconstruction algorithm [170] is utilised. Its core function is to compare a prediction of the accumulated charged and timing distribution from each PMT, generated for a particular particle identity and track parameters, to that observed in the neutrino event. It determines the preferred values by maximising a likelihood function (or minimising a log-likelihood function) which includes information from PMTs which were hit and those that were not hit. The `fitQun` algorithm is based on the key concepts of the MiniBooNE reconstruction algorithm [171].

The `fitQun` algorithm improves upon the previous `APFit` algorithm [172] which has been used for many previous SK analyses. `APFit` fits the vertex from timing information and then fits the direction of the particle from PMT hits within a 43 deg Cherenkov cone (assuming an ultra-relativistic particle) using a fitting estimator. A Hough transformation is used to find the radius of a ring (related to the momentum through Equation 3.2) as well as the number of rings contained within the event. The analysis presented here uses the `fitQun` algorithm as it improves both the accuracy of the fit parameters and the rejection of neutral

1534 current π^0 events as compared to APFit [173, 174].

1535 Any event in SK can consist of prompt (or primary) and decay (or secondary)
1536 particles. For example, a charged current muon neutrino interaction can gen-
1537 erate two particles that have the potential of generating Cherenkov photons
1538 (assuming the proton is below the Cherenkov threshold): the prompt muon,
1539 and the secondary decay-electron from the muon, approximately $2\mu\text{s}$ later. To
1540 reconstruct all particles within an event, it is divided into time clusters which are
1541 called “subevents”. Subevents after the primary subevent are considered to
1542 be decay electrons.

1543 The main steps of the `fitQun` reconstruction algorithm are:

- 1544 • **Vertex pre-fitting:** An estimate of the vertex is made using a goodness-of-fit
1545 metric based on PMT hit times
- 1546 • **Peak finding:** The initial time of each subevent is determined by clustering
1547 events by time residuals
- 1548 • **Single-ring fits:** Given the pre-fit vertex and estimated time of interaction,
1549 a maximum likelihood technique searches for a single particle generating
1550 light. Electron, muon, charged pion, and proton hypotheses are considered
- 1551 • **Multi-ring fits:** Seeded from the single-ring fits, hypotheses with multiple
1552 light-producing particles are considered using the same maximum likeli-
1553 hood technique. Electron-like or charged pion-like rings are added until
1554 the likelihood stops improving

1555 To find all the subevents in an event, a vertex goodness metric is calculated
1556 for some vertex position \vec{x} and time t ,

$$G(\vec{x}, t) = \sum_i^{\text{hit PMTs}} \exp \left(-\frac{1}{2} \left(\frac{T_{Res}^i(\vec{x}, t)}{\sigma} \right)^2 \right), \quad (5.1)$$

1557 where

$$T_{Res}^i(\vec{x}, t) = t^i - t - |R_{PMT}^i - \vec{x}| / c_n, \quad (5.2)$$

1558 is the residual hit time. It is the difference in time between the PMT hit time
 1559 t^i , of the i^{th} PMT, and the expected time of the PMT hit if the photon was at
 1560 the vertex. R_{PMT}^i is the position of the i^{th} PMT, c_n is the speed of light in water
 1561 and $\sigma = 4\text{ns}$ which is comparable to the time resolution of the PMT. When the
 1562 proposed fit values of time and vertex are close to the true values, $T_{Res}^i(\vec{x}, t)$ tends
 1563 to zero resulting in subevents appearing as spikes in the goodness metric. The
 1564 proposed fit vertex and time are grid-scanned, and the values which maximise
 1565 the goodness metric are selected as the “pre-fit vertex”. Whilst this predicts a
 1566 vertex for use in the clustering algorithm, the final vertex is fit using the higher-
 1567 precision maximum likelihood method described below.

1568 Once the pre-fit vertex has been determined, the goodness metric is scanned as
 1569 a function of t to determine the number of subevents. A peak-finding algorithm
 1570 is then used on the goodness metric, requiring the goodness metric to exceed
 1571 some threshold and drop below a reduced threshold before any subsequent
 1572 additional peaks are considered. The thresholds are set such that the rate of
 1573 false peak finding is minimised while still attaining good data to Monte Carlo
 1574 agreement. To improve performance, the pre-fit vertex for each delayed subevent
 1575 is re-calculated after PMT hits from the previous subevent are masked. This
 1576 improves the decay-electron tagging performance. Once all subevents have
 1577 been determined, the time window around each subevent is then defined by the
 1578 earliest and latest time which satisfies $-180 < T_{Res}^i < 800\text{ns}$. The subevents and
 1579 associated time windows are then used as seeds for further reconstruction.

1580 For a given subevent, the `fitQun` algorithm constructs a likelihood based on
 1581 the accumulated charge q_i and time information t_i from the i^{th} PMT,

$$L(\Gamma, \vec{\theta}) = \prod_j^{\text{unhit}} P_j(\text{unhit}|\Gamma, \vec{\theta}) \prod_i^{\text{hit}} \{1 - P_i(\text{unhit}|\Gamma, \vec{\theta})\} f_q(q_i|\Gamma, \vec{\theta}) f_t(t_i|\Gamma, \vec{\theta}). \quad (5.3)$$

1582 Where $\vec{\theta}$ defines the track parameters; vertex position, direction vector and
 1583 momenta, and Γ represents the particle hypothesis. $P_i(\text{unhit}|\Gamma, \vec{\theta})$ is the proba-
 1584 bility of the i^{th} tube to not register a hit given the track parameters and particle
 1585 hypothesis. The charge likelihood, $f_q(q_i|\Gamma, \vec{\theta})$, and time likelihood, $f_t(t_i|\Gamma, \vec{\theta})$,
 1586 represents the probability density function of observing charge q_i and time t_i on
 1587 the i^{th} PMT given the specified track parameters and particle hypothesis.

1588 The predicted charge is calculated based on contributions from both the
 1589 direct light and the scattered light. The direct light contribution is determined
 1590 based on the integration of the Cherenkov photon profile along the track. PMT
 1591 angular acceptance, water quality, and calibration measurements discussed in
 1592 subsection 3.1.2 are included to accurately predict the charge probability density
 1593 at each PMT. The scattered and reflected light is calculated in a similar way,
 1594 although it includes a scattering function that depends on the vertex of the
 1595 particle and the position of the PMT. The charge likelihood is calculated by
 1596 comparing the prediction to the observed charge in the PMT which is tuned
 1597 to the PMT simulation.

1598 The time likelihood is approximated to depend on the vertex \vec{x} , direction \vec{d} ,
 1599 and time t of the track as well as the particle hypothesis. The expected time
 1600 for PMT hits is calculated by assuming unscattered photons being emitted from
 1601 the midpoint of the track, S_{mid} ,

$$t_{\text{exp}}^i = t + S_{\text{mid}}/c + |R_{\text{PMT}}^i - \vec{x} - S_{\text{mid}}\vec{d}|/c_n, \quad (5.4)$$

1602 where c is the speed of light in a vacuum. The time likelihood is then expressed
 1603 in terms of the residual difference between the PMT hit time and the expected
 1604 hit time, $t_{\text{Res}}^i = t^i - t_{\text{exp}}^i$. The particle hypothesis and momentum also affect the
 1605 Cherenkov photon distribution. These parameters modify the shape of the time
 1606 likelihood density since in reality not all photons are emitted at the midpoint of
 1607 the track. As with the charge likelihood, the contributions from both the direct
 1608 and scattered light to the time likelihood density are calculated separately, which
 1609 are both calculated from particle gun Monte Carlo studies.

The track parameters and particle identity which maximise $L(\Gamma, \vec{\theta})$ are defined as the best-fit parameters. In practice MINUIT [175] is used to minimise the value of $-\ln L(\Gamma, \vec{\theta})$. The `fiTQun` algorithm considers an electron-like, muon-like, and charged pion-like hypothesis for events with a single final state particle, denoted “single-ring events”. The particle’s identity is determined by taking the ratio of the likelihood of each of the hypotheses. For instance, electrons and muons are distinguished by considering the value of $\ln(L(e, \vec{\theta}_e)/L(\mu, \vec{\theta}_\mu))$ in comparison to the reconstructed momentum of the electron hypothesis, as illustrated by Figure 5.4. The coefficients of the discriminator between electron-like and muon-like events are determined from Monte Carlo studies [170]. Similar distributions exist for distinguishing electron-like events from π^0 -like events, and muon-like events from pion-like events. The cuts are defined as,

$$\begin{aligned} \text{Electron/Muon} : & \ln(L_e/L_\mu) > 0.2 \times p_e^{rec} [\text{MeV}], \\ \text{Electron}/\pi^0 : & \ln(L_e/L_{\pi^0}) < 175 - 0.875 \times m_{\gamma\gamma} [\text{MeV}], \\ \text{Muon/Pion} : & \ln(L_\mu/L_{\pi^\pm}) < 0.15 \times p_\mu^{rec} [\text{MeV}], \end{aligned} \quad (5.5)$$

as taken from [176], where p_e^{rec} and p_μ^{rec} are the reconstructed momentum of the single-ring electron and muon fits, respectively. $m_{\gamma\gamma}$ represents the reconstructed invariant mass of the two photons emitted from π^0 decay. Typically, the distance between a particular entry in these two-dimensional distributions and the cut-line is termed the PID parameter and is illustrated in Figure 5.5.

The `fiTQun` algorithm also considers a π^0 hypothesis. To do this, it performs a fit looking for two standard electron-hypothesis tracks which point to the same four-vertex. This assumes the electron tracks are generated from photon-conversion so the electron tracks actually appear offset from the proposed π^0 vertex. For these fits, the conversion length, direction, and momentum of each photon are also considered as track parameters which are then fit in the same methodology as the standard single-ring hypotheses.

Whilst lower energy events are predominantly single-ring events, higher energy neutrino events can generate final states with multiple particles which

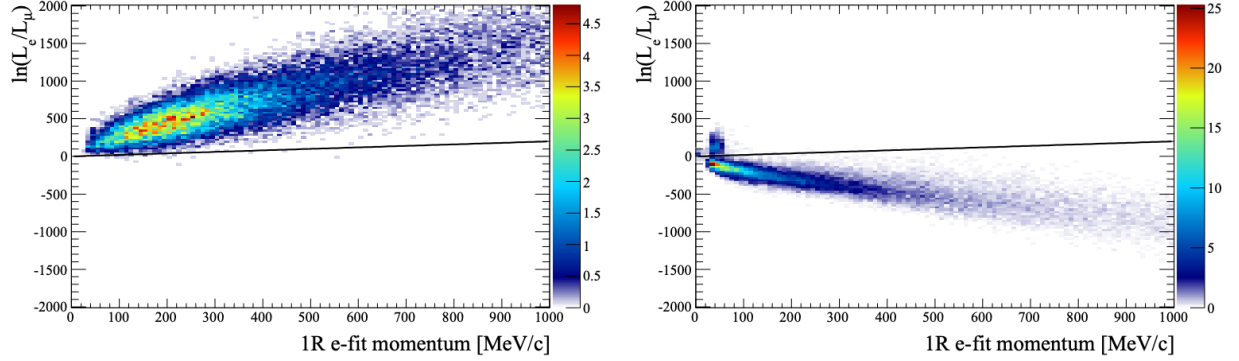


Figure 5.4: The difference of the electron-like and muon-like log-likelihood compared to the reconstructed single-ring fit momentum for atmospheric ν_e (left) and ν_μ (right) samples. The black line represents the cut used to discriminate electron-like and muon-like events, with coefficients obtained from Monte Carlo studies. Figures from [170].

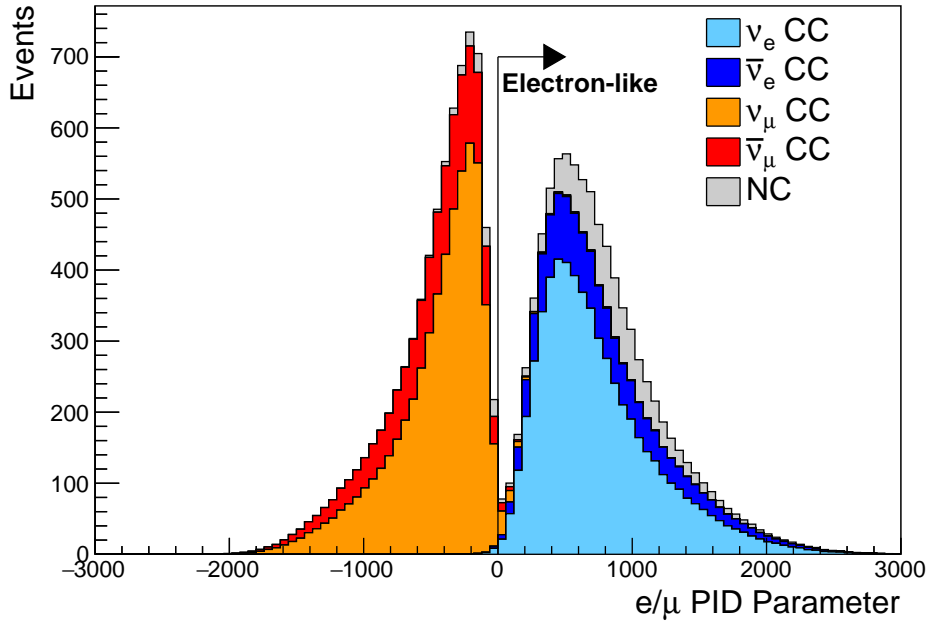


Figure 5.5: The electron/muon PID separation parameter for all sub-GeV single-ring events in SK-IV. The charged current (CC) component is broken down in four flavours of neutrino (ν_μ , $\bar{\nu}_\mu$, ν_e and $\bar{\nu}_e$). Events with positive values of the parameter are determined to be electron-like.

1636 generate Cherenkov photons. These “multi-ring” hypotheses are also considered
 1637 in the `fitQun` algorithm. When calculating the charge likelihood density, the
 1638 predicted charge associated with each ring is calculated separately and then
 1639 summed to calculate the total accumulated charge on each PMT. Similarly, the
 1640 time likelihood for the multi-ring hypothesis is calculated assuming each ring

is independent. Each track is time-ordered based on the time of flight from the center of the track to the PMT and the direct light from any ring incident on the PMT is assumed to arrive before any scattered light. To reduce computational resource usage, the multi-ring fits only consider electron-like and charged pion-like rings as the pion fit can be used as a proxy for a muon fit due to their similar mass. Due to the pions ability to interact through the strong force, they are more likely to hard-scatter. That means a single charged pion can produce multiple rings in different directions. There is an additional freedom, the fraction of kinetic energy lost in a single ring segment, which is added into the `fitQun` pion fit to cover this difference. Pion and muon rings are indistinguishable when this fraction tends to unity.

Multi-ring fits proceed by proposing another ring to the previous fit and then fitting the parameters in the method described above. Typically, multi-ring fits have the largest likelihood because of the additional degrees of freedom introduced. A likelihood value is calculated for the n -ring and $(n + 1)$ -ring hypotheses, where the additional ring is only included if the likelihood value is above 9.35, based on Monte Carlo studies in [177].

5.2.1 Validation of Reconstruction in SK-V

Understanding how the modelling of the detector conditions and stability effects the reconstruction is critical for ensuring accurate measurements. It is important to note that the detector systematics used in the 2020 T2K-only [72] oscillation analysis are determined using data-to-Monte Carlo comparisons of the SK-IV data [178]. Due to tank-open maintenance occurring between SK-IV and SK-V, the dark rate of each PMT was observed to increase in SK-V due to light exposure for a significant time during the repairs. This increase can be seen in Figure 5.6. Run-10 of the T2K experiment was conducted in the SK-V period, so the consistency of SK-IV and SK-V data needs to be studied to determine whether the SK-IV-defined systematics can be applied to the run-10 data. Consequently, the author of this thesis assessed the quality of `fitQun` event reconstruction for SK-V data.

This comparison study was performed using the stopping muon data set for both the SK-IV and SK-V periods. This data sample is used due to the high rate of interactions ($O(200)$ events per hour) as well as having similar energies to muons from CCQE ν_μ interactions from beam interactions. The rate of cosmic muons does depend on the solar activity cycle [179] but has been neglected in this comparison study. This is because the shape of the distributions is most important for the purposes of being compared to the detector systematics. The SK-IV and SK-V data samples consist of 2398.42 and 626.719 hours of data which equates to 686k and 192k events respectively. These samples do not correspond to the full data sets of either period but do contain enough events to be systematics limited rather than statistics limited.

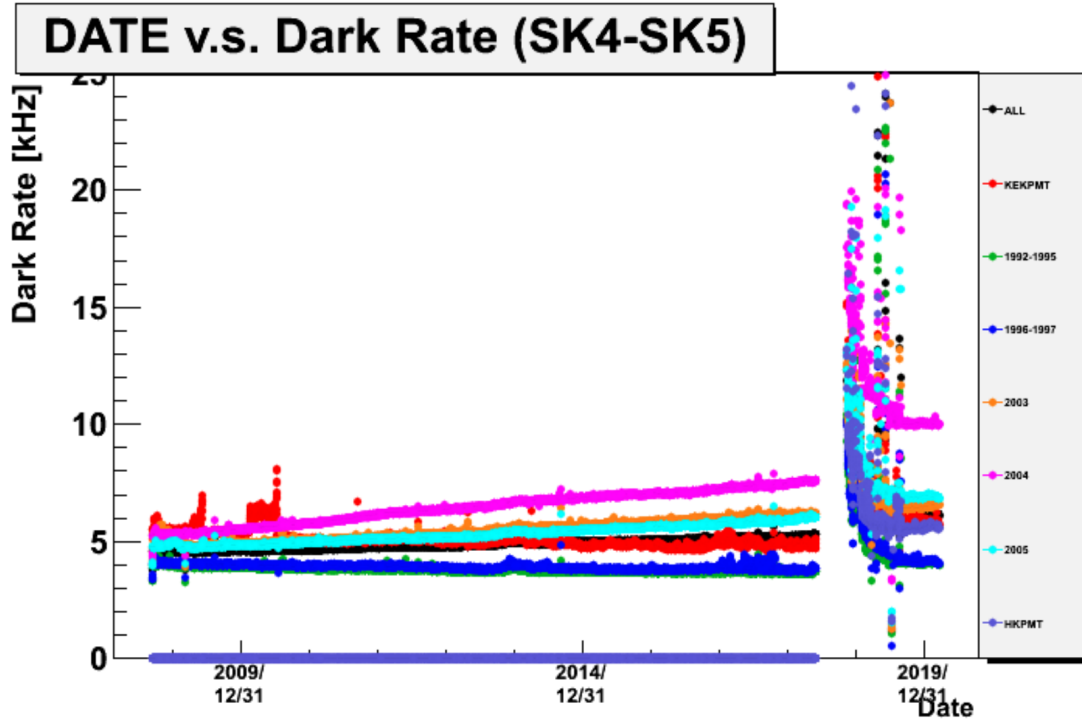


Figure 5.6: The variation of the measured dark rate as a function of date, broken down by PMT type. The SK-IV and SK-V periods span September 2008 to May 2018 and January 2019 to July 2020, respectively. The break in measurement in 2018 corresponds to the period of tank repair and refurbishment. Figure adapted from [178].

The predicted charge calculated in the `fitQun` algorithm includes a contribution from the photoelectron emission due to dark noise. Therefore, the increase

in the SK-V dark rate needs to be accounted for. In practice, the average dark rate in each SK period is calculated and used as an input in the reconstruction. This is calculated by averaging the dark rate per run for each period separately, using the calibration measurements detailed in subsection 3.1.2. The average dark rate from SK-IV and SK-V were found to be 4.57kHz and 6.30kHz, respectively. The charges associated with the muon and decay electron subevents are illustrated in Figure 5.7. The photoelectron emission from dark noise is more significant for events that have lower energy. This is because this contribution becomes more comparable to the number of photoelectrons emitted from incident photons in lower-energy events. This behaviour is observed in the data, where the charge deposited by the muon subevent is mostly unaffected by the increase in dark rate, whilst the charge associated with the decay-electron is clearly affected.

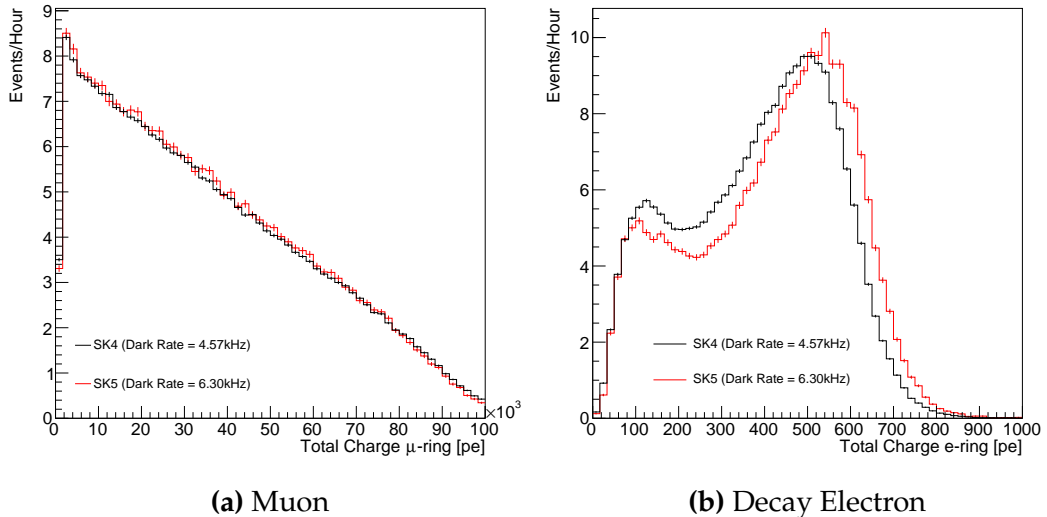


Figure 5.7: Comparison of the measured raw charge deposited per event from the stopping muon data samples between SK-IV (Blue) and SK-V (Red), split by the primary muon subevent (left) and the associated decay electron subevent (right).

The energy scale systematic is estimated from data-to-Monte Carlo differences in the stopping muon sample in [58] and found to be 2.1%. To determine the consistency of SK-IV and SK-V with respect to the energy scale systematic, the muon momentum distribution is compared between the two SK periods. As the total number of Cherenkov photons is integrated across the track length,

₁₇₀₀ the reconstructed momentum divided by track length (or range) is compared
₁₇₀₁ between SK-IV and SK-V as illustrated in Figure 5.8.

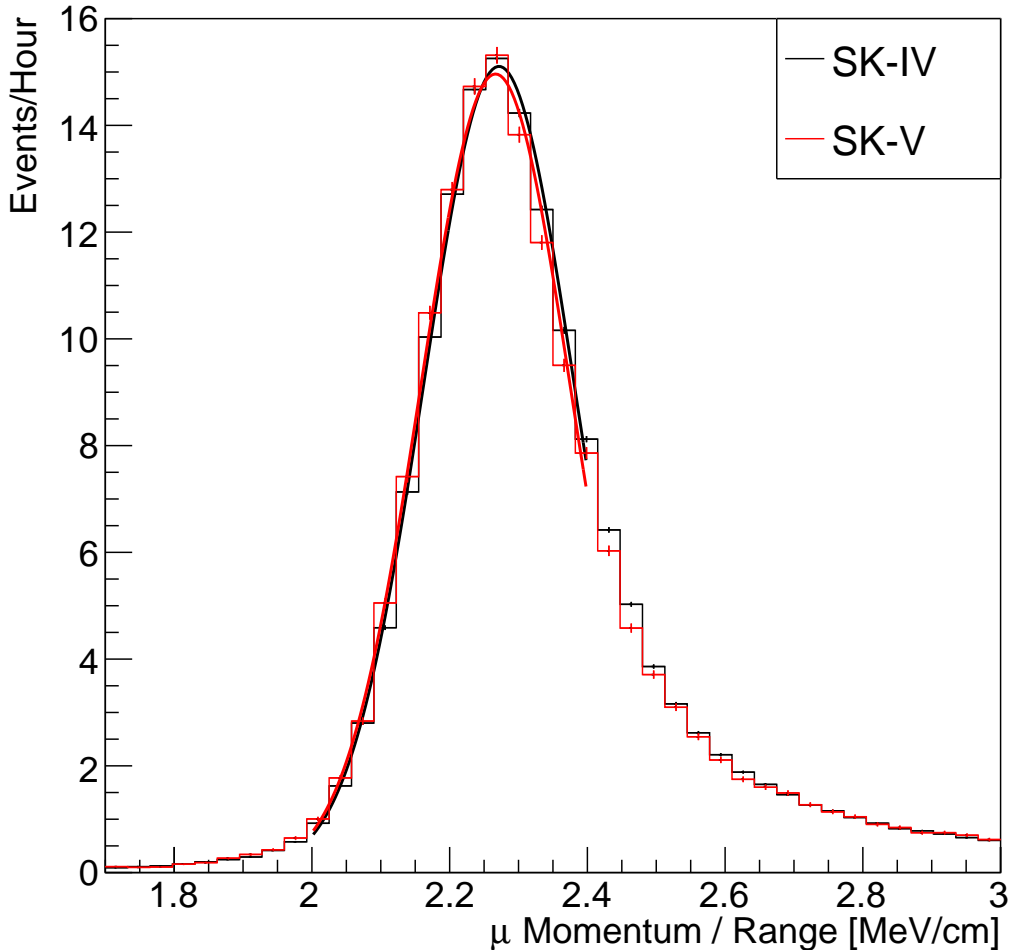


Figure 5.8: The distribution of the reconstructed momentum from the muon ring divided by the distance between the reconstructed muon and decay electron vertices as found in the stopping muon data sets of SK-IV (Black) and SK-IV (Red). Only events with one tagged decay electron are considered. A Gaussian fit is considered in the range $[2.0, 2.4]\text{MeV}/\text{cm}$ and illustrated as the solid curve.

₁₇₀₂ The consistency between these muon distributions has been computed in two
₁₇₀₃ ways. Firstly, a Gaussian is fit to the peak of each distribution separately, whose
₁₇₀₄ mean is found to be $(2.272 \pm 0.003)\text{MeV}/\text{cm}$ and $(2.267 \pm 0.006)\text{MeV}/\text{cm}$ for SK-
₁₇₀₅ IV and SK-V respectively. The ratio of these is equal to 1.002 ± 0.003 . The means of
₁₇₀₆ the Gaussian fits are consistent with the expected stopping power of a minimum

ionising muon for a target material (water) with $Z/A \sim 0.5$ [180]. The second consistency check is performed by introducing a nuisance parameter, α , which modifies the SK-V distribution. The value of α which minimises the χ^2 value between the SK-IV and SK-V is determined by scanning across a range of values. This is repeated by applying the nuisance parameter as both a multiplicative factor and an additive shift. The χ^2 distributions for different values of α is illustrated in Figure 5.9. The values which minimise the χ^2 are found to be 0.0052 and 1.0024 for the additive and multiplicative implementations, respectively. No evidence of shifts larger than the 2.1% uncertainty on the energy scale systematic has been found in the reconstructed momentum distribution of SK-IV and SK-V.

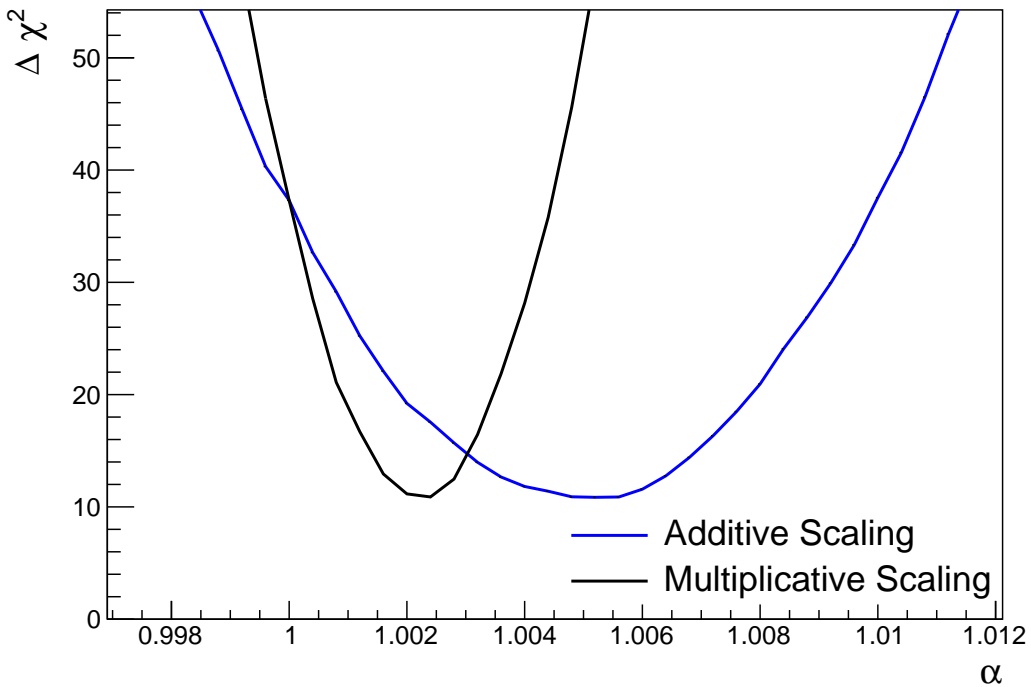


Figure 5.9: The χ^2 difference between the SK-IV and SK-V reconstructed muon momentum divided by range when the SK-V is modified by the scaling parameter α . Both additive (Blue) and multiplicative (Black) scaling factors have been considered. In practice, the additive scaling factor actually uses the value of $(\alpha - 1.0)$ but is illustrated like this so the results can be shown on the same axis range.

1717 5.3 Event Reduction at SK

1718 In normal data-taking operations, the SK detector observes many background
1719 events alongside the beam and atmospheric neutrino signal events of physics
1720 interest for this thesis. Cosmic ray muons and flasher events, which are the spon-
1721 taneous discharge of a given PMT, contribute the largest amount of background
1722 events in the energy range relevant to this thesis. Therefore the data recorded
1723 is reduced with the aim of removing these background events. The reduction
1724 process is detailed in [53, 84] and briefly summarised below.

1725 Atmospheric neutrino events observed in the SK detector are categorised
1726 into three different types of samples: fully contained (FC), partially contained
1727 (PC) and up-going muon (Up- μ), using PMT hit signatures in the inner and
1728 outer detector (ID and OD, respectively). To identify FC neutrino events, it is
1729 required that the neutrino interacts inside the fiducial volume of the ID and that
1730 no significant OD activity is observed. For this analysis, an event is defined to be
1731 in the fiducial volume provided the event vertex is at least 0.5m away from the
1732 ID walls. PC events have the same ID requirements but can have a larger signal
1733 present inside the OD. Typically, only high energy muons from ν_μ interactions can
1734 penetrate the ID wall. The Up- μ sample contains events where muons are created
1735 from neutrino interactions in the OD water or rock below the tank. They then
1736 propagate upwards through the detector. Downward-going muons generated
1737 from neutrino interactions above the tank are neglected because of the difficulty
1738 in separating their signature from the cosmic muon shower background. The
1739 sample categories are visually depicted in Figure 5.10.

1740 Based on the event characteristics, as defined by the `fitQun` event reconstruc-
1741 tion software, the FC events are categorised by

- 1742 • **Visible Energy:** equal to the sum of the reconstructed kinetic energy of
1743 particles above the Cerenkov threshold for all rings present in the event.
1744 The purpose is to separate events into sub-GeV and multi-GeV categories.

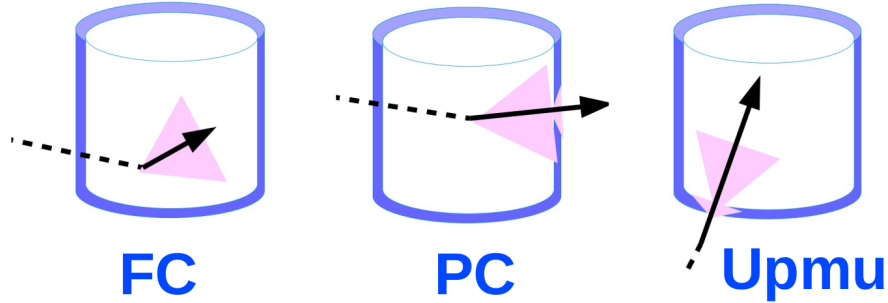


Figure 5.10: A depiction of the topology patterns for fully-contained (FC), partially-contained (PC), and up-going muon ($\text{Up-}\mu$) samples included in this analysis.

- 1745 • **Number of observed Cerenkov rings.** The purpose is to separate single-
1746 ring and multi-ring events, where single-ring events predominantly consist
1747 of quasi-elastic interactions and multi-ring events are typically resonant
1748 pion production or deep inelastic scattering events.
- 1749 • **Particle identification parameter of the most energetic ring:** A value de-
1750 termined from the maximum likelihood value based on `fitQun`'s electron,
1751 muon, or pion hypothesis. The purpose is to separate electron-like and
1752 muon-like events.
- 1753 • **Number of decay electrons:** The purpose is to separate quasi-elastic events
1754 (which have one decay electron emitted from the muon decay) and resonant
1755 pion production events (which have two decay electrons emitted from the
1756 muon and pion).

1757 The PC and Up- μ categories are broken down into “through-going” and
1758 “stopping” samples depending on whether the muon leaves the detector. This is
1759 because the PC stopping events deposit the entire energy of the interaction into
1760 the detector, resulting in better reconstruction. The energy of events that exit the
1761 detector has to be estimated, with a typically worse resolution, which introduces
1762 much larger systematic uncertainties. Through-going Up- μ samples are further
1763 broken down by whether any hadronic showering was observed in the event
1764 which typically indicates DIS interactions. The expected neutrino energy for the
1765 different categories is given in Figure 5.11. FC sub-GeV and multi-GeV events

¹⁷⁶⁶ peak around 0.7GeV and 3GeV respectively, with slightly different peak energies
¹⁷⁶⁷ for ν_e and ν_μ oscillation channels. PC and Up- μ are almost entirely comprised
¹⁷⁶⁸ of ν_μ events and peak around 7GeV and 100GeV, respectively.

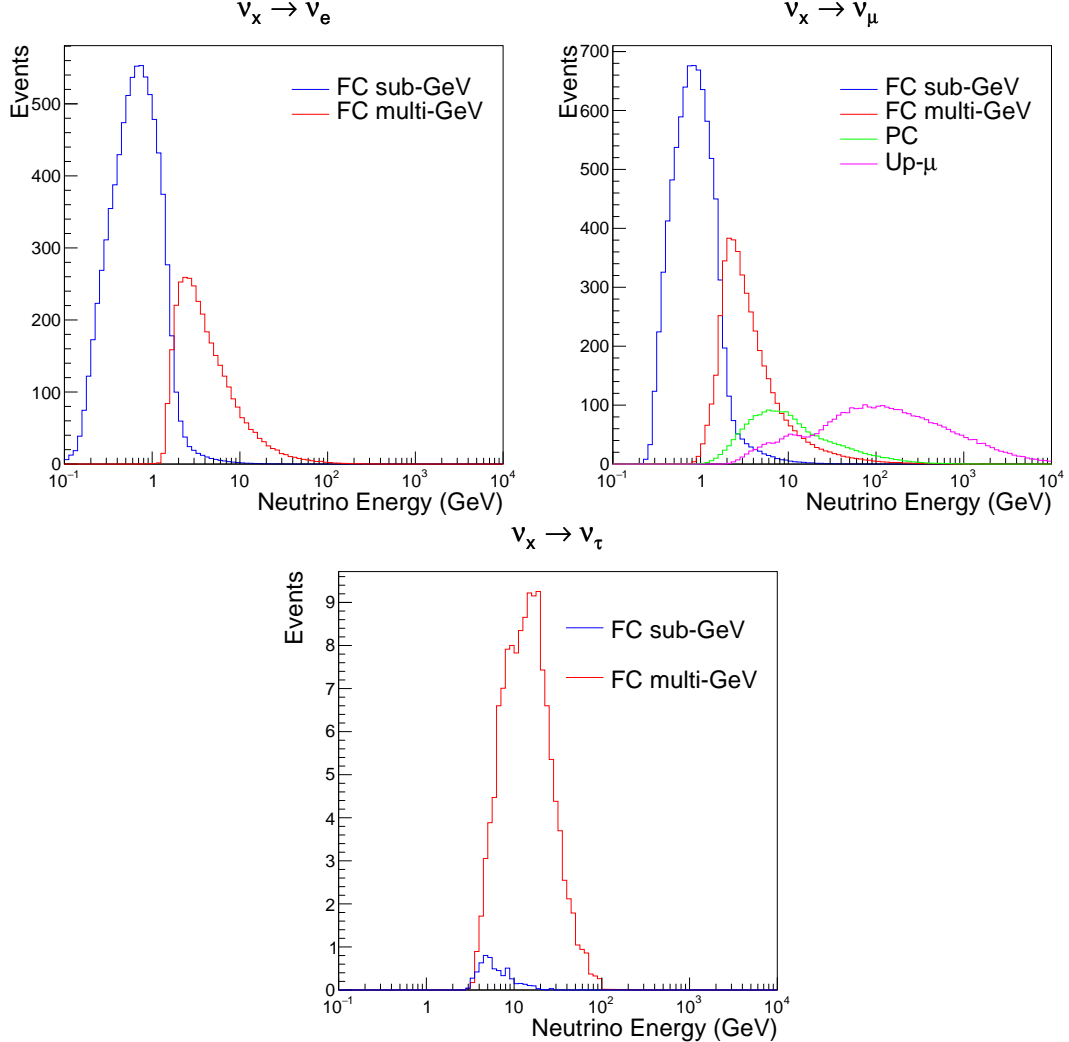


Figure 5.11: The predicted neutrino flux of the fully contained (FC) sub-GeV and multi-GeV, partially contained (PC), and upward-going muon (Up- μ) events. The prediction is broken down by the $\nu_x \rightarrow \nu_e$ prediction (top left), $\nu_x \rightarrow \nu_\mu$ prediction (top right) and $\nu_x \rightarrow \nu_\tau$ prediction (bottom). ν_x represents the flavours of neutrinos produced in the cosmic ray showers (electron and muon). Asimov A oscillation parameters are assumed (given in Table 2.2).

¹⁷⁶⁹ The first two steps in the FC reconstruction remove the majority of cosmic
¹⁷⁷⁰ ray muons by requiring a significant amount of ID activity compared to that
¹⁷⁷¹ measured in the OD. Events that pass this cut are typically very high momentum
¹⁷⁷² muons or events that leave very little activity in the OD. Consequently, a third

reduction step is then applied to select cosmic-ray muons that pass the initial reduction step. A purpose-built cosmic muon fitter is used to determine the entrance (or exit) position of the muon and a cut is applied to OD activity contained within 8m of this position. Flasher events are removed in the fourth reduction step which is based on the close proximity of PMT hits surrounding the PMT producing the flash. Events that pass all these reduction steps are reconstructed with the APFit algorithm. The fifth step of the reduction uses information from the more precise fitter to repeat the previous two steps with tighter cuts. Muons below the Cherenkov threshold can not generate optical photons in the ID but the associated decay electron can due to its lower mass. These are the types of events targeted in the fifth reduction step. The final cuts require the event vertex to be within the fiducial volume (0.5m from the wall although the nominal distance is 2.0m), visible energy $E_{vis} > 30\text{MeV}$ and fewer than 16 hits within the higher energy OD cluster. The culmination of the fully contained reduction results in 8.09 events/day in the nominal fiducial volume [81]. The uncertainty in the reconstruction is calculated by comparing Monte Carlo prediction to data. The largest discrepancy is found to be 1.3% in the fourth reduction step.

The PC and Up- μ events are processed through their own reduction processes detailed in [53]. Both of these samples are reconstructed with the APFit algorithm rather than `fiTQun`. This is because the efficiency of reconstructing events that leave the detector has not been sufficiently studied for reliable systematic uncertainties with `fiTQun`. The PC and Up- μ samples acquire events at approximately 0.66 and 1.44 events/day.

Beam neutrinos events undergo the same reduction steps as FC events and are then subject to further cuts [181]. The GPS system that links the timing between the beam facility and SK needs to be operating correctly and there should be no activity within the detector in the previous $100\mu\text{s}$ before the trigger. The events then need to triggered between $-2\mu\text{s}$ and $10\mu\text{s}$ of the expected spill timing.

1802 The beam neutrino samples are not split by visible energy since their energy
 1803 range is smaller than the atmospheric neutrino events. Following the T2K
 1804 analysis in [72], only single-ring beam neutrino events are considered. Similar to
 1805 atmospheric event selection, the number of decay electrons is used as a proxy for
 1806 distinguishing CCQE and CCRES events. The expected neutrino energy, broken
 1807 down by the number of decay electrons, is given in Figure 5.12.

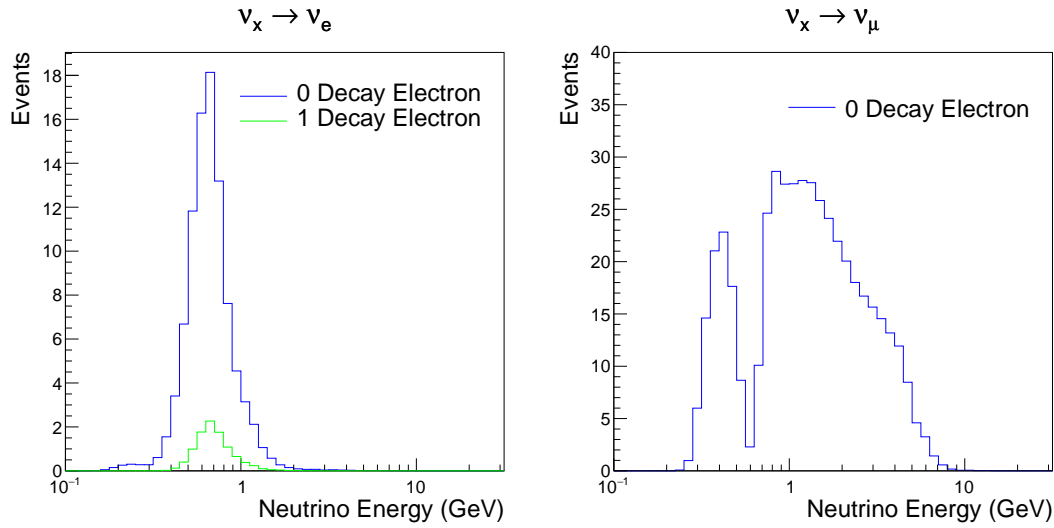


Figure 5.12: The predicted flux of beam neutrinos, as a function of neutrino energy. The predictions are broken down by the number of decay electrons associated with the particular events. Asimov A oscillation parameters are assumed (given in Table 2.2).

6

1808

1809

Sample Selections and Systematics

1810 The oscillation analysis presented within this thesis is built upon a simultaneous
1811 fit to atmospheric samples at SK, neutrino beam samples in the near detector,
1812 and beam samples at SK. This is the first simultaneous oscillation analysis of
1813 beam and atmospheric samples supported by the T2K and SK collaborations.
1814 Notably, the author of this thesis has been responsible for the building and
1815 developing the MaCh3 framework to support all sets of samples simultaneously.
1816 The definitions of the samples are documented in section 6.1, section 6.2, and
1817 section 6.3, respectively. The data collected and used within this analysis is
1818 detailed in Table 6.1. The near and far detector data corresponds to T2K runs
1819 2-9 and runs 1-10, respectively. The accumulated POT and beam power for runs
1820 1 – 10 are illustrated in Figure 6.1.

Data Type	Total
Near Detector FHC	1.15×10^{21} POT
Near Detector RHC	8.34×10^{20} POT
Far Detector FHC	1.97×10^{21} POT
Far Detector RHC	1.63×10^{21} POT
Atmospheric SK-IV	3244.4 days

Table 6.1: The amount of data collected in each detector used within this analysis. The data collected at the near and far detector, for both neutrino beam (FHC) and antineutrino beam (RHC), is measured as the number of protons on target (POT).

The difference in POT recorded at the near and far detector is due to the difference in downtime. The SK detector is very stable with almost 100% of data recorded during beam operation. Due to various technical and operational issues, the downtime of the near detector is significantly higher due to its more complex design and operating requirements.

The systematic parameters invoked within the flux, detector, and interaction models used within this analysis are documented in section 6.4. The standard configuration of the joint beam and atmospheric data fit utilises far detector systematics provided in the official inputs from the two experiments. Additionally, a correlated detector model which fits the parameters used in sample selections to data has been developed and documented in subsection 6.4.5.

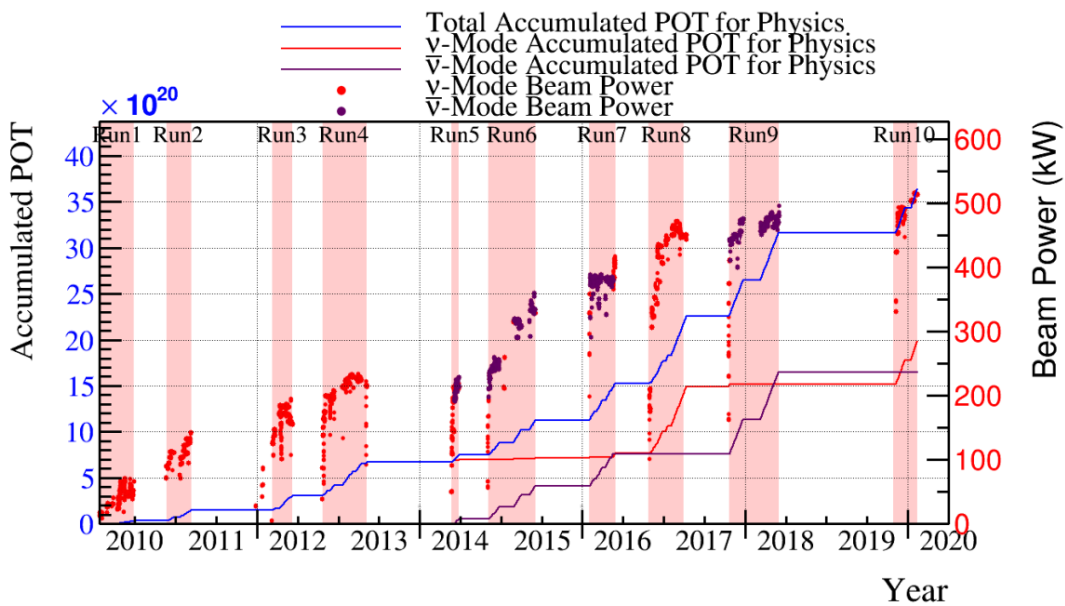


Figure 6.1: The accumulated beam data, measured as the number of protons on target (POT). The total data (blue) is given which comprises of the neutrino beam (red) and antineutrino (purple) components. The beam power for neutrino and antineutrino beams is given as the markers using the same colour scheme. The timescale runs from Run 1 which started in January 2010 until Run 10 which ended in February 2020. The ratio of accumulated data in neutrino and antineutrino beam is 54.7% : 45.3%.

1832 6.1 Atmospheric Samples

1833 The atmospheric event selection follows the official SK-IV analysis presented
1834 in [84] and is documented below. The Monte Carlo prediction used within this
1835 analysis corresponds to 500 years worth of neutrino events, which is scaled down
1836 to match the SK-IV livetime of 3244.4 days.

1837 The fully contained (FC), partially contained (PC), and upward going muon
1838 events ($\text{up-}\mu$) which pass the reduction cuts discussed in section 5.3 are further
1839 broken down into different samples based on reconstruction information. This
1840 section details the samples used within this oscillation analysis, alongside the
1841 chosen binning.

1842 FC events are first separated by the visible energy deposited within the
1843 detector. This is calculated as the sum of the reconstructed kinetic energy
1844 above the Cherenkov threshold for all rings present in the event. Events are
1845 separated by whether they were above or below $E_{\text{vis}} = 1.33\text{GeV}$. This separates
1846 “subGeV” and “multiGeV” events. Typically, lower energy events consist of
1847 charged current quasi-elastic (CCQE) interactions which are better understood
1848 and simpler to reconstruct resulting in smaller systematic uncertainties. Events
1849 are further separated by the number of rings associated with the event due to
1850 similar reasoning. As the oscillation probability is dependant upon the flavour
1851 of neutrino, electron and muon events are separated using a similar likelihood
1852 method to that discussed in section 5.2. To reduce computational resources
1853 required for the reconstruction, only electron and pion hypotheses are considered
1854 so this separation cut depends on the ratio of the electron to pion likelihoods,
1855 $\log(L_e/L_\pi)$. Finally, the number of decay electrons is used to classify events.
1856 Charged current resonant pion production (CCRES) interactions generate a final-
1857 state pion. This can decay, mostly likely through a muon, into a decay electron.
1858 Therefore any electron-like event with one decay electron or muon-like event
1859 with two decay electrons was most likely produced by a CCRES interaction.
1860 Consequently, the number of decay electrons can be used to distinguish CCQE

¹⁸⁶¹ and CCRES interaction modes. Ultimately, FC subGeV events are separated
¹⁸⁶² into the samples listed in Table 6.2.

Sample Name	Description
SubGeV- <i>e</i> like-0dcy	Single ring <i>e</i> -like events with zero decay electrons
SubGeV- <i>e</i> like-1dcy	Single ring <i>e</i> -like events with one or more decay electrons
SubGeV- <i>μ</i> like-0dcy	Single ring <i>μ</i> -like events with zero decay electrons
SubGeV- <i>μ</i> like-1dcy	Single ring <i>μ</i> -like events with one decay electrons
SubGeV- <i>μ</i> like-2dcy	Single ring <i>μ</i> -like events with two or more decay electrons
SubGeV- <i>π</i> 0like	Two <i>e</i> -like ring events with zero decay electrons and reconstructed π^0 mass $85 \leq m_{\pi^0} < 215$ MeV

Table 6.2: The fully contained subGeV samples, defined as events with visible energy $E_{vis} < 1.33$ GeV, used within this oscillation analysis.

¹⁸⁶³ In addition to the cuts discussed above, multiGeV samples also have addi-
¹⁸⁶⁴ tional cuts to separate samples which target neutrino and antineutrino events.
¹⁸⁶⁵ As discussed in section 2.5, the matter resonance only occurs for neutrinos in the
¹⁸⁶⁶ normal hierarchy and antineutrinos in the inverted mass hierarchy. Therefore,
¹⁸⁶⁷ having flavour-enriched samples aids in the determination of the mass hierarchy.
¹⁸⁶⁸ For a CCRES interaction,

$$\begin{aligned}
 \bar{\nu}_e + N &\rightarrow e^+ + N' + \pi^-, \\
 \nu_e + N &\rightarrow e^- + N' + \pi^+ \\
 &\quad \downarrow \mu^+ + \nu_\mu \\
 &\quad \downarrow e^+ + \nu_e + \bar{\nu}_\mu.
 \end{aligned} \tag{6.1}$$

¹⁸⁶⁹ The π^- emitted from a $\bar{\nu}_e$ interaction is more likely to be captured by an
¹⁸⁷⁰ oxygen nucleus than the π^+ from ν_e interactions [182]. These pions then decay,
¹⁸⁷¹ mostly through muons, to electrons. Therefore the number of tagged decay
¹⁸⁷² electrons associated with an event gives an indication of whether the interaction
¹⁸⁷³ was due to a neutrino or antineutrino: zero for $\bar{\nu}_e$ events, and one for ν_e events.
¹⁸⁷⁴ The ability to separate neutrino from antineutrino events is illustrated in Table 6.4,
¹⁸⁷⁵ where the MultiGeV-*e*like-nue has 78% purity of CC neutrino interactions with
¹⁸⁷⁶ only 7% antineutrino background, the rest consisting of NC backgrounds.

1877 The number of decay electrons discriminator works reasonably well for single-
 1878 ring events. However, this is not the case for multi-ring events. A multiGeV
 1879 multiring electron-like (MME) likelihood cut was introduced in [183, 184]. This
 1880 is a two-stage likelihood selection cut. Four observables are used in the first
 1881 likelihood cut to distinguish $CC\nu_e$ and $CC\bar{\nu}_e$ events from background:

- 1882 • The number of decay electrons
 1883 • The maximum distance between the vertex of the neutrino and the decay
 1884 electrons
 1885 • The energy deposited by the highest energy ring
 1886 • The particle identification of that highest energy ring

1887 Background events consist of $CC\nu_\mu$ and NC interactions. Typically, the
 1888 majority of the energy in these background events is carried by the hadronic
 1889 system. Additionally, muons tend to travel further than the pions from $CC\nu_e$
 1890 before decaying. Thus, the parameters used within the likelihood cut target these
 1891 typical background interaction kinematics.

Sample Name	Description
MultiGeV-elike-nue	Single ring e -like events with zero decay electrons
MultiGeV-elike-nuebar	Single ring e -like events with one or more decay electrons
MultiGeV-mulike	Single ring μ -like events
MultiRing-elike-nue	Two or more ring events with leading energy e -like ring and passed both MME and $\nu/\bar{\nu}$ separation cuts
MultiRing-elike-nuebar	Two or more ring events with leading energy e -like ring and passed MME and failed $\nu/\bar{\nu}$ separation cuts
MultiRing-mulike	Two or more ring events with leading energy μ -like ring and only requires $E_{vis} > 0.6\text{GeV}$
MultiRing-Other1	Two or more ring events with leading energy e -like ring and failed the MME likelihood cut

Table 6.3: The fully contained multiGeV samples used within this oscillation analysis. Both the sample name and description are given.

1892 Neutrino and antineutrino events are then separated by a second likelihood
 1893 method ($\nu/\bar{\nu}$ separation) detailed in [58]. This uses the number of decay electrons,

1894 the number of reconstructed rings, and the event’s transverse momentum. The
1895 last two parameters are used because higher-energy samples tend to have more
1896 pions produced above the Cherenkov threshold which results in more rings
1897 compared to an antineutrino interaction. Furthermore, the angular distribution
1898 also tends to be more forward peaked in antineutrino interactions as compared
1899 to neutrino interactions [84]. These FC multiGeV sample definitions are de-
1900 tailed in Table 6.3.

1901 The PC and up- μ samples are split by the amount of energy deposited within
1902 the outer detector, into “stopping” and “through-going” samples. If an event
1903 leaves the detector, the energy it takes with it has to be estimated which increases
1904 the systematic uncertainty compared to events entirely contained within the
1905 inner detector. This estimation is particularly poor at high energies, thus the
1906 up- μ through-going events are not binned in reconstructed momentum. The
1907 through-going up- μ are further separated by the presence of any electromagnetic
1908 showering in the event, as the assumption of non-showering muon does not give
1909 reliable reconstruction for these types of events [53]. In total, 13 FC, 2 PC, and
1910 3 up- μ atmospheric samples are included within this analysis.

1911 The atmospheric samples are binned in direct observables: reconstructed
1912 lepton momentum and direction, as given by Table 6.5. The distribution of
1913 the reconstructed lepton momentum (for samples that only have one bin in
1914 reconstructed zenith angle) and reconstructed direction for each atmospheric
1915 sample used within this analysis is illustrated in Figure 6.2.

1916 The reconstructed lepton momemtum, illustrated by interaction mode break-
1917 down, of some representative atmospheric samples is given in Figure 6.3. The
1918 equivalent distributions of all atmospheric samples used within this analy-
1919 sis can be found in [185]. The low energy samples tend to be dominated by
1920 the interaction mode they target (CCQE for SubGeV-elike-0dcy and CC1 π for
1921 SubGeV-elike-1dcy samples). The higher energy samples include much more
1922 CCOther interactions, especially at larger reconstructed lepton momentum.

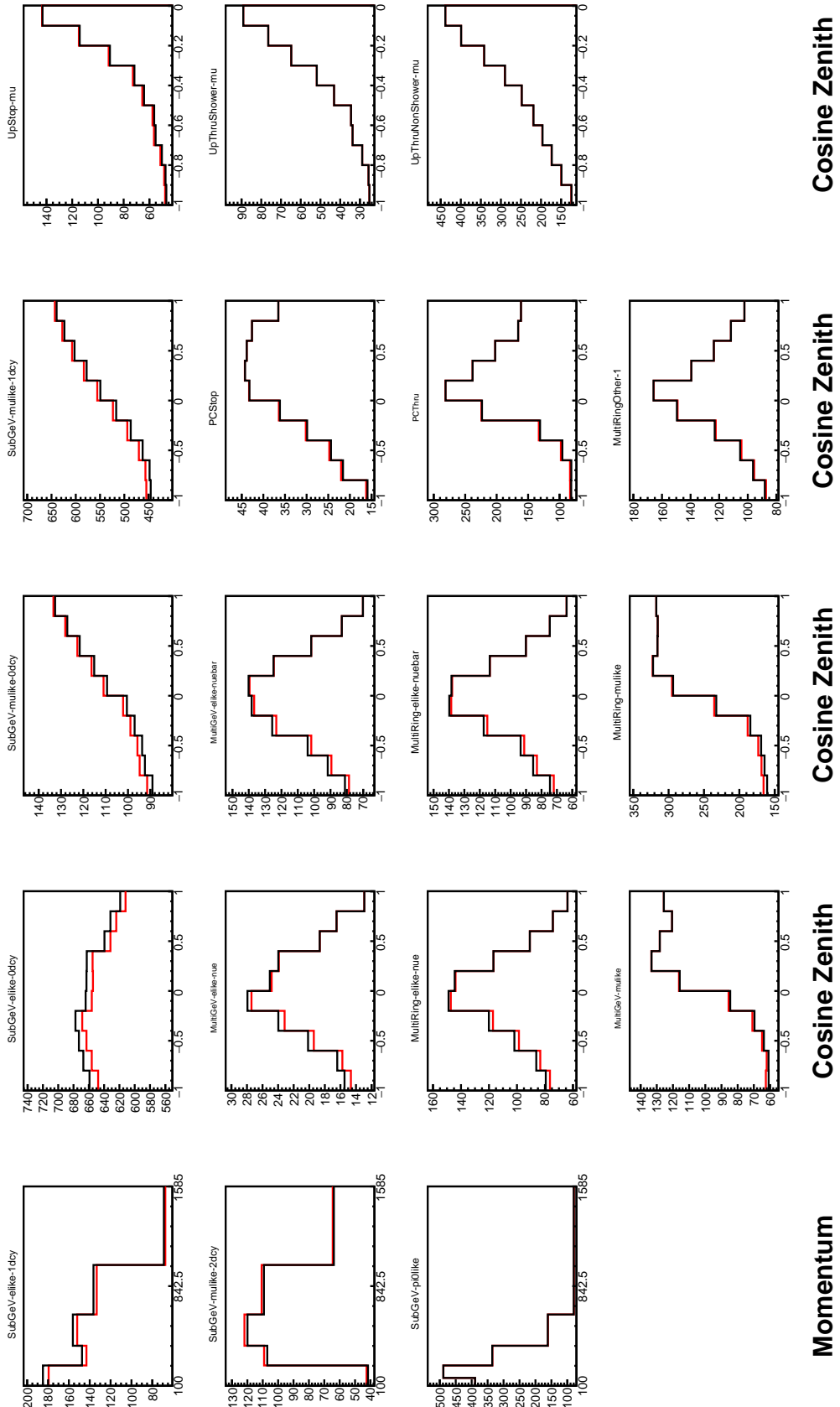


Figure 6.2: Comparison of the SK-IV atmospheric samples between predictions made with the CP-violating Asimov A (Black) and CP-conserving Asimov B (Red) oscillation parameter sets (given in Table 2.2). The subGeV samples CCRES and π^0 -like samples are given in their reconstructed lepton momentum. All other samples are presented in their reconstructed zenith angle projection.

Sample	$CC\nu_e$	$CC\bar{\nu}_e$	$CC(\nu_\mu + \bar{\nu}_\mu)$	$CC(\nu_\tau + \bar{\nu}_\tau)$	NC
SubGeV- <i>elike</i> -0dcy	72.17	23.3	0.724	0.033	3.77
SubGeV- <i>elike</i> -1dcy	86.81	1.773	7.002	0.062	4.351
SubGeV- <i>mulike</i> -0dcy	1.003	0.380	90.07	0.036	8.511
SubGeV- <i>mulike</i> -1dcy	0.023	0.	98.46	0.029	1.484
SubGeV- <i>mulike</i> -2dcy	0.012	0.	99.25	0.030	0.711
SubGeV- <i>pi0like</i>	6.923	2.368	0.928	0.011	89.77
MultiGeV- <i>elike</i> -nue	78.18	7.041	3.439	1.886	9.451
MultiGeV- <i>elike</i> -nuebar	56.68	37.81	0.174	0.614	4.718
MultiGeV- <i>mulike</i>	0.024	0.005	99.67	0.245	0.058
MultiRing- <i>elike</i> -nue	59.32	12.39	4.906	3.385	20
MultiRing- <i>elike</i> -nuebar	52.39	31.03	1.854	1.585	13.14
MultiRing- <i>mulike</i>	0.673	0.080	97.33	0.342	1.578
MultiRingOther-1	27.98	2.366	34.93	4.946	29.78
PCStop	8.216	3.118	84.45	0.	4.214
PCThru	0.564	0.207	98.65	0.	0.576
UpStop-mu	0.829	0.370	98.51	0.	0.289
UpThruNonShower-mu	0.206	0.073	99.62	0.	0.103
UpThruShower-mu	0.128	0.054	99.69	0.	0.132

Table 6.4: The purity of each atmospheric sample used within this analysis, broken down by charged current (CC) and neutral current (NC) interactions and which neutrino flavour interacted within the detector. Each row sums to 100% by definition. Asimov A oscillation parameter sets are assumed (given in Table 2.2). Electron neutrino and antineutrino events are separated to illustrate the ability of the separation likelihood cuts used within the multiGeV and multiring sample selections.

Sample	$\cos(\theta_Z)$ Bins	Momentum Bin Edges ($\log_{10}(P)$ MeV)
SubGeV- <i>elike</i> -0dcy	10	2.0, 2.4, 2.6, 2.8, 3.0, 3.2
SubGeV- <i>elike</i> -1dcy	1	2.0, 2.4, 2.6, 2.8, 3.0, 3.2
SubGeV- <i>mulike</i> -0dcy	10	2.0, 2.4, 2.6, 2.8, 3.0, 3.2
SubGeV- <i>mulike</i> -1dcy	10	2.0, 2.4, 2.6, 2.8, 3.0, 3.2
SubGeV- <i>mulike</i> -2dcy	1	2.0, 2.4, 2.6, 2.8, 3.0, 3.2
SubGeV- <i>pi0like</i>	1	2.0, 2.2, 2.4, 2.6, 2.8, 3.2
MultiGeV- <i>elike</i> -nue	10	3.0, 3.4, 3.7, 4.0, 5.0
MultiGeV- <i>elike</i> -nuebar	10	3.0, 3.4, 3.7, 4.0, 5.0
MultiGeV- <i>mulike</i>	10	3.0, 3.4, 5.0
MultiRing- <i>elike</i> -nue	10	3.0, 3.4, 3.7, 5.0
MultiRing- <i>elike</i> -nuebar	10	3.0, 3.4, 3.7, 5.0
MultiRing- <i>mulike</i>	10	2.0, 3.124, 3.4, 3.7, 5.0
MultiRing- <i>Other1</i>	10	3.0, 3.4, 3.7, 4.0, 5.0
PC-Stop	10	2.0, 3.4, 5.0
PC-Through	10	2.0, 3.124, 3.4, 3.7, 5.0
Upmu-Stop	10	3.2, 3.4, 3.7, 8.0
Upmu-Through-Showering	10	2.0, 8.0
Upmu-Through-NonShowering	10	2.0, 8.0

Table 6.5: The reconstructed cosine zenith and lepton momentum binning assigned to the atmospheric samples. The “ $\cos(\theta_Z)$ Bins” column illustrates the number of bins uniformly distributed over the $-1.0 \leq \cos(\theta_Z) \leq 1.0$ region for fully and partially contained samples and $-1.0 \leq \cos(\theta_Z) \leq 0.0$ region for up- μ samples.

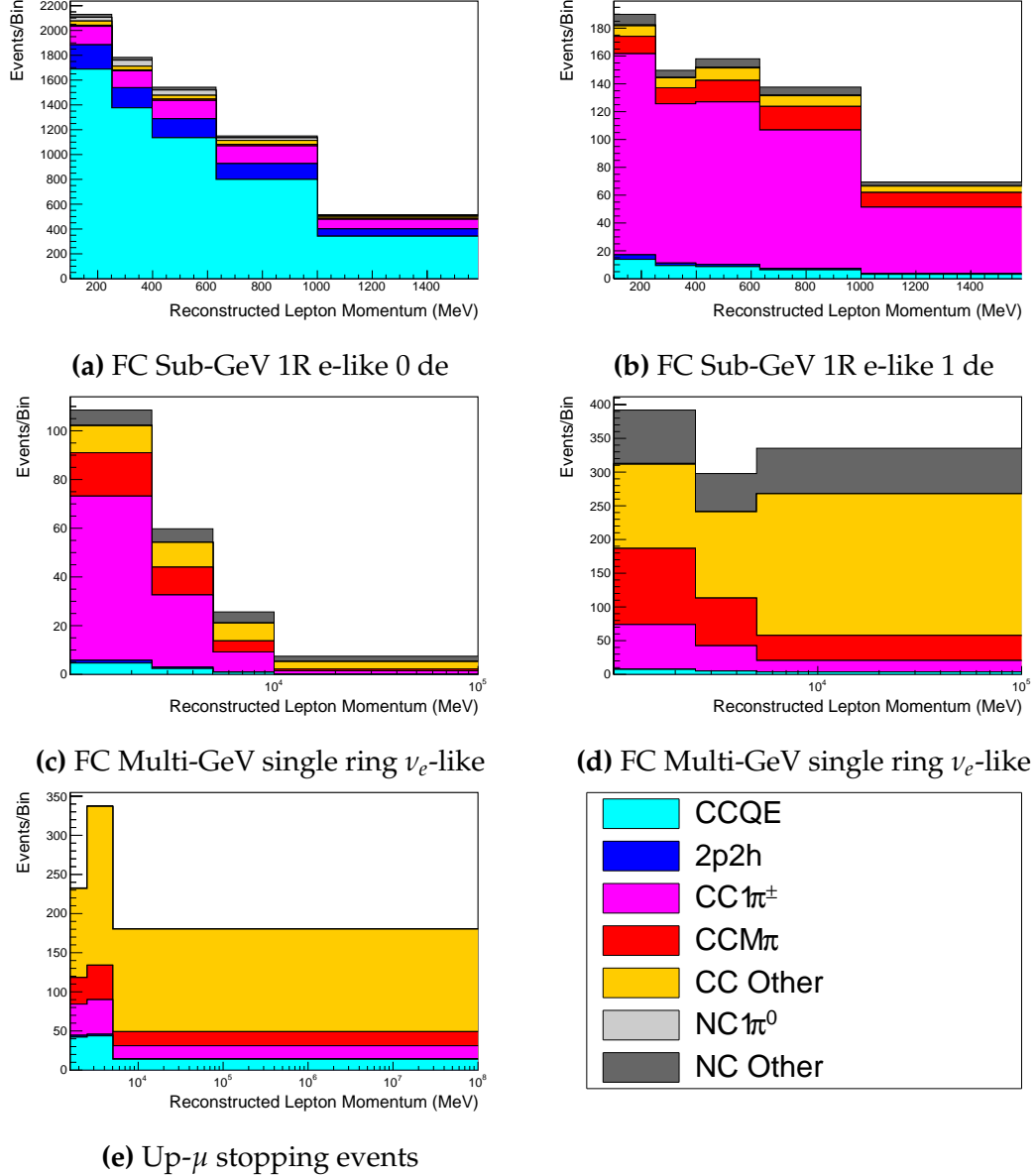


Figure 6.3: Breakdown by interaction mode of some representative atmospheric samples used within this analysis, illustrated as a function of reconstructed lepton momentum. The binning is provided in Table 6.5. Asimov A oscillation parameters are used to generate these plots. The interaction mode breakdown of all atmospheric samples used within this analysis can be found in [185].

6.2 Near Detector Beam Samples

The near detector sample selections are documented in detail within [186] and summarised below. Samples are selected based upon which of the two Fine Grained Detectors (FGD) the vertex is reconstructed in as well as the operating mode of the beam: FHC or RHC. Wrong-sign neutrino background samples are considered in the RHC mode in order to add additional constraints on model parameters. Samples from the wrong-sign component of the FHC beam mode are not included as they are statistically insignificant compared to those samples already listed.

The reconstruction algorithm uses a clustering algorithm to group hits within the TPC. It then adds information from the upstream FGD to form a track that passes through both sub-detectors. In FHC(RHC), the highest momentum negative(positive) curvature track is defined as the muon candidate. Before being assigned a sample, these candidate muon events must pass CC-inclusive cuts, as defined in [187]:

- Event Timing: The DAQ must be operational and the event must occur within the expected beam time window consistent with the beam spill
- TPC Requirement: The muon-candidate track path must intercept one or more TPCs
- Fiducial volume: The event must originate from within the fiducial volume defined in [188]
- Upstream Background: Remove events that have muon tracks that originate upstream of the FGDs by requiring no high-momentum tracks within 150mm upstream of the candidate vertex. Additionally, events that occur within the downstream FGD are vetoed if a secondary track starts within the upstream FGD

- 1949 • Broken track removal: All candidates where the muon candidate is broken
1950 in two are removed

- 1951 • Muon PID: Measurements of dE/dx in a TPC are used to distinguish muon-
1952 like events, from electron-like or proton-like, using a likelihood cut

1953 In addition to these cuts, RHC neutrino events also have to undergo the
1954 following cuts to aid in the separation of neutrino and antineutrino [189]:

- 1955 • TPC Requirement: The track path must intercept TPC2
1956 • Positive Track: The highest momentum track must have a positive recon-
1957 structed charge
1958 • TPC1 Veto: Remove any events originating upstream of TPC1

1959 Once all CC-inclusive events have been determined, they are further split by
1960 pion multiplicity: CC0 π , CC1 π , and CCOther. Pions in the TPCs are selected by
1961 requiring a second track to be observed, which is separate from the muon track
1962 and is in the same beam spill window and sub-detector. The number of FGD
1963 pions is equal to the number of Michel electrons which were tagged within the
1964 same sub-detector and spill window. If this value is equal to zero, the number
1965 of FGD pions is equivalent to the number of pion-like tracks which have dE/dx
1966 measurements consistent with the pion hypothesis. The pion tracks from both
1967 FGD and TPC events are required to have a vertex consistent with that of the
1968 muon candidate. The Michel electron tagging is preferential as a delayed Michel
1969 is almost always a pion meaning this cut has a higher purity [187, 190], whereas a
1970 track in the FGD that is consistent with a pion could be another particle resulting
1971 in a lower purity. Michel electrons are neglected in the TPC as the pions very
1972 rarely stop due to the low density.

1973 CC0 π , CC1 π , and CCOther samples are defined with the following cuts:

- 1974 • ν_μ CC0 π Selection: No electrons in TPC and no charged pions or decay
1975 electrons within the TPC or FGD

- ν_μ **CC1 π Selection:** Exactly one charged pion in either the TPC or FGD
- ν_μ **CCOther Selection:** All events which are not classified into the above two selections

Counting the three selections for each FGD in FHC and RHC running, including the wrong-sign background in RHC, 18 near detector samples are used within this analysis. These samples are binned in reconstructed lepton momentum (illustrated in Figure 6.4) and direction with respect to the beam. The binning is chosen such that each event has at least 20 Monte Carlo events in each bin [188]. This is to ensure that the bins are coarse enough to ensure the reduction of statistical errors, whilst also being fine enough to sample the high-resolution peak regions. The exact binning is detailed in [188].

6.3 Far Detector Beam Samples

The beam neutrino events which occur at the SK detector, which pass the reduction cuts detailed in section 5.3, are separated based on whether the beam was operating in FHC or RHC mode. The events are then separated into three samples: electron-like (1Re), muon-like (1R μ), and CC1 π^+ -like (1Re1de) which are observed as electron-like events with an associated decay electron [178]. As discussed in section 6.1, positively charged pions emitted from neutrino interactions are more likely to produce decay electrons than negatively charged pions. Consequently, the CC1 π^+ -like sample is only selected when the beam is operating in FHC mode. Therefore, five beam samples measured at SK are used in this analysis.

The fiducial volume definition for beam samples is slightly different from that used for the atmospheric samples. It uses both the distance to the closest wall (dWall) and the distance to the wall along the trajectory of the particle (toWall). This allows events that originate close to the wall but are facing into the tank to be included within the analysis, which would have otherwise been removed. These additional events are beneficial for a statistics-limited experiment. The exact

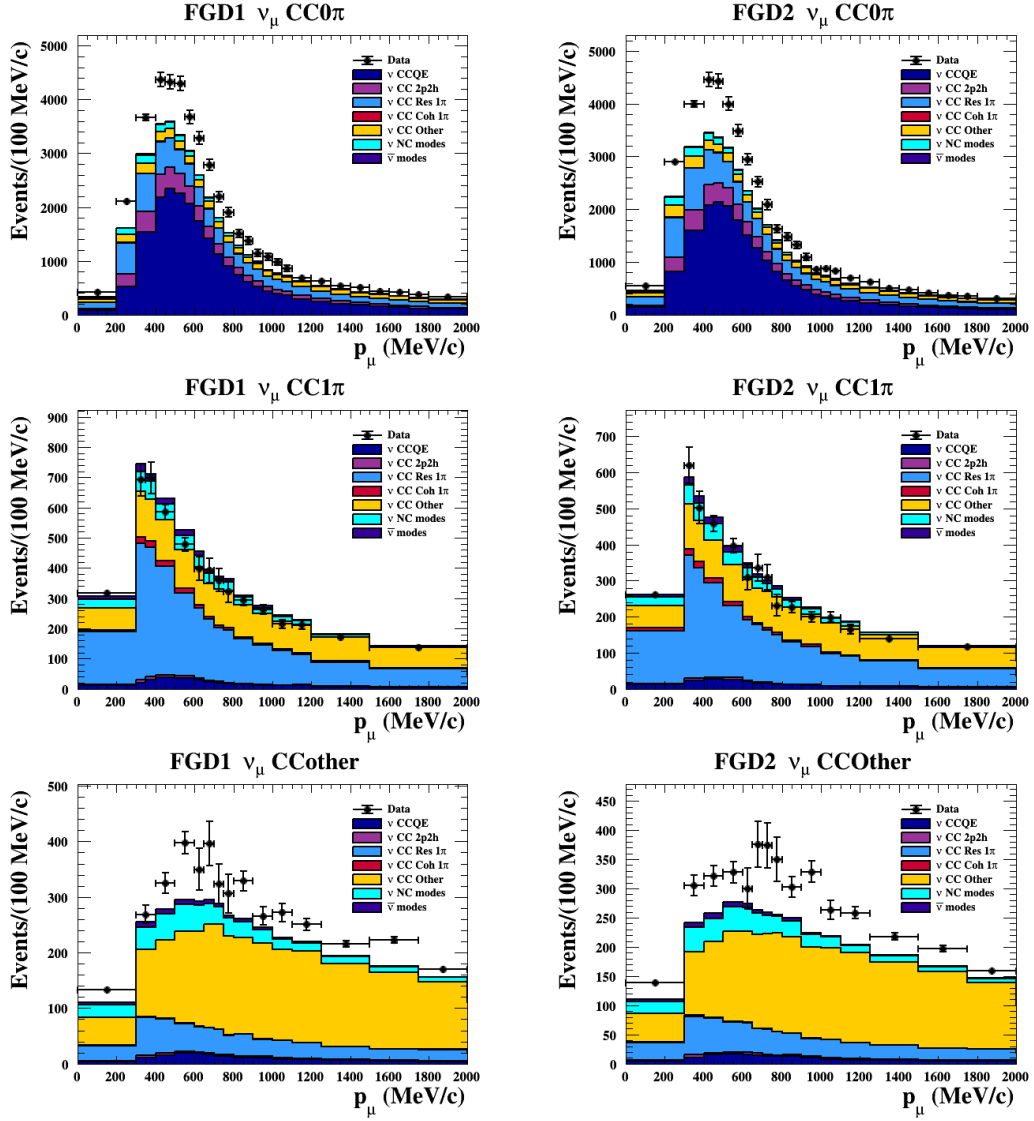


Figure 6.4: The nominal Monte Carlo predictions compared to data for the FGD1 and FGD2 samples in neutrino beam mode, broken down into the $CC\nu_\mu 0\pi$, $CC\nu_\mu 1\pi$ and $CC\nu_\mu$ Other categories. Figures taken from [186].

2004 cut values for both `dWall` and `tWall` are different for each of the three types of
2005 sample and are optimised based on T2K sensitivity to δ_{CP} [176, 191]. They are:

2006 **1Re event selection** For an event to be classified as a 1Re-like, the event must sat-
2007 isfy:

- 2008 • Fully-contained and have $dWall > 80\text{cm}$ and $tWall > 170\text{cm}$
- 2009 • Total of one ring which is reconstructed as electron-like with reconstructed

2010 momentum $P_e > 100\text{MeV}$

2011 • Zero decay electrons are associated with the event

2012 • Passes π^0 rejection cut discussed in section 5.2

2013 The zero decay electron cut removes non-CCQE interactions and the π^0
 2014 rejection cut is designed to remove neutral current π^0 background events which
 2015 can be easily reconstructed as 1Re-like events.

2016 The zero decay electron cut removes non-CCQE interactions and the π^0
 2017 rejection cut is designed to remove neutral current π^0 background events which
 2018 can be easily reconstructed as 1Re-like events.

2019 **CC1 π^+ event selection** This event selection is very similar to that of the 1Re
 2020 sample. The only differences are that the dWall and toWall criteria are changed
 2021 to $> 50\text{cm}$ and $> 270\text{cm}$, respectively, and exactly one decay electron is required
 2022 from the π^+ decay.

2023 **1R μ event selection** A 1R μ -like event is determined by the following cuts:

2024 • Fully-contained and have dWall $> 50\text{cm}$ and toWall $> 250\text{cm}$

2025 • Total of one ring which is reconstructed as muon-like with reconstructed
 2026 momentum $P_\mu > 200\text{MeV}$

2027 • Fewer than two decay electrons are associated with the event

2028 • Passes π^+ rejection cut discussed in section 5.2

2029 All of these samples are binned in reconstructed neutrino energy. This is
 2030 possible under a particular interaction mode assumption, as the direction from
 2031 the source is known extremely well. For the 1Re-like and 1R μ -like samples,

$$E_\nu^{rec} = \frac{(M_N - V_{nuc})E_l - m_l^2/2 + M_N V_{nuc} - V_{nuc}^2/2 + (M_P^2 + M_N^2)/2}{M_N - V_{nuc} - E_l + P_l \cos(\theta_{beam})}. \quad (6.2)$$

2032 Where M_N , M_P and m_l are the masses of the neutron, proton and outgoing
 2033 lepton, respectively. $V_{nuc} = 27\text{MeV}$ is the binding energy of the oxygen nucleus
 2034 [178], θ_{beam} is the angle between the beam and the direction of the outgoing
 2035 lepton, and E_l and P_l are the energy and momentum of that outgoing lepton.

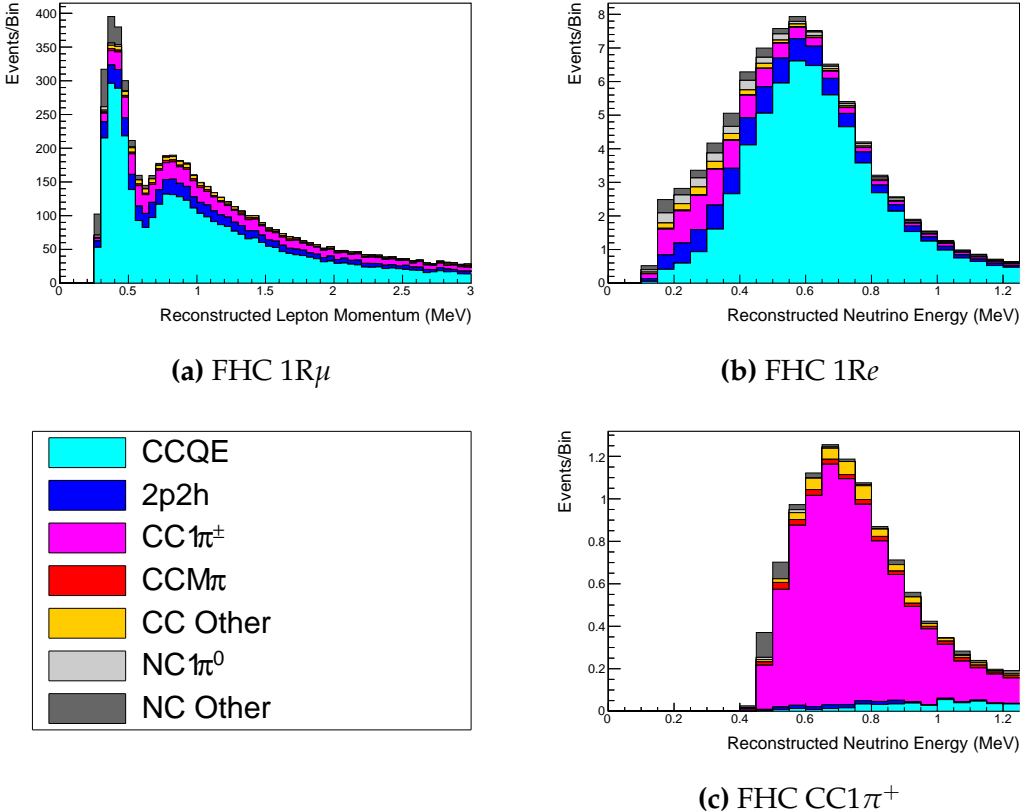


Figure 6.5: The reconstructed neutrino energy, as defined by Equation 6.2 and Equation 6.3, for the 1R μ -like, 1R e -like, and CC1 π^+ -like samples. The AsimovA oscillation parameters are assumed (given in Table 2.2). These samples are the FHC mode samples. For ease of viewing, the 1R μ sample only shows the $0 \leq E_\nu^{rec} < 3.0\text{GeV}$ but the binning extends to 30.0GeV .

2036 The reconstructed neutrino energy of the CC1 π^+ -like events also accounts
 2037 for the delta resonance produced within the interaction,

$$E_\nu^{rec} = \frac{2M_N E_l + M_{\Delta^{++}}^2 - M_N^2 - m_l^2}{2(M_N - E_l + P_l \cos(\theta_{beam}))}. \quad (6.3)$$

2038 Where $M_{\Delta^{++}}$ is the mass of the delta baryon. Binding energy effects are not
 2039 considered as a two-body process, with the delta baryon, is assumed. This follows
 2040 the T2K oscillation analysis presented in [72], although recent developments of

2041 the interaction model in the latest T2K oscillation analysis do include effects
2042 from binding energy in this calculation [192].

2043 The reconstructed neutrino energy for the FHC samples is illustrated in
2044 Figure 6.5. As expected, the $1R\mu$ -like and $1Re$ -like samples are heavily dominated
2045 by CCQE interactions, with smaller contributions from $2p2h$ meson exchange and
2046 resonant pion production interactions. The $CC1\pi^+$ -like sample predominantly
2047 consists of charged current resonant pion production interactions. The $1Re$ -like
2048 and $CC1\pi^+$ -like samples are also binned by the angle between the neutrino beam
2049 and the reconstructed lepton momentum. This is to aid in charged current and
2050 neutral current separation, as indicated in Figure 6.6. This is because the neutral
2051 current backgrounds are predominantly due to π^0 -decays, which decay into two
2052 γ rays. The opening angle of which (alongside the different final state kinematics)
2053 can produce a slightly broader angular distribution compared to the final state
2054 particles originating from charged current ν_e interactions.

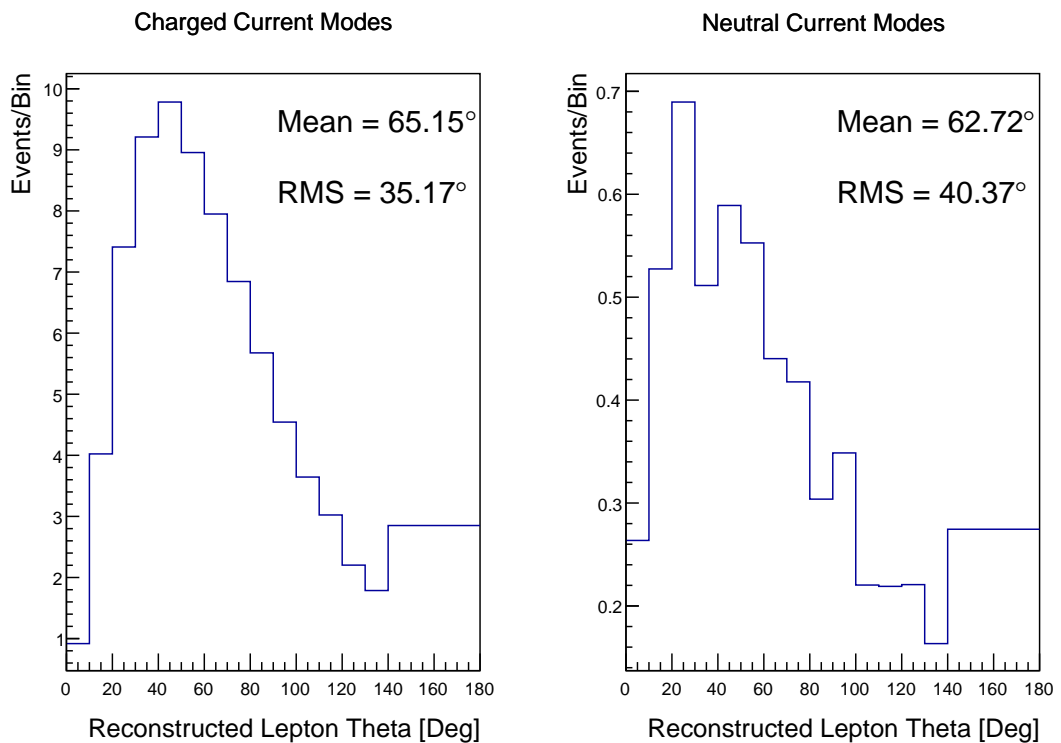


Figure 6.6: The distribution of the angle between the neutrino beam direction and the reconstructed final state lepton, for the FHC 1Re-like sample. The distribution is broken down by neutrino interaction mode into charged current (left) and neutral current (right) components. Asimov A oscillation parameter sets are assumed (given in Table 2.2). The RMS of the charged and neutral current plots are 35.17° and 40.37° , respectively.

2055 6.4 Systematic Uncertainties

2056 The systematic model parameters for this analysis are split into groups, or blocks,
2057 depending on their purpose. They consist of flux uncertainties, neutrino-matter
2058 interaction systematics, and detector efficiencies. There are also uncertainties on
2059 the oscillation parameters to which this analysis is not sensitive, namely Δm_{21}^2
2060 and $\sin^2(\theta_{12})$. These oscillation parameter uncertainties are taken from the 2020
2061 PDG measurements [73]. As described in chapter 4, each model parameter used
2062 within this analysis requires a prior uncertainty. This is provided via separate
2063 covariance matrices for each block. The covariance matrices can include prior
2064 correlations between parameters within a single block, but the separate treatment
2065 means prior correlations can not be included for parameters in different groups.
2066 Some parameters in these models have no reasonably motivated uncertainties
2067 and are assigned flat priors which do not modify the likelihood penalty. In
2068 practice, these flat prior parameters are actually assigned a Gaussian with a
2069 very large width to ensure the covariance matrix is positive definite. They are
2070 then checked at run time to determine if they contribute to the likelihood. The
2071 flux, neutrino interaction, and detector modeling simulations have already been
2072 discussed in section 5.1 and section 5.2. The uncertainties invoked within each
2073 of these models are described below.

2074 6.4.1 Beam Flux

2075 The neutrino beam flux systematics are based upon the uncertainty in the mod-
2076 eling of the components of the beam simulation. This includes the model of
2077 hadron productions and reinteractions, the shape, intensity, and alignment of
2078 the beam with respect to the target, and the uniformity of the magnetic field
2079 produced by the horn, alongside other effects. The uncertainty, as a function
2080 of neutrino energy, is illustrated in Figure 6.7 which includes a depiction of
2081 the total uncertainty as well as the contribution from individual components.
2082 The uncertainty around the peak of the energy distribution ($E_\nu \sim 0.6\text{GeV}$) is

2083 dominated by uncertainties in the beam profile and alignment. Outside of this
2084 region, uncertainties on hadron production dominate the error.

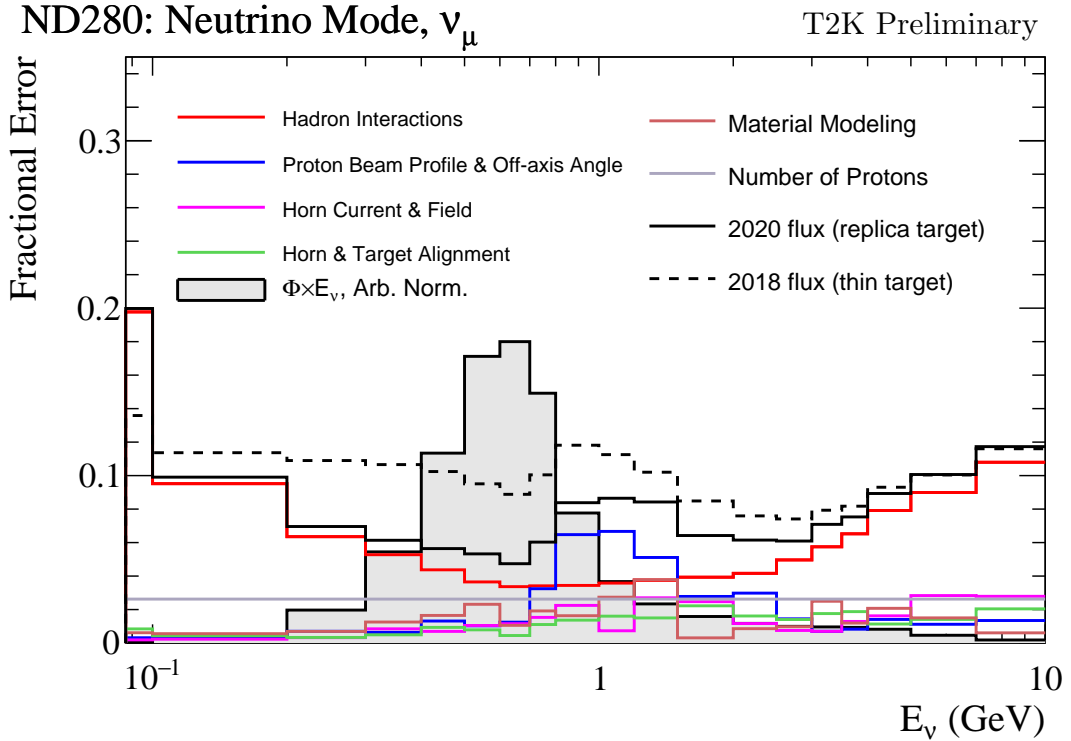


Figure 6.7: The total uncertainty evaluated on the near detector ν_μ flux prediction constrained by the replica-target data, illustrated as a function of neutrino energy. The solid(dashed) line indicates the uncertainty used within this analysis(the T2K 2018 analysis [193]). The solid histogram indicates the neutrino flux as a function of energy. Figure taken from [194].

2085 The beam flux uncertainties are described by one hundred parameters. They
2086 are split between the ND280 and SK detectors and binned by neutrino flavour:
2087 ν_μ , $\bar{\nu}_\mu$, ν_e and $\bar{\nu}_e$. The response is then broken down as a function of neutrino
2088 energy. The bin density in the neutrino energy is the same for the ν_μ in FHC
2089 and $\bar{\nu}_\mu$ in RHC beams, and narrows for neutrino energies close to the oscillation
2090 maximum of $E_\nu = 0.6\text{GeV}$. This binning is specified in Table 6.6. All of these
2091 systematic uncertainties are applied as normalisation parameters with Gaussian
2092 priors centered at 1.0 and error specified from a covariance matrix provided
2093 by the T2K beam group [194].

Neutrino Flavour	Sign	Neutrino Energy Bin Edges (GeV)
μ	Right	0., 0.4, 0.5, 0.6, 0.7, 1., 1.5, 2.5, 3.5, 5., 7., 30.
μ	Wrong	0., 0.7, 1., 1.5, 2.5, 30.
e	Right	0., 0.5, 0.7, 0.8, 1.5, 2.5, 4., 30.
e	Wrong	0., 2.5, 30.

Table 6.6: The neutrino energy binning for the different neutrino flavours. “Right” sign indicates neutrinos in the FHC beam and antineutrinos in the RHC beam. “Wrong” sign indicates antineutrinos in the FHC beam and neutrinos in the RHC beam. The binning of the detector response is identical for the FHC and RHC modes as well as at ND280 and SK.

2094 6.4.2 Atmospheric Flux

2095 The atmospheric neutrino flux is modeled by the HKKM model [49]. 16 systematic
 2096 uncertainties are applied to control the normalisation of each neutrino flavour,
 2097 energy, and direction. They are summarised below:

- 2098 • **Absolute Normalisation:** The overall normalisation of each neutrino flavour
 2099 is controlled by two independent systematic uncertainties, for $E_\nu < 1\text{GeV}$
 2100 and $E_\nu > 1\text{GeV}$, respectively. This is driven mostly by hadronic interaction
 2101 uncertainties for the production of pions and kaons [49]. The strength of
 2102 the response is dependent upon the neutrino energy. The uncertainty is
 2103 parameterized following Figure 11 in [49].
- 2104 • **Relative Normalisation:** Uncertainties on the ratio of $(\nu_\mu + \bar{\nu}_\mu) / (\nu_e + \bar{\nu}_e)$
 2105 are controlled by the difference between the HKKM model [49], FLUKA
 2106 [52] and Bartol models [48]. Three independent parameters are applied in
 2107 the energy ranges: $E_\nu < 1\text{GeV}$, $1\text{GeV} < E_\nu < 10\text{GeV}$, and $E_\nu > 10\text{GeV}$.
- 2108 • **$\nu/\bar{\nu}$ Normalisation:** The uncertainties in the π^+/π^- (and kaon equivalent)
 2109 production uncertainties in the flux of $\nu/\bar{\nu}$. The response is applied using
 2110 the same methodology as the relative normalisation parameters.
- 2111 • **Up/Down and Vertical/Horizontal Ratio:** Similar to the above two sys-
 2112 tematics, the difference between the HKKM, FLUKA, and Bartol model

2113 predictions, as a function of $\cos(\theta_Z)$, is used to control the normalisation of
2114 events as a function of zenith angle.

- 2115 • **K/ π Ratio:** Higher energy neutrinos ($E_\nu > 10\text{GeV}$) mostly originate in
2116 kaon decay. Measurements of the ratio of K/ π production [195] are used to
2117 control the systematic uncertainty of the expected ratio of pion and kaon
2118 production.
- 2119 • **Solar Activity:** As the 11-year solar cycle can affect the Earth's magnetic
2120 field, the flux of primary cosmic rays varies across the same period. The
2121 uncertainty is calculated by taking a ± 1 year variation, equating to a 10%
2122 uncertainty for the SK-IV period.
- 2123 • **Atmospheric Density:** The height of the interaction of the primary cosmic
2124 rays is dependent upon the atmospheric density. The HKKM assumes the
2125 US standard 1976 [145] profile. This systematic controls the uncertainty in
2126 that model.

2127 The total uncertainty is dominated by the absolute and relative normalisation
2128 parameters. The effect of which is illustrated in Figure 6.8. Generally, the
2129 uncertainty is large at low energy, reducing to $O(10\%)$ around the peak of the
2130 flux distribution and then increasing once the neutrino energy exceeds 10GeV.

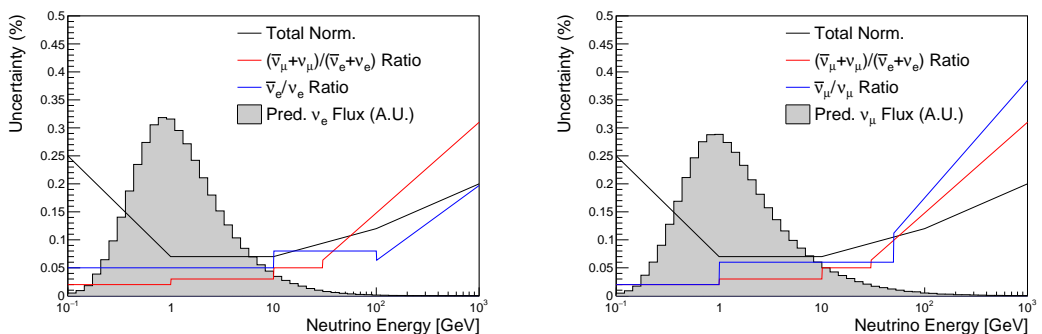


Figure 6.8: The uncertainty evaluated on the atmospheric ν_e (left) and ν_μ (right) flux predictions. The absolute normalisation and flavour ratio uncertainties are given. The solid histogram indicates the neutrino flux as a function of energy.

2131 Updates to the HKKM and Bartol models are underway [150] to use a similar
2132 tuning technique to that used in the beam flux predictions. After those updates,
2133 it may be possible to include correlations in the hadron production uncertainty
2134 systematics for beam and atmospheric flux predictions.

2135 6.4.3 Neutrino Interaction

2136 Neutrino interactions in the detectors are modeled by NEUT. The two indepen-
2137 dent oscillation analyses, T2K-only [196] and the SK-only [58], have developed
2138 separate interaction models. To maximise sensitivity out of this simultaneous
2139 beam and atmospheric analysis, a correlated interaction model has been defined
2140 in [185]. Where applicable, correlations allow the systematic uncertainties applied
2141 to the atmospheric samples to be constrained by near detector neutrino beam
2142 measurements. This can lead to stronger sensitivity to oscillation parameters
2143 as compared to an uncorrelated model.

2144 The low-energy T2K systematic model has a more sophisticated treatment
2145 of CCQE, 2p2h, and CCRES uncertainties, where extensive comparisons of
2146 this model have been performed to external data [196]. However, the model
2147 is not designed for high-energy atmospheric events, like those illustrated in
2148 Figure 5.11. Therefore the high energy systematic model from the SK-only
2149 analysis is implemented for the relevant multi-GeV, PC, and up- μ samples.
2150 The T2K CCQE model is more sophisticated so it has been implemented for
2151 all samples within this analysis, where separate low-energy and high-energy
2152 dials have been implemented. The low-energy dials are constrained by the near
2153 detector measurements and are uncorrelated to their high-energy counterparts.
2154 The author of this thesis was responsible for implementing and validating the
2155 combined cross-section model as documented in [185, 197].

2156 The high energy systematic model includes parameters developed from
2157 comparisons of Nieves and Rein-Seghal models which affect resonant pion
2158 producing interactions, comparisons of the GRV98 and CKMT models which
2159 control DIS interactions, and hadron multiplicity measurements which modulate

the normalisation of multi-pion producing events. The uncertainty on the ν_τ cross-section is particularly large and is controlled by a 25% normalisation uncertainty. These uncertainties are applied via normalisation or shape parameters. The former linearly scales the weight of all affected Monte-Carlo events, whereas the latter can increase or decrease a particular event's weight depending on its neutrino energy and mode of interaction. The response of the shape parameters is defined by third-order polynomial splines which return a weight for a particular neutrino energy. To reduce computational resources for the far detector fit, the response is binned by neutrino energy and sample binning: lepton momentum and cosine zenith binning for atmospheric splined responses and reconstructed neutrino energy and direction binning for beam samples. In total, 17 normalisation and 15 shape parameters are included in the high-energy model within this analysis.

Figure 6.9 indicates the predicted neutrino energy distribution for both beam and subGeV atmospheric samples. There is clearly significant overlap in neutrino energy between the subGeV atmospheric and beam samples, allowing similar kinematics in the final state particles. Figure 6.10 illustrates the fractional contribution of the different interaction modes per sample.

Comparing beam and atmospheric samples which target CCQE interactions (S.G. e-like 0de, S.G. μ -like [0,1]de, [FHC,RHC] 1R μ -like and [FHC,RHC] 1R e-like samples), there is a very similar contribution of CCQE, CC 2p2h, and CC1 π^\pm interactions. The samples which target CC1 π^\pm interactions, (S.G. e-like 0de, S.G. μ -like 2de and FHC 1R+1d.e e-like) also consist of very similar mode interactions.

As a consequence of the similarity in energy and mode contributions, correlating the systematic model between the beam and subGeV atmospheric samples ensures that this analysis attains the largest sensitivity to oscillation parameters while still ensuring neutrino interaction systematics are correctly accounted for. Due to its more sophisticated CCQE and 2p2h model, the T2K systematic model was chosen as the basis of the correlated model.

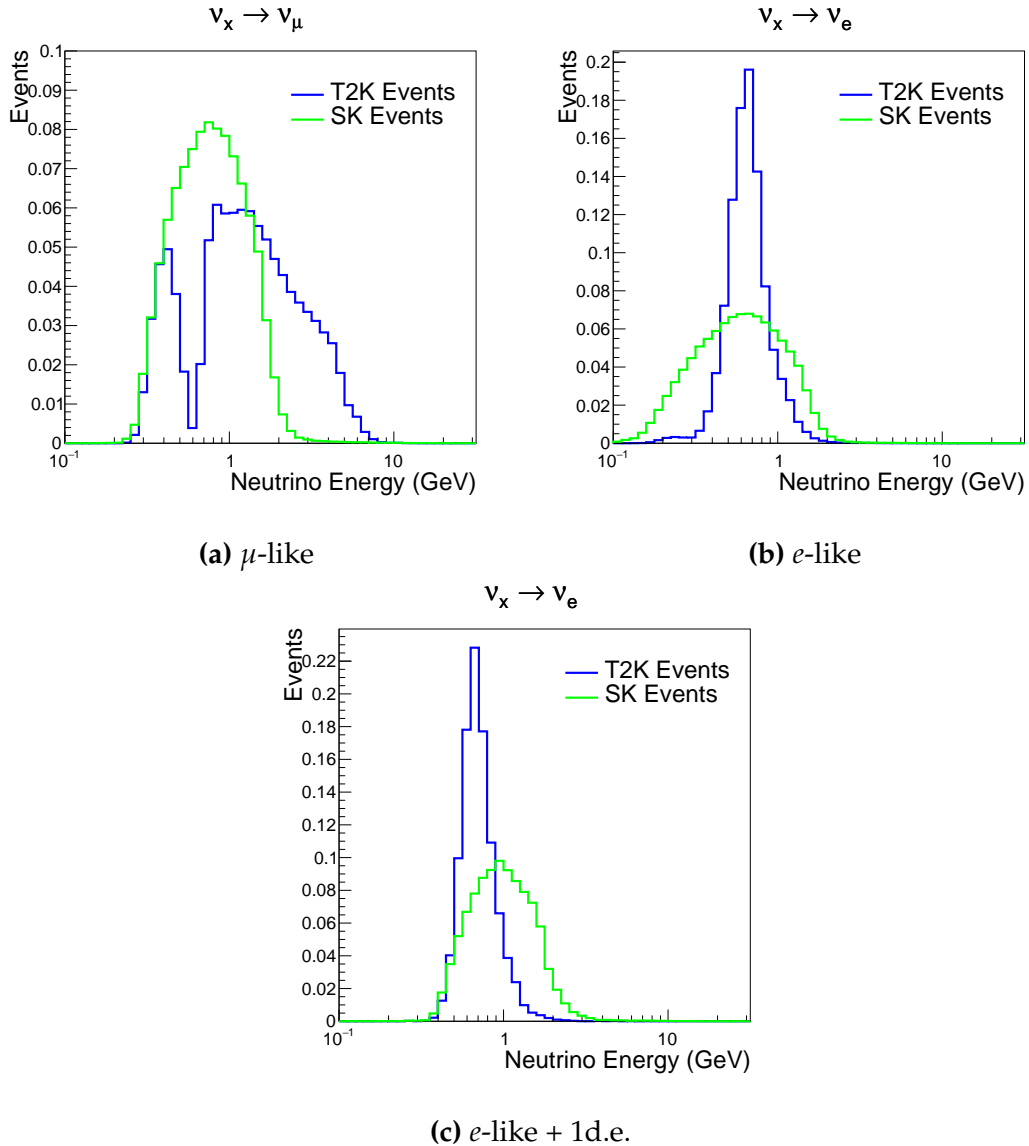


Figure 6.9: The predicted neutrino energy distribution for subGeV atmospheric and beam samples. FHC and RHC beam samples are summed together Asimov A oscillation parameters are assumed (given in Table 2.2). Beam and atmospheric samples with similar cuts are compared against one another.

2190 The T2K systematic model [196] is applied in a similar methodology to the
 2191 SK model parameters. It consists of 19 shape parameters and 24 normalisation
 2192 parameters. Four additional parameters, which model the uncertainty in the
 2193 binding energy, are applied in a way to shift the momentum of the lepton emitted
 2194 from a nucleus. This controls the uncertainty specified on the 27MeV binding
 2195 energy assumed within Equation 6.2. The majority of these parameters are

	CC QE	CC 2p2h	CC $1\pi^\pm$	CC $M\pi$	CC Other	NC $1\pi^0$	NC $1\pi^\pm$	NC $M\pi$	NC Coh.	NC Other
FHC 1R+1d.e. e-like	0.04	0.02	0.83	0.03	0.04	0.01	0.01	0.01	0.00	0.01
RHC 1R e-like	0.62	0.12	0.11	0.01	0.02	0.06	0.01	0.01	0.01	0.04
FHC 1R e-like	0.68	0.12	0.10	0.00	0.02	0.04	0.01	0.00	0.00	0.02
RHC 1R μ -like	0.62	0.13	0.17	0.02	0.03	0.00	0.02	0.00	0.00	0.00
FHC 1R μ -like	0.62	0.12	0.16	0.02	0.03	0.00	0.03	0.00	0.00	0.00
S.G. π^0 -like	0.05	0.01	0.02	0.00	0.01	0.68	0.06	0.07	0.06	0.04
S.G. μ -like 2de	0.04	0.01	0.80	0.10	0.04	0.00	0.00	0.00	0.00	0.00
S.G. μ -like 1de	0.72	0.11	0.12	0.01	0.02	0.00	0.01	0.00	0.00	0.00
S.G. μ -like 0de	0.68	0.11	0.10	0.01	0.02	0.01	0.05	0.01	0.00	0.02
S.G. e-like 1de	0.05	0.01	0.75	0.10	0.05	0.00	0.01	0.02	0.00	0.01
S.G. e-like 0de	0.73	0.11	0.10	0.01	0.02	0.02	0.00	0.00	0.00	0.00

Figure 6.10: The interaction mode contribution of each sample given as a fraction of the total event rate in that sample. Asimov A oscillation parameters are assumed (given in Table 2.2). The Charged Current (CC) modes are broken into quasi-elastic (QE), 2p2h, resonant charged pion production ($1\pi^\pm$), multi-pion production ($M\pi$), and other interaction categories. Neutral Current (NC) interaction modes are given in interaction mode categories: π^0 production, resonant charged pion production, multi-pion production, and others.

2196 assigned a Gaussian prior uncertainty. Those that have no reasonably motivated
 2197 uncertainty, or those which have not been fit to external data, are assigned a
 2198 flat prior which does not affect the penalty term.

2199 On top of the combination of the SK and T2K interaction models, several
 2200 other parameters have been specifically developed for the joint oscillation anal-
 2201 ysis. The majority of the atmospheric samples' δ_{CP} sensitivity comes from the
 2202 normalisation of subGeV electron-like events. These are modeled using a spectral
 2203 function to approximate the nuclear ground state. However, the near detector is
 2204 not able to constrain the model so an additional systematic is introduced which
 2205 models an alternative Continous Random Phase Approximation (CRPA) nuclear
 2206 ground state. This dial approximates the event weights if a CRPA model had

been assumed rather than a spectral function. This dial only applies to ν_e and $\bar{\nu}_e$ as the near detector does not constraint ν_e cross-section measurements. It is applied as a shape parameter.

Further additions to the model have been introduced due to the inclusion of the subGeV π^0 atmospheric sample. This particularly targets charged current and neutral current π^0 producing interactions to help constrain the systematic uncertainties. Therefore, an uncertainty that affects neutral current resonant π^0 production is incorporated into this analysis. Comparisons of NEUT's NC resonant pion production predictions have been made to MiniBooNE [198] data and a consistent 16% to 21% underprediction is observed [185]. Consequently, a conservative 30% normalisation parameter is invoked.

Down-going events are mostly insensitive to oscillation parameters and can act similar to the near detector within an accelerator experiment (Details will be discussed in chapter 7). This region of phase space can act as a sideband and allows the cross-section model and near detector constraint to be studied. The distribution of events in this region is calculated using the technique outlined in subsection 4.3.4. The results are illustrated in Figure 6.11. For CCQE-targeting samples, the application of the near detector constraint is well within the statistical fluctuation of the down-going data. This means there is no significant tension is observed between the data and the Monte Carlo prediction after the near detector constraint is applied. This is not the case for samples with target CCRES interactions. The electron-like data is consistent with the constrained prediction at high reconstructed momenta but diverges at lower momentum, whereas the muon-like sample is under-predicted throughout the range of momenta. To combat this disagreement, an additional cross-section systematic dial, specifically designed to inflate the low pion momentum systematics was developed in [185]. This is a shape parameter implemented through a splined response.

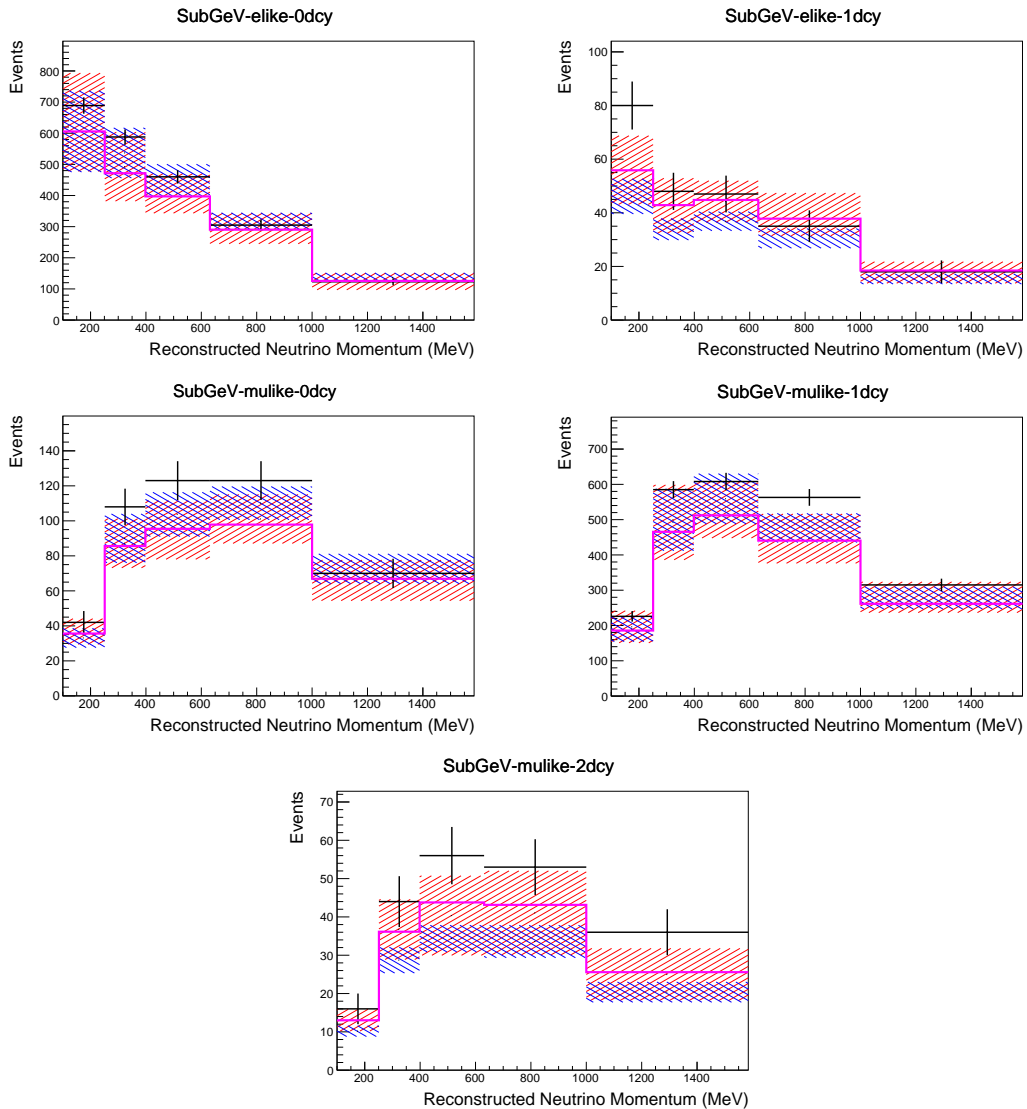


Figure 6.11: Down-going atmospheric subGeV single-ring samples comparing the mean and error of the pre-fit and post-fit Monte Carlo predictions in red and blue, respectively. The magenta histogram illustrates the Monte Carlo prediction using the generated dial values. The black points illustrate the down-going data with statistical errors given. The mean and errors of the Monte Carlo predictions are calculated by the techniques documented in subsection 4.3.4. The pre-fit spectrum is calculated by throwing the cross-section and atmospheric flux dial values from the pre-fit covariance matrix. The post-fit spectrum is calculated by sampling the cross-section dial values from an ND fit MCMC chain, whilst still throwing the atmospheric flux dials from the pre-fit covariance.

2234 6.4.4 Near Detector

2235 The systematics applied due to uncertainties arising from the response of the near
 2236 detector is documented in [125]. The response is described by 574 normalisation
 2237 parameters binned in the selected sample as well as momentum and angle,

2238 P_μ and $\cos(\theta_\mu)$, of the final-state muon. These are applied via a covariance
2239 matrix with each parameter being assigned a Gaussian prior from that covariance
2240 matrix. These normalisation parameters are built from underlying systematics,
2241 e.g. pion secondary interaction systematics, which are randomly thrown and
2242 the variation in each $P_\mu \times \cos(\theta_\mu)$ bin is determined. Two thousand throws are
2243 evaluated and a covariance matrix response is created. This allows significant
2244 correlations between FGD1 and FGD2 samples, as well as adjacent $P_\mu \times \cos(\theta_\mu)$
2245 bins. Statistical uncertainties are accounted for by including fluctuations of each
2246 event's weight from a Poisson distribution.

2247 Similar to the cross-section systematics, MaCh3 and BANFF are used to
2248 constrain the uncertainty of these systematics through independent validations.
2249 Each fitter generates a post-fit covariance matrix which is compared and passed
2250 to the far-detector oscillation analysis working group. As the analysis presented
2251 within this thesis uses the MaCh3 framework, a joint oscillation analysis fit of all
2252 three sets of samples and their respective systematics is performed.

2253 6.4.5 Far Detector

2254 Two configurations of the far detector systematic model implementation have
2255 been considered. Firstly, the far detector systematic uncertainties for beam and
2256 atmospheric samples are taken from their respective analysis inputs, denoted
2257 “official inputs” analysis, with no correlations assumed between the beam and at-
2258 mospheric samples. The beam- and atmospheric-specific inputs are documented
2259 in subsubsection 6.4.5.1 and subsubsection 6.4.5.2. Secondly, an alternative
2260 detector model has been developed which correlates the response of the SK
2261 detector systematics between the beam and atmospheric samples. Here, the
2262 distribution of parameters used for applying event cuts (e.g. electron-muon
2263 PID separation) is modified within the fit. It follows a similar methodology to
2264 the beam far detector systematics implementation but performs a joint fit of
2265 the beam and atmospheric data. This alternative implementation is detailed
2266 in subsubsection 6.4.5.3.

2267 **6.4.5.1 Beam Samples**

2268 There are 45 systematics which describe the response of the far detector to
2269 beam events [178], split into 44 normalisation parameters and one energy scale
2270 systematic. The energy scale systematic is applied as a multiplicative scaling
2271 of the reconstructed neutrino energy. It is estimated from data-to-Monte Carlo
2272 differences in the stopping muon sample in [58] and found to be 2.1%. The
2273 normalisation parameters are assigned a Gaussian error centered at one with
2274 width taken from a covariance matrix. A detailed breakdown of the generation
2275 of the covariance matrix is found in [191]. To build the covariance matrix, a fit
2276 is performed on atmospheric data which has been selected using beam sample
2277 selection cuts. These cuts use the variables, L^i , where the index i is detailed in
2278 Table 6.7. Each L^i is a smear, α , and shift, β parameter such that,

$$L_j^i \rightarrow \bar{L}_j^i = \alpha_j^i L + \beta_j^i. \quad (6.4)$$

2279 Where L_j^i (\bar{L}_j^i) correspond to nominal(varied) PID cut parameters given in
2280 Table 6.7. The shift and smear parameters are nuisance parameters with no prior
2281 constraints. They are binned by final-state topology, j , where the binning is given
2282 in Table 6.8. The final-state topology binning is because the detector will respond
2283 differently to events that have one or multiple rings. For example, the detector
2284 will be able to distinguish single-ring events better than two overlapping ring
2285 events, resulting in different systematic uncertainty for one-ring events compared
2286 to two-ring events. This approach is used to allow the cut parameter distributions
2287 to be modified within the fit, allowing for better data to Monte Carlo agreement.

Cut Variable	Parameter Name
0	<code>fitQun e/mu PID</code>
1	<code>fitQun e/pi0 PID</code>
2	<code>fitQun mu/pi PID</code>
3	<code>fitQun Ring-Counting Parameter</code>

Table 6.7: List of cut variables that are included within the shift/smear fit documented in [191].

Category	Description
1e	Only one electron above Cherenkov threshold in the final state
1 μ	Only one muon above Cherenkov threshold in the final state
1e+other	One electron and one or more other charged particles above Cherenkov threshold in the final state
1 μ +other	One muon and one or more other charged particles above Cherenkov threshold in the final state
1 π^0	Only one π^0 in the final state
1 π^\pm or 1p	Only one hadron (typically charged pion or proton) in the final state
Other	Any other final state

Table 6.8: Reconstructed event topology categories on which the SK detector systematics [191] are based.

2288 The mis-modeling of π^0 events is also considered. If one of the two rings
 2289 from a π^0 event is missed, this will be reconstructed as a CC ν_e -like event. This
 2290 is one of the largest systematics hindering the electron neutrino appearance
 2291 analyses. Consequently, additional systematics have been introduced to con-
 2292 strain the mis-modeling of π^0 events in SK, binned by reconstructed neutrino
 2293 energy. To evaluate this systematic uncertainty, a set of “hybrid- π^0 ” samples is
 2294 constructed. These events are built by overlaying one electron-like ring from
 2295 the SK atmospheric neutrino samples or decay electron ring from a stopping
 2296 cosmic ray muon with one simulated photon ring. Both rings are chosen so
 2297 that momenta and opening angle follow the decay kinematics of NC π^0 events
 2298 from the T2K-MC. Hybrid- π^0 Monte Carlo samples with both rings from the
 2299 SK Monte Carlo are produced to compare with the hybrid- π^0 data samples and
 2300 the difference in the fraction of events that pass the ν_e selection criteria is used
 2301 to assign the systematic errors. In order to investigate any data to Monte Carlo
 2302 differences that may originate from either the higher energy ring or lower energy
 2303 ring, two samples are built; a sample in which the electron constitutes the higher
 2304 energy ring from the π^0 decay (called the primary sample) and another one in
 2305 which it constitutes the lower energy ring (called the secondary sample). The
 2306 standard T2K ν_e fitQun event selection criteria are used to select events.

2307 Final contributions to the covariance matrix are determined by supplemen-
 2308 tary uncertainties obtained by comparing stopping muon data to Monte Carlo

prediction, as first introduced in section 5.2. The efficiency of tagging decay electrons is estimated by the stopping muon data to Monte Carlo differences by comparing the number of one decay electron events to the number of events with one or fewer decay electrons. Similarly, the rate at which fake decay electrons are reconstructed by `fiTQun` is estimated by comparing the number of two decay electron events to the number of events with one or two reconstructed decay electrons. The two sources of systematics are added in quadrature weighted by the number of events with one true decay electron yielding a 0.2% systematic uncertainty. A fiducial volume systematic of $\pm 2.5\text{cm}$ which corresponds to a 0.5% shift in the normalisation of events is also applied. Additional normalisation uncertainties based on neutrino flavour and interaction mode are also defined in [178, 199, 200].

Two additional sources of uncertainty are included: secondary and photoneuclear interactions. These are estimated by varying the underlying parameters are building a distribution of sample event rates. These contributions are then added in quadrature to the above covariance matrix. The final uncertainty on the SK detector systematics are provided in Figure 6.12.

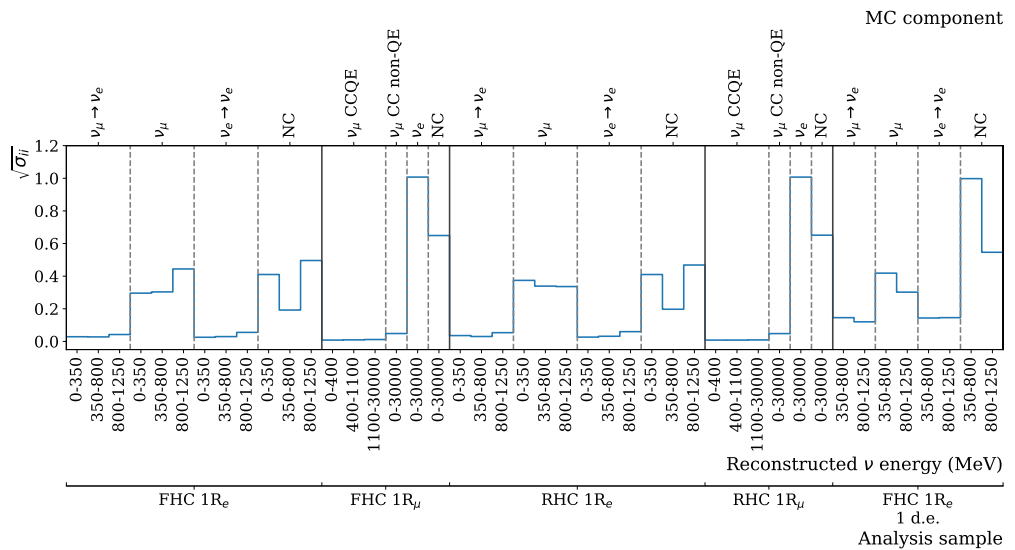


Figure 6.12: The fractional uncertainty on each of the 44 parameters describing the SK detector systematics (The energy scale systematic is neglected). The parameters are split by sample, oscillation channel, interaction mode and reconstructed neutrino energy.

2326 6.4.5.2 Atmospheric Samples

2327 The detector systematics for atmospheric samples, documented in [84], are split
2328 into two sub-groups: those which are related to particle identification and ring
2329 counting systematics, and those which are related to calibration, separation,
2330 and reduction uncertainties.

2331 The particle identification systematics consist of five parameters. The ring sep-
2332 aration systematic enforces an anti-correlated response between the single-ring
2333 and multi-ring samples. This is implemented as a fractional increase/decrease
2334 in the overall normalisation of each sample, depending on the distance to the
2335 nearest wall from an event's vertex. The coefficients of the normalisation are
2336 estimated prior to the fit and depend on the particular atmospheric sample. Two
2337 electron-muon separation systematics are included within this model which
2338 anti-correlates the response of the electron-like and muon-like samples: one for
2339 single-ring events and another for multi-ring events.

2340 The multi-ring electron-like separation likelihood, discussed in section 6.1,
2341 encodes the ability of the detector to separate neutrino from anti-neutrino events.
2342 Two normalisation parameters vary the relative normalisation of multi-ring ν_e
2343 and $\bar{\nu}_e$ samples whilst keeping a consistent overall event rate.

2344 There are 22 systematics related to calibration measurements, including effects
2345 from backgrounds, reduction, and showering effects. They are documented in
2346 [84] and are briefly summarised in Table 6.9. They are applied via normalisation
2347 parameters, with the separation systematics requiring the conservation of event
2348 rate across all samples.

2349 6.4.5.3 Correlated Detector Model

2350 A complete uncertainty model of the SK detector would be able to determine
2351 the systematic shift on the sample spectra for a variation of the underlying
2352 parameters, e.g. PMT angular acceptance. However, this is computationally
2353 intensive, requiring Monte Carlo predictions to be made for each plausible
2354 variation. Consequently, an effective parameter model has been utilised for

Index	Description
0	Partially contained reduction
1	Fully contained reduction
2	Separation of fully contained and partially contained events
3	Separation of stopping and through-going partially contained events in top of detector
4	Separation of stopping and through-going partially contained events in barrel of detector
5	Separation of stopping and through-going partially contained events in bottom of detector
6	Background due to cosmic rays
7	Background due to flasher events
8	Vertex systematic moving events into and out of fiducial volume
9	Upward going muon event reduction
10	Separation of stopping and through-going in upward going muon events
11	Energy systematic in upward going muon events
12	Reconstruction of the path length of upward going muon events
13	Separation of showering and non-showering upward going muon events
14	Background of stopping upward going muon events
15	Background of non-showering through-going upward going muon events
16	Background of showering through-going upward going muon events
17	Efficiency of tagging two rings from π^0 decay
18	Efficiency of decay electron tagging
19	Background from downgoing cosmic muons
20	Asymmetry of energy deposition in tank
21	Energy scale deposition

Table 6.9: Sources of systematic errors specified within the grouped into the “calibration” systematics model.

2355 a correlated detector model following from the T2K-only model implementation
 2356 documented in subsubsection 6.4.5.1. It correlates the detector systematics
 2357 between the far-detector beam and subGeV atmospheric samples due to their
 2358 similar energies and interaction types. As there are no equivalent beam samples,
 2359 the multi-GeV, multiring, PC, and Up- μ samples will be subject to the particle
 2360 identification systematics implementation as described in subsubsection 6.4.5.2
 2361 rather than using this correlated detector model. The calibration systematics also
 2362 described in the aforementioned chapter still apply to all atmospheric samples.
 2363 The correlated detector model utilises the same smear and shift parameters
 2364 documented in subsubsection 6.4.5.1, split by final state topology. Beyond this,

the shift and smear parameters are split by visible energy deposited within the detector, with binning specified in Table 6.10. This is because atmospheric events are categorised by subGeV and multi-GeV events based on visible energy, so this splitting is required when correlating the systematic model for beam and atmospheric events. Alongside the technical requirement, higher energy events will be better reconstructed due to fractionally less noise within the detector. As a result of the inclusion of visible energy binning, Equation 6.4 becomes

$$L_{jk}^i \rightarrow \bar{L}_{jk}^i = \alpha_{jk}^i L + \beta_{jk}^i, \quad (6.5)$$

where k is the visible energy bin.

Index	Range (MeV)
0	$30 \geq E_{vis} > 300$
1	$300 \geq E_{vis} > 700$
2	$700 \geq E_{vis} > 1330$
3	$E_{vis} \geq 1330$

Table 6.10: Visible energy binning for which the correlated SK detector systematics are based

The implementation of this systematic model takes the events reconstructed values of the cut parameters, modifies them by the particular shift and smear parameter for that event, and then re-applies event selection. This causes event migration, which is a new feature incorporated into the MaCh3 framework which is only achievable due to the event-by-event reweighting scheme.

Particular care has to be taken when varying the ring counting parameter. This is because the number of rings is a finite value (one-ring, two-ring, etc.) which can not be continuously varied through this shift and smear technique. Consequently a continuous ring counting parameter, RC_i , is calculated for the i^{th} event, following the definition in [177]: the preferred likelihoods from all considered one-ring (L_{1R}) and two-ring (L_{2R}) fits are determined. The difference

2384 is computed as $\Delta_{LLH} = \log(L_{1R}) - \log(L_{2R})$. The ring counting parameter is
 2385 then defined as

$$RC_i = \text{sgn}(\Delta_{LLH}) \times \sqrt{|\Delta_{LLH}|}, \quad (6.6)$$

2386 where $\text{sgn}(x) = x/|x|$. This ring counting parameter corresponds to an
 2387 intermediate likelihood value used within the `fitQun` algorithm to decide the
 2388 number of rings associated with a particular event. However, fake-ring merging
 2389 algorithms are applied after this likelihood value is used. Consequently, this
 2390 ring counting parameter does not always exactly correspond to the number of
 2391 reconstructed rings. This can be seen in Figure 6.13.

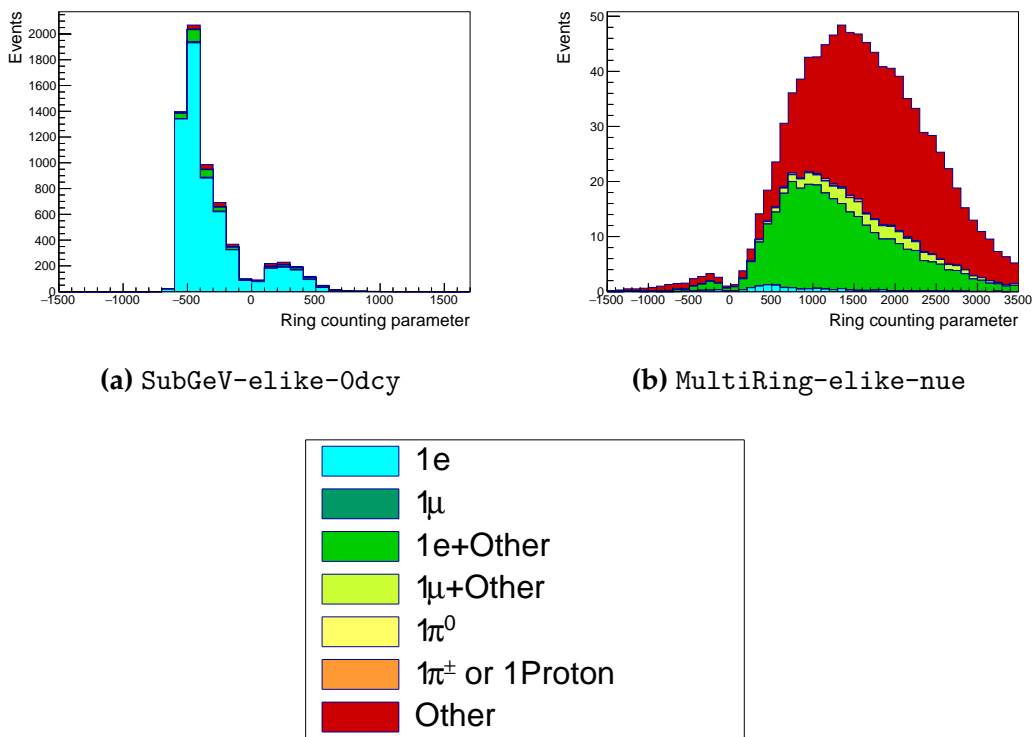


Figure 6.13: The ring counting parameter as defined in Equation 6.6 for the SubGeV-elike-0dcy and MultiRing-elike-nue samples.

2392 As the `fitQun` algorithm does not provide a likelihood value after the fake-
 2393 ring algorithms have been applied, the ring counting parameter distribution is
 2394 correlated to the final number of reconstructed rings through “maps”. These

2395 are two-dimensional distributions of the ring counting parameter and the final
 2396 number of reconstructed rings. An example is illustrated in Figure 6.14. In
 2397 principle, the `fitQun` reconstruction algorithm should be re-run after the variation
 2398 in the ring counting parameter. However, this is not computationally viable.
 2399 Therefore the “maps” are used as a reweighting template.

2400 The maps are split by final state topology and true neutrino flavour and
 2401 all `fitQun`-reconstructed Monte Carlo events are used to fill them. The maps
 2402 are row-normalised to represent the probability of X rings for a given RC_i
 2403 value. Prior to the oscillation fit, an event’s nominal weight is calculated as
 2404 $W^i(N_{Rings}^i, L_{jk}^i)$, where N_{Rings}^i is the reconstructed number of rings for the i^{th}
 2405 event and $W^i(x, y)$ is the bin content in map associated with the i^{th} event, where
 2406 x number of rings and y is ring counting parameter. Then during the fit, the
 2407 value of $R = W^i(N_{Rings}^i, \bar{L}_{jk}^i) / W^i(N_{Rings}^i, L_{jk}^i)$ is calculated as the event weight
 2408 for the i^{th} event. This is the only cut variable that uses a reweighting technique
 2409 rather than event migration.

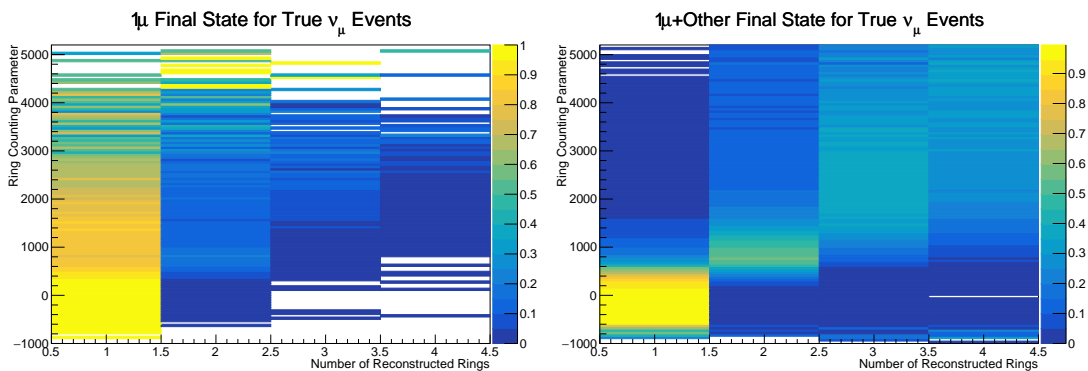


Figure 6.14: The ring counting parameter, defined in Equation 6.6, as a function of the number of reconstructed rings as found by the `fitQun` reconstruction algorithm. Left: true ν_μ events with only one muon above the Cherenkov threshold in the final state. Right: true ν_μ events with one muon and at least one other charged particle above the Cherenkov threshold in the final state.

2410 The π^0 systematics introduced in subsection 6.4.4 are applied via a covariance
 2411 matrix. This is not possible in the alternative model as no covariance matrix
 2412 is used. Thus, the implementation of the π^0 systematics has been modified.
 2413 The inputs from the hybrid π^0 sample are included via the use of “ χ^2 maps”,

which are two-dimensional histograms in α_{jk}^i and β_{jk}^i parameters over some range. Illustrative examples of the χ^2 maps are given in Figure 6.15. Due to their nature, the shift and smear parameters are typically very correlated. A map is produced for each cut parameter given in Table 6.7 and for each visible energy bin given in Table 6.10.

The maps are filled through the χ^2 comparison of the hybrid π^0 Monte Carlo and data in the particle identification parameters documented in Table 6.7. The Monte Carlo distribution is modified by the α_{jk}^i and β_{jk}^i scaling, whilst cross-section and flux nuisance parameters are thrown from their prior uncertainties. The χ^2 between the scaled Monte Carlo and data is calculated and the relevant point in the χ^2 map is filled.

The implementation within this alternative detector model is to add the bin contents of the maps, for the relevant values of the α_{jk}^i and β_{jk}^i parameters, to the likelihood penalty. Only $1\pi^0$ final state topology shift and smear parameters use this prior uncertainty.

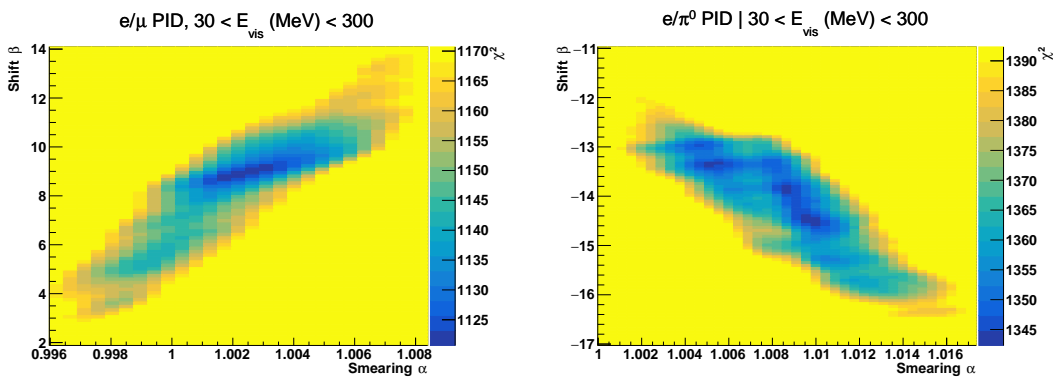


Figure 6.15: The χ^2 between the hybrid- π^0 Monte Carlo and data samples, as a function of smear (α) and shift (β) parameters, for events which have $1\pi^0$ final state topology. Left: Electron-muon separation PID parameter for events with $30 \leq E_{\text{vis}}(\text{MeV}) < 300$. Right: Electron- π^0 separation PID parameter for events with $30 \leq E_{\text{vis}}(\text{MeV}) < 300$.

Similarly, the implementation of the supplementary systematics documented in subsubsection 6.4.5.1 needs to be modified. A new framework [201] was built in tandem between the author of this thesis and the T2K-SK working group [178] so the additional parameters can be incorporated into the MaCh3 framework. These are applied as normalisation parameters, depending on the particular

2434 interaction mode, number of tagged decay electrons, and whether the primary
2435 particle generated Cherenkov light. They are assigned Gaussian uncertainties
2436 with widths described by a covariance matrix. Furthermore, the secondary
2437 interaction and photo-nuclear effects need to be accounted for in this detector
2438 model using a different implementation than that in subsubsection 6.4.5.1. This
2439 was done by including a shape parameter for each of the secondary interactions
2440 and the photo-nuclear systematic parameters.

2441 There are a total of 224 α_{jk}^i and β_{jk}^i parameters, of which 32 have prior
2442 constraints from the hybrid π^0 samples.

2443 One final complexity of this correlated detector model is that the two sets
2444 of samples, beam and subGeV atmospheric, use slightly different parameters
2445 to distinguish electron and muon-like events. The T2K samples use the value
2446 of $\log(L_e/L_\mu)$ whereas the atmospheric samples use the value of $\log(L_e/L_\pi)$,
2447 where L_X is the likelihood for hypothesis X. This is because the T2K fits use
2448 single-ring f iTQun fitting techniques, whereas multi-ring fits are applied to the
2449 atmospheric samples where only the electron and pion hypothesis are considered.
2450 The correlation between the two likelihood ratios is illustrated in Figure 6.16. As
2451 discussed in section 5.2, the pion hypothesis is a very good approximation of the
2452 muon hypothesis due to their similar mass. Consequently, using the same shift
2453 and smear parameters correlated between the beam and subGeV atmospheric
2454 samples is deemed a good approximation.

2455 6.5 Likelihood Calculation

2456 This analysis performs a joint oscillation parameter fit of the ND280 beam
2457 samples, the T2K far detector beam samples, and the SK atmospheric samples
2458 introduced in this chapter.

2459 Once the Monte Carlo predictions of each beam and atmospheric sample
2460 have been built, a likelihood needs to be constructed. This is done by comparing
2461 the binned Monte Carlo prediction to binned data. The Monte Carlo prediction
2462 is calculated at a particular point, $\vec{\theta}$, in the model parameter space such that

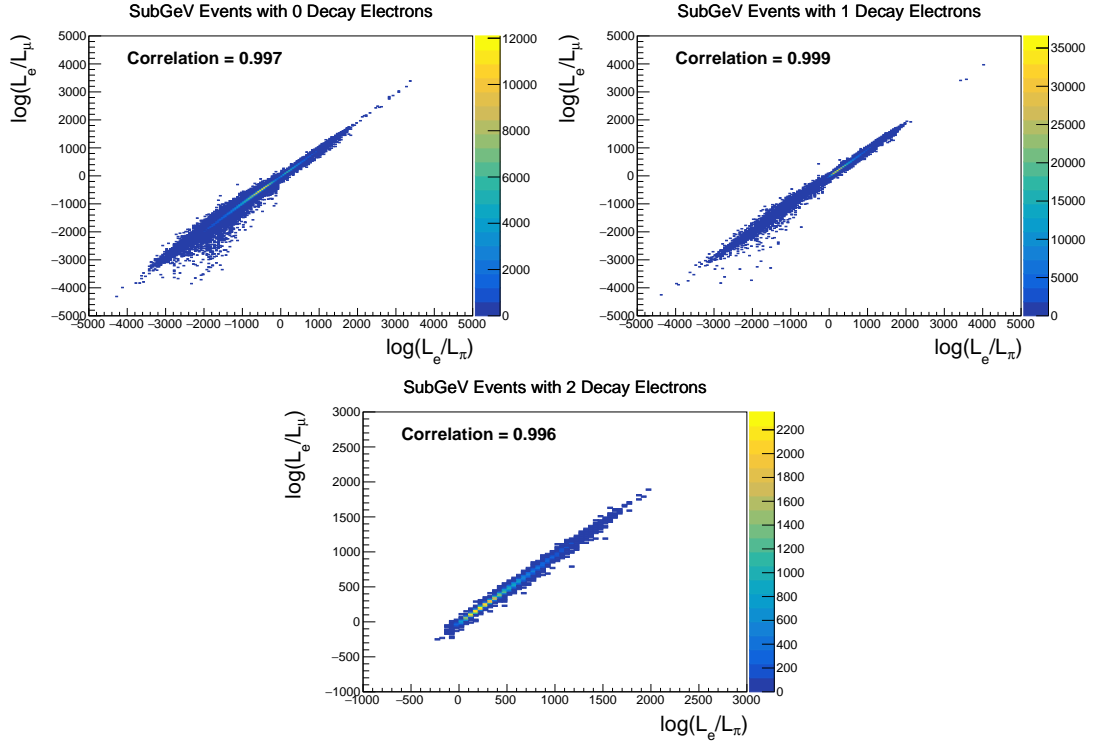


Figure 6.16: The distribution of $\log(L_e/L_\mu)$ compared to $\log(L_e/L_\pi)$ for subGeV events with zero (top left), one (top right) or two (bottom) decay electrons. The correlation in the distribution is calculated as 0.997, 0.999 and 0.996, respectively.

2463 $N_i^{MC} = N_i^{MC}(\vec{\theta})$, where N_i represents the bin content of the i^{th} bin. The data
 2464 and Monte Carlo spectra are represented by N_i^D and N_i^{MC} , respectively. The bin
 2465 contents for the beam near detector, beam far detector and atmospheric samples
 2466 are denoted with ND , FD , and Atm , respectively. The binning index, i , runs
 2467 over all the bins within a sample. Taking the FHC1Rmu far detector sample as
 2468 an example, the binning index runs over all the reconstructed neutrino energy
 2469 bins. The likelihood calculation between the data and the Monte Carlo prediction
 2470 for a particular bin follows a Poisson distribution, where the data is treated as
 2471 a fluctuation of the simulation.

2472 The data can consist of either real data or an ‘Asimov’ Monte Carlo prediction,
 2473 which is typically used for sensitivity studies and denoted ‘Asimov data’. The
 2474 process for building Asimov data is as follows. The Monte Carlo prediction is
 2475 reweighted using a particular set of oscillation parameters (potentially those
 2476 listed in Table 2.2) and systematic parameter tune. The resulting spectra for each

sample is then defined to be the Asimov data for that sample. Whilst this results in unphysical non-integer data predictions, it eliminates statistical fluctuations from the data. Therefore, the results of a fit to Asimov data should not include any biases from statistical fluctuations. Furthermore, these results should produce posterior probability distributions consistent with the parameters which were used to make the data prediction. That is to say, the fit results should return the known parameters. Any biases seen would be attributed to correlations between each oscillation parameter and correlations between oscillation and systematic parameters. Consequently, Asimov fit results present the maximum precision at which the oscillation parameters could be measured to.

Following the T2K analysis presented in [72], the likelihood contribution for the near detector samples also includes a Monte Carlo statistical uncertainty term, derived from the Barlow and Beeston statistical treatment [202, 203]. It includes a contribution to the likelihood that which treats the generated Monte Carlo prediction as a statistical fluctuation of the actual true simulation assuming an infinite amount of statistics had been created. The technical implementation of this additional likelihood term is documented in [186] and briefly summarised as follows. The term is defined as,

$$\frac{(\beta_i - 1)^2}{2\sigma_{\beta_i}^2}, \quad (6.7)$$

where β_i represents a scaling parameter for the i^{th} bin that relates the bin content for the amount of Monte Carlo actually generated N_i^{MC} to the bin content if an infinite amount of Monte Carlo statistics had been generated $N_{i,true}^{MC}$, such that $N_{i,true}^{MC} = \beta_i \times N_i^{MC}$. In the case where a sufficient amount of Monte Carlo statistics had been generated, $\beta_i = 1$. An analytical solution for β_i is given in [186]. Additionally, $\sigma_{\beta_i} = \sqrt{\sum_i w_i^2 / N_i^{MC}}$ where $\sqrt{\sum_i w_i^2}$ represents the sum of the square of the weights of the Monte Carlo events which fall into bin i .

An additional contribution to the likelihood comes from the variation of the systematic model parameters. For those parameters with well-motivated uncertainty estimates, a covariance matrix, V , describes the prior knowledge of

each parameter as well as any correlations between the parameters. Due to a technical implementation, a single covariance matrix describes each “block” of model parameters, e.g. beam flux systematics. The covariance matrix associated with the k^{th} block is denoted V^k . This substitution results in $\vec{\theta} = \sum_k^{N_b} \vec{\theta}^k$ and $V = \sum_k^{N_b} V^k$ where N_b denotes the number of blocks. A single covariance matrix is provided for: the oscillation parameters, the beam flux parameters, the atmospheric flux parameters, the neutrino interaction systematics, the near detector parameters, the beam far detector systematics, and the atmospheric far detector systematics. The number of parameters in the k^{th} block is defined as $n(k)$.

The equation for the likelihood \mathcal{L} includes all the terms discussed above. It is defined as,

$$\begin{aligned}
-\ln(\mathcal{L}) = & \\
& \sum_i^{\text{NDbins}} N_i^{\text{ND},\text{MC}}(\vec{\theta}) - N_i^{\text{ND},D} + N_i^{\text{ND},D} \times \ln \left[N_i^{\text{ND},D} / N_i^{\text{ND},\text{MC}}(\vec{\theta}) \right] + \frac{(\beta_i - 1)^2}{2\sigma_{\beta_i}^2} \\
& + \sum_i^{\text{FDbins}} N_i^{\text{FD},\text{MC}}(\vec{\theta}) - N_i^{\text{FD},D} + N_i^{\text{FD},D} \times \ln \left[N_i^{\text{FD},D} / N_i^{\text{FD},\text{MC}}(\vec{\theta}) \right] \\
& + \sum_i^{\text{Atmbins}} N_i^{\text{Atm},\text{MC}}(\vec{\theta}) - N_i^{\text{Atm},D} + N_i^{\text{Atm},D} \times \ln \left[N_i^{\text{Atm},D} / N_i^{\text{Atm},\text{MC}}(\vec{\theta}) \right] \\
& + \frac{1}{2} \sum_k^{N_b} \sum_i^{n(k)} \sum_j^{n(k)} (\vec{\theta}^k)_i (V^k)_{ij}^{-1} (\vec{\theta}^k)_j.
\end{aligned} \tag{6.8}$$

The negative log-likelihood value is determined at each step of the MCMC to build the posterior distribution defined in chapter 4. This value is minimised when the Monte Carlo prediction tends towards the data spectrum.

7

2519

2520

Oscillation Probability Calculation

2521 It is important to understand how and where the sensitivity to the oscillation parameters comes from for both atmospheric and beam samples. An
2522 overview of how these samples respond to changes in δ_{CP} , Δm_{32}^2 , and $\sin^2(\theta_{23})$
2523 is given in section 2.5. This section also explains the additional complexities
2524 involved when performing an atmospheric neutrino analysis as compared to
2525 a beam-only analysis.

2526 Without additional techniques, atmospheric sub-GeV upward-going neutrinos ($E_\nu < 1.33\text{GeV}, \cos(\theta_Z) < 0.$) can artificially inflate the sensitivity to $\delta_{CP,zaza}$
2527 due to the quickly varying oscillation probability in this region. Therefore, a
2528 “sub-sampling” approach has been developed to reduce these biases ensuring
2529 accurate and reliable sensitivity measurements. This technique ensures that small-
2530 scale unresolvable features of the oscillation probability have been averaged over
2531 whilst the large-scale features in the oscillation probability are unaffected. The
2532 documentation and validation of this technique are found in section 7.1. The
2533 oscillation probability calculation is computationally intensive due to the large
2534 number of matrix multiplications needed. Consequently, the CUDAProb3 imple-
2535 mentation choice made within the fitting framework, as detailed in section 7.2,
2536 ensures that the analysis can be done in a timely manner.

Whilst the beam neutrinos are assumed to propagate through a constant density slab of material, the density variations through the Earth result in more complex oscillation patterns for atmospheric neutrinos. Furthermore, the uncertainty in the electron density can modify the oscillation probability for the denser core layers of the Earth. The model of the Earth used within this analysis is detailed in section 7.3. This includes information about the official SK-only methodology as well as improvements that have been made to remove some of the approximations used in that analysis. Another complexity of atmospheric neutrino oscillation studies is that the height of production in the atmosphere is not known on an event-by-event basis. An analytical averaging technique that approximates the uncertainty of the oscillation probability has been followed, with the author of this thesis being responsible for the implementation and validation. This implementation of an external technique is described in section 7.4.

7.1 Treatment of Fast Oscillations

As shown in Figure 7.1, atmospheric neutrino oscillations have a significantly more complex structure for upgoing neutrinos with energy below 1GeV. This is because the L/E dependence of the oscillation probability in this region induces rapid variations for small changes in L or E . As discussed in section 2.5, this is also the region in which atmospheric neutrinos have sensitivity to δ_{CP} . In practice, the direction of the neutrino is inferred from the direction of the final state particles traveling in the detector. The correlation between these two directions can be particularly weak for low-energy neutrino interactions. This creates a distinct difference from the beam neutrinos where the position of the source is very precisely known.

As a consequence of the unresolvable structure, an event rate consistent with the averaged oscillation probability is observed in the subGeV upgoing region. This creates a computational problem: A significantly large amount of Monte Carlo statistics would be required to accurately predict the number of events if Monte Carlo averaging was the only technique used. This section describes

2568 the ‘sub-sampling’ approach developed for this analysis and compares it to the
2569 methodology used within the SK-only analysis.

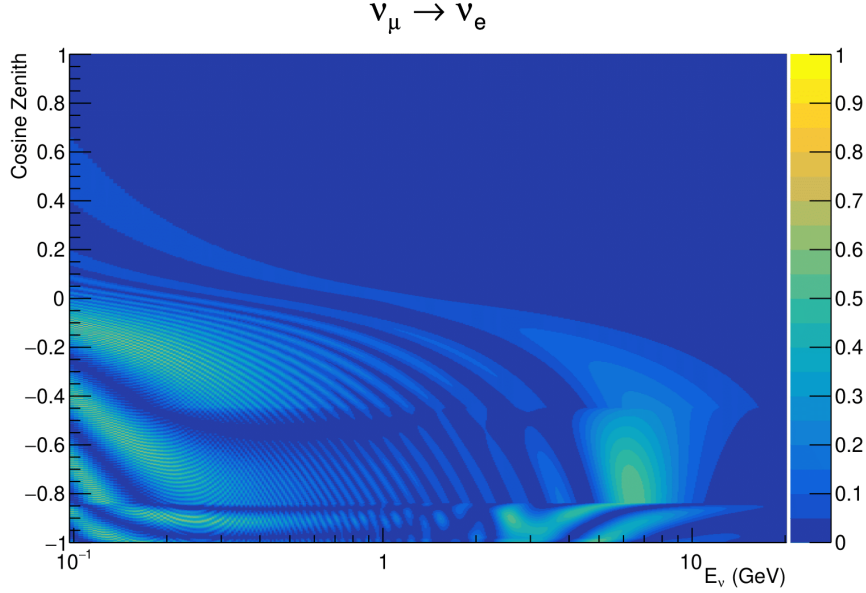


Figure 7.1: The oscillation probability $P(\nu_\mu \rightarrow \nu_e)$, given as a function of neutrino energy and zenith angle, which highlights an example of the “fast” oscillations in the sub-GeV upgoing region.

2570 The official SK-only analysis uses the osc3++ oscillation parameter fitter
2571 [76]. To perform the fast oscillation averaging, it uses a ‘nearest-neighbour’
2572 technique. For a given Monte Carlo neutrino event, the nearest twenty Monte
2573 Carlo neighbours in reconstructed lepton momentum and zenith angle are
2574 found and a distribution of their neutrino energies is built. The RMS, σ , of
2575 this distribution is then used to compute an average oscillation probability for
2576 the given neutrino Monte Carlo event.

2577 For the i^{th} event, the oscillation weight is calculated as

$$W_i = \frac{1}{5}P(E_i, \bar{L}_i) + \frac{1}{5}\sum_{\beta=-1, -0.5, 0.5, 1} P(E_i + \beta\sigma_i, L_\beta), \quad (7.1)$$

2578 where $P(E, L)$ is the oscillation probability calculation for neutrino energy E
2579 and path length L and the two path lengths, \bar{L}_i and L_β are described below. All
2580 of the oscillation probability calculations are performed with a fixed zenith angle
2581 such that the same density profile is used. The uncertainty in the production

height is controlled by using an “average” production height, \bar{L}_i , which represents the average path length computed using twenty production heights taken from the Honda flux model’s prediction [51]. These inputs are provided in 5% intervals of the cumulative distribution function. The value of \bar{L}_i is calculated as:

$$\bar{L}_i = \frac{1}{20} \sum_{j=1}^{20} \sqrt{(R_E + h_j)^2 - R_E^2 (1 - \cos^2 \theta_i)} - R_E \cos \theta_i. \quad (7.2)$$

Where R_E is the Earth’s radius and θ_i is the zenith angle of the i^{th} event. The production heights h_j represent the $(j \times 5)^{th}$ percentile of the cumulative distribution function. L_β values (where the values of β are given in Equation 7.1) are similarly calculated but instead use different combinations of four production heights,

$$\begin{aligned} L_{-1.0} &= \frac{1}{4} L(45, 50, 55, 60), \\ L_{-0.5} &= \frac{1}{4} L(35, 40, 65, 70), \\ L_{+0.5} &= \frac{1}{4} L(25, 30, 75, 68), \\ L_{+1.0} &= \frac{1}{4} L(15, 20, 85, 89). \end{aligned} \quad (7.3)$$

Where $L(i, j, k, l)$ represents the sum of the path lengths with fixed zenith angle and production heights corresponding to the i^{th} , j^{th} , k^{th} and l^{th} percentile of the cumulative distribution function. The values that are taken as β (and values for L_β) are chosen to smooth the oscillation contours in Δm_{32}^2 without incurring loss of sensitivity [204].

This averaging technique works because of the inference between the zenith angle and the reconstructed direction of final state particles in the detector. For low-energy neutrinos, where the resolution of the true neutrino direction is poor, σ_i will be large, resulting in significant averaging effects. Contrary to this, the inferred direction of high-energy neutrinos will be much closer to the true value, meaning that σ_i will be smaller, culminating in small averaging effects.

In practice, these calculations are performed prior to the fit as only oscillation parameters at fixed points are considered. The MCMC technique used in this thesis requires oscillation probabilities to be evaluated at arbitrary parameter values, not known *a priori*. Calculating the five oscillation probabilities per event required by the SK technique is computationally infeasible, so a different averaging technique is used. However, the concept of the averaging technique can be taken from it.

To perform a similar averaging as the SK analysis, a sub-sampling approach using binned oscillograms has been devised. A coarsely binned oscillogram is defined in $\cos(\theta_Z)$ and E_ν . For a given set of oscillation parameters, a single oscillation probability will be assigned to each coarse bin. This value will then apply to all Monte Carlo events which fall into that bin. To assign these oscillation probabilities, the probability is calculated at $N \times N$ points on a grid within a particular bin. This ensemble of oscillation probabilities is averaged to define the coarse bin's oscillation probability, assuming a flat prior in E_ν and $\cos(\theta_Z)$ within the bin. Figure 7.2 illustrates the $N = 2$ example where the assigned value to a coarse bin is the average of the four fine bins which fall in that coarse bin. Whilst the coarse bin edges do not have to be linear on either axis, the sub-division of the fine bins is linear within the range of a coarse bin.

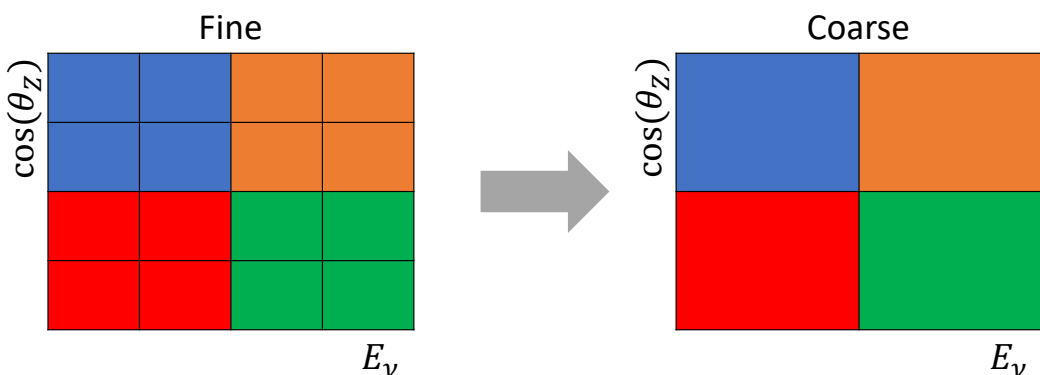


Figure 7.2: Illustration of the averaging procedure for $N = 2$. The oscillation probabilities calculated on the finer left binning are averaged to obtain the oscillation probabilities in the coarser right binning. These averaged oscillation probabilities with the coarser binning are then applied to each event during the fit.

2621 The coarse binning is defined with 67×52 bins in true neutrino energy \times
 2622 cosine zenith. It is picked to be identical to that provided in [204]. In general, the
 2623 binning is logarithmically spaced in neutrino energy but has some hand-picked
 2624 bin edges around the matter resonance to smoothly increased the bin density.
 2625 This is to avoid smearing this region which can be well sampled by the Monte
 2626 Carlo. The cosine zenith binning is approximately linearly spaced across the
 2627 allowable range but the values of layer transitions are hit precisely: -0.8376 (core-
 2628 mantle) and -0.4464 (mantle/transition zone). Bins are spread further apart for
 2629 downgoing events as this is a region unaffected by the fast oscillation wavelengths
 2630 and reduces the total number of calculations required to perform the calculation.

2631 The choice of N is justified based on two studies. Firstly, the variation of event
 2632 rates of each sample is studied as a function of N . For a given set of oscillation
 2633 parameters thrown from the PDG prior constraints (detailed in Table 2.1), the
 2634 oscillation probabilities are calculated using a given value of N . Each sample
 2635 is re-weighted and the event rate is stored. The value of N is scanned from
 2636 1, which corresponds to no averaging, to 19, which corresponds to the largest
 2637 computationally viable subdivision binning. The event rate of each sample at
 2638 large N is expected to converge to a stationary value due to the fine binning fully
 2639 sampling the small-scale structure. Figure 7.3 illustrates this behaviour for the
 2640 SubGeV_elike_0dcy sample for 9 different throws of the oscillation parameters.

2641 Denoting the event rate for one sample for a given throw t at each N by λ_t^N ,
 2642 the average over all considered N values ($\bar{\lambda}_t = \frac{1}{24} \sum_{N=1}^{24} \lambda_t^N$) is computed. The
 2643 variance in the event rate at each N is then calculated as

$$\text{Var}[\lambda^N] = \frac{1}{N_{\text{throws}}} \sum_{t=1}^{N_{\text{throws}}} (\lambda_t^N - \bar{\lambda}_t)^2 - \left[\frac{1}{N_{\text{throws}}} \sum_{t=1}^{N_{\text{throws}}} (\lambda_t^N - \bar{\lambda}_t) \right]^2. \quad (7.4)$$

2644 In practice, the following procedure is undertaken. For a particular throw,
 2645 the difference between the event rate at a particular choice of N and the mean
 2646 of the distribution is calculated. This is illustrated in Figure 7.4. This value
 2647 is then calculated for all the 2000 throws, generating a distribution of $\lambda_t^N - \bar{\lambda}_t$.

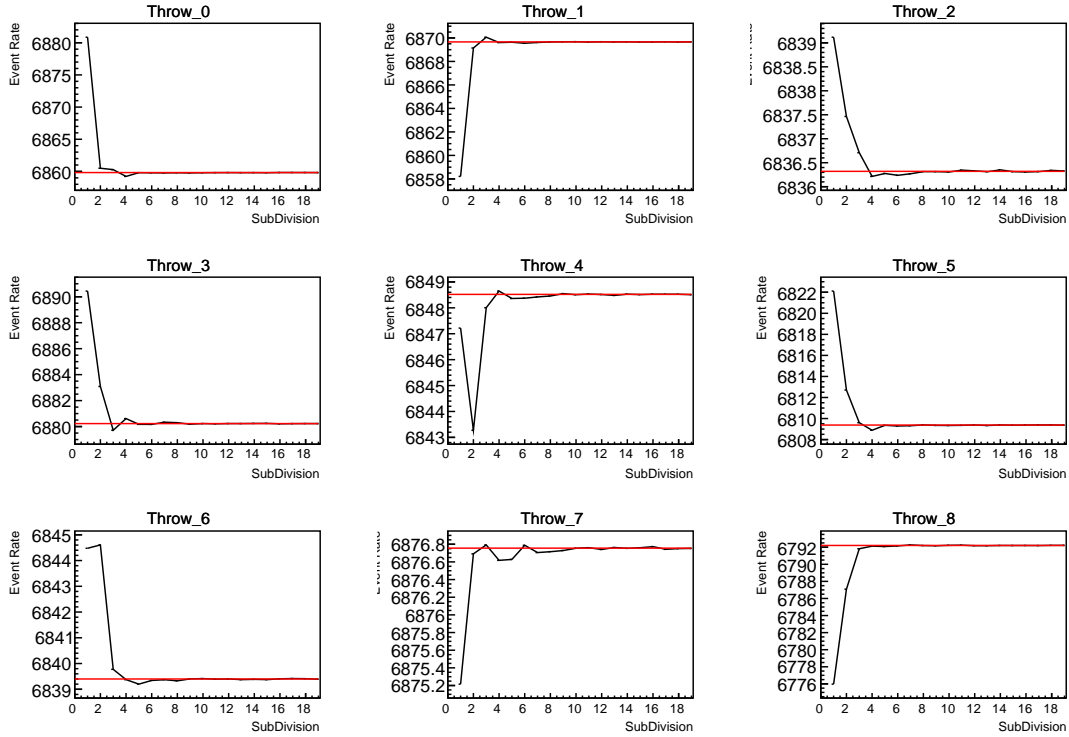


Figure 7.3: Event rate of the SubGeV_elike_0dcy sample as a function of the number of sub-divisions per coarse bin. Each subplot represents the event rate of the sample at a different oscillation parameter set thrown from the PDG priors detailed in Table 2.1. The red line in each subplot represents the mean of the event rate over the different values of sub-divisions for that particular oscillation parameter throw.

2648 This is repeated for each of the values of N considered within this study. The
 2649 distributions of this value, for $N = \{1, 5\}$, are given in Figure 7.5. As expected,
 2650 the distribution gets narrower and tends towards zero for the higher values of N .

2651 The aim of the study is to find the lowest value of N such that this variance
 2652 is below 0.001. This utilises the width of the distributions given in Figure 7.5.
 2653 This is the typical threshold used by T2K fitters to validate systematic imple-
 2654 mentation so has been set as the same criteria. The results of this study for
 2655 each atmospheric sample used within this thesis are illustrated in Figure 7.6 for
 2656 2000 throws of the oscillation parameters. As can be seen, the variance is below
 2657 the threshold at $N = 10$, and is driven primarily by the SubGeV_mulike_1dcy
 2658 and SubGeV_elike_0dcy samples.

2659 The second study to determine the value of N is as follows. The likelihood
 2660 for each sample is computed against an Asimov data set created with Asimov A

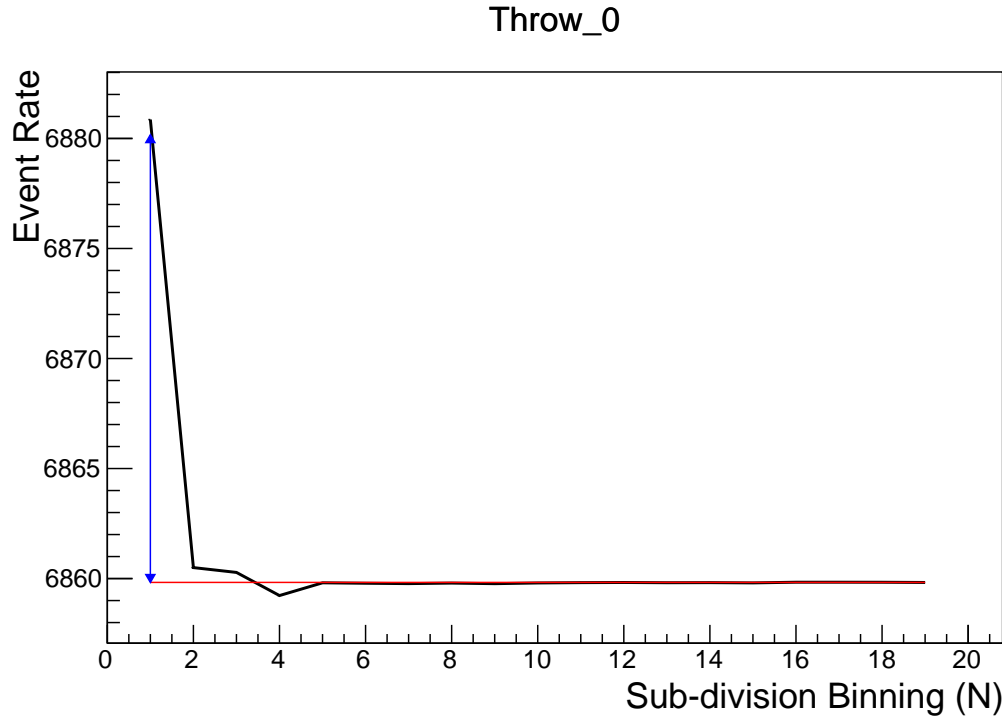


Figure 7.4: Event rate of the SubGeV_elike_0dcy sample, for a particular oscillation parameter throw, as a function of the number of sub-divisions, N , per coarse bin. The difference between the mean event rate (red), $\bar{\lambda}$, and the event rate at $N = 1$, $\lambda^{N=1}$ is defined as $\lambda^N - \bar{\lambda}$ and illustrated by the blue arrow.

oscillation parameters (Table 2.2). Following Equation 7.4, the variance of the log-likelihood over all considered N is computed. The results are shown in Figure 7.7.

A choice of $N = 10$ sub-divisions per coarse bin has a variance in both event rate and log-likelihood residuals less than the required threshold of 0.001. The largest value of the likelihood variance is of order 10^{-7} , corresponding to an error on the log-likelihood of about 3×10^{-4} which is small enough to be negligible for the oscillation analysis.

Figure 7.8 illustrates the effect of the smearing using $N = 10$. The fast oscillations in the sub-GeV upgoing region have been replaced with a normalisation effect whilst the large matter resonance structure remains.

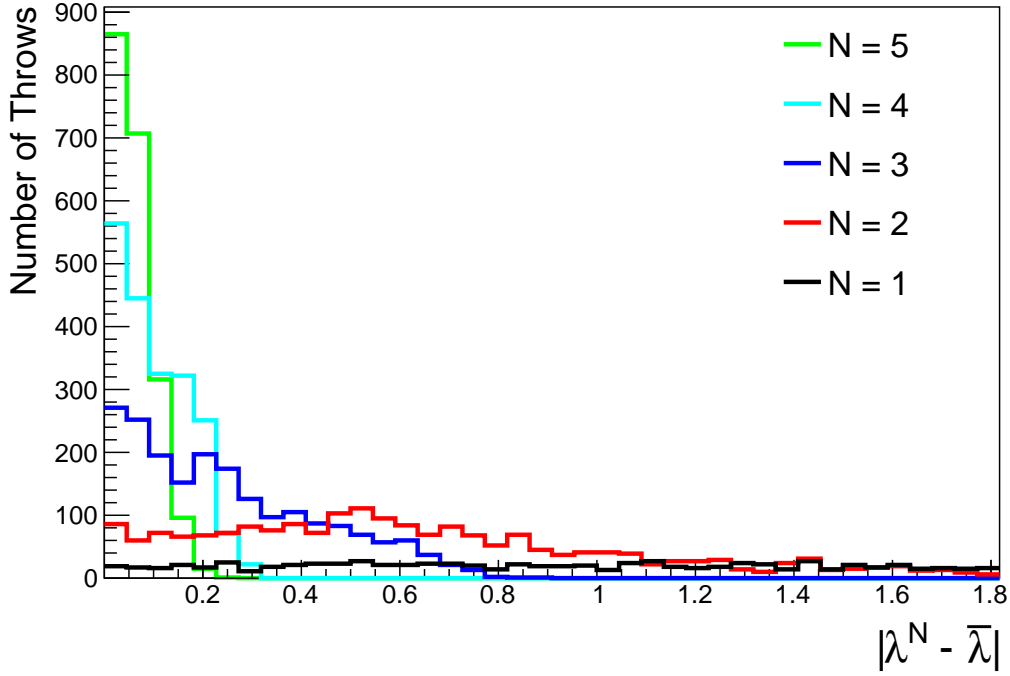


Figure 7.5: The distribution of $\lambda^N - \bar{\lambda}$ for various values of N . As expected, the distribution gets narrower for larger values of N .

2671 7.2 Calculation Engine

2672 As previously discussed in section 7.1, the calculation of oscillation probabilities
 2673 is performed at run-time. Consequently, the time per calculation is crucial for fit
 2674 performance. The initial fitting framework used for this analysis was developed
 2675 with ProbGPU [205]. This is a GPU-only implementation of the prob3 engine
 2676 [206]. It is primarily designed for neutrino propagation in a beam experiment
 2677 (single layer of constant density) with the atmospheric propagation code not
 2678 being used prior to the analysis in this thesis.

2679 Another engine, CUDAProb3 [207], has been interfaced with the fitting frame-
 2680 work used in this analysis. This interfacing was done by the author of this
 2681 thesis. It has been specifically optimised for atmospheric neutrino oscillation
 2682 calculation so does not contain the code to replace the beam oscillation calculation.
 2683 The engine utilises object-orientated techniques as compared to the functional
 2684 implementation of ProbGPU. This allows the energy and cosine zenith arrays to

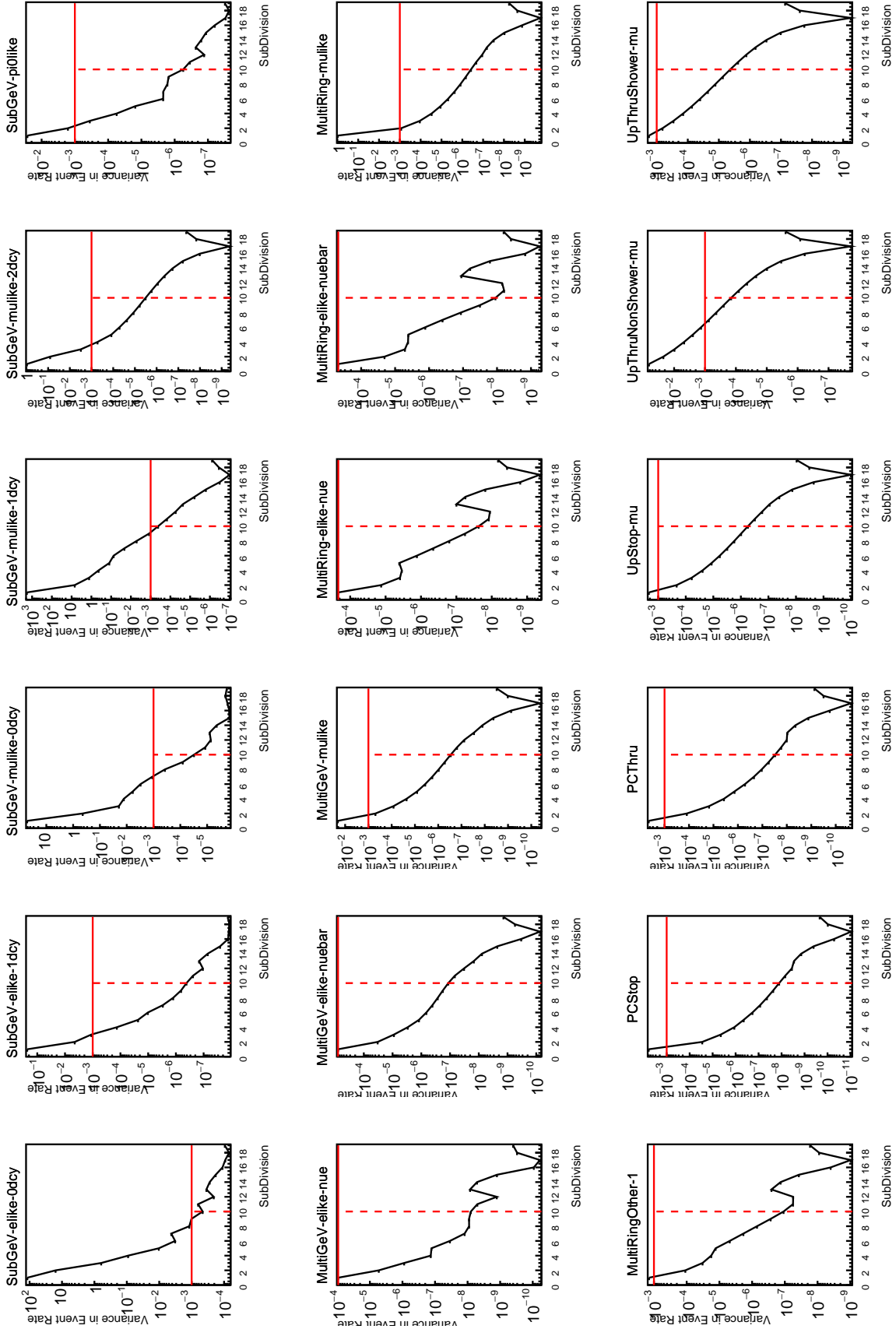


Figure 7.6: Variance of event rate for each atmospheric sample as a function of the number of sub-divisions per coarse bin. The solid red line indicates the 0.1% threshold and the dashed red line indicates the variance at a sub-division $N = 10$.

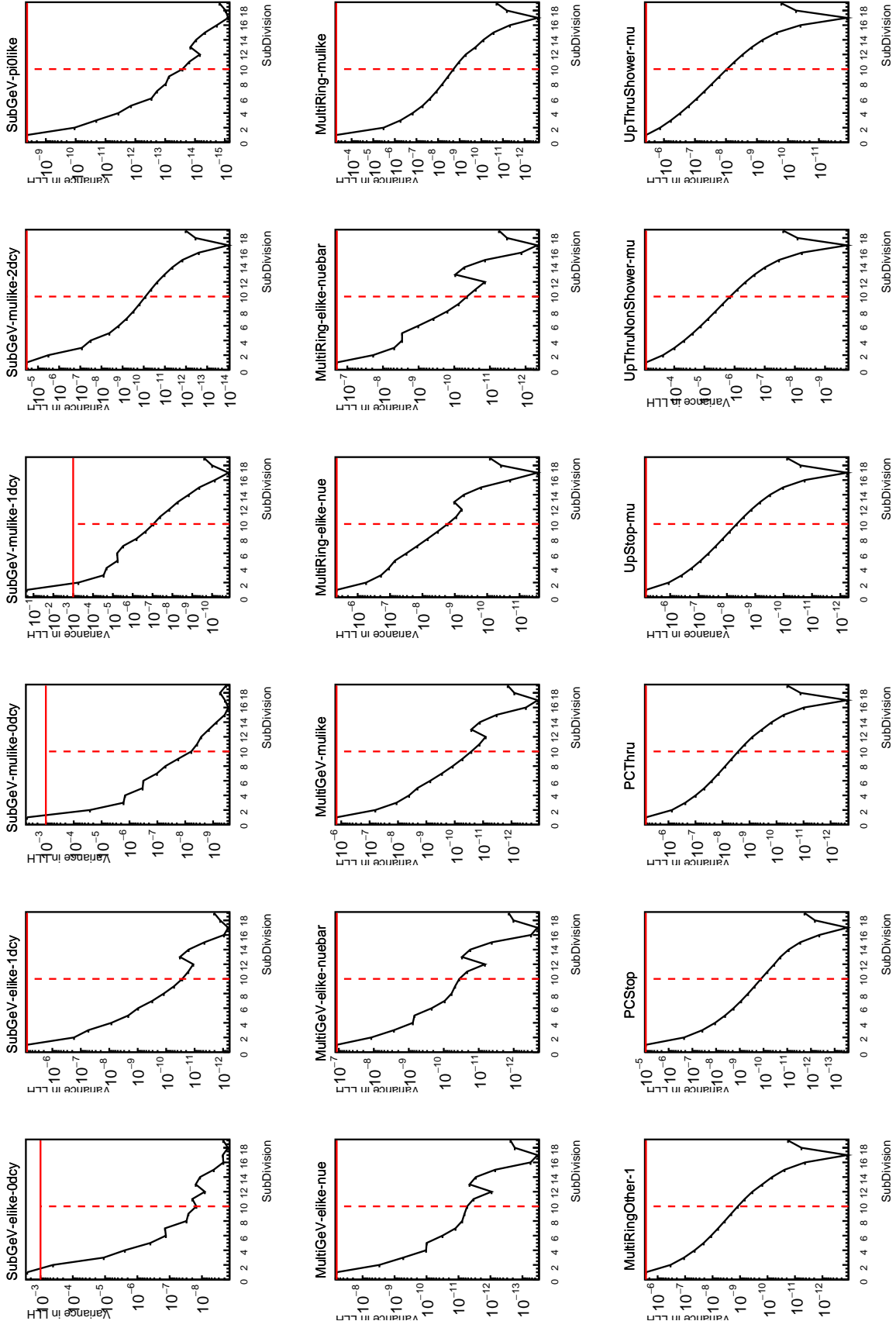


Figure 7.7: Variance of sample likelihood, when compared to 'Asimov data' set at Asimov A, for each atmospheric sample as a function of the number of sub-divisions per coarse bin. The solid red line indicates the 0.1% threshold and the dashed red line is a graphical indication of the variance at a sub-division $N = 10$.

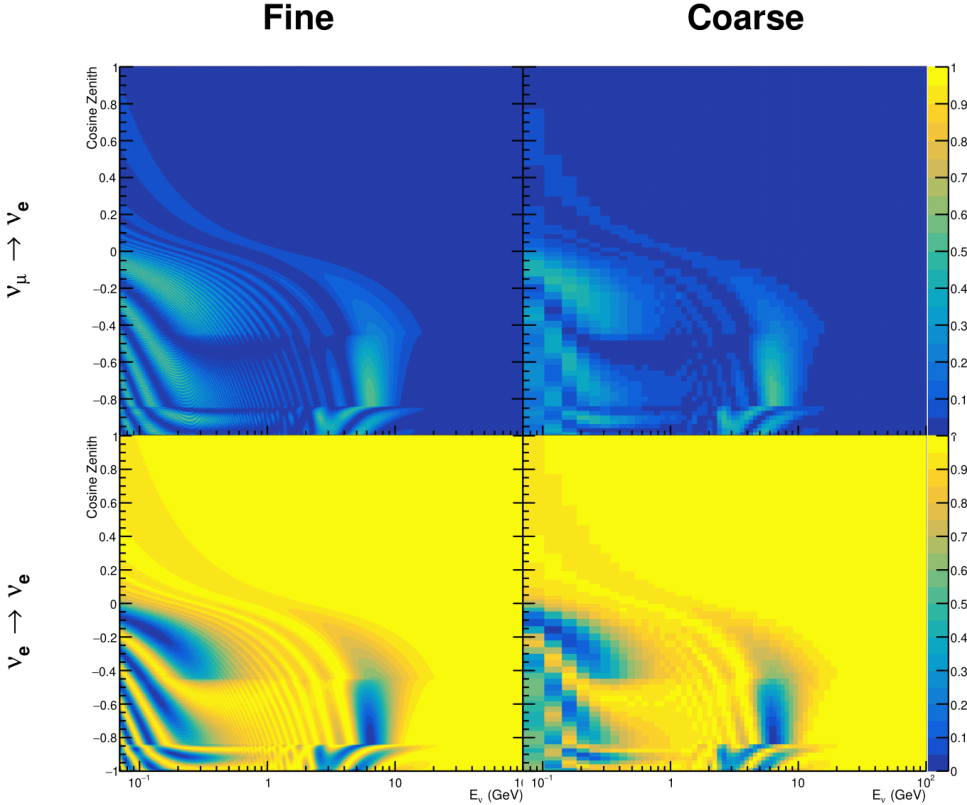


Figure 7.8: The oscillation probability, $P(\nu_\mu \rightarrow \nu_e)$ (top row) and $P(\nu_e \rightarrow \nu_e)$ (bottom row), given as a function of neutrino energy and zenith angle. The left column gives the “fine” binning used to calculate the oscillation probabilities and the right column illustrates the “coarse” binning used to reweight the Monte Carlo events. The fine binning choice is given with $N = 10$, which was determined to be below the threshold from Figure 7.6 and Figure 7.7.

be kept on GPU memory, rather than having to load these arrays onto GPU memory for each calculation. Reducing the memory transfer between CPU and GPU significantly reduces the time required for calculation. This can be seen in Figure 7.9, where the GPU implementation of CUDAProb3 is approximately three times faster than the ProbGPU engine.

Another significant advantage of CUDAProb3 is that it contains a CPU multi-threaded implementation which is not possible with the ProbGPU or prob3 engines. This eliminates the requirement for GPU resources when submitting jobs to batch systems. As illustrated in Figure 7.9, the calculation speed depends on the number

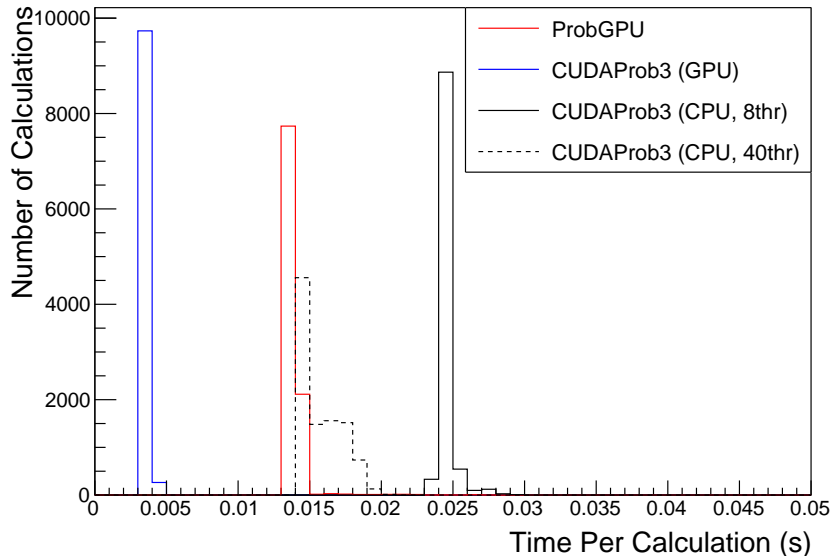


Figure 7.9: The calculation time taken to both calculate the oscillation probabilities and fill the “coarse” oscillograms, following the technique given in section 7.1, for the CUDAProb3 and ProbGPU (Red) calculation engines. CUDAProb3 has both a GPU (Blue) and CPU (Black) implementation, where the CPU implementation is multi-threaded. Therefore, 8-threads (solid) and 40-threads (dashed) configurations have been tested. Prob3, which is a CPU single-thread implementation has a mean step time of 1.142s.

of available threads. Using 8 threads (which is typical of the batch systems being used) is approximately twice as slow as the ProbGPU engine implementation, but would allow the fitting framework to be run on many more resources. This fact is utilised for any SK-only fits but GPU resources are required for any fits which include beam samples due to the ProbGPU requirement. Based on the benefits shown by the implementation in this section, efforts are being placed into including linear propagation for beam neutrino propagation into the engine [208].

7.3 Matter Density Profile

For an experiment observing neutrinos propagating through the Earth, a model of the Earth’s density profile is required. The model used within this analysis is based on the Preliminary Reference Earth Model (PREM) [77], as illustrated in Figure 2.8. Table 2.3 documents the density and radii of the layers used within the constant density approximation used by the SK-only analysis [76]. The

density measurements provided in the PREM model are provided in terms of mass density, whereas neutrino oscillations are sensitive to the electron number density. This value can be computed as the product of the chemical composition, or the Z/A value, and the mass density of each layer. Currently, the only way to measure the chemical composition value for layers close to the Earth's core is through neutrino oscillations. The chemical composition of the upper layers of the Earth's Mantle and the Transition zone is well known due to it being predominantly pyrolite which has a chemical composition value of 0.496 [209]. The chemical composition dial for the core layers is set to a value of 0.468, as calculated in [210]. As this value is less well known, it is assigned a Gaussian error with a standard deviation equivalent to the difference in chemical composition in core and mantle layers. Figure 7.10 illustrates the effect of moving from the $Z/A = 0.5$ method which is used in the official SK-only analysis to these more precise values.

The beam oscillation probability in this thesis uses a baseline of 295km, density 2.6g/cm^3 , and chemical composition 0.5 as is done by the official T2K-only analysis [211].

For a neutrino with given $E_\nu, \cos(\theta_Z)$, the oscillation probability calculation engine must be passed a list of the matter regions that the neutrino traversed, with the path length and fixed density in each region. However, a neutrino passing through the earth experiences a range of radii, and thus a range of densities, in each region. In the SK-only analysis, the earth density model used is piecewise-constant, thereby ignoring this effect. For this thesis, the density values for the calculation engine are found by averaging the earth density along the neutrino's path in each layer,

$$\langle \rho \rangle_i = \frac{1}{t_{i+1} - t_i} \int_{t_i}^{t_{i+1}} \rho(t) dt, \quad (7.5)$$

where t_i are the intersection points between each layer and t is the path length of the trajectory across the layer. This leads to an improved approximation. For this averaging, the simplification of the PREM model developed in [212] is

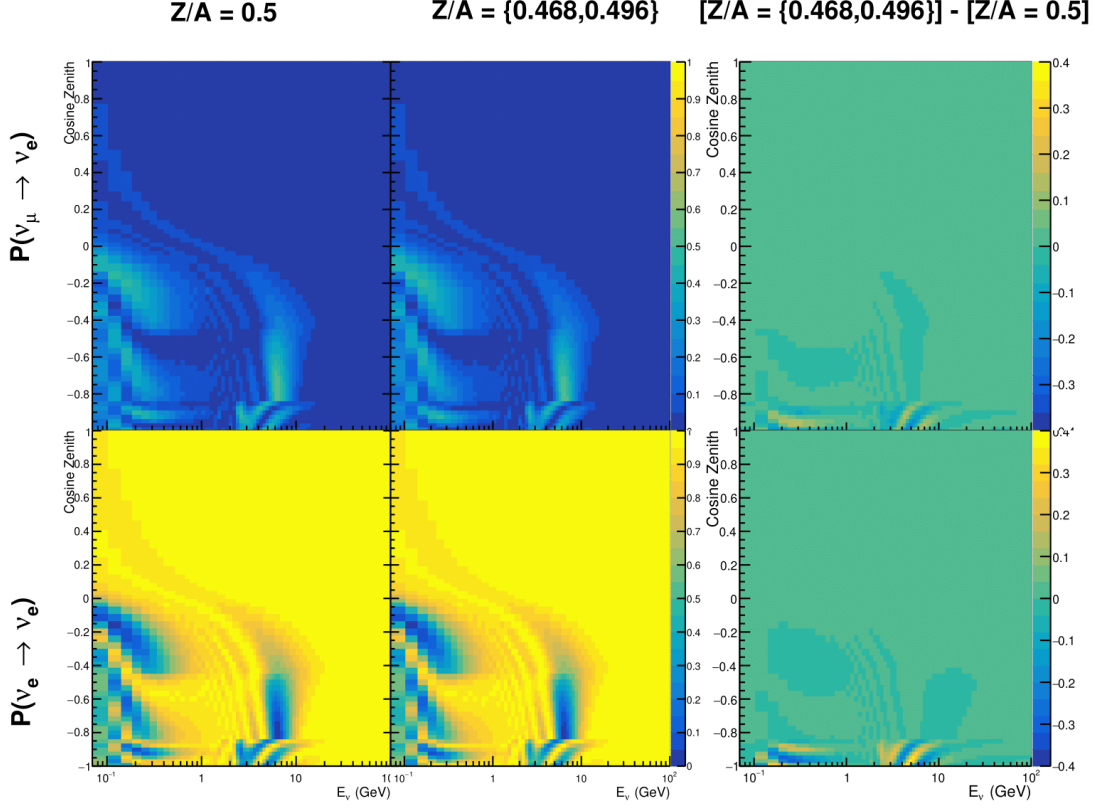


Figure 7.10: The oscillation probability, $P(\nu_\mu \rightarrow \nu_e)$ (top row) and $P(\nu_e \rightarrow \nu_e)$ (bottom row), given as a function of neutrino energy and zenith angle. The left column gives probabilities where the constant $Z/A = 0.5$ approximation which is used in the official SK-only analysis. The middle column gives the probabilities where $Z/A = [0.468, 0.498]$ values are used, as given in Table 2.3. The right column illustrates the difference in oscillation probability between the two different techniques.

used. The layers of the prem model are combined into four to reduce calculation time, with a quadratic fit to each section. This fit was not performed by the author of the thesis and is documented in [204]. The coefficients of the quadratic fit to each layer are given in Table 7.1 with the final distribution illustrated in Figure 7.11. The quadratic approximation is clearly much closer to the PREM model as compared to the constant density approximation.

The effect of using the quadratic density per $\cos(\theta_Z)$ model is highlighted in Figure 7.12. The slight discontinuity in the oscillation probability around $\cos(\theta_Z) \sim -0.45$ in the fixed density model, which is due to the transition to

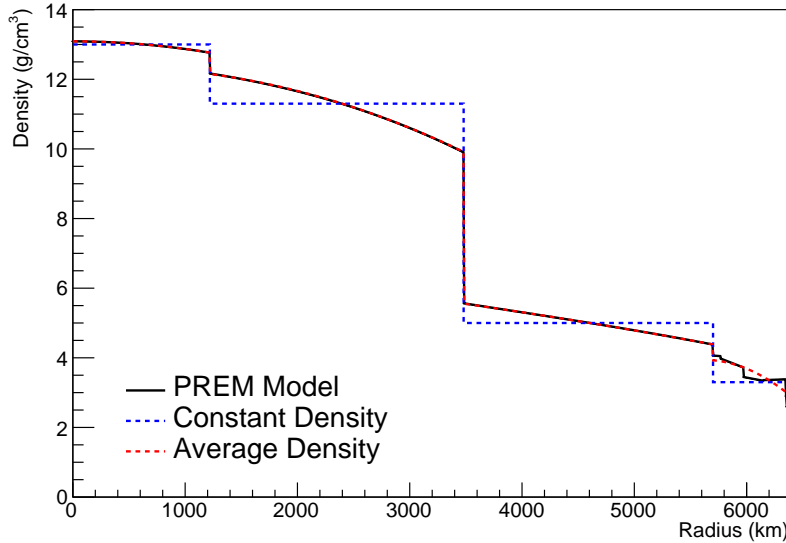


Figure 7.11: The density of the Earth given as a function of the radius, as given by the PREM model (Black), the constant density four-layer approximation (Blue), as used in the official SK-only analysis, and the quadratic approximation of the PREM model (Red).

Layer	Outer Radius [km]	Density [g/cm ³]
Inner Core	1220	$13.09 - 8.84x^2$
Outer Core	3480	$12.31 + 1.09x - 10.02x^2$
Lower Mantle	5701	$6.78 - 1.56x - 1.25x^2$
Transition Zone	6371	$-50.42 + 123.33x - 69.95x^2$

Table 7.1: The quadratic polynomial fits to the PREM model for four assumed layers of the PREM model. The fit to calculate the coefficients is given in [204], where $x = R / R_{\text{Earth}}$.

mantle layer boundary, has been reduced. This is expected as the difference in the density across this boundary is significantly smaller in the quadratic density model as compared to the constant density model. Whilst the difference in density across the other layer transitions is reduced, there is still a significant difference. This means the discontinuities in the oscillation probabilities remain but are significantly reduced. However, as the quadratic density approximation matches the PREM model well in this region, these discontinuities are due to the Earth model rather than an artifact of the oscillation calculation.

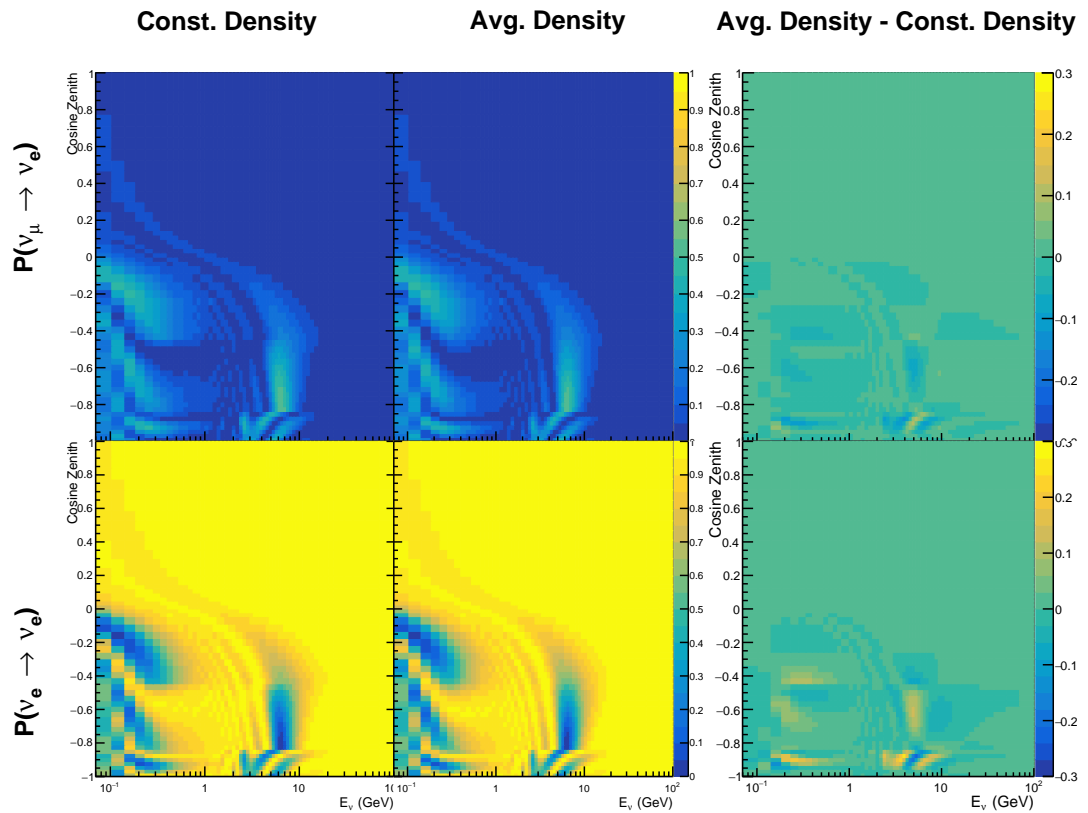


Figure 7.12: The oscillation probability, $P(\nu_\mu \rightarrow \nu_e)$ (top row) and $P(\nu_e \rightarrow \nu_e)$ (bottom row), given as a function of neutrino energy and zenith angle. The left column gives probabilities where the four-layer constant density approximation is used. The middle column gives the probabilities where the density is integrated over the trajectory, using the quadratic PREM approximation, for each $\cos(\theta_Z)$ is used. The right column illustrates the difference in oscillation probability between the two different techniques.

2752 7.4 Production Height Averaging

2753 As discussed in section 2.5, the height at which the cosmic ray flux interacts
2754 in the atmosphere is not known on an event-by-event basis. The production
2755 height can vary from the Earth’s surface to $\sim 50\text{km}$ above that. The SK-only
2756 analysis methodology (described in section 7.1) for including the uncertainty
2757 on the production height is to include variations from the Honda model when
2758 pre-calculating the oscillation probabilities prior to the fit. This technique is not
2759 possible for this analysis which uses continuous oscillation parameters that can
2760 not be known prior to the fit. Consequently, an analytical averaging technique
2761 was developed in [204]. The author of this thesis was not responsible for the
2762 derivation of the technique but has performed the implementation and validation
2763 of the technique for this analysis alone.

2764 Using the 20 production heights per Monte Carlo neutrino event, provided
2765 as 5% percentiles from the Honda flux model, a production height distribution
2766 $p_j(h|E_\nu, \cos \theta_Z)$ is built for each neutrino flavour $j = \nu_e, \bar{\nu}_e, \nu_\mu, \bar{\nu}_\mu$. In practice, a
2767 histogram is filled with 20 evenly spaced bins in production height h between
2768 0 and 50km. The neutrino energy and cosine zenith binning of the histogram
2769 are the same as that provided in section 7.1. The average production height,
2770 $\bar{h} = \int dh \frac{1}{4} \sum_j p_j(h|E_\nu, \cos(\theta_Z))$, is calculated. This assumes a linear average over
2771 the four flavours of neutrino which are considered to be generated in cosmic
2772 ray showers. The production height binning of this histogram is then translated
2773 into $\delta t(h) = t(\bar{h}) - t(h)$, where $t(x)$ is the distance travelled along the trajectory
2774 in the atmosphere from some production height, x .

2775 For the i^{th} traversed layer, the transition amplitude, $D_i(t_{i+1}, t_i)$, is computed.
2776 The time-ordered product of these is then used as the overall transition amplitude
2777 via

$$A(t_{n+1}, t_0) = D_n(t_{n+1}, t_n) \dots D_1(t_2, t_1) D_0(t_1, t_0), \quad (7.6)$$

2778 where,

$$\begin{aligned} D_n(t_{n+1}, t_n) &= \exp[-iH_n(t_{n+1} - t_n)] \\ &= \sum_{k=1}^3 C_k \exp[ia_k(t_{n+1} - t_n)] \end{aligned} \quad (7.7)$$

2779 is expressed as a diagonalised time-dependent solution to the Schrodinger
 2780 equation. The 0th layer is the propagation through the atmosphere and is the
 2781 only term that depends on the production height. Using the substitution $t_0 =$
 2782 $t(\bar{h}) - \delta t(h)$, it can be shown that

$$D_0(t_1, t_0) = D_0(t_1, \bar{h})D_0(\delta t). \quad (7.8)$$

2783 Thus Equation 7.6 becomes

$$\begin{aligned} A(t_{n+1}, t_0) &= D_n(t_{n+1}, t_n) \dots D_1(t_2, t_1)D_0(t_1, \bar{h})D(\delta t) \\ &= A(t_{n+1}, \bar{h}) \sum_{k=1}^3 C_k \exp[ia_k \delta t], \\ &= \sum_{k=1}^3 B_k \exp[ia_k \delta t]. \end{aligned} \quad (7.9)$$

2784 The oscillation probability averaged over production height is then calculated
 2785 as

$$\begin{aligned} \bar{P}(\nu_j \rightarrow \nu_i) &= \int d(\delta t) p_j(\delta t | E_\nu, \cos \theta_Z) P(\nu_j \rightarrow \nu_i) \\ &= \int d(\delta t) p_j(\delta t | E_\nu, \cos \theta_Z) A(t_{n+1}, t_0) A^*(t_{n+1}, t_0) \\ &= \sum_{km} (B_k)_{ij} (B_m)_{ij}^* \int d(\delta t) p_j(\delta t | E_\nu, \cos \theta_Z) \exp[i(a_k - a_m) \delta t]. \end{aligned} \quad (7.10)$$

2786 It is important to note that the exact value of \bar{h} used does not matter as the
 2787 values of δt would change to compensate for any modification to the value of \bar{h} .

2788 In practice, implementation in CUDAProb3 [207] is relatively straightforward
 2789 as the majority of these terms are already calculated in the standard oscillation
 2790 calculation. Figure 7.13 illustrates the results of the production height averaging.

2791 As expected, the main effect is observed in the low-energy downward-going
 2792 and horizontal-going events. Upward-going events have to travel the radius
 2793 of the Earth, $R_E = 6371\text{km}$, where the production height uncertainty is a small
 2794 fraction of the total path length.

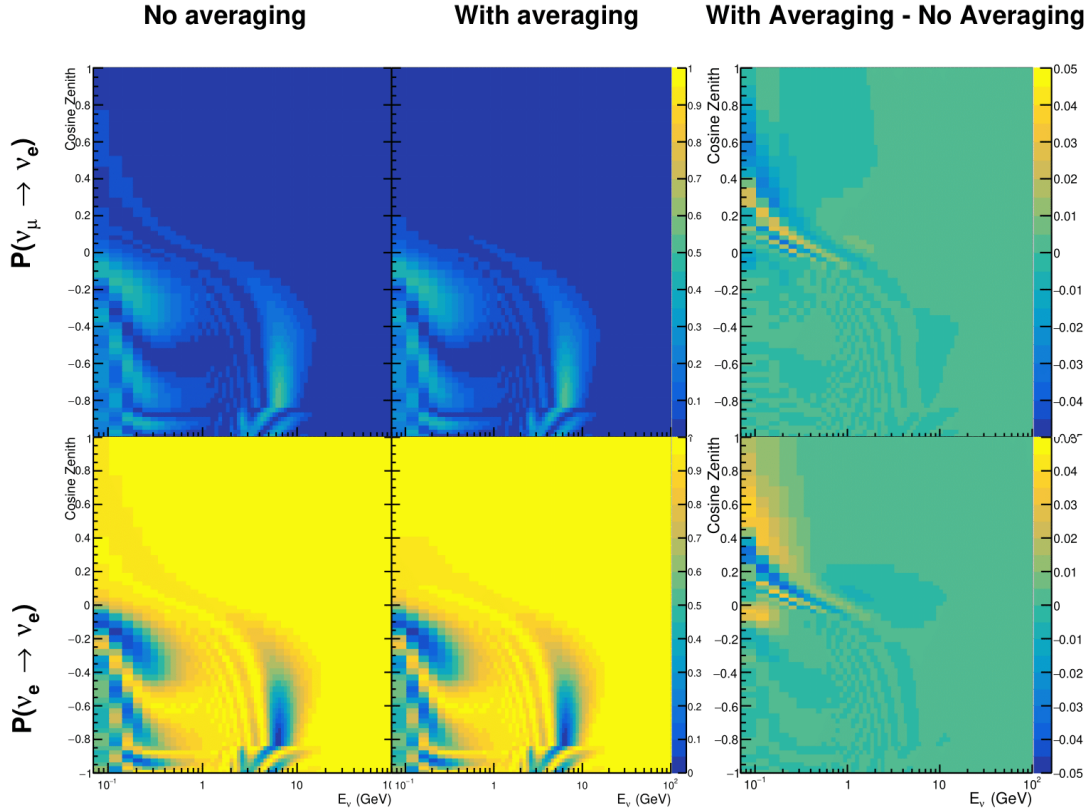


Figure 7.13: The oscillation probability, $P(\nu_\mu \rightarrow \nu_e)$ (top row) and $P(\nu_e \rightarrow \nu_e)$ (bottom row), given as a function of neutrino energy and zenith angle. The left column gives probabilities where a fixed production height of 25km is used. The middle column gives the probabilities where the production height is analytically averaged. The right column illustrates the difference in oscillation probability between the two different techniques.

8

2795

2796

Oscillation Analysis

2797 Using the samples and systematics defined in chapter 6, this chapter documents
2798 a simultaneous beam and atmospheric oscillation analysis from the T2K and SK
2799 experiments. The MaCh3 Bayesian MCMC framework introduced in chapter 4
2800 is used for all studies performed within this thesis.

2801 The MaCh3 framework used throughout this thesis has been validated through
2802 many tests. The code that handles the beam far detector samples was developed
2803 by the author and validated by comparison to the 2020 T2K analysis [72]. The
2804 sample event rates and likelihood evaluations of beam samples generated by the
2805 framework used within this thesis were compared to those from the T2K analysis
2806 by the author of this thesis. Variations of the sample predictions were compared
2807 at $\pm 1\sigma$ and $\pm 3\sigma$ and good agreement was found in all cases. A similar study, led
2808 by Dr. C. Wret was used to validate the near detector portion of the code [197].
2809 The implementation of the atmospheric samples within MaCh3 was completed
2810 and cross-checked by the author of this thesis against the P-Theta framework
2811 (introduced in section 3.2). Both fitters are provided with the same inputs and can
2812 therefore cross-validate each other. These validations compared the event rate and
2813 likelihood calculation. Documentation of all the above validations can be found
2814 in [197]. These stringent validations ensure that the code is doing as intended.

2815 8.1 Monte Carlo Prediction

- 2816 Using the three sets of dial values (generated, pre-fit, and post-fit tunes) defined in
 2817 subsection 6.4.3, the predicted event rates for each sample are given in Table 8.1.
 2818 The oscillated (AsimovA defined in Table 2.2) and un-oscillated event rates
 2819 are calculated for each tune.

Sample	Total Predicted Events					
	Generated		Pre-fit		Post-fit	
	Osc	UnOsc	Osc	UnOsc	Osc	UnOsc
SubGeV- <i>elike</i> -0dcy	7121.0	7102.6	6556.8	6540.0	7035.2	7015.7
SubGeV- <i>elike</i> -1dcy	704.8	725.5	693.8	712.8	565.7	586.0
SubGeV- <i>mulike</i> -0dcy	1176.5	1737.2	1078.6	1588.1	1182.7	1757.1
SubGeV- <i>mulike</i> -1dcy	5850.7	8978.1	5351.7	8205.1	5867.0	9009.9
SubGeV- <i>mulike</i> -2dcy	446.9	655.2	441.6	647.7	345.9	505.6
SubGeV- <i>pi0like</i>	1438.8	1445.4	1454.9	1461.1	1131.1	1136.2
MultiGeV- <i>elike</i> -nue	201.4	195.6	201.1	195.3	202.6	196.7
MultiGeV- <i>elike</i> -nuebar	1141.5	1118.3	1060.7	1039.5	1118.5	1095.7
MultiGeV- <i>mulike</i>	1036.7	1435.8	963.1	1334.1	1015.2	1405.9
MultiRing- <i>elike</i> -nue	1025.1	982.2	1026.8	984.3	1029.8	986.4
MultiRing- <i>elike</i> -nuebar	1014.8	984.5	991.0	962.0	1008.9	978.5
MultiRing- <i>mulike</i>	2510.0	3474.4	2475.6	3425.8	2514.6	3480.4
MultiRingOther-1	1204.5	1279.1	1205.8	1280.3	1207.4	1281.0
PCStop	349.2	459.2	338.4	444.7	346.8	456.1
PCThru	1692.8	2192.5	1661.5	2149.8	1689.2	2187.8
UpStop-mu	751.2	1295.0	739.7	1271.6	750.4	1293.0
UpThruNonShower-mu	2584.4	3031.6	2577.9	3019.4	2586.8	3034.0
UpThruShower-mu	473.0	488.6	473.2	488.7	473.8	489.4
FHC1Rmu	328.0	1409.2	301.1	1274.7	345.1	1568.0
RHC1Rmu	133.0	432.3	122.7	396.2	135.0	443.9
FHC1Re	84.6	19.2	77.4	18.2	93.7	19.7
RHC1Re	15.7	6.4	14.6	6.1	15.9	6.3
FHC1Re1de	10.5	3.2	10.3	3.1	8.8	2.9

Table 8.1: The Monte Carlo predicted event rate of each far detector sample used within this analysis. Three model parameter tunes are considered, as defined in subsection 6.4.3. Un-oscillated and oscillated predictions are given, where the oscillated predictions assume Asimov A oscillation parameters provided in Table 2.2.

2820 Generally, the samples that target CCQE interaction modes observe a decrease
 2821 in prediction when using the pre-fit dial values. This is in accordance with the
 2822 Monte Carlo being produced at $M_A^{QE} = 1.21\text{GeV}$ [156] whilst the pre-fit dial

2823 value is set to $M_A^{QE} = 1.03\text{GeV}$ as suggested by [196]. Furthermore, the predicted
 2824 event rates of samples that target CCRES interaction modes are significantly
 2825 reduced when considering the post-BANFF fit. This follows the observations
 2826 in subsection 6.4.3. The strength of the accelerator neutrino experiment can
 2827 be seen in the remarkable difference between the oscillated and unoscillated
 2828 predictions in the FHC1Rmu and RHC1Rmu samples. There is a very clear decrease
 2829 in the expected event rate between the oscillated and un-oscillated predictions
 2830 which is not as obvious as in the atmospheric samples. This is due to the fact that
 2831 the beam energy is tuned to the maximum disappearance probability, which is
 2832 not the case for the naturally generated atmospheric neutrinos.

2833 8.1.1 Likelihood Scans

2834 Using the definition of the likelihood presented in section 6.5, the contribution
 2835 of each sample to the likelihood from a variation of a particular parameter can
 2836 be studied. This process identifies which samples drive the determination of the
 2837 oscillation parameters in the joint fit. Figure 8.1 presents the variation of all the
 2838 samples (beam and atmospheric) at the far detector to the oscillation parameters
 2839 of interest: δ_{CP} , $\sin^2(\theta_{13})$, $\sin^2(\theta_{23})$, and Δm_{32}^2 . These plots are colloquially called
 2840 ‘likelihood scan’ (or ‘log-likelihood scans’). The process of making these plots is
 2841 as follows. An Asimov data set (following the technique detailed in section 6.5) is
 2842 built using the AsimovA oscillation parameters and pre-fit systematic tune. The
 2843 Monte Carlo is then reweighted using the value of the oscillation parameter at
 2844 each point on the x-axis of the scan. The likelihood is then calculated between
 2845 the Asimov data and Monte Carlo prediction and plotted.

2846 Due to the caveat of fixed systematic parameters and the correlations between
 2847 oscillation parameters being ignored when creating these likelihood scans, the
 2848 value of $\chi^2 = 1$ (or $-2 \times \ln(\text{Likelihood}) = 1$) does not equate to the typical
 2849 1σ sensitivity. However, it does give an indication of which samples respond
 2850 mostly strongly to variations in a particular oscillation parameter. The point at

2851 which the likelihood tends to zero illustrates the value of the parameter used
 2852 to build the Asimov data prediction.

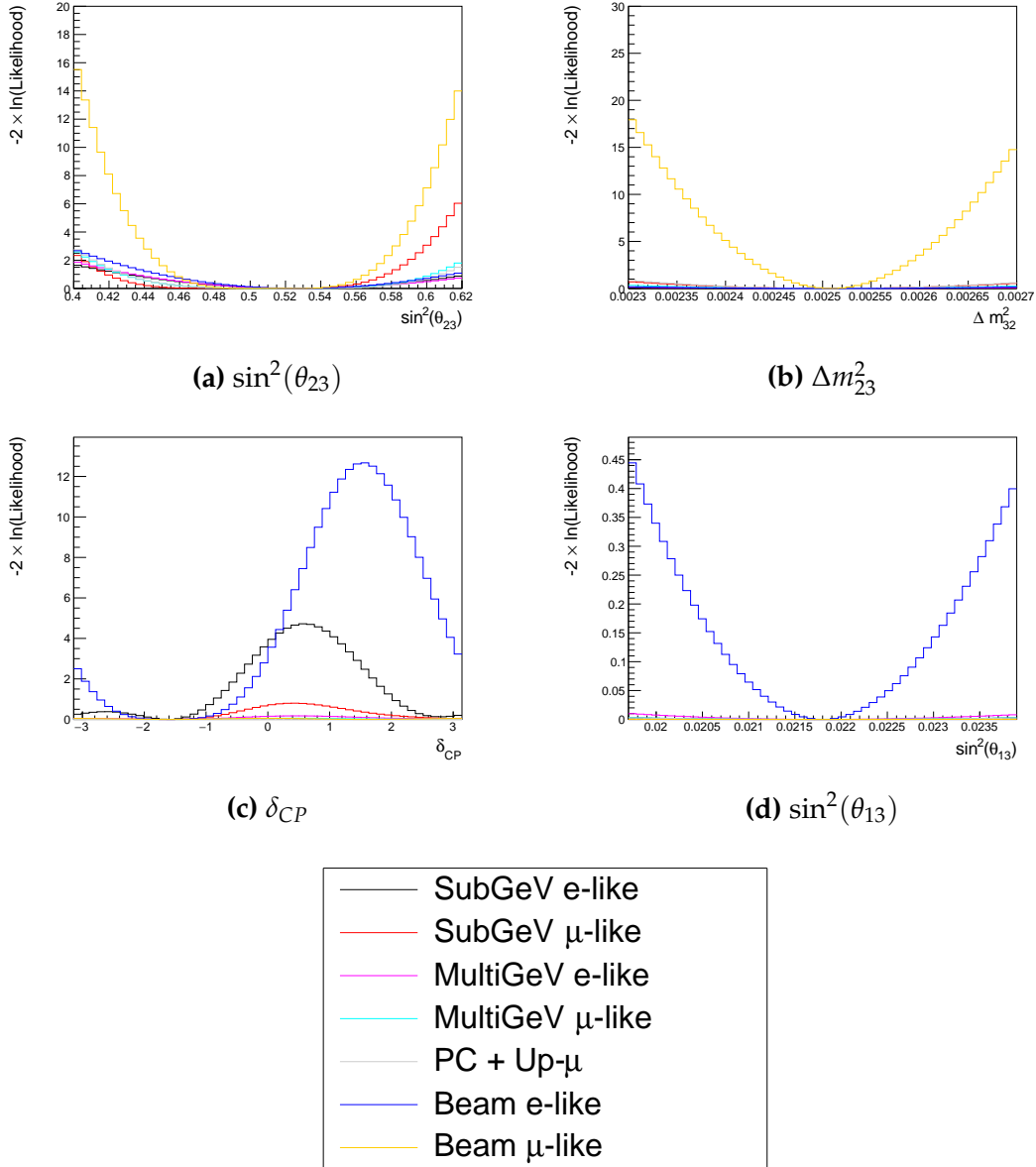


Figure 8.1: The response of the likelihood, as defined in section 6.5, illustrating the response of the samples to a variation of an oscillation parameter.

2853 The sensitivity to $\sin^2(\theta_{23})$ is mostly dominated by the beam muon-like
 2854 samples. The response of an individual atmospheric sample is small but non-
 2855 negligible such that the summed response over all atmospheric samples becomes
 2856 comparable to that of the muon-like beam samples. Consequently, the sensitivity

of the joint fit to $\sin^2(\theta_{23})$ would be expected to be greater than the beam-only analysis. The only sample that responds to the $\sin^2(\theta_{13})$ oscillation parameter is the electron-like beam samples. Consequently, no increase in sensitivity beyond that of the T2K-only analysis would be expected from the joint fit. Regardless, the sensitivity of the beam sample is significantly weaker than the external reactor constraint so prior knowledge will dominate any sensitivity to $\sin^2(\theta_{13})$ which is included within this thesis. The Δm_{21}^2 and $\sin^2(\theta_{12})$ parameters are not considered as there is simply no sensitivity in any sample considered within this analysis. The response to Δm_{32}^2 is completely dominated by the beam muon-like samples. This is because the beam neutrino energy is specifically tuned to match the maximal disappearance probability. Despite this, improvements to the $|\Delta m_{32}^2|$ sensitivity may be expected due to additional mass hierarchy determination added by the atmospheric samples.

Two-dimensional scans of the appearance ($\sin^2(\theta_{13})$ - δ_{CP}) and disappearance ($\sin^2(\theta_{23})$ - Δm_{32}^2) parameters are illustrated in Figure 8.2 and Figure 8.3, respectively. The caveat of fixed systematic parameters and correlations between other oscillation parameters being neglected still apply.

The appearance log-likelihood scans show the distinct difference in how the beam and atmospheric samples respond. The beam samples have an approximately constant width of the 2σ and 3σ contours, throughout all ranges of δ_{CP} . Whereas, the response of the atmospheric samples to $\sin^2(\theta_{13})$ is very strongly correlated to the value of δ_{CP} . At higher values of $\sin^2(\theta_{13})$, two lobes appear around $\delta_{CP} \sim -\pi/2$ and $\delta_{CP} \sim 2.4$. Consequently, this difference allows some of the degeneracy in a beam-only fit to be broken. Comparing the beam-only and joint fit likelihood scans, the 2σ continuous contour in δ_{CP} for beam samples becomes closed when the atmospheric samples are added. This may result in a stronger sensitivity to δ_{CP} . Similarly, the width of the 3σ contours also becomes dependent upon the value of δ_{CP} . Furthermore, atmospheric samples have little sensitivity to $\sin^2(\theta_{13})$ on their own, as evidenced in Figure 8.1, but may improve sensitivity to the parameter when combined within the simultaneous

2887 fit. It is important to remember that these likelihood scans are not sensitivity
2888 measurements as the systematic parameters are fixed and the correlation between
2889 oscillation parameters is neglected. However, they are a very encouraging result
2890 for the joint fit.

2891 The disappearance log-likelihood scans in $\sin^2(\theta_{23})$ - Δm_{32}^2 space (Figure 8.3)
2892 show the expected behaviour when considering the one-dimensional scans
2893 already discussed. The uncertainty on the width of $|\Delta m_{32}^2|$ is mostly driven by the
2894 beam samples. However, the width of this contour in the inverted mass region
2895 ($\Delta m_{32}^2 < 0$) is significantly reduced due to the ability of the atmospheric samples
2896 to select the correct (normal) mass hierarchy. The width of the uncertainty
2897 in $\sin^2(\theta_{23})$ is also reduced compared to the beam-only sensitivities, with a
2898 further decrease in the inverted hierarchy region due to the better mass hierarchy
2899 determination.

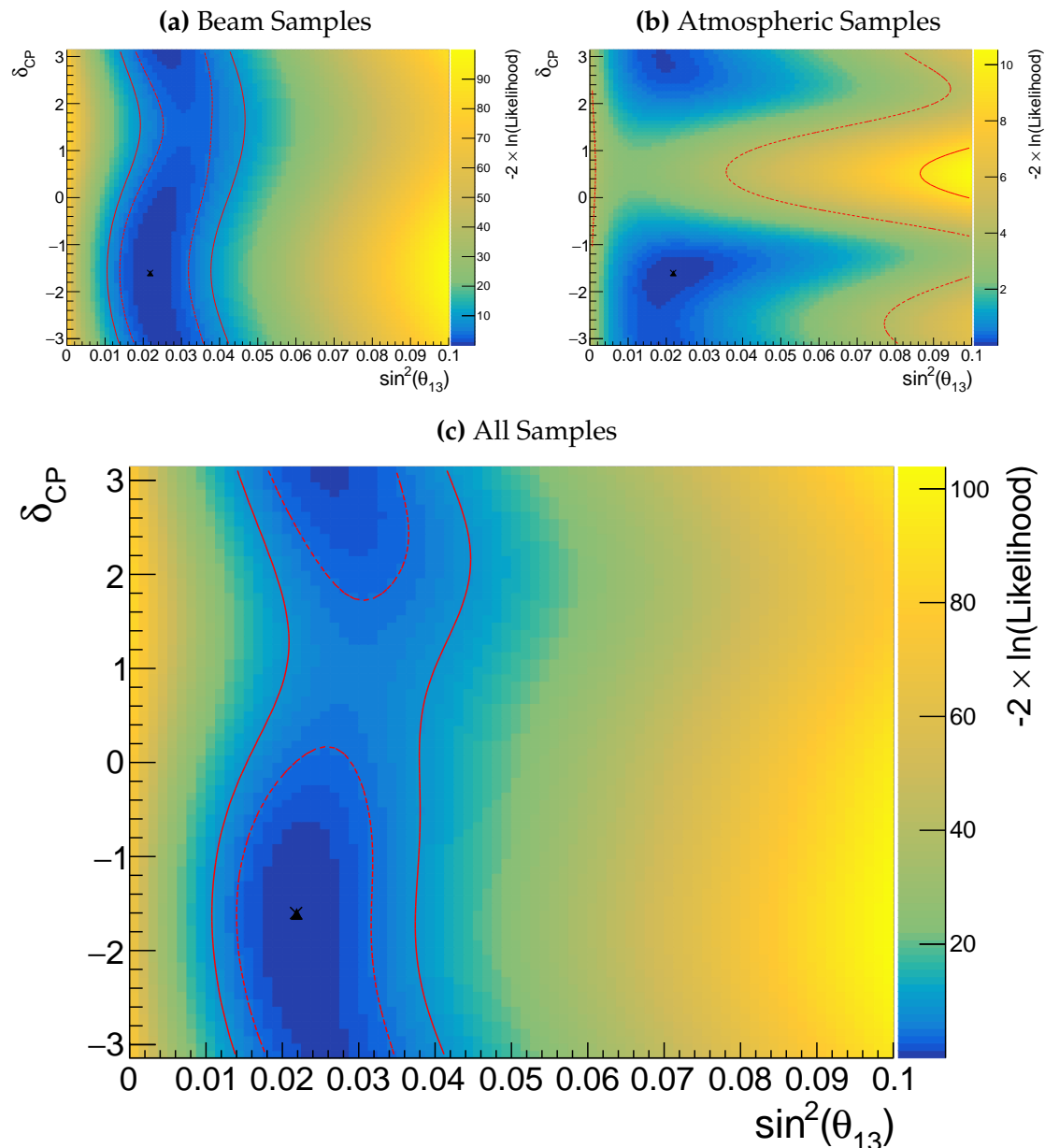


Figure 8.2: Two-dimensional log-likelihood scan of the appearance ($\sin^2(\theta_{13}) - \delta_{CP}$) parameters showing the response of the beam samples (top left), atmospheric samples (top right) and the summed response (bottom). The Asimov A oscillation parameters, defined in Table 2.2, are known to be the true point (Black Cross). The position of the smallest log-likelihood is highlighted with the triangle. Prior uncertainty terms of the oscillation parameters are neglected. The two(three) sigma contour levels are illustrated with the dashed(solid) red line.

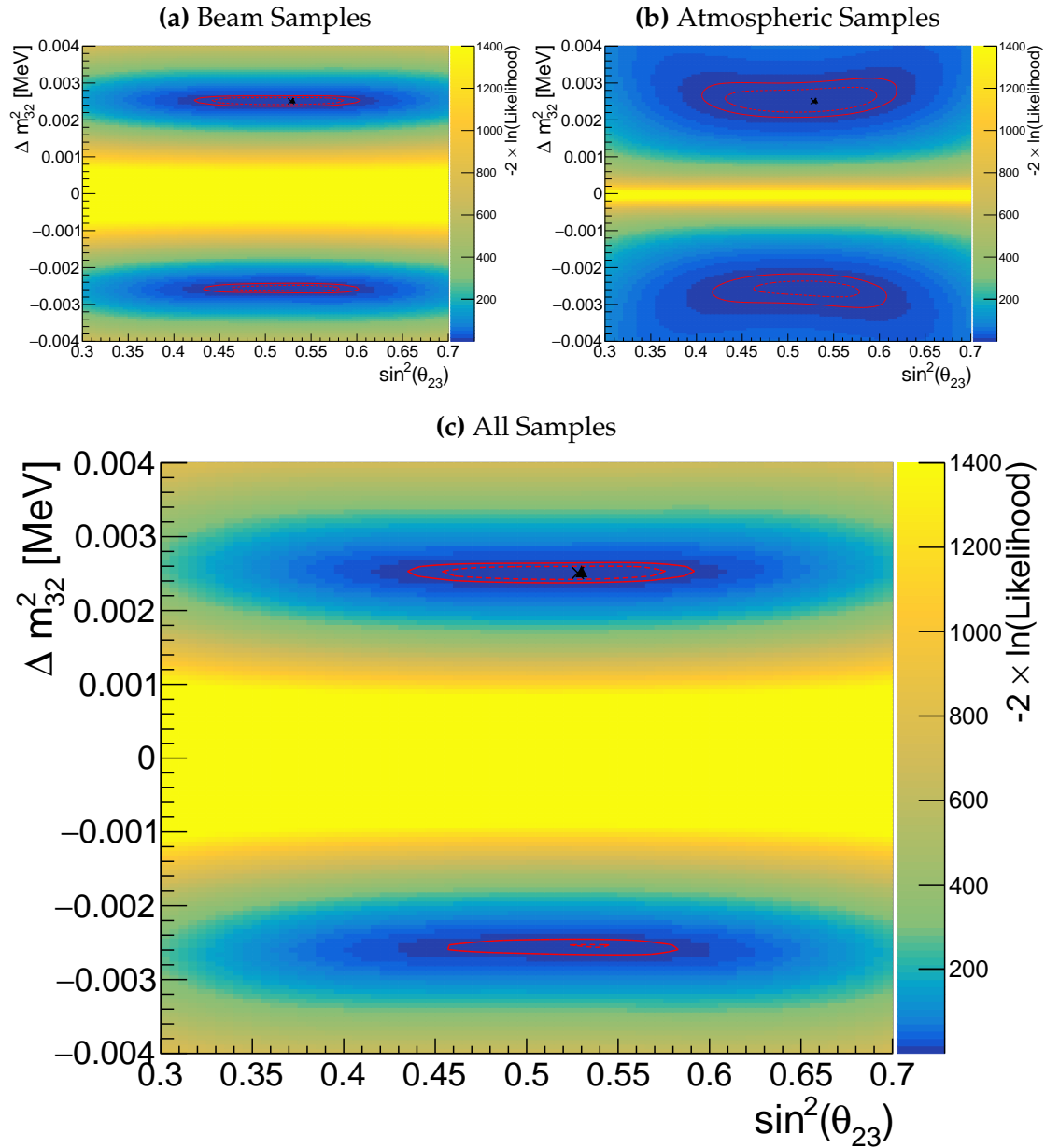


Figure 8.3: Two-dimensional log-likelihood scan of the disappearance ($\sin^2(\theta_{23})$)- Δm_{32}^2) parameters showing the response of the beam samples (top left), atmospheric samples (top right) and the summed response (bottom). The Asimov A oscillation parameters, defined in Table 2.2, are known to be the true point (Black Cross). The position of the smallest log-likelihood is highlighted with the triangle. Prior uncertainty terms of the oscillation parameters are neglected. The two(three) sigma contour levels are illustrated with the dashed(solid) red line.

The likelihood scans illustrated thus far only consider the sensitivity of this analysis for a fixed set of true oscillation parameters, namely Asimov A defined in Table 2.2. Whilst computationally infeasible to run many fits at different parameter sets, it is possible to calculate the likelihood response to different Asimov data sets. Figure 8.4 and Figure 8.5 illustrate how the sensitivity changes for differing true values of δ_{CP} and $\sin^2(\theta_{23})$, respectively. For both of these plots, the other oscillation parameters are fixed at their Asimov A values. Consequently, the caveat of fixed systematic parameters and correlations between other oscillation parameters being neglected still applies.

To explain how these plots are made, consider Figure 8.4. This plot is built by considering multiple one-dimensional log-likelihood scans, each creating an Asimov data set with the value of δ_{CP} taken from the x-axis. The likelihood to this particular Asimov data set is calculated after reweighting the Monte Carlo prediction to each value of δ_{CP} on the y-axis.

Figure 8.4 illustrates the sensitivity to δ_{CP} . To interpret this plot, larger contours results in more phase space being excluded from the 1σ region. The 1σ intervals contain regions where the beam and atmospheric samples have discontinuous contours. For example, for the x-axis value of $\delta_{CP} = 0$, the beam samples sensitivity would include two discontinuous regions excluded from the 1σ interval: $\delta_{CP} \sim 0$ and $\delta_{CP} \sim \pi$. This behaviour is also seen in atmospheric samples response but at a value of $\delta_{CP} \sim -1$. This difference allows the joint fit to have increased sensitivity to these regions. Consequently, the difference between the beam-only and joint beam-atmospheric fit should be studied using multiple Asimov data sets.

Despite the increased sensitivity at 1σ , the 2σ intervals from the joint fit are more similar to the two independent sensitivities and the off-diagonal degeneracies mostly remain. This indicates that the joint fit has the strength to aid parameter determination but can not entirely break the degeneracies in δ_{CP} at higher confidence levels.

Figure 8.5 illustrates a similar analysis as above, although the value of $\sin^2(\theta_{23})$ is varied and δ_{CP} is fixed to the Asimov A parameter value. Due to the beam parameters and baseline being tuned to specifically target this oscillation parameter, the average sensitivity of the beam samples is stronger than the atmospheric samples. However, the degeneracy around maximal mixing ($\sin^2(\theta_{23}) = 0.5$) is significantly more peaked in the beam samples compared to the atmospheric samples. This means that a value of $\sin^2(\theta_{23}) \sim 0.56$ would be contained within the 1σ confidence interval for a true value of $\sin^2(\theta_{23}) \sim 0.46$ if using the beam-only analysis, whereas it would be excluded in the joint analysis.

This behaviour is strengthened when considering the 2σ intervals, to the point where two distinct discontinuous regions of the 2σ intervals exist around the Asimov point $\sin^2(\theta_{23}) \sim 0.41, 0.6$. Given the caveat of only considering likelihood scans, the joint analysis would mostly eliminate the discontinuous intervals in these regions. This means that the joint fit could feasibly have an increased preference for the correct octant hypothesis.

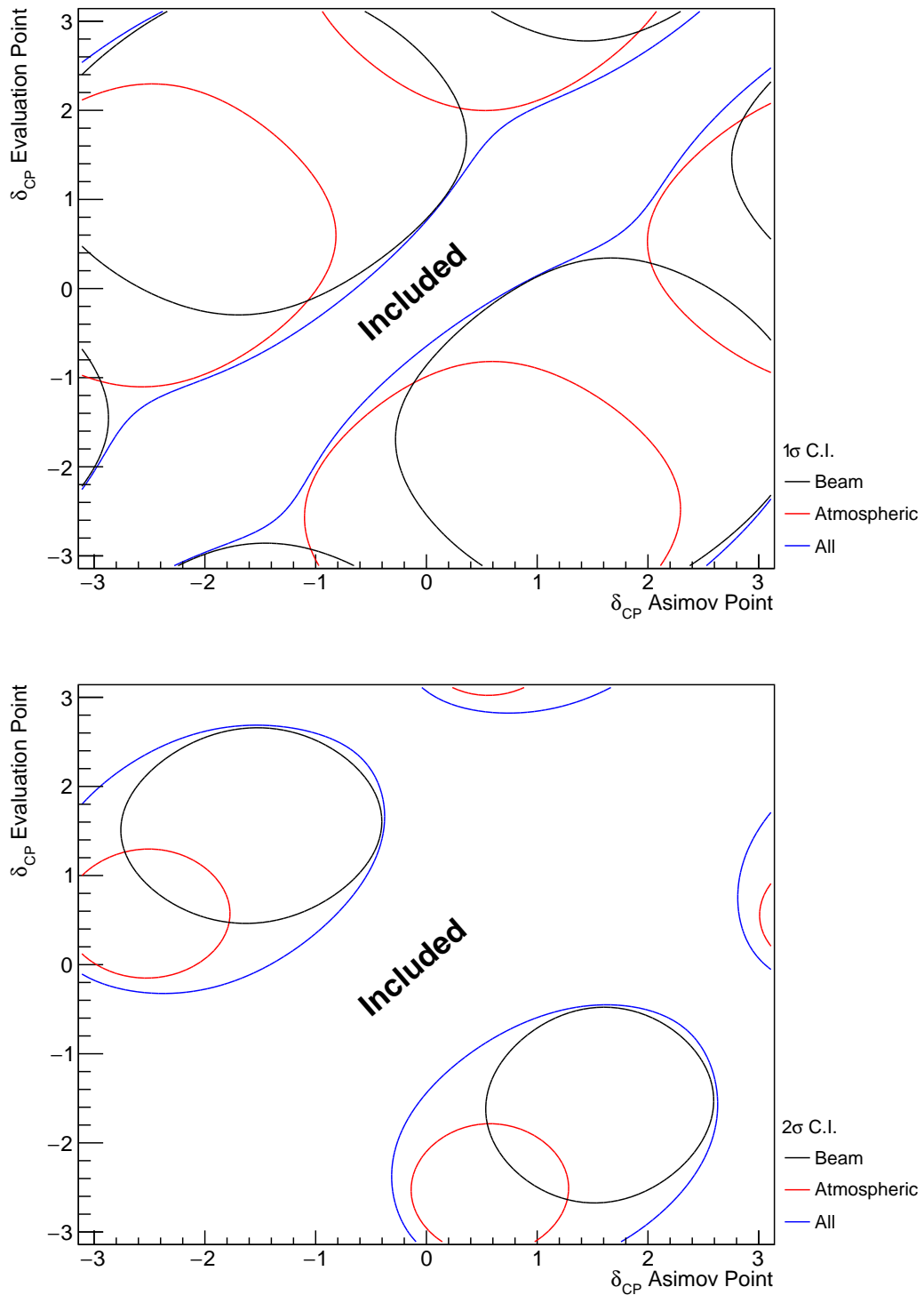


Figure 8.4: A series of one-dimensional likelihood scans over δ_{CP} , where an Asimov data set is built for each value of δ_{CP} on the x-axis and the likelihood is evaluated for each value of δ_{CP} on the y-axis. The diagonal represents the minimum log-likelihood and defines the region included within the 1σ (Top) and 2σ (Bottom) confidence intervals. The beam (black) and atmospheric (red) samples are individually plotted and the joint fit (blue) is the sum of the two.

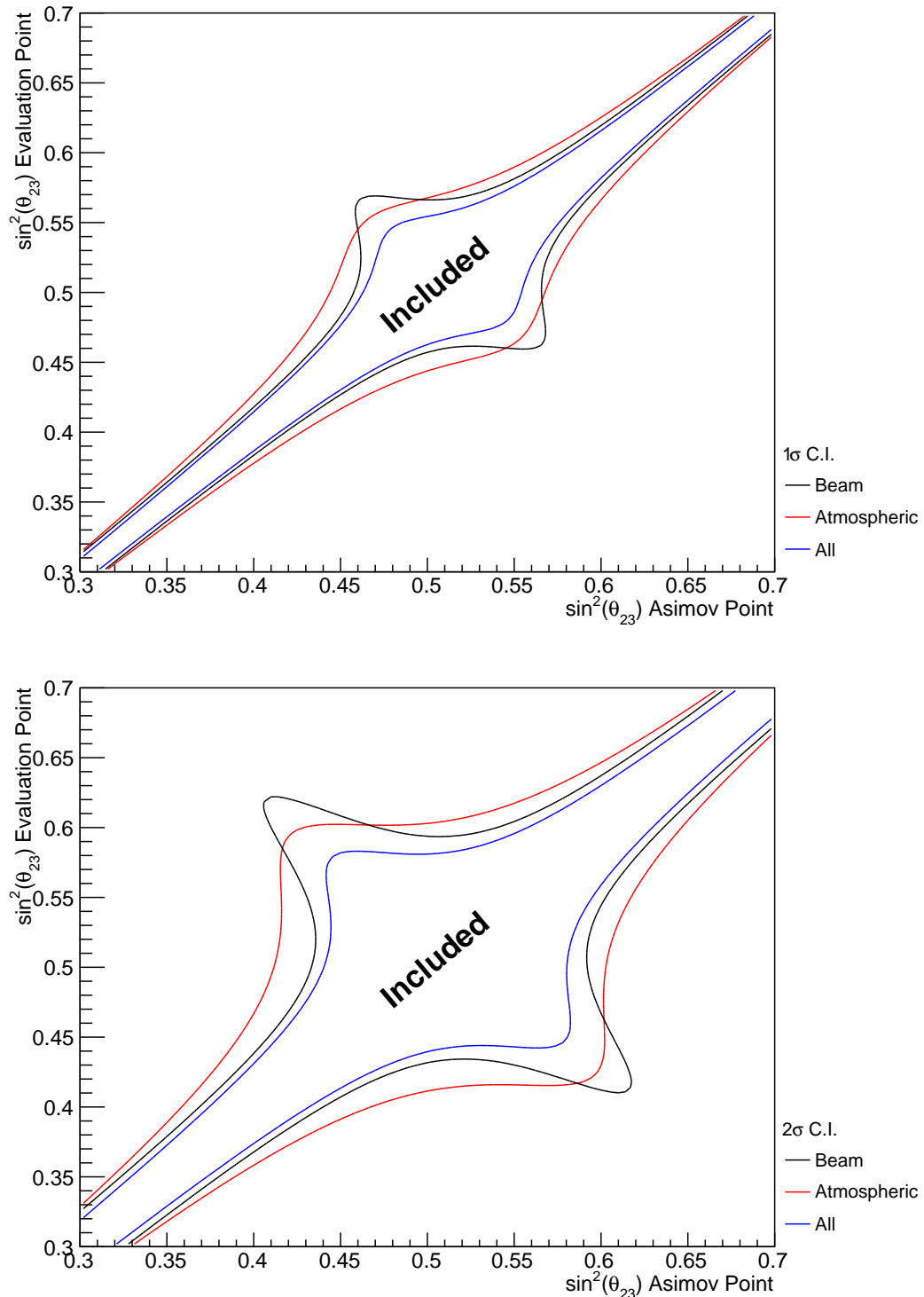


Figure 8.5: A series of one-dimensional likelihood scans over $\sin^2(\theta_{23})$, where an Asimov data set is built for each value of $\sin^2(\theta_{23})$ on the x-axis and the likelihood is evaluated for each value of $\sin^2(\theta_{23})$ on the y-axis. The diagonal represents the minimum log-likelihood and defines the region included within the 1σ (Top) and 2σ (Bottom) confidence intervals. The beam (black) and atmospheric (red) samples are individually plotted and the joint fit (blue) is the sum of the two.

Alongside oscillation parameters (Figure 8.1), the sensitivity to systematic parameters can also be studied for the joint fit. As some of these parameters are correlated between the beam and atmospheric events, the response of the atmospheric samples can modify the constraint. This means the systematics can have additional constraints than they would from a beam-only analysis. Therefore, the response from the beam and the atmospheric samples to various systematic parameters has been compared in Figure 8.6. The Asimov data set has been created using the AsimovA oscillation parameter and the pre-fit systematic tune. For example, the systematic parameter controlling the effective axial mass coupling in CCQE interactions, M_A^{QE} , is clearly dominated by the ND constraint. An example where the response of the atmospheric sample is approximately similar to the near detector constraint is the 2p2h CtoO normalisation systematic. This systematic models the scaling of the 2p2h interaction cross-section on a carbon target to an oxygen target. There are also systematics which have no near detector constraint. For example, the systematic parameters which describe the normalisation of the NC1Gamma and NCOther interaction modes. The atmospheric and beam samples can have similar sensitivity to these systematics due to their similar composition in energy and interaction mode. As an example of how the atmospheric samples can help constrain systematic parameters used within the T2K-only analysis, these NC background events in beam electron-like samples will be more constrained with the additional sensitivity of atmospheric samples. This would be expected to reduce the overall uncertainty of the beam electron-like event rates in the joint analysis compared to the beam-only studies. This could modify the sensitivity of the beam samples due to the more constrained background events.

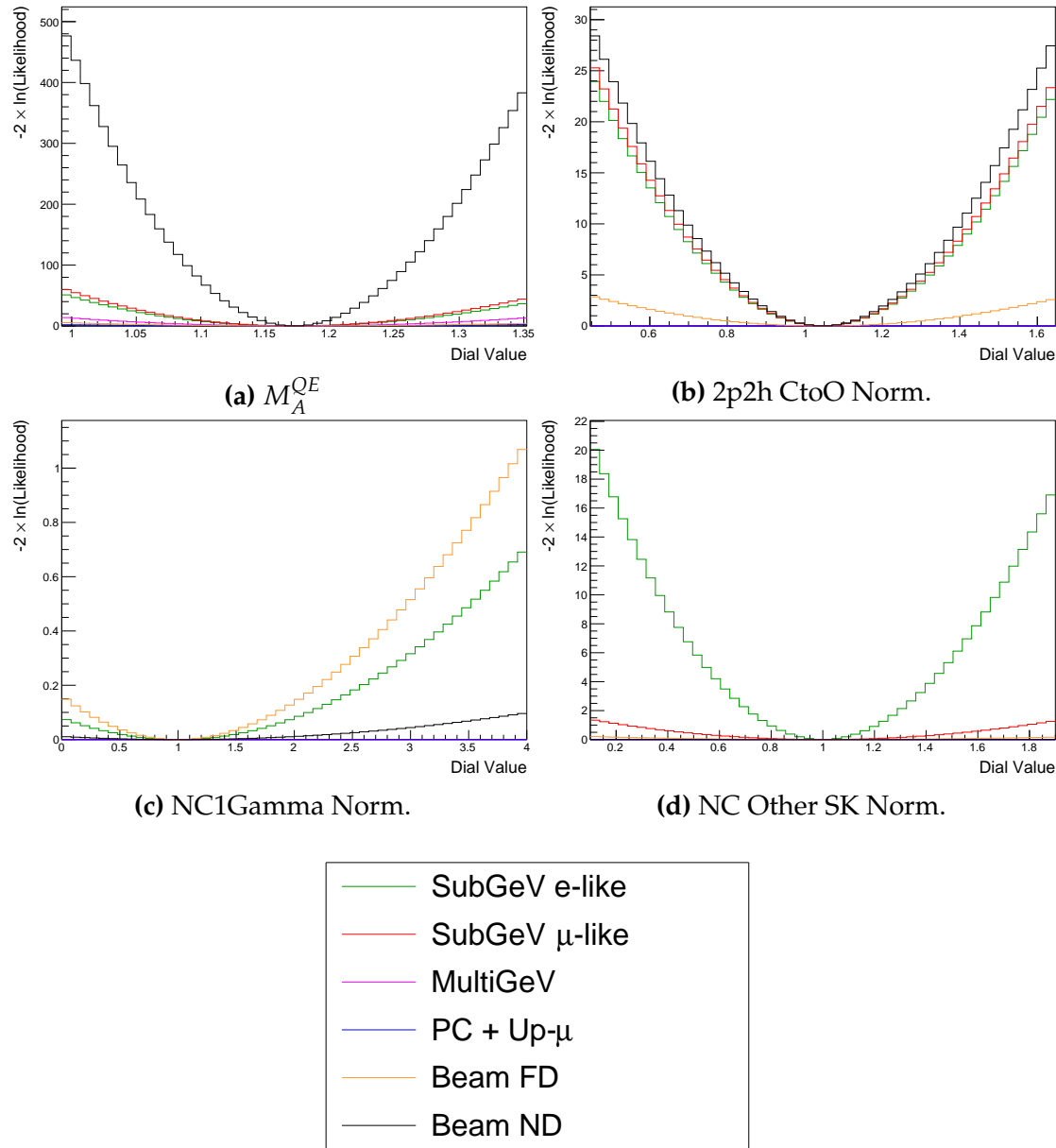


Figure 8.6: The response of the likelihood, as defined in section 8.2, illustrating the response of the samples to the various cross-section systematic parameters.

2969 8.2 Sensitivities

2970 DB: Indicate line or marker as true point in captions

2971 The sensitivities of the joint T2K and SK oscillation analysis are presented
2972 in the form of Asimov fits. These fits consider beam samples from the near
2973 and far detector alongside atmospheric samples at SK. This technique builds an
2974 Asimov data set (following section 6.5) using the AsimovA oscillation parameters
2975 and post-BANFF systematic tune, which is then fit. This technique eliminates
2976 statistical fluctuations from the data therefore providing the maximum sensitivity
2977 of the analysis.

2978 In practice, the Asimov fits presented within this analysis are modified from
2979 the above definition. An Asimov prediction of both beam and atmospheric far
2980 detector samples is fit whilst the true data is used for near detector samples. The
2981 Asimov predictions at the far detector are built using the post-BANFF tune (as
2982 discussed in section 3.2). These modifications mean that the results are equivalent
2983 to performing a far detector Asimov fit using inputs from the BANFF data fit.
2984 Consequently, this allows the results to be cross-checked with the results from
2985 the P-Theta analysis. The comparison has been performed and is documented in
2986 [213]. No significant discrepancies were found between the fitters.

2987 This section proceeds with the following studies. Firstly, the sensitivity
2988 of the atmospheric samples using the correlated detector model is detailed in
2989 subsection 8.2.1. This includes studying the choice of applying the 2020 PDG
2990 reactor constraint [73] to the atmospheric samples, which is documented in
2991 subsection 8.2.2. Additionally, the effect of applying the near-detector constraints
2992 onto the atmospheric samples is discussed in subsection 8.2.3. The main result is
2993 the sensitivity of the simultaneous beam and atmospheric fit. The sensitivities,
2994 both with and without the application of the reactor constraint, are presented
2995 in subsection 8.2.4 and subsection 8.2.5, respectively. To indicate the benefit
2996 of the joint analysis, the sensitivities are compared to the 2020 T2K beam-only
2997 sensitivities [72, 214] in subsection 8.2.6 and subsection 8.2.7. The T2K analysis is

used as a reference as it uses the same samples and a similar systematic model. As shown in subsection 8.1.1, the response of the beam and atmospheric samples change depending upon the true set of oscillation parameters assumed. Therefore, subsection 8.2.8 documents the sensitivities at an alternative oscillation parameter set. It is important to note that these results have been presented at the Neutrino 2022 conference on behalf of the T2K and SK collaborations [104].

8.2.1 Atmospheric-Only Sensitivity Without Reactor Constraint

This section presents the results of an Asimov fit using samples from the near detector and only atmospheric samples from the far detector. The results are presented as one-dimensional or two-dimensional histograms which have been marginalised over all other parameters using the technique outlined in subsection 4.3.1. Each histogram displays the posterior probability density and illustrates the credible intervals, calculated using the technique in subsection 4.3.2. For this fit, a flat prior is used for $\sin^2(\theta_{13})$, such that the reactor constraint is not applied. The Asimov data is generated assuming the AsimovA oscillation parameter set defined in Table 2.2 and the post-BANFF systematic parameter tune.

Figure 8.7 illustrates the posterior probability density for δ_{CP} , marginalised over both hierarchies. The fit favours the known oscillation parameter ($\delta_{CP} = -1.601$) although the posterior probability is very flat through the range of $-\pi < \delta_{CP} < -1$ and $2 < \delta_{CP} < \pi$. There is also a region around $\delta_{CP} \sim 0.4$ which is disfavoured at 2σ . This indicates that the SK samples can rule out some parts of the CP conserving parameter space reasonably well, near $\delta_{CP} \sim 0.4$, when the true value of $\delta_{CP} \sim -\pi/2$.

The posterior probability density in Δm_{32}^2 is given in Figure 8.8. This distribution includes steps in both the normal hierarchy (NH, $\Delta m_{32}^2 > 0$) and the inverse hierarchy (IH, $\Delta m_{32}^2 < 0$). The highest posterior probability density is found within the NH 1σ credible interval, which agrees with the known oscillation parameter value, $2.509 \times 10^{-3}\text{eV}^2$. However, all of the credible intervals span both of the hierarchy hypotheses.

Without Reactor Constraint, Both Hierarchies

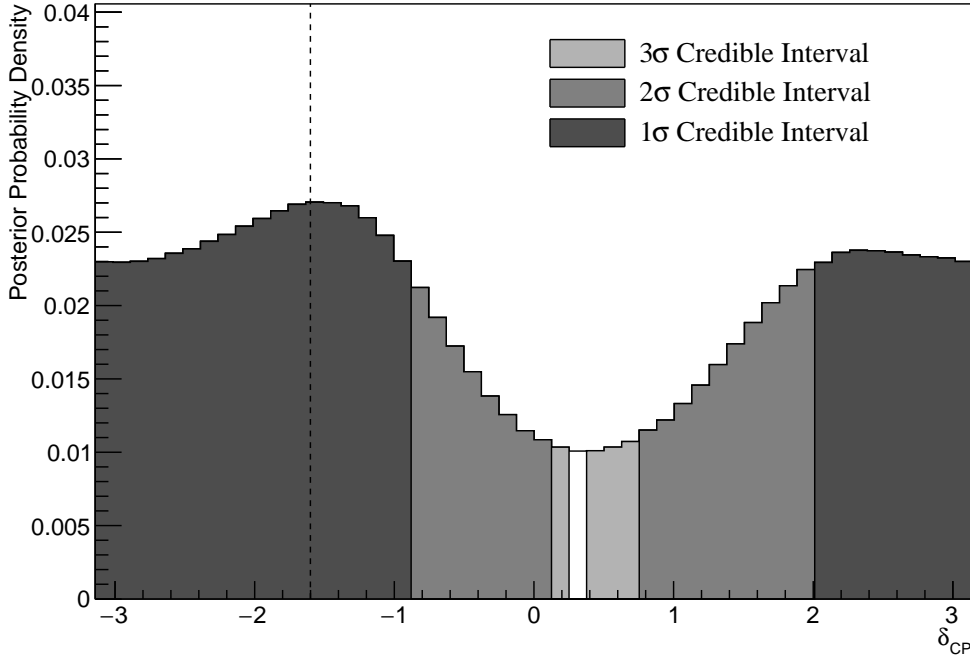


Figure 8.7: The one-dimensional posterior probability density distribution in δ_{CP} , marginalised over both hierarchies, from the SK atmospheric-only fit. The reactor constraint is not applied.

	LO ($\sin^2 \theta_{23} < 0.5$)	UO ($\sin^2 \theta_{23} > 0.5$)	Sum
NH ($\Delta m_{32}^2 > 0$)	0.17	0.40	0.58
IH ($\Delta m_{32}^2 < 0$)	0.13	0.29	0.42
Sum	0.31	0.69	1.00

Table 8.2: The distribution of steps in an SK atmospheric-only fit, presented as the fraction of steps in the upper (UO) and lower (LO) octants and the normal (NH) and inverted (IH) hierarchies. The reactor constraint is not applied. The Bayes factors are calculated as $B(\text{NH}/\text{IH}) = 1.37$ and $B(\text{UO}/\text{LO}) = 2.24$.

Following the discussion in subsection 4.3.3, the Bayes factor for hierarchy preference can be calculated by determining the fraction of steps that fall into the NH and the IH regions, as an equal prior is placed on both hypotheses. A similar calculation can be performed by calculating the fraction of steps which fall in the lower octant (LO, $\sin^2 \theta_{23} < 0.5$) or upper octant (UO, $\sin^2 \theta_{23} > 0.5$). The fraction of steps, broken down by hierarchy and octant, are given in Table 8.2. The Bayes factor for preferred hierarchy hypothesis is $B(\text{NH}/\text{IH}) = 1.37$. Jeffrey's

Without Reactor Constraint, Both Hierarchies

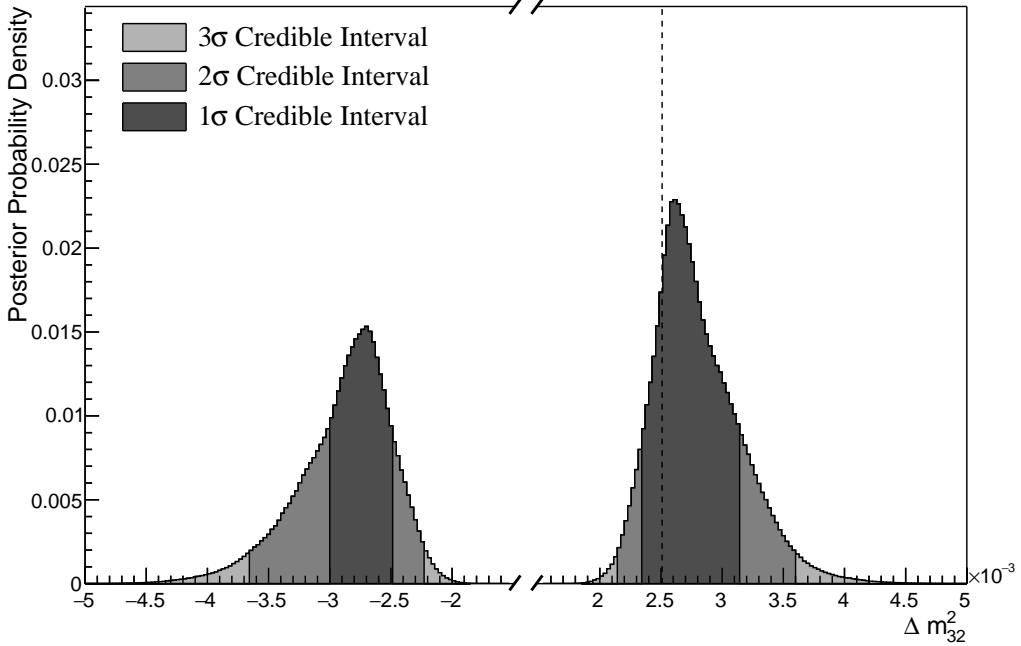


Figure 8.8: The one-dimensional posterior probability density distribution in Δm_{32}^2 , marginalised over both hierarchies, from the SK atmospheric-only fit. The reactor constraint is not applied.

scale, given in Table 4.1, states this value of the Bayes factor indicates a weak preference for the normal hierarchy hypothesis. The Bayes factor for choice of octant is $B(\text{UO}/\text{LO}) = 2.24$. This is also classified as a weak preference for the UO. Both of these show that the fit is returning the correct choice of hypotheses (NH and UO) for the known Asimov A oscillation parameters defined in Table 2.2.

The 1 σ credible intervals, broken down by hierarchy, and position in parameter space of the highest posterior probability density is given in Table 8.3. These are taken from the one-dimensional projections of the oscillation parameters, marginalised over all other parameters within the fit. As the distribution is binned, the highest posterior density is presented as the center of the bin with highest posterior density with an error equal to the bin width. For the known Asimov value of $\delta_{CP} = -1.601$, the 1 σ credible interval rules out a region between $\delta_{CP} = -0.88$ and $\delta_{CP} = 1.96$, when marginalising over both hierarchies. The position of the highest posterior density is $\delta_{CP} = -1.57 \pm 0.07$ which is clearly

Parameter	Interval	HPD
δ_{CP} , (BH)	$[-\pi, -0.88], [2.01, \pi]$	-1.57 ± 0.07
δ_{CP} , (NH)	$[-\pi, -0.88], [1.88, \pi]$	-1.57 ± 0.07
δ_{CP} , (IH)	$[-\pi, -0.88], [2.01, \pi]$	-1.57 ± 0.07
Δm_{32}^2 (BH) [$\times 10^{-3}\text{eV}^2$]	$[-3.00, -2.49], [2.34, 3.14]$	2.65 ± 0.02
Δm_{32}^2 (NH) [$\times 10^{-3}\text{eV}^2$]	$[2.41, 3.04]$	2.64 ± 0.03
Δm_{32}^2 (IH) [$\times 10^{-3}\text{eV}^2$]	$[-3.11, -2.41]$	-2.70 ± 0.03
$\sin^2(\theta_{23})$ (BH)	$[0.476, 0.584]$	0.542 ± 0.006
$\sin^2(\theta_{23})$ (NH)	$[0.488, 0.596]$	0.554 ± 0.006
$\sin^2(\theta_{23})$ (IH)	$[0.476, 0.584]$	0.542 ± 0.006

Table 8.3: The position of the highest posterior probability density (HPD) and width of the 1σ credible interval for the SK atmospheric-only fit. The reactor constraint is not applied. The values are presented by which hierarchy hypothesis is assumed: marginalised over both hierarchies (BH), normal hierarchy only (NH), and inverted hierarchy only (IH).

3048 compatible with the known oscillation parameter value.

3049 The sensitivity of the atmospheric samples to $\sin^2(\theta_{13})$ is presented in Fig-
 3050 ure 8.9. The likelihood scans presented in Figure 8.1 suggest that the sensitivity
 3051 to $\sin^2(\theta_{13})$ will be small. This behaviour is also seen in the fit results, where the
 3052 width of the 1σ credible intervals span the region of $\sin^2(\theta_{13}) = [0.008, 0.08]$. This
 3053 is more than an order of magnitude worse than the constraint from reactor
 3054 experiments [73].

3055 As previously discussed, the correlations between oscillation parameters are
 3056 also important to understand how the atmospheric samples respond. Figure 8.10
 3057 illustrates the two dimensional $\sin^2(\theta_{13}) - \delta_{CP}$ sensitivity, marginalised over
 3058 all other parameters. The shape of the 1σ credible interval shows that the
 3059 constraining power of the fit on δ_{CP} is dependent upon the value of $\sin^2(\theta_{13})$.
 3060 Furthermore, they show a strong resemblance to the likelihood scans illustrated
 3061 in Figure 8.2. Whilst the atmospheric samples do not strongly constrain the
 3062 value of $\sin^2(\theta_{13})$, the value of $\sin^2(\theta_{13})$ does impact the atmospheric samples'
 3063 sensitivity to δ_{CP} .

Without Reactor Constraint, Both Hierarchies

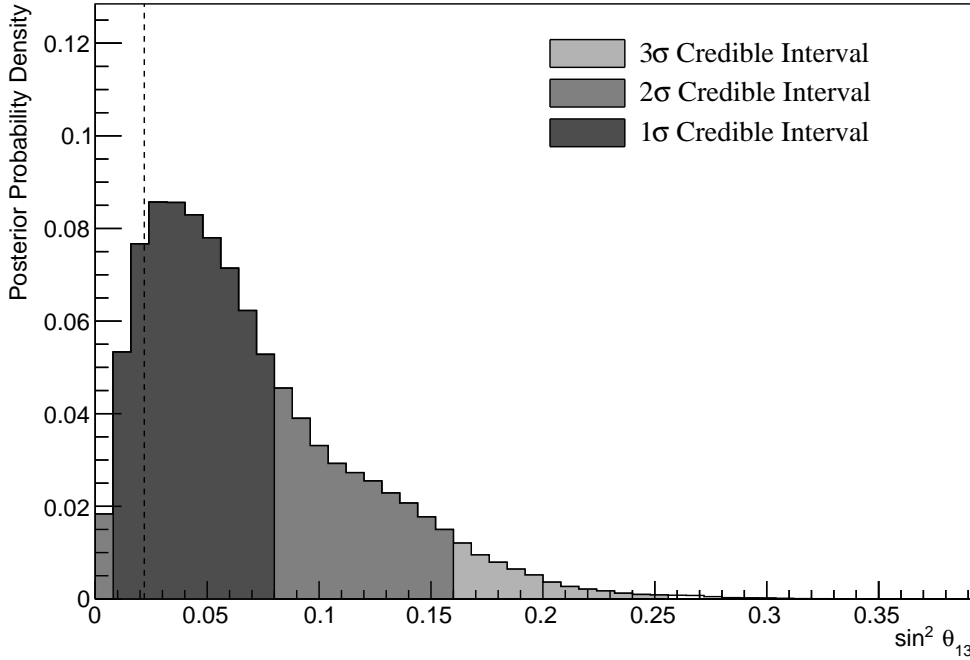


Figure 8.9: The one-dimensional posterior probability density distribution in $\sin^2(\theta_{13})$, marginalised over both hierarchies, from the SK atmospheric-only fit. The reactor constraint is not applied.

3064 The $\sin^2(\theta_{23}) - \Delta m_{32}^2$ disappearance contours are illustrated in Figure 8.11.
 3065 As expected, the area contained in the inverted hierarchy 1σ credible interval is
 3066 slightly smaller than that in the normal hierarchy. This follows from the Bayes
 3067 factor showing a weak preference for NH meaning that more of the steps will exist
 3068 in the $\Delta m_{32}^2 > 0$ region. The known oscillation parameters of $\sin^2(\theta_{23}) = 0.528$
 3069 and $\Delta m_{32}^2 = 2.509 \times 10^{-3} \text{ eV}^2$ are contained within the 1σ credible interval.

3070 Figure 8.12 illustrates the two-dimensional projections for each permutation of
 3071 oscillation parameters which this analysis is sensitive to: δ_{CP} , $\sin^2(\theta_{13})$, $\sin^2(\theta_{23})$,
 3072 and Δm_{32}^2 . The purpose of this plot is to illustrate the correlations between
 3073 the oscillation parameters. The contours are calculated whilst marginalising
 3074 over both hierarchies, however, only the NH is illustrated when plotting the
 3075 Δm_{32}^2 parameter. As expected the correlations play a significant role in these
 3076 sensitivity measurements, especially the choice of the $\sin^2(\theta_{13})$ constraint. Most
 3077 notably, the application of reactor constraint would be expected to alter both the

Without Reactor Constraint, Both Hierarchies

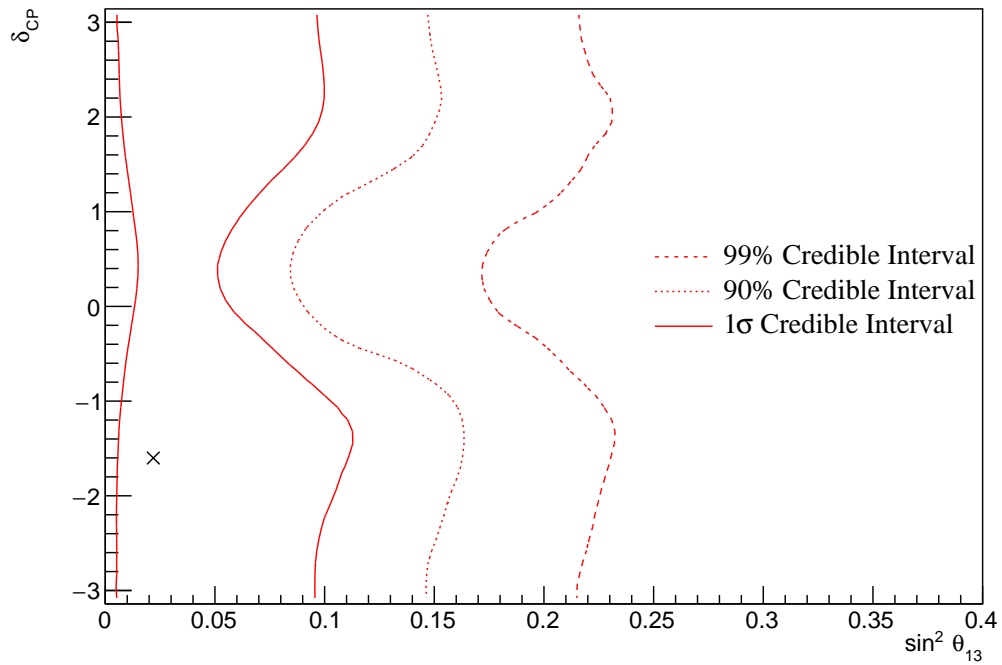


Figure 8.10: The two-dimensional posterior probability density distribution in δ_{CP} – $\sin^2(\theta_{13})$, marginalised over both hierarchies, from the SK atmospheric-only fit. The reactor constraint is not applied.

³⁰⁷⁸ width and position of the Δm_{32}^2 intervals due to the strong correlation between
³⁰⁷⁹ the parameters.

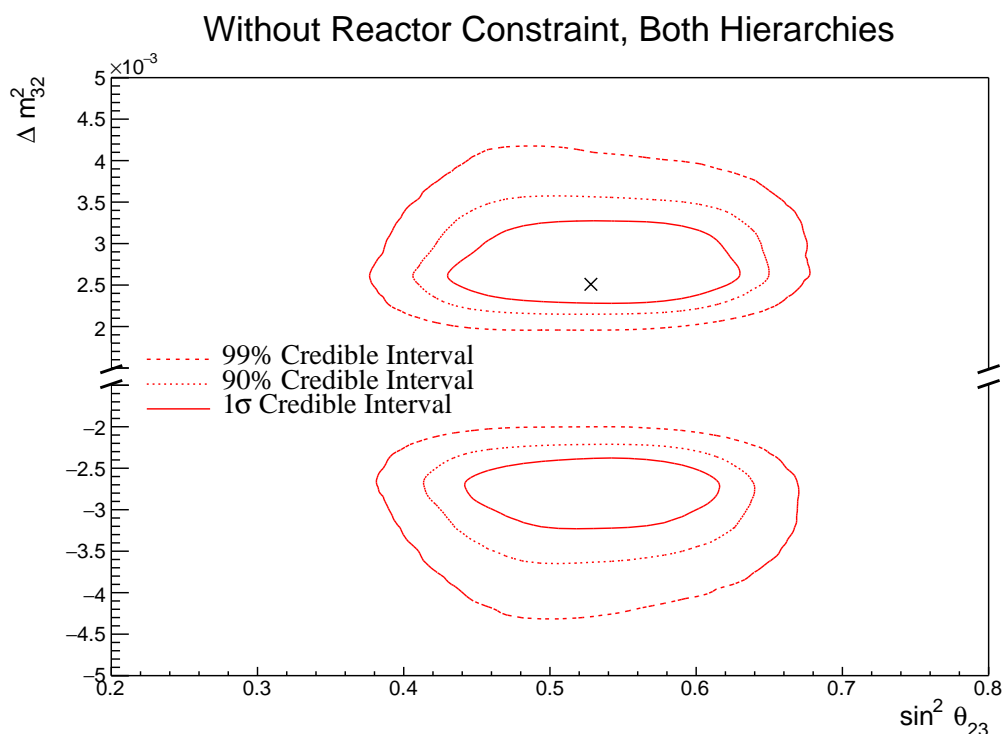


Figure 8.11: The two-dimensional posterior probability density distribution in $\Delta m_{32}^2 - \sin^2(\theta_{23})$, marginalised over both hierarchies, from the SK atmospheric-only fit. The reactor constraint is not applied.

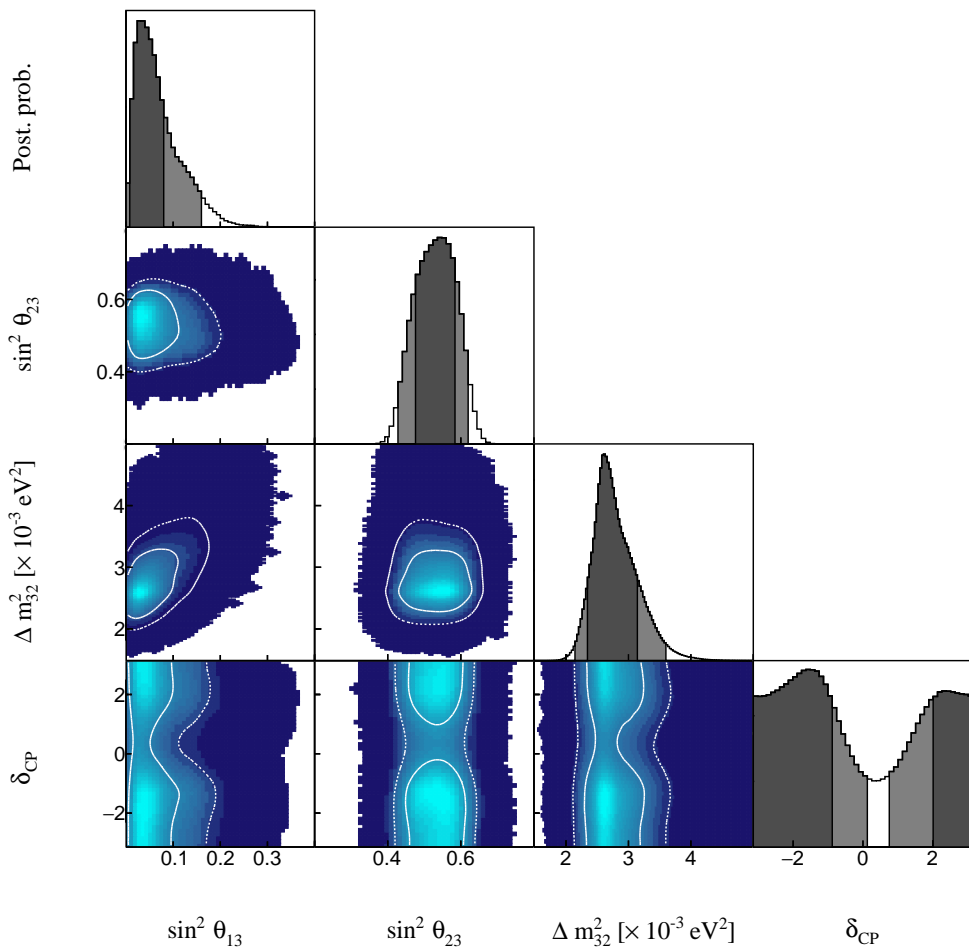


Figure 8.12: The posterior probability density distribution from the SK atmospheric-only fit. The reactor constraint is not applied. The distribution is given for each two-dimensional permutation of the oscillation parameters of interest. The one-dimensional distribution of each parameter is also given.

3080 8.2.2 Atmospheric-Only Sensitivity With Reactor Constraint

3081 The results in subsection 8.2.1 discuss the atmospheric sensitivity when the reactor
 3082 constraint is not applied. The correlations illustrated in Figure 8.12 indicate that
 3083 the marginalisation effects could contribute to differing sensitivities when the
 3084 external reactor constraint is applied. Using the technique discussed in subsec-
 3085 tion 4.1.1, the posterior distribution of the fit in subsection 8.2.1 can be reweighted
 3086 to include the reactor constraint of $\sin^2(\theta_{13}) = (2.18 \pm 0.08) \times 10^{-2}$ [73].

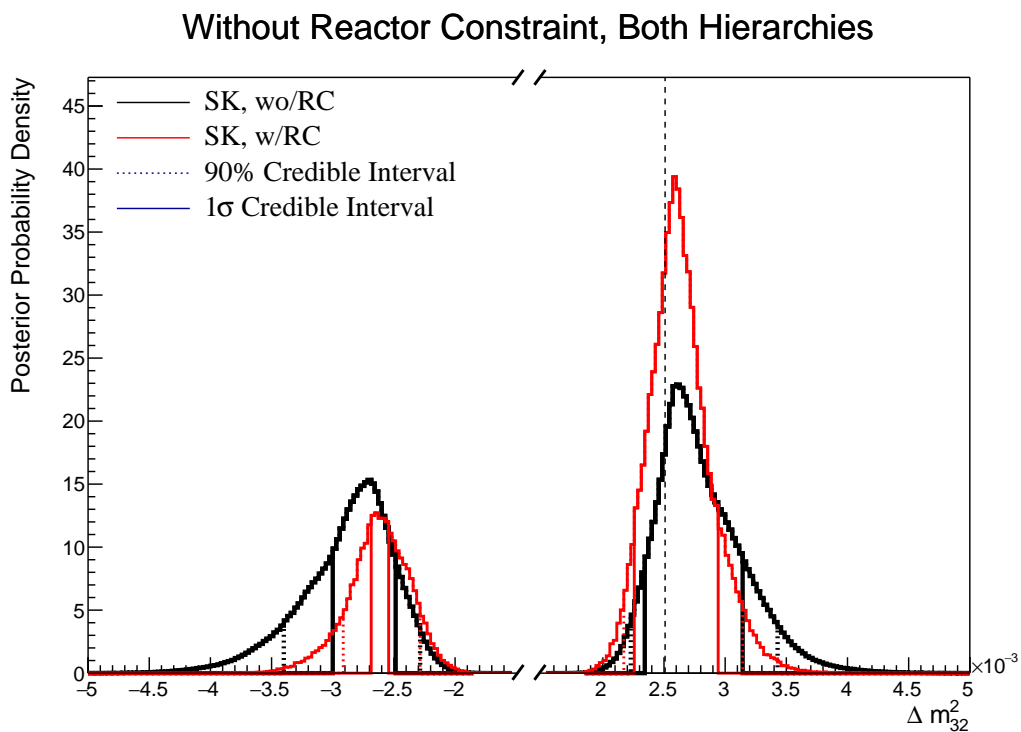


Figure 8.13: The one-dimensional posterior probability density distribution in Δm_{32}^2 compared between the SK atmospheric-only fit (Black) and the SK atmospheric fit with the reactor constraint applied (Red). The distributions are marginalised over both hierarchies.

3087 The reactor constraint increases the sensitivity of the atmospheric samples to
 3088 Δm_{32}^2 as illustrated in Figure 8.13. The 1σ credible interval in Δm_{32}^2 is determined
 3089 to be $[-2.69, -2.54] \times 10^{-3} \text{ eV}^2$ and $[2.25, 2.94] \times 10^{-3} \text{ eV}^2$. The width of the IH
 3090 credible interval is reduced by $\sim 70\%$ when the reactor constraint is applied. Due
 3091 to the marginalisation effects observed in Figure 8.12, the favoured region of Δm_{32}^2
 3092 moves closer to zero for both hierarchies. A clear explanation of this behaviour is

3093 illustrated in Figure 8.14, which shows the posterior distribution in the Δm_{32}^2 –
 3094 $\sin^2(\theta_{13})$ parameters. The correlation between Δm_{32}^2 and $\sin^2(\theta_{13})$ is such that
 3095 lower values of $\sin^2(\theta_{13})$ tend towards lower values of $|\Delta m_{32}^2|$. Therefore the
 3096 application of the reactor constraint moves the posterior distribution towards
 3097 the known oscillation parameter.

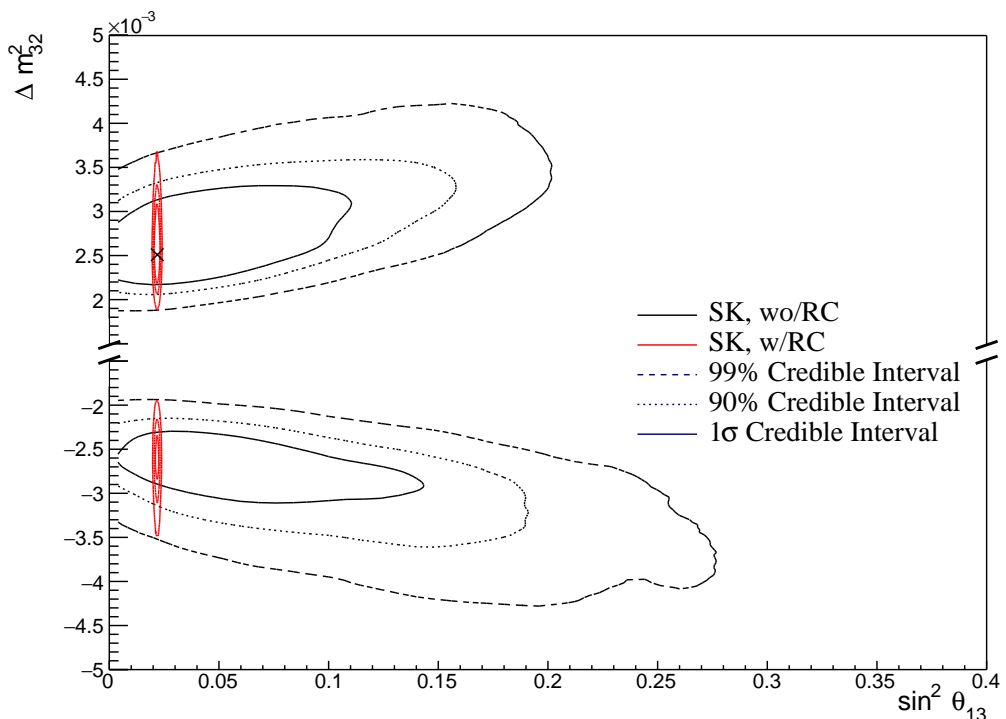


Figure 8.14: The two-dimensional posterior probability density distribution in Δm_{32}^2 – $\sin^2(\theta_{13})$ compared between the SK atmospheric-only fit (Black) and the SK atmospheric fit with the reactor constraint (Red). The distributions are marginalised over both hierarchies.

	LO ($\sin^2 \theta_{23} < 0.5$)	UO ($\sin^2 \theta_{23} > 0.5$)	Sum
NH ($\Delta m_{32}^2 > 0$)	0.21	0.53	0.74
IH ($\Delta m_{32}^2 < 0$)	0.08	0.18	0.26
Sum	0.29	0.71	1.00

Table 8.4: The distribution of steps in an SK atmospheric with reactor constraint fit, presented as the fraction of steps in the upper (UO) and lower (LO) octants and the normal (NH) and inverted (IH) hierarchies. The Bayes factors are calculated as $B(\text{NH}/\text{IH}) = 2.85$ and $B(\text{UO}/\text{LO}) = 2.39$.

3098 Table 8.4 presents the fraction of steps in each hierarchy and octant model
3099 for the fit after the reactor constraint has been applied. The reactor constraint
3100 significantly increases the NH preference, increasing the Bayes factor from
3101 $B(\text{NH}/\text{IH}) = 1.37$ to $B(\text{NH}/\text{IH}) = 2.85$ when the reactor constraint is applied.
3102 This is still defined as a weak preference for NH hypothesis according to Jeffrey's
3103 scale, however, it is a stronger preference than when the constraint is not applied.
3104 The preference for the correct octant model is also slightly increased by the
3105 application of the reactor constraint.

3106 8.2.3 Impact of Near Detector Constraints for Atmospheric Sam- 3107 ples

3108 The choice of applying the near detector constraints to the low-energy atmo-
3109 spheric samples was introduced in subsection 6.4.3. This subsection illustrates the
3110 effect of removing the ND constraint on the sensitivity of the atmospheric samples
3111 to the oscillation parameters. To do this, the fit presented in subsection 8.2.1 has
3112 been compared to another fit where the constraints from the near detector have
3113 not been included. This is the only case where the near detector constraints are
3114 neglected throughout this chapter. For both fits, the Asimov data was generated
3115 assuming the ‘AsimovA’ oscillation parameter set defined in Table 2.2 and the
3116 post-BANFF systematic parameter tune.

3117 The change in sensitivity on δ_{CP} is given in Figure 8.15. The reactor constraint
3118 is not applied in either of the fits within this comparison. The fit which includes
3119 the near detector constraint is slightly more peaked at the known oscillation
3120 parameter value. The width of the 1σ credible intervals are approximately the
3121 same (identical to within a bin width) and the same conclusion holds for the
3122 higher credible intervals. The change in sensitivity to other oscillation parameters
3123 has been studied and no significant discrepancies were found. As expected, the
3124 sensitivities are statistics dominated such that the exact choice of constraint does
3125 not significantly affect the physics conclusions one would make from this analysis.

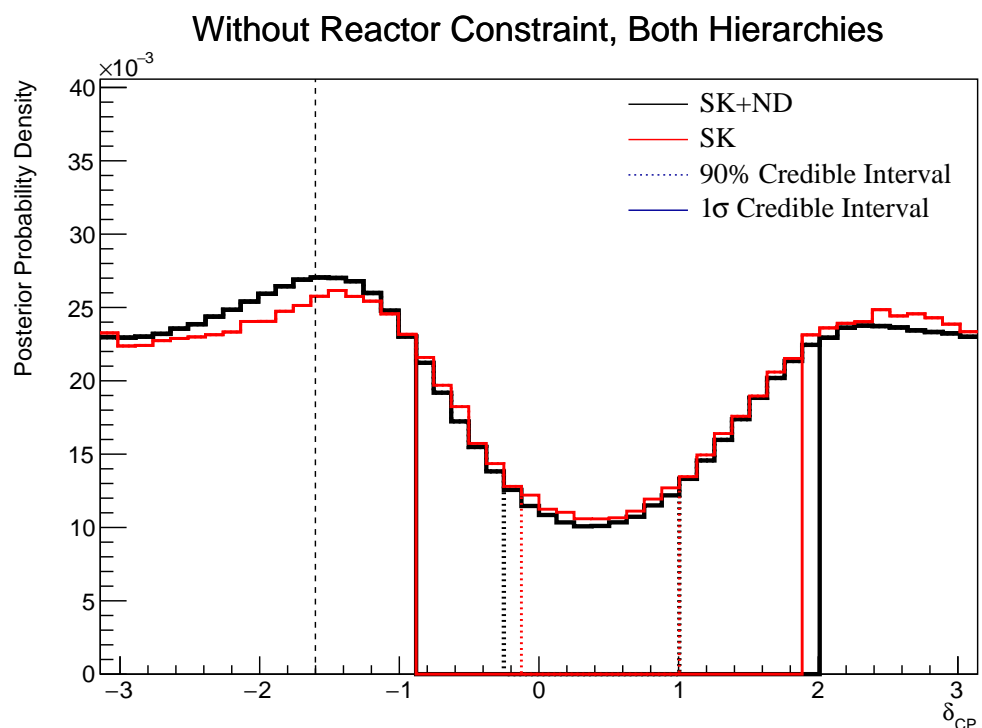


Figure 8.15: The one-dimensional posterior probability density distribution in δ_{CP} compared between the SK atmospheric-only fit where the near detector constraint is (Black) and is not (Red) applied. The distributions are marginalised over both hierarchies.

3126 8.2.4 Atmospheric and Beam Sensitivity without Reactor Con- 3127 straint

3128 This section presents the sensitivities of the simultaneous beam and atmospheric
 3129 analysis where the reactor constraint is not applied. Similar to the previous
 3130 studies, the Asimov data is built assuming the post-BANFF systematic tune and
 3131 Asimov A oscillation parameters defined in Table 2.2. This fit uses all 18 near
 3132 detector beam samples, 5 far detector beam samples, and 18 atmospheric samples.

Without Reactor Constraint, Both Hierarchies

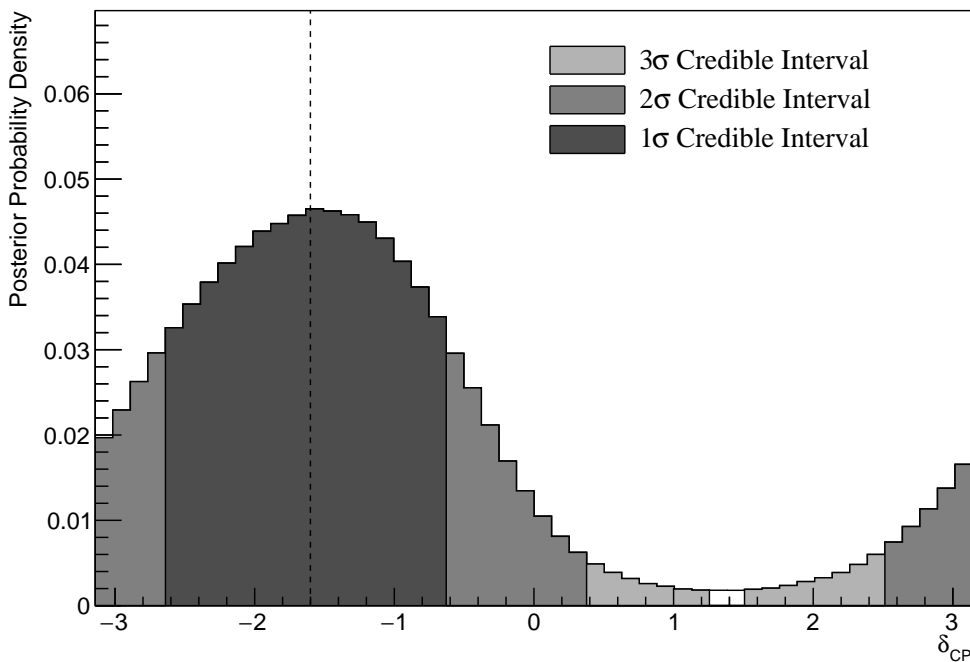


Figure 8.16: The one-dimensional posterior probability density distribution in δ_{CP} , marginalised over both hierarchies, from the joint beam-atmospheric fit. The reactor constraint is not applied.

3133 The sensitivity to δ_{CP} , marginalised over both hierarchies, is given in Fig-
 3134 ure 8.16. The credible intervals and highest posterior distribution for each
 3135 oscillation parameter is given in Table 8.5. The highest posterior probability
 3136 density is $\delta_{CP} = -1.57 \pm 0.07$ and is compatible with the known value of
 3137 $\delta_{CP} = -1.601$. The CP-conserving values of $\delta_{CP} = 0, \pm\pi$ are disfavoured at
 3138 1σ credible interval. There is also a region around $\delta_{CP} = 1.4$ which is disfavoured
 3139 at more than 3σ . Whilst these conclusions can only be made at this particular

³¹⁴⁰ Asimov point, it does show that if the true value of δ_{CP} were CP-violating,
³¹⁴¹ this joint analysis would be able to disfavour CP conserving values at over 1σ
³¹⁴² without any external constraints.

Parameter	Interval	HPD
δ_{CP} , (BH)	$[-2.64, -0.63]$	-1.57 ± 0.07
δ_{CP} , (NH)	$[-2.76, -0.63]$	-1.45 ± 0.07
δ_{CP} , (IH)	$[-2.39, -0.88]$	-1.57 ± 0.07
Δm_{32}^2 (BH) [$\times 10^{-3}\text{eV}^2$]	[2.45, 2.58]	2.49 ± 0.01
Δm_{32}^2 (NH) [$\times 10^{-3}\text{eV}^2$]	[2.47, 2.56]	2.51 ± 0.01
Δm_{32}^2 (IH) [$\times 10^{-3}\text{eV}^2$]	$[-2.60, -2.51]$	-2.55 ± 0.01
$\sin^2(\theta_{23})$ (BH)	[0.480, 0.545]	0.509 ± 0.003
$\sin^2(\theta_{23})$ (NH)	[0.480, 0.545]	0.509 ± 0.003
$\sin^2(\theta_{23})$ (IH)	[0.480, 0.545]	0.521 ± 0.003

Table 8.5: The position of the highest posterior probability density (HPD) and width of the 1σ credible interval for the joint beam-atmospheric fit. The reactor constraint is not applied. The values are presented by which hierarchy hypothesis is assumed: marginalised over both hierarchies (BH), normal hierarchy only (NH), and inverted hierarchy only (IH).

³¹⁴³ The sensitivity to Δm_{32}^2 is illustrated in Figure 8.17. Notably, the 1σ credible
³¹⁴⁴ interval is entirely contained within the NH region, as further evidenced by
³¹⁴⁵ Table 8.5. This illustrates good sensitivity to the mass hierarchy as it is correctly
³¹⁴⁶ selecting the correct hypothesis. This is reflected in the 1σ credible intervals being
³¹⁴⁷ approximately the same when they are constructed considering both hierarchies
³¹⁴⁸ and when considering only the NH region. The NH distribution favours this
³¹⁴⁹ region surrounding the known Asimov point, $\Delta m_{32}^2 = 2.509 \times 10^{-3}\text{eV}^2$, where the
³¹⁵⁰ highest posterior probability density is at $\Delta m_{32}^2 = (2.51 \pm 0.01) \times 10^{-3}\text{eV}^2$.

³¹⁵¹ The fraction of steps in each of the mass hierarchy regions and octants of
³¹⁵² $\sin^2(\theta_{23})$ is given in Table 8.6. The Bayes factors are determined to be $B(\text{NH}/\text{IH}) =$
³¹⁵³ 3.67 and $B(\text{UO}/\text{LO}) = 1.74$. Jeffrey's scale states that this value of the mass
³¹⁵⁴ hierarchy Bayes factor illustrates substantial evidence for the NH hypothesis.

3155 This corresponds to the correct hypothesis given the known oscillation parameters
 3156 and is a stronger statement than the atmospheric-only analysis can provide. It is
 3157 important to note that this substantial preference requires no external constraints.
 3158 The Bayes factor for octant determination represents a weak preference for the
 3159 upper octant therefore selecting the correct octant hypothesis.

	LO ($\sin^2 \theta_{23} < 0.5$)	UO ($\sin^2 \theta_{23} > 0.5$)	Sum
NH ($\Delta m_{32}^2 > 0$)	0.29	0.50	0.79
IH ($\Delta m_{32}^2 < 0$)	0.08	0.13	0.21
Sum	0.37	0.63	1.00

Table 8.6: The distribution of steps in a joint beam-atmospheric fit, presented as the fraction of steps in the upper (UO) and lower (LO) octants and the normal (NH) and inverted (IH) hierarchies. The reactor constraint is not applied. The Bayes factors are calculated as $B(\text{NH}/\text{IH}) = 3.67$ and $B(\text{UO}/\text{LO}) = 1.74$.

Without Reactor Constraint, Both Hierarchies

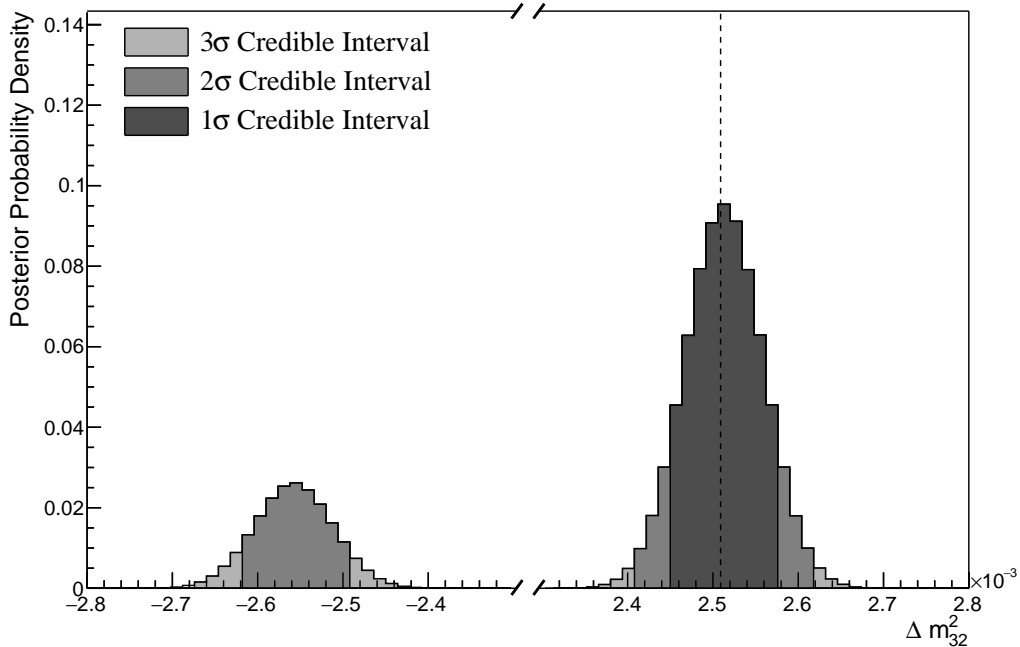


Figure 8.17: The one-dimensional posterior probability density distribution in Δm_{32}^2 , marginalised over both hierarchies, from the joint beam-atmospheric fit. The reactor constraint is not applied.

3160 The sensitivity to $\sin^2(\theta_{23})$ is presented in Figure 8.18. There is a clear

3161 preference for the upper octant but the peak of the distribution is relatively
 3162 flat. It peaks at $\sin^2(\theta_{23}) = 0.509 \pm 0.003$ which is in the region of the known
 3163 value of $\sin^2(\theta_{23}) = 0.528$. The difference in the highest posterior distribution
 3164 and the width of the credible interval is relatively unchanged when consid-
 3165 ering different hierarchy hypotheses showing no strong correlation between
 3166 $\sin^2(\theta_{23})$ and $|\Delta m_{32}^2|$.

Without Reactor Constraint, Both Hierarchies

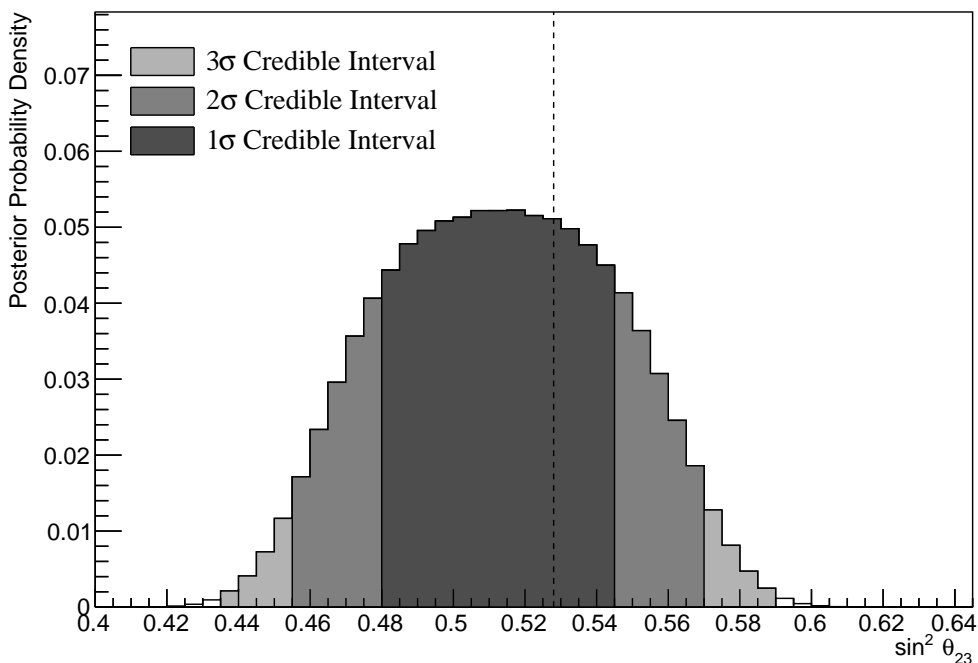


Figure 8.18: The one-dimensional posterior probability density distribution in $\sin^2(\theta_{23})$, marginalised over both hierarchies, from the joint beam-atmospheric fit. The reactor constraint is not applied.

3167 The sensitivity presented as a function of the appearance parameters ($\sin^2(\theta_{13}) -$
 3168 δ_{CP}) is given in Figure 8.19. As expected, the contours follow the likelihood
 3169 shape given in Figure 8.2, where the 2σ credible intervals have a closed con-
 3170 tour excluding the region around $\delta_{CP} \sim 1.2$. The width of the 3σ credible
 3171 interval in $\sin^2(\theta_{13})$ is dependent upon the value of δ_{CP} . Close to the Asimov
 3172 point, $\delta_{CP} = -1.601$, the width of the 3σ credible interval approximately spans
 3173 $\sin^2(\theta_{13}) = [0.013, 0.04]$. This is reduced to a region of $\sin^2(\theta_{13}) = [0.023, 0.042]$
 3174 at the most disfavoured value of δ_{CP} . The 1σ credible interval is consistent with

the known oscillation parameter. Application of the reactor constraint would be expected to decrease the width of the 1σ credible intervals in δ_{CP} due to the triangular shape of the posterior probability.

The sensitivity in terms of the disappearance parameters, $\sin^2(\theta_{23}) - \Delta m_{32}^2$, is given in Figure 8.20. The area contained within the IH contours is significantly smaller than the area within the NH contours. The IH credible intervals are also notably tighter in the $\sin^2(\theta_{23})$ dimension. No significant correlation is observed between $\sin^2(\theta_{23})$ and $|\Delta m_{32}^2|$.

Without Reactor Constraint, Both Hierarchies

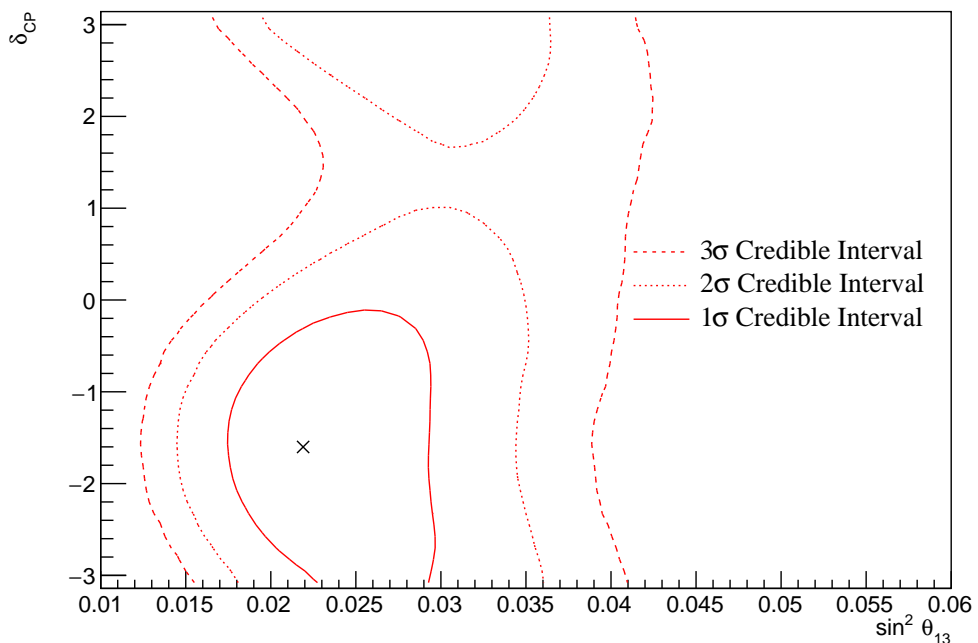


Figure 8.19: The two-dimensional posterior probability density distribution in $\delta_{CP} - \sin^2(\theta_{13})$, marginalised over both hierarchies, from the joint beam-atmospheric fit. The reactor constraint is not applied.

The two-dimensional posterior distribution for each permutation of the oscillation parameters of interest is given in Figure 8.21. The most notable observation is that the $\sin^2(\theta_{13})$ and $\sin^2(\theta_{23})$ are anti-correlated. If the value of $\sin^2(\theta_{13})$ was constrained closer to the known oscillation parameter value, the preferred value of $\sin^2(\theta_{23})$ would increase. This would move the highest posterior probability closer in line with the known value and could lead to an increase in the preference for the UO hypothesis.

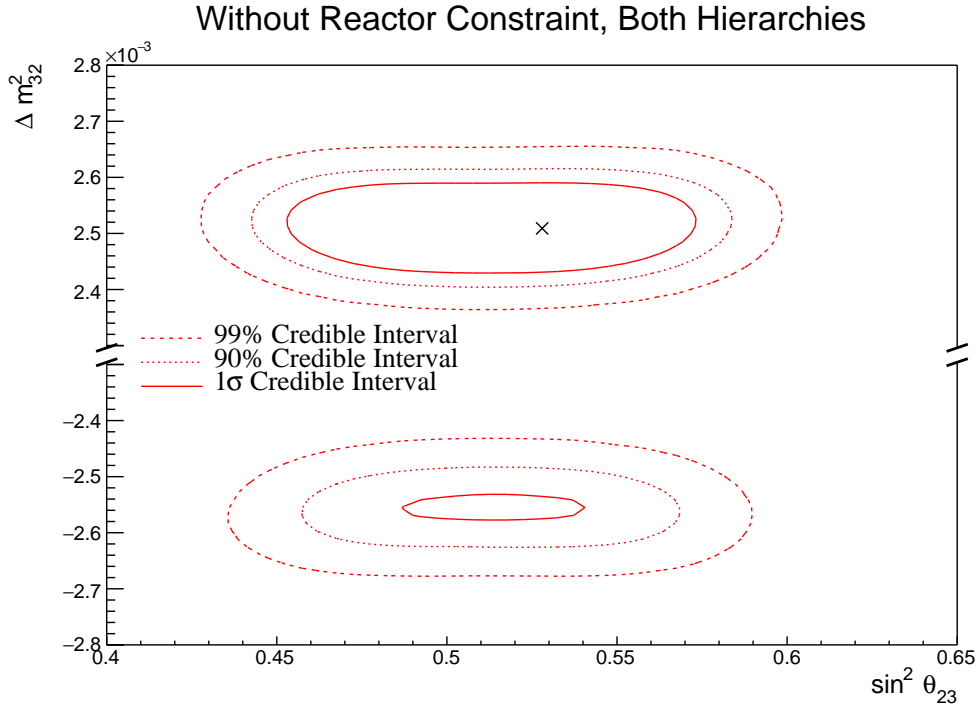


Figure 8.20: The two-dimensional posterior probability density distribution in Δm_{32}^2 – $\sin^2(\theta_{23})$, marginalised over both hierarchies, from the joint beam-atmospheric fit. The reactor constraint is not applied.

Furthermore, the δ_{CP} and $|\Delta m_{32}^2|$ oscillation parameters are anti-correlated, such that higher values of $|\Delta m_{32}^2|$ prefer lower values of δ_{CP} . Whilst this is an interesting result on its own, the width of the Δm_{32}^2 contours also depend on $\sin^2(\theta_{13})$. This introduces another correlation effect that could modify the sensitivity to δ_{CP} once the reactor constraint is applied.

The correlation between $\sin^2(\theta_{13})$ and Δm_{32}^2 can be seen in Figure 8.22. A much larger fraction of the posterior distribution is contained in the NH for lower values of $\sin^2(\theta_{13})$. Consequently, the application of the reactor constraint would be expected to significantly increase the preference for NH.

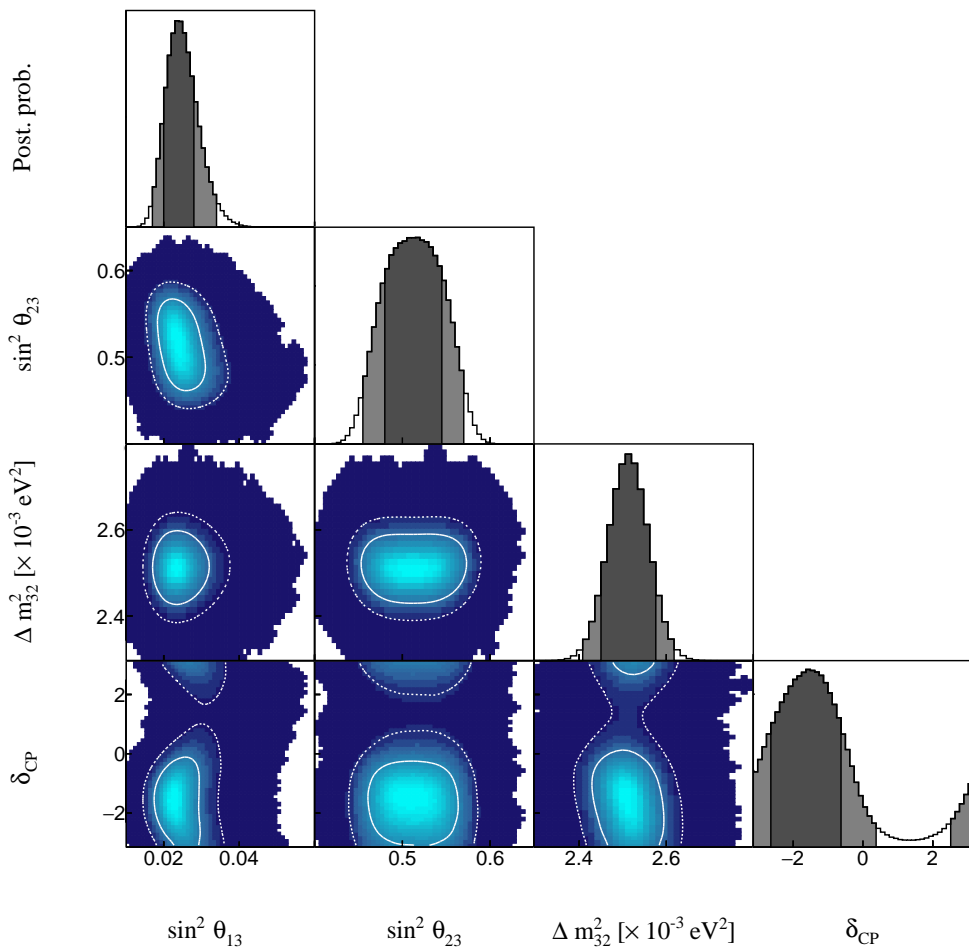


Figure 8.21: The posterior probability density distribution from the joint beam-atmospheric fit. The reactor constraint is not applied. The distribution is given for each two-dimensional permutation of the oscillation parameters of interest. The one-dimensional distribution of each parameter is also given.

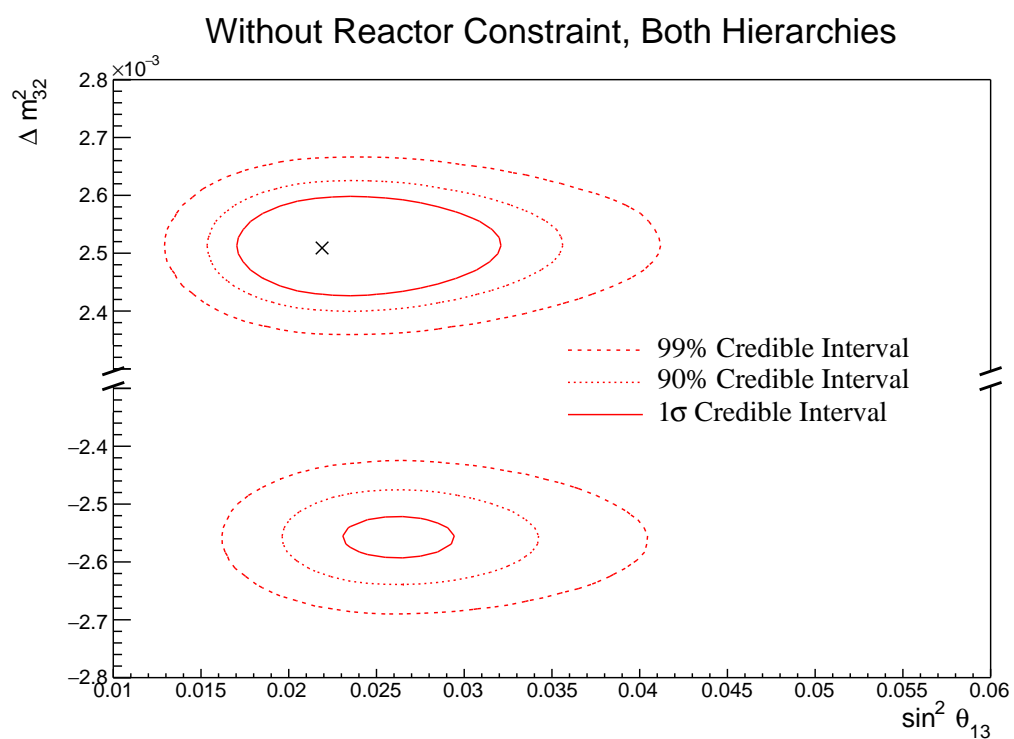


Figure 8.22: The two-dimensional posterior probability density distribution in Δm_{32}^2 – $\sin^2(\theta_{13})$, marginalised over both hierarchies, from the joint beam-atmospheric fit. The reactor constraint is not applied.

3199 8.2.5 Atmospheric and Beam Sensitivity with Reactor Constraint

3200 This section presents the sensitivities of the joint beam-atmospheric fit when
 3201 the reactor constraint is applied to $\sin^2(\theta_{13})$. As with the previous studies, the
 3202 Asimov data is made using the AsimovA oscillation parameter set defined in
 3203 Table 2.2 and the post-BANFF systematic parameter tune.

With Reactor Constraint, Both Hierarchies

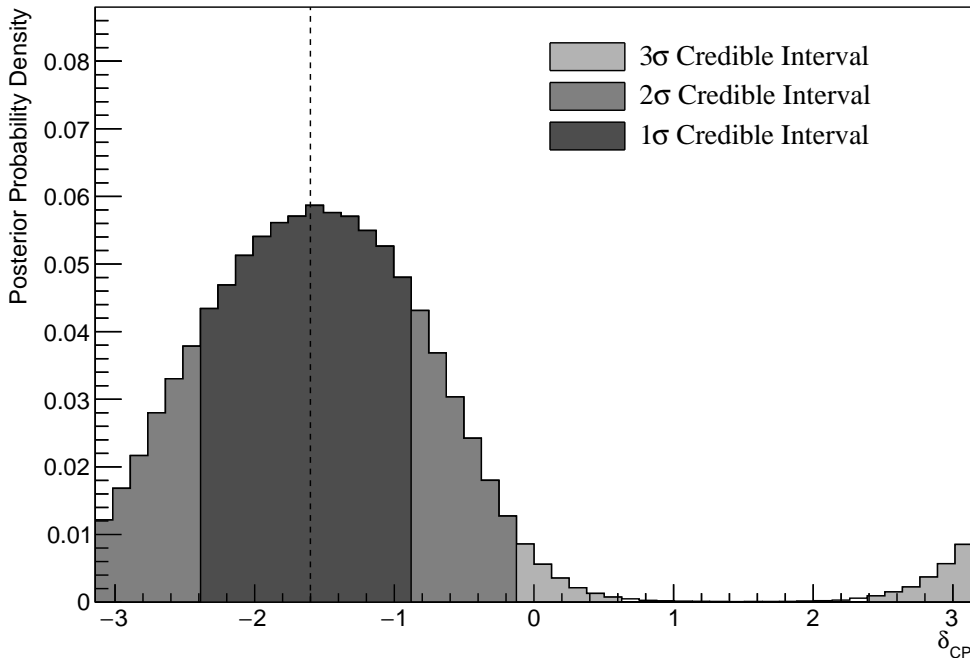


Figure 8.23: The one-dimensional posterior probability density distribution in δ_{CP} , marginalised over both hierarchies, from the joint beam-atmospheric fit where the reactor constraint is applied.

3204 Figure 8.23 illustrates the sensitivity to δ_{CP} , marginalised over both hierarchies.
 3205 The CP-conserving value of $\delta_{CP} = 0$ is disfavoured at 2σ whilst the value of $\delta_{CP} =$
 3206 $\pm\pi$ is very close to being disfavoured at 2σ . Furthermore, the 3σ credible interval
 3207 excludes the region of $\delta_{CP} = [0.63, 2.39]$, thus clearly disfavouring the region of
 3208 $\delta_{CP} = \pi/2$ at more than 3σ for this particular set of known oscillation parameters.
 3209 The width of the 1σ credible intervals and the position of the highest posterior
 3210 probability density is given in Table 8.7. The highest posterior probability density
 3211 in δ_{CP} is calculated as $\delta_{CP} = -1.57 \pm 0.07$ showing no significant biases in the
 3212 determination of the known oscillation parameters.

The effect of applying the reactor constraint for δ_{CP} in the joint beam-atmospheric fit is presented in Figure 8.24. The reactor constraint significantly improves the ability of the fit to select the known parameter value. This behaviour is evidenced by the tightening of the 1σ and 90% credible intervals and the disfavoured region, centered at $\delta_{CP} \sim \pi/2$, becoming wider when the reactor constraint is applied. This follows from the correlations shown in Figure 8.19, where a lower value of $\sin^2(\theta_{13})$ results in tighter constraints on δ_{CP} .

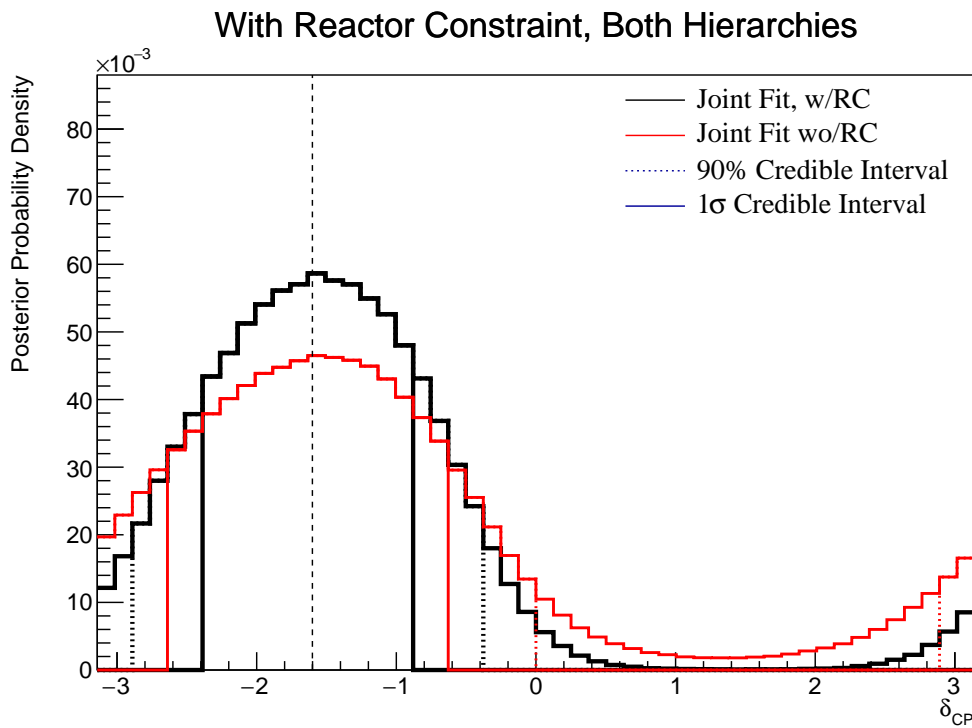


Figure 8.24: The one-dimensional posterior probability density distribution in δ_{CP} compared between the joint beam-atmospheric fit (Red) and the joint beam-atmospheric fit with the reactor constraint (Black). The distributions are marginalised over both hierarchies.

The sensitivity to $\sin^2(\theta_{23})$, marginalised over both hierarchies, is given in Figure 8.25. The highest posterior probability density is located at $\sin^2(\theta_{23}) = 0.527 \pm 0.03$ which agrees with the known value of $\sin^2(\theta_{23}) = 0.528$. The distribution clearly favours the UO with almost the entirety of the 1σ credible interval being contained in that region. Figure 8.26 highlights the sensitivity of the joint fit both with and without the reactor constraint. The fit where the

Parameter	Interval	HPD
δ_{CP} , (BH)	[-2.39, -0.88]	-1.57 ± 0.07
δ_{CP} , (NH)	[-2.39, -0.75]	-1.57 ± 0.07
δ_{CP} , (IH)	[-2.14, -1.01]	-1.57 ± 0.07
Δm_{32}^2 (BH) [$\times 10^{-3}\text{eV}^2$]	[2.45, 2.56]	2.49 ± 0.01
Δm_{32}^2 (NH) [$\times 10^{-3}\text{eV}^2$]	[2.47, 2.56]	2.51 ± 0.01
Δm_{32}^2 (IH) [$\times 10^{-3}\text{eV}^2$]	[-2.60, -2.51]	-2.55 ± 0.01
$\sin^2(\theta_{23})$ (BH)	[0.490, 0.555]	0.527 ± 0.03
$\sin^2(\theta_{23})$ (NH)	[0.490, 0.555]	0.527 ± 0.03
$\sin^2(\theta_{23})$ (IH)	[0.500, 0.560]	0.539 ± 0.03

Table 8.7: The position of the highest posterior probability density (HPD) and width of the 1σ credible interval for the joint beam-atmospheric fit where the reactor constraint is applied. The values are presented by which hierarchy hypothesis is assumed: marginalised over both hierarchies (BH), normal hierarchy only (NH), and inverted hierarchy only (IH).

reactor constraint is applied selects the known value much better. This is a result of the marginalisation effects between the $\sin^2(\theta_{13})$ and $\sin^2(\theta_{23})$ parameters, as observed in Figure 8.21.

The fraction of steps from the joint fit, after the reactor constraint is applied, is given in Table 8.8 and split by the two hierarchy and two octant hypotheses. The reactor constraint significantly reduces the fraction of steps that are contained within the IH-LO region from 0.08 to 0.03, whilst significantly increasing the fraction of steps within the NH-UO region from 0.50 to 0.62. The application of the reactor constraint increases the Bayes factor from $B(\text{NH}/\text{IH}) = 3.67$ to $B(\text{NH}/\text{IH}) = 6.47$. There is a very clear preference for the NH, with the Jeffreys scale stating a substantial preference for both fits. The Bayes factor for UO preference is calculated as $B(\text{UO}/\text{LO}) = 2.64$. Whilst still a weak preference, this is certainly a stronger statement than the sensitivity when the reactor constraint is not applied.

The sensitivity of the joint beam-atmospheric fit to Δm_{32}^2 , with the reactor constraint applied, is presented in Figure 8.27. The 1σ credible interval is

With Reactor Constraint, Both Hierarchies

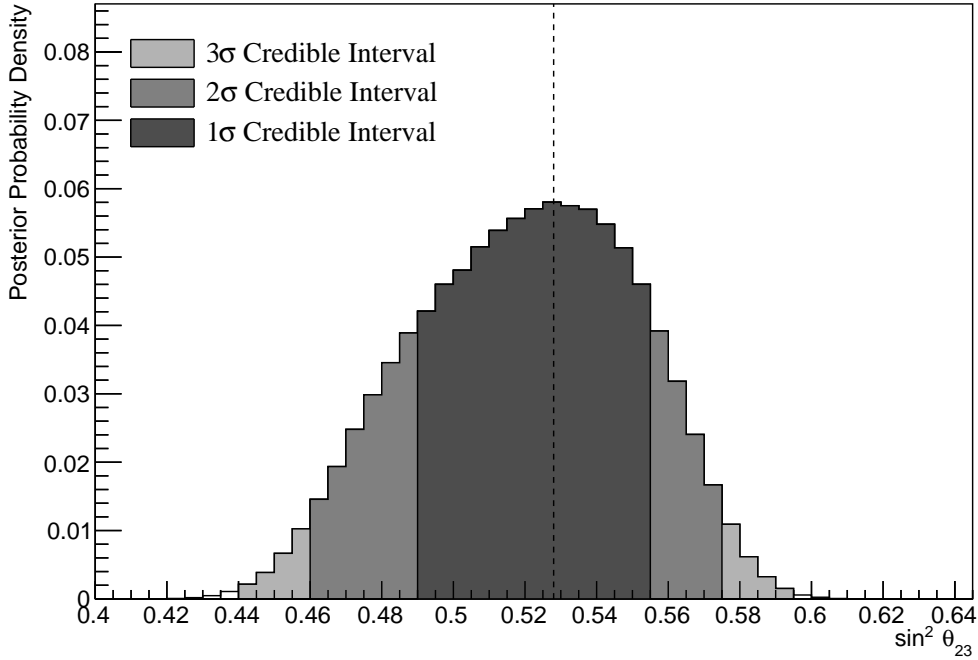


Figure 8.25: The one-dimensional posterior probability density distribution in $\sin^2(\theta_{23})$, marginalised over both hierarchies, from the joint beam-atmospheric fit where the reactor constraint is applied.

	LO ($\sin^2 \theta_{23} < 0.5$)	UO ($\sin^2 \theta_{23} > 0.5$)	Sum
NH ($\Delta m_{32}^2 > 0$)	0.24	0.62	0.87
IH ($\Delta m_{32}^2 < 0$)	0.03	0.10	0.13
Sum	0.27	0.73	1.00

Table 8.8: The distribution of steps in a joint beam-atmospheric with the reactor constraint fit applied, presented as the fraction of steps in the upper (UO) and lower (LO) octants and the normal (NH) and inverted (IH) hierarchies. The Bayes factors are calculated as $B(\text{NH}/\text{IH}) = 6.47$ and $B(\text{UO}/\text{LO}) = 2.64$.

3242 entirely contained within the NH region and the position of the highest posterior
 3243 probability density is given as $(2.49 \pm 0.01) \times 10^{-3} \text{ eV}^2$. This illustrates no bias
 3244 between the fit results and the known oscillation parameters. The application
 3245 of the reactor constraint does not significantly move the position or width of
 3246 the credible intervals.

3247 The sensitivity to the appearance parameters $(\sin^2(\theta_{13}) - \delta_{CP})$ is given in
 3248 Figure 8.28. The distribution is mostly uncorrelated between the two parameters

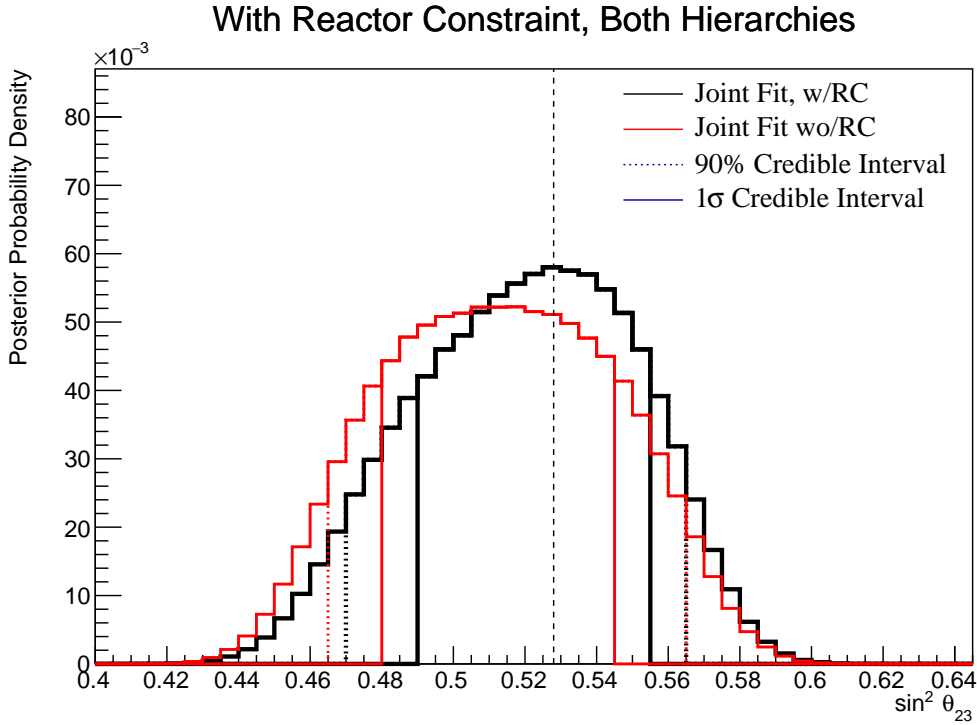


Figure 8.26: The one-dimensional posterior probability density distribution in $\sin^2(\theta_{23})$ compared between the joint beam-atmospheric fit (Red) and the joint beam-atmospheric fit with the reactor constraint (Black). The distributions are marginalised over both hierarchies.

and is centered at the known oscillation parameters. The 1σ credible interval excludes $\delta_{CP} = 0$ and $\delta_{CP} = \pm\pi$. Furthermore, the 3σ credible intervals exclude the region of $\delta_{CP} = \pi/2$.

The sensitivity to the disappearance parameters ($\sin^2(\theta_{23}) - \Delta m_{32}^2$) is illustrated in Figure 8.29. The 1σ credible interval is entirely contained within the NH region reflecting the same results as the one-dimensional marginalised results in Figure 8.27. Both the NH and IH regions favour the UO, with a visually similar preference in both hierarchies. The width of the 1σ contour, in Δm_{32}^2 , does not significantly depend upon the value or octant of $\sin^2(\theta_{23})$. This shows that there are no strong correlations between these two parameters.

Figure 8.30 illustrates the posterior distribution for each permutation of two oscillation parameters of interest. The application of the reactor constraint significantly reduces the correlations previously seen in Figure 8.21.

With Reactor Constraint, Both Hierarchies

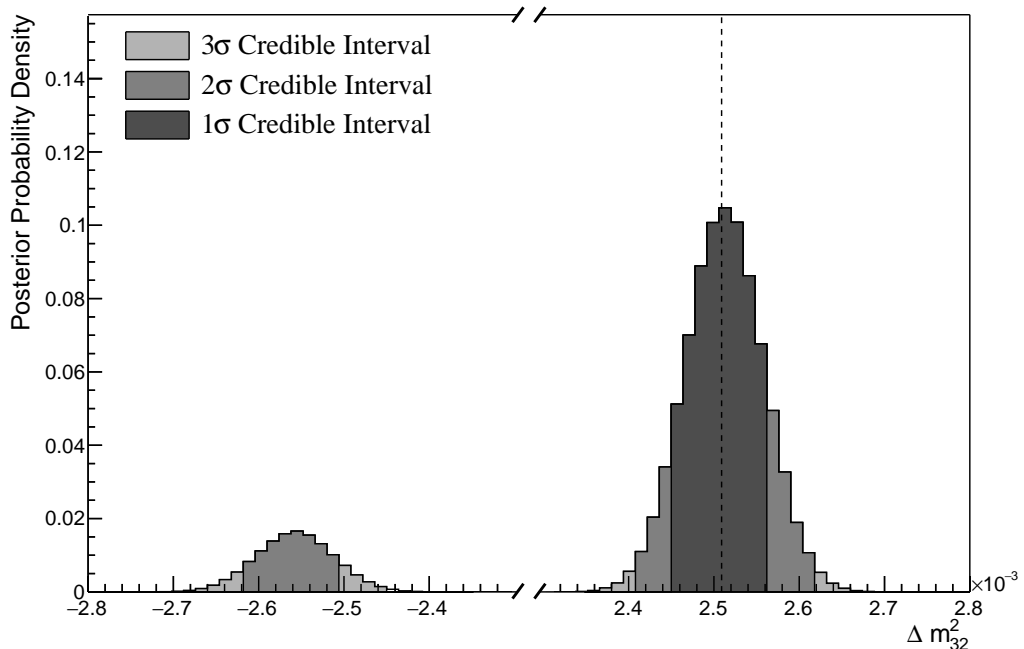


Figure 8.27: The one-dimensional posterior probability density distribution in Δm_{32}^2 , marginalised over both hierarchies, from the joint beam-atmospheric fit where the reactor constraint is applied.

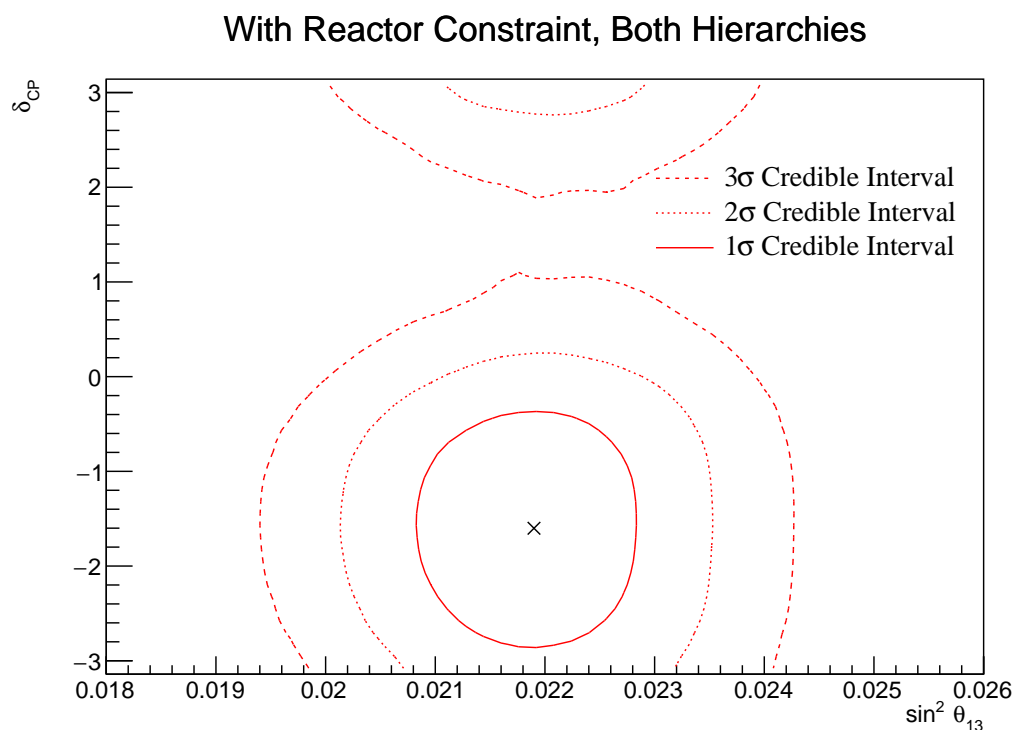


Figure 8.28: The two-dimensional posterior probability density distribution in $\delta_{CP} - \sin^2(\theta_{13})$, marginalised over both hierarchies, from the joint beam-atmospheric fit where the reactor constraint is applied.

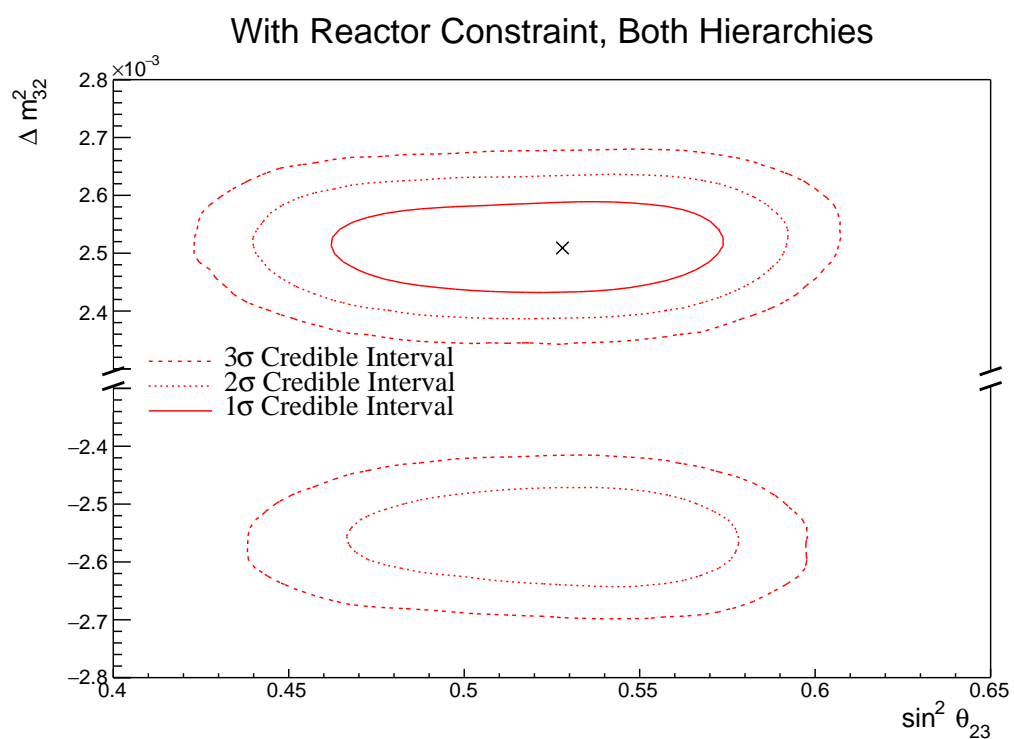


Figure 8.29: The two-dimensional posterior probability density distribution in $\Delta m_{32}^2 - \sin^2(\theta_{23})$, marginalised over both hierarchies, from the joint beam-atmospheric fit where the reactor constraint is applied.

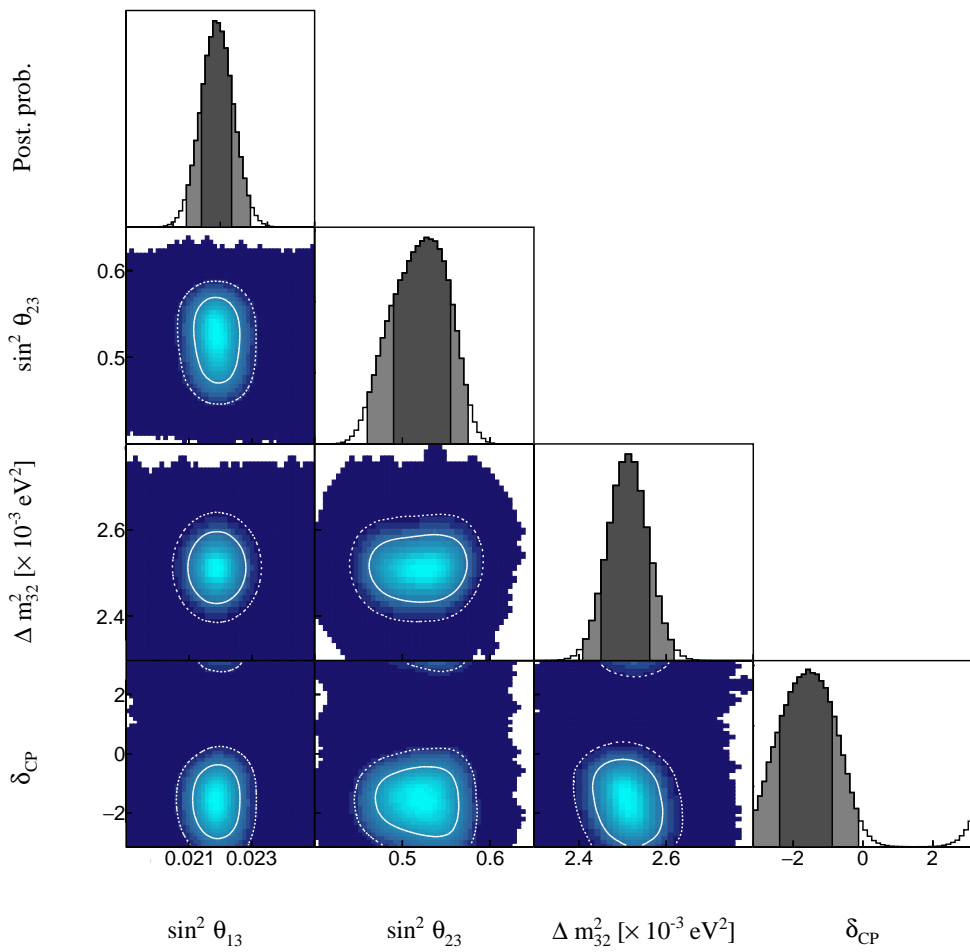


Figure 8.30: The posterior probability density distribution from the joint beam-atmospheric fit where the reactor constraint is applied. The distribution is given for each two-dimensional permutation of the oscillation parameters of interest. The one-dimensional distribution of each parameter is also given.

3262 8.2.6 Comparison to Latest T2K Sensitivities without Reactor 3263 Constraint

3264 The benefits of the joint beam-atmospheric analysis can be determined by compar-
 3265 ing the sensitivities to the beam-only analysis presented in [72, 214]. This section
 3266 presents those comparisons for sensitivities built using the Asimov A oscillation
 3267 parameters defined in Table 2.2 and the post-BANFF systematic tune. The reactor
 3268 constraint is not applied within either of the fits used in these comparisons.

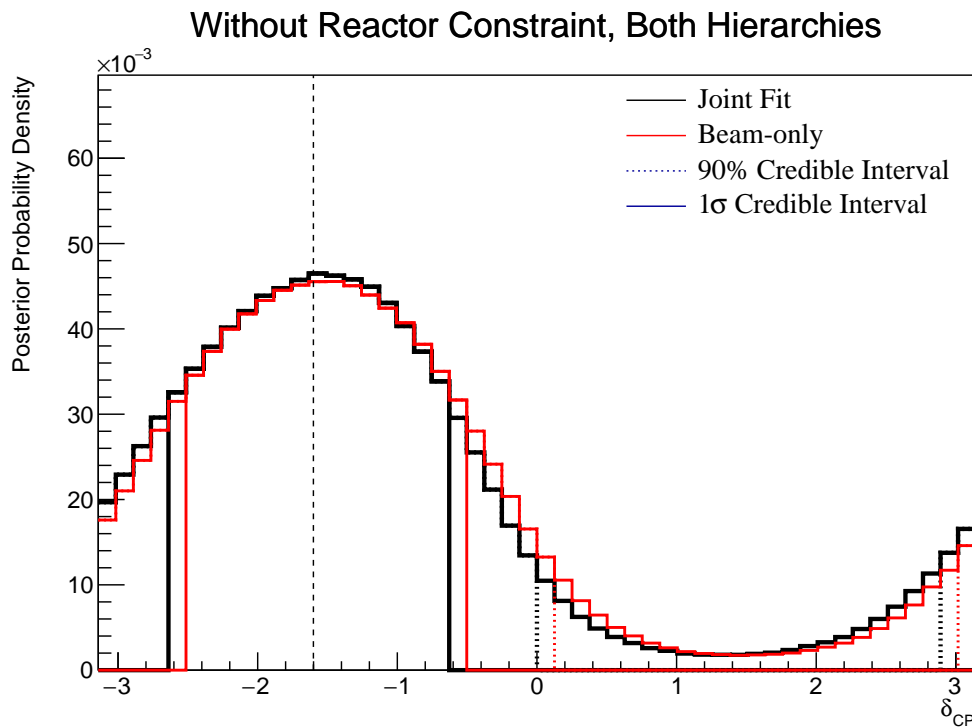


Figure 8.31: The one-dimensional posterior probability density distribution in δ_{CP} compared between the joint beam-atmospheric fit (Black) and the latest T2K sensitivities (Red) [72, 214]. The reactor constraint is not applied in either fit. The distributions are marginalised over both hierarchies.

3269 The sensitivity, marginalised over both hierarchies, to δ_{CP} from the joint beam-
 3270 atmospheric and beam-only fits is presented in Figure 8.31. As expected from the
 3271 likelihood scans (Figure 8.4), the sensitivity to δ_{CP} is not significantly increased.
 3272 This is because the known oscillation parameter value lies at the position where
 3273 the beam samples dominate the sensitivity compared to the SK samples.

The sensitivity to Δm_{32}^2 is compared between the joint beam-atmospheric fit and beam-only fit in Figure 8.32. The 1σ credible interval of the joint beam-atmospheric fit is entirely contained within the NH region. This shows the significant increase in the ability of the fit to determine the correct mass hierarchy, compared to the beam-only analysis. This is further evidenced by the fact that the 90% credible intervals from the joint fit are also tighter in the IH region compared to the beam-only analysis. The Bayes factor for mass hierarchy determination for the beam-only and joint beam-atmospheric fits are $B(\text{NH}/\text{IH}) = 1.91$ and $B(\text{NH}/\text{IH}) = 3.67$, respectively. According to Jeffrey's scale, the beam-only analysis represents a weak preference for the NH hypothesis whereas the joint fit returns a substantial preference for the NH hypothesis. Notably, this conclusion does not require any external constraints and clearly illustrates the benefit of the joint analysis.

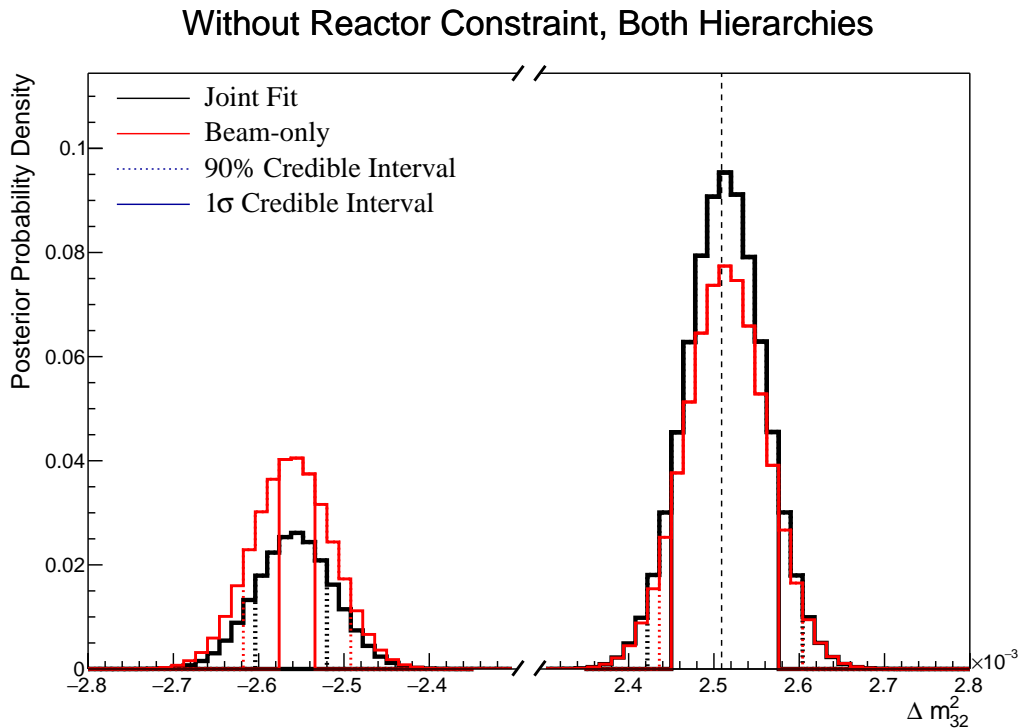


Figure 8.32: The one-dimensional posterior probability density distribution in Δm_{32}^2 compared between the joint beam-atmospheric fit (Black) and the latest T2K sensitivities (Red) [72, 214]. The reactor constraint is not applied in either fit. The distributions are marginalised over both hierarchies.

3287 The sensitivity to $\sin^2(\theta_{23})$, marginalised over both hierarchies, for both the
 3288 beam-only and joint beam-atmospheric analysis are presented in Figure 8.33. The
 3289 peak of the posterior distribution from the joint analysis is more aligned with the
 3290 known value of $\sin^2(\theta_{23}) = 0.528$ compared to the beam-only analysis. The Bayes
 3291 factors for the beam-only and joint beam-atmospheric fit are $B(\text{UO}/\text{LO}) = 1.56$
 3292 and $B(\text{UO}/\text{LO}) = 1.74$, respectively. Therefore, the joint beam-atmospheric fit
 3293 does prefer the UO more strongly than the beam-only analysis, albeit slightly.

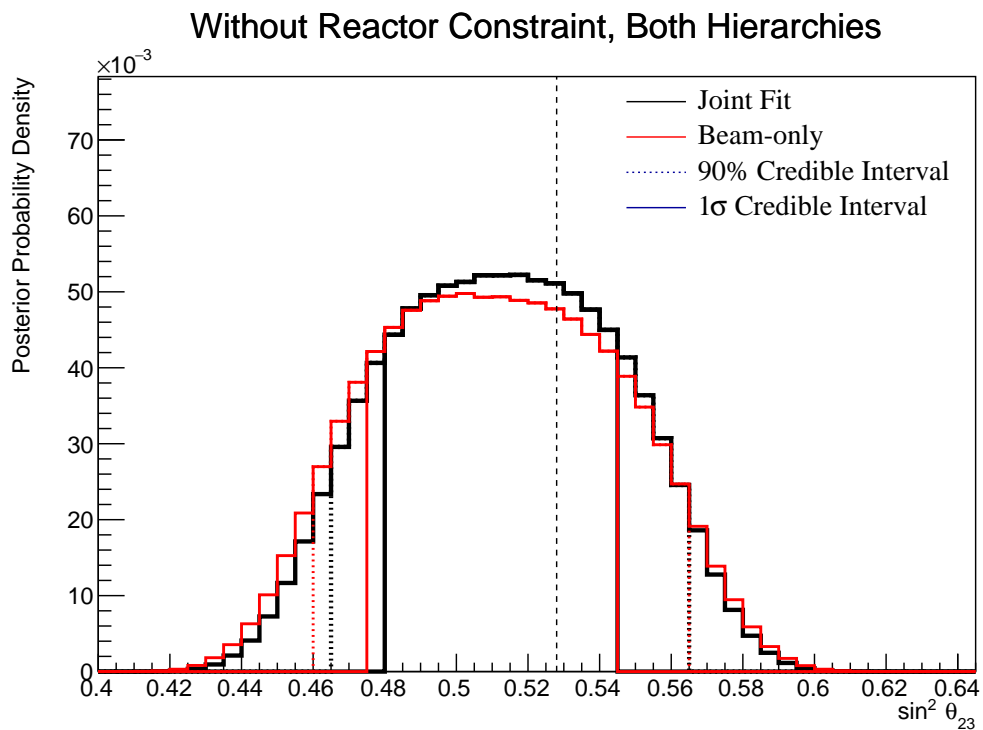


Figure 8.33: The one-dimensional posterior probability density distribution in $\sin^2(\theta_{23})$ compared between the joint beam-atmospheric fit (Black) and the latest T2K sensitivities (Red) [72, 214]. The reactor constraint is not applied in either fit. The distributions are marginalised over both hierarchies.

3294 Whilst the beam-only and joint beam-atmospheric fits have similar sensi-
 3295 tivity to δ_{CP} and $\sin^2(\theta_{23})$ when projected in one-dimension, the benefit of the
 3296 joint analysis becomes more obvious when the sensitivities are presented in
 3297 two-dimensions. The sensitivity of the two fits to the appearance parameters
 3298 ($\delta_{CP} - \sin^2(\theta_{13})$) is illustrated in Figure 8.34. The width of the 99% joint fit
 3299 credible interval in $\sin^2(\theta_{13})$ is squeezed in the region of $\delta_{CP} \sim 0$ compared to

the beam-only analysis. This is the same behaviour that is seen in the appearance likelihood scans presented in Figure 8.2. The 1σ and 90% also exhibit slightly tighter constraints on δ_{CP} . This is most prevalent in the region of $\delta_{CP} \sim 0$ and $\sin^2(\theta_{13}) \sim 0.03$. Whilst the atmospheric samples do not have significant sensitivity to $\sin^2(\theta_{13})$ (as shown in Figure 8.1), they aid in breaking the degeneracy between the oscillation parameters allowing for tighter constraints.

The sensitivity to the disappearance parameters $\sin^2(\theta_{23}) - \Delta m_{32}^2$ is presented in Figure 8.35 for both the beam-only and joint beam-atmospheric fits. Whilst the one-dimensional sensitivity comparisons considered so far show the improvements of the joint fit, the two-dimensional projection really shows the benefit of adding the atmospheric samples to the beam samples. The area contained within the IH credible intervals is drastically reduced in the joint fit. This follows from the better determination of the mass hierarchy seen in the Bayes factor comparisons. Even in the NH region, the widths of the credible intervals in $\sin^2(\theta_{23})$ decreases, albeit to a smaller extent.

The comparison in sensitivity to $\delta_{CP} - \Delta m_{32}^2$ is illustrated in Figure 8.36. The contours from the joint beam-atmospheric fit are much smaller in the IH region as compared to the beam-only analysis. This culminates in a region around $\delta_{CP} \sim \pi/2$ in the H region which is excluded at 3σ . This behaviour is not present within the beam-only analysis. Consistent with the previous observations, the area contained within the IH credible intervals is significantly reduced in comparison to the beam-only analysis.

The sensitivity to Δm_{32}^2 , as a function of $\sin^2(\theta_{13})$, is presented in Figure 8.37. Similar to previous observations, the Δm_{32}^2 contours within IH region of the joint fit are much smaller than the beam-only analysis. Notably, the joint fit IH 1σ credible intervals exclude the region around the reactor constraint. This suggests that the application of the reactor constraint would further increase the preference for NH in the joint fit compared to its effect on the beam-only analysis.

The beam-only and joint beam-atmospheric fits have a slightly different contour shape between the $\sin^2(\theta_{13})$ and $\sin^2(\theta_{23})$ parameters, as illustrated

Without Reactor Constraint, Both Hierarchies

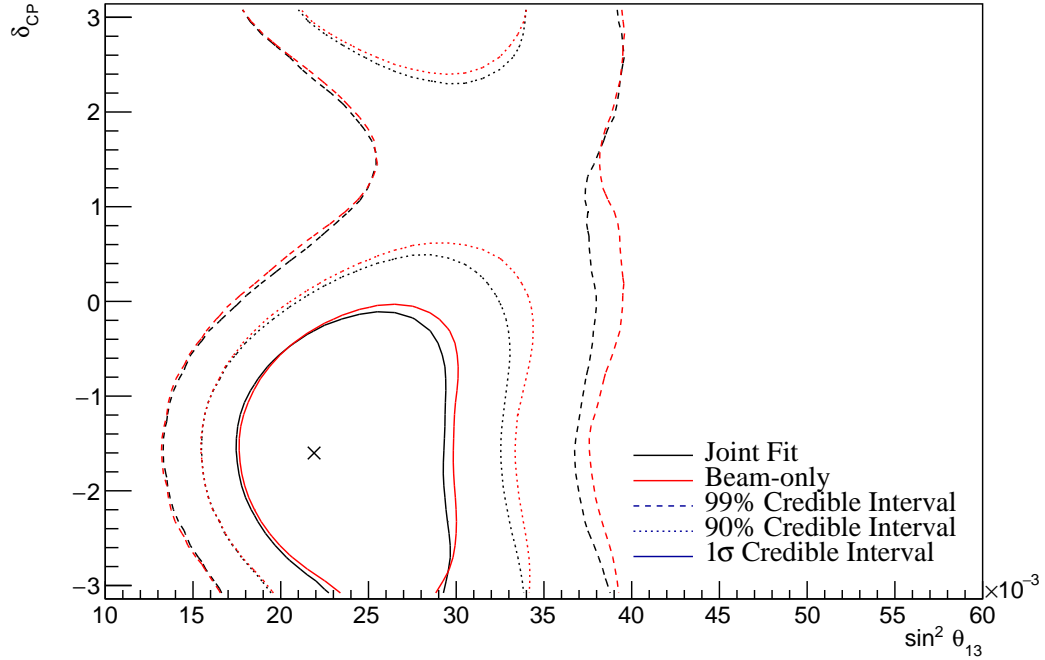


Figure 8.34: The two-dimensional posterior probability density distribution in δ_{CP} – $\sin^2(\theta_{13})$ compared between the joint beam-atmospheric fit (Black) and the latest T2K sensitivities (Red) [72, 214]. The reactor constraint is not applied in either fit. The distributions are marginalised over both hierarchies.

3330 by Figure 8.38. The joint analysis disfavours the wrong octant hypothesis more
 3331 strongly in the region of high $\sin^2(\theta_{13})$. This change in correlation means that the
 3332 application of the reactor constraint could affect the two analyses differently.

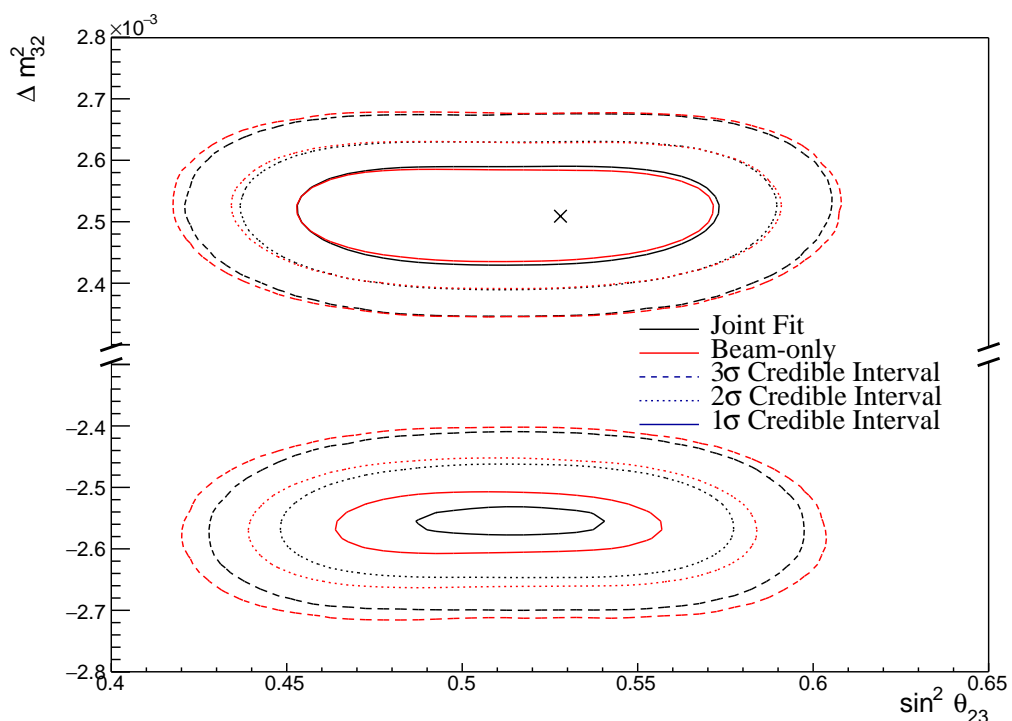


Figure 8.35: The two-dimensional posterior probability density distribution in Δm_{32}^2 – $\sin^2(\theta_{23})$ compared between the joint beam-atmospheric fit (Black) and the latest T2K sensitivities (Red) [72, 214]. The reactor constraint is not applied in either fit. The distributions are marginalised over both hierarchies.

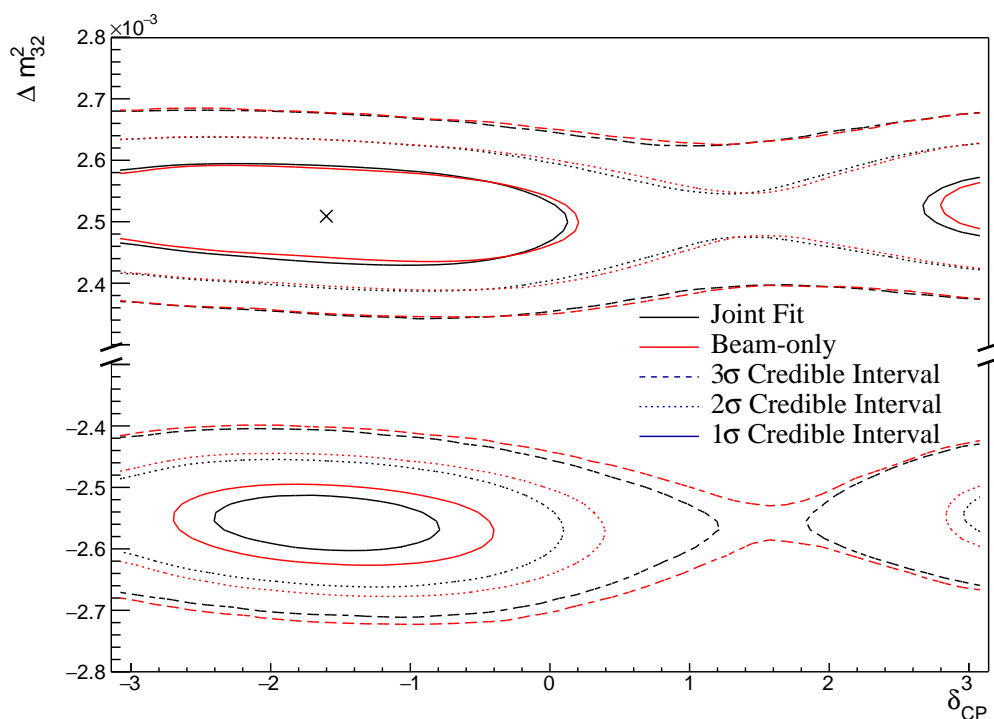


Figure 8.36: The two-dimensional posterior probability density distribution in Δm_{32}^2 – δ_{CP}^3 compared between the joint beam-atmospheric fit (Black) and the latest T2K sensitivities (Red) [72, 214]. The reactor constraint is not applied in either fit. The distributions are marginalised over both hierarchies.

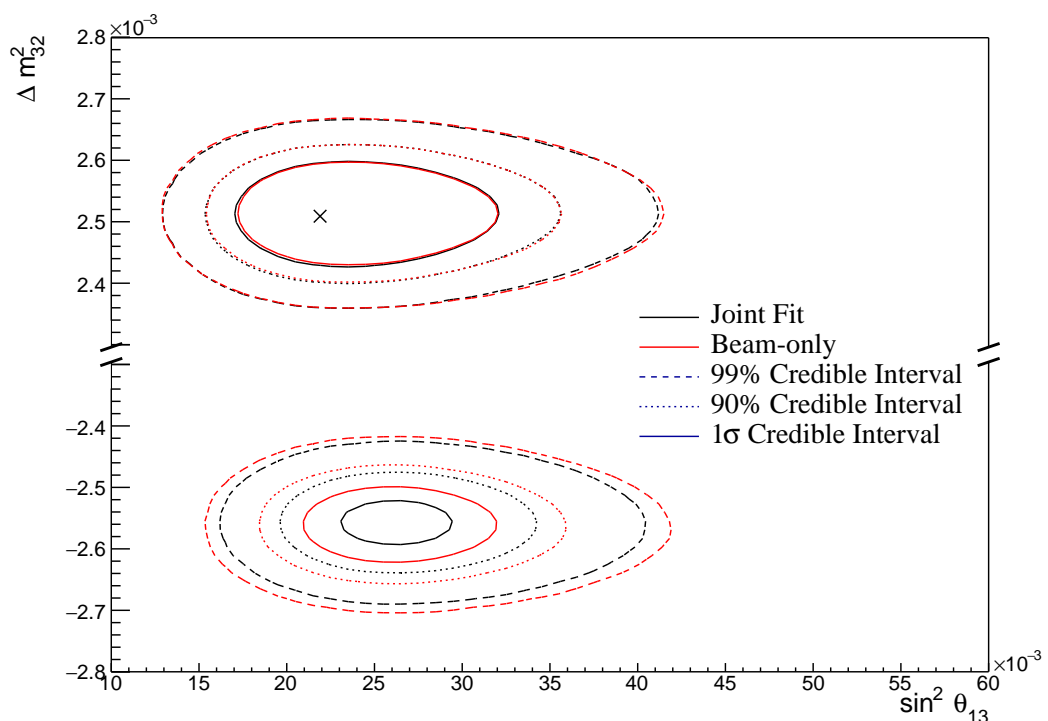


Figure 8.37: The two-dimensional posterior probability density distribution in Δm_{32}^2 – $\sin^2(\theta_{23})$ compared between the joint beam-atmospheric fit (Black) and the latest T2K sensitivities (Red) [72, 214]. The reactor constraint is not applied in either fit. The distributions are marginalised over both hierarchies.

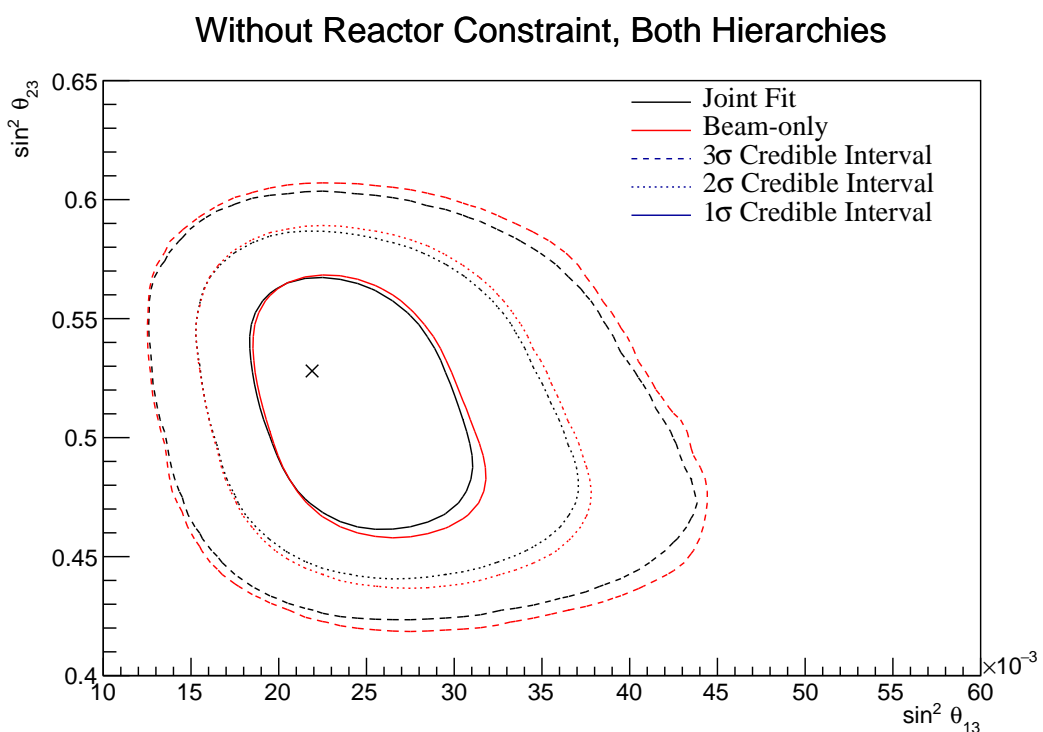


Figure 8.38: The two-dimensional posterior probability density distribution in $\sin^2(\theta_{23})$ – $\sin^2(\theta_{13})$ compared between the joint beam-atmospheric fit (Black) and the latest T2K sensitivities (Red) [72, 214]. The reactor constraint is not applied in either fit. The distributions are marginalised over both hierarchies.

3333 8.2.7 Comparison to Latest T2K Sensitivities with Reactor Con- 3334 straint

3335 This section illustrates the comparison between the joint beam-atmospheric and
 3336 beam-only fits when the reactor constraint is applied. As shown in Figure 8.37,
 3337 the application of the reactor constraint is expected to significantly increase
 3338 the joint fit's preference for the NH hypothesis, compared to the beam-only
 3339 analysis. Figure 8.39 illustrates the sensitivities of the two fits to the disappearance
 3340 parameters ($\sin^2(\theta_{23}) - \Delta m_{32}^2$). This plot further illustrates the benefit of the joint
 3341 beam-atmospheric analysis. The 1σ credible interval in the IH region is entirely
 3342 removed in the joint analysis but not for the beam-only analysis.

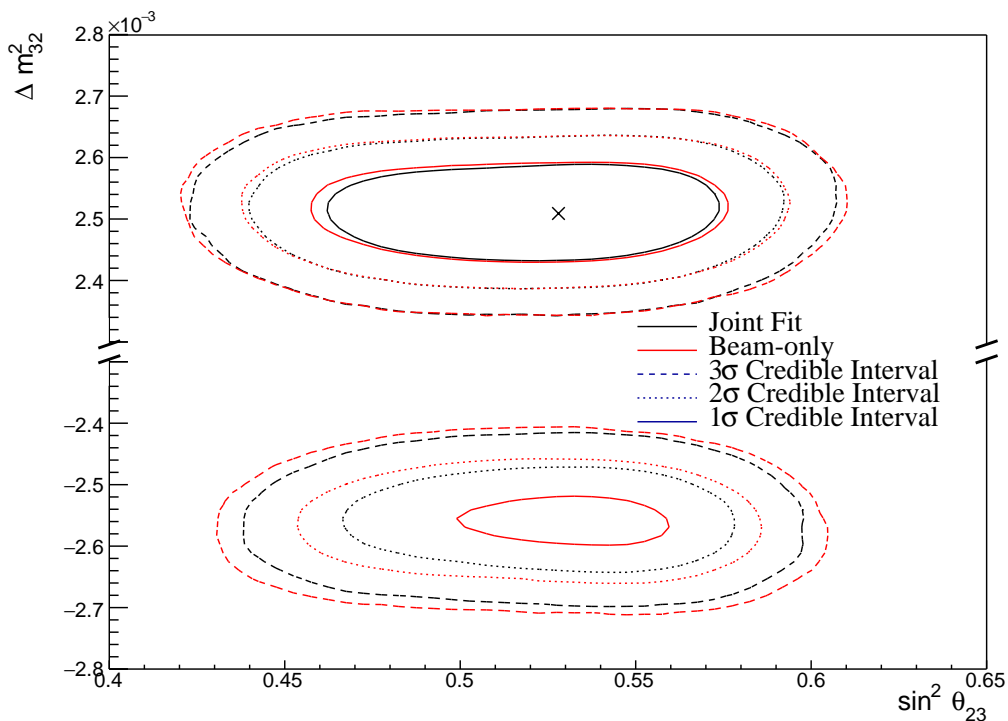


Figure 8.39: The two-dimensional posterior probability density distribution in $\Delta m_{32}^2 - \sin^2(\theta_{23})$ compared between the joint beam-atmospheric fit (Black) and the latest T2K sensitivities (Red) [72, 214]. The reactor constraint is applied in both fits. The distributions are marginalised over both hierarchies.

3343 The credible intervals of the joint fit are also tighter in the $\sin^2(\theta_{23})$ dimension
 3344 than the beam-only analysis in both mass hierarchy regions. This shows that
 3345 beyond the ability of the joint fit to prefer the NH more strongly than the beam-

only analysis, the precision to which it can measure $\sin^2(\theta_{23})$ is also improved. The Bayes factor for NH preference is calculated as $B(\text{NH}/\text{IH}) = 6.47$ and $B(\text{NH}/\text{IH}) = 3.09$ for the joint beam-atmospheric and beam-only analysis, respectively. This important conclusion illustrates that the joint beam-atmospheric analysis can provide a substantial preference for the NH hypothesis whilst the beam-only analysis can not.

The Bayes factors for UO preference which are $B(\text{UO}/\text{LO}) = 2.86$ and $B(\text{UO}/\text{LO}) = 2.47$ for the joint beam-atmospheric and beam-only analysis, respectively. Both of these represent a mild preference for the UO but there is a stronger preference observed in the joint analysis.

The sensitivity of the beam-only and joint beam-atmospheric analyses, to the appearance parameters ($\delta_{CP} - \sin^2(\theta_{13})$), are compared in Figure 8.40. These results are marginalised over both hierarchies. For this particular set of known oscillation parameters (AsimovA defined in Table 2.2), the beam-only analysis dominates the sensitivity. The joint fit does slightly increase the sensitivity to δ_{CP} but it does not change any conclusions that would be made. As expected, the prior knowledge dominates any sensitivity either fit would have on $\sin^2(\theta_{13})$.

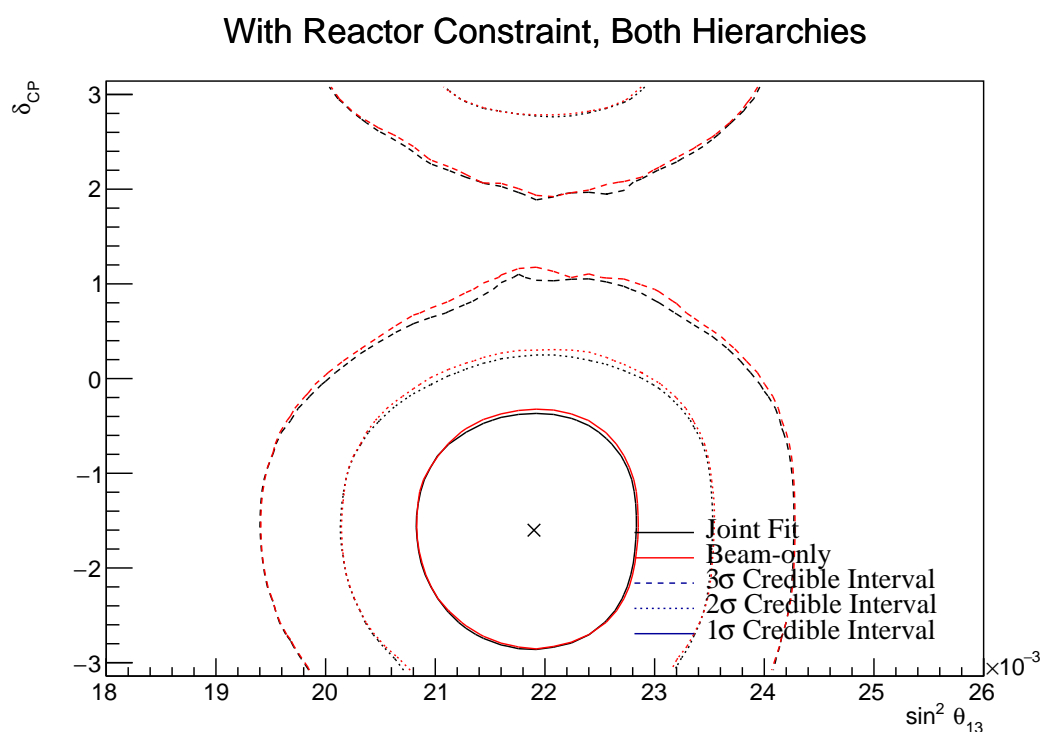


Figure 8.40: The two-dimensional posterior probability density distribution in δ_{CP} – $\sin^2(\theta_{13})$ compared between the joint beam-atmospheric fit (Black) and the latest T2K sensitivities (Red) [72, 214]. The reactor constraint is applied in both fits. The distributions are marginalised over both hierarchies.

3363 8.2.8 Alternate Asimov Parameter Set

3364 Figure 8.4 and Figure 8.5 show that the choice of the parameter set at which the
 3365 Asimov data is made can affect the conclusion. ‘AsimovA’ oscillation parameters
 3366 are defined at a region of δ_{CP} which is preferred by the T2K experiment. This
 3367 explains why the addition of the atmospheric samples does not significantly in-
 3368 crease the sensitivity to δ_{CP} , as illustrated in subsection 8.2.6 and subsection 8.2.7.
 3369 This section presents the sensitivities when ‘AsimovB’ oscillation parameters,
 3370 as defined in Table 2.2, are assumed (alongside the post-BANFF tune) when
 3371 building the Asimov data.

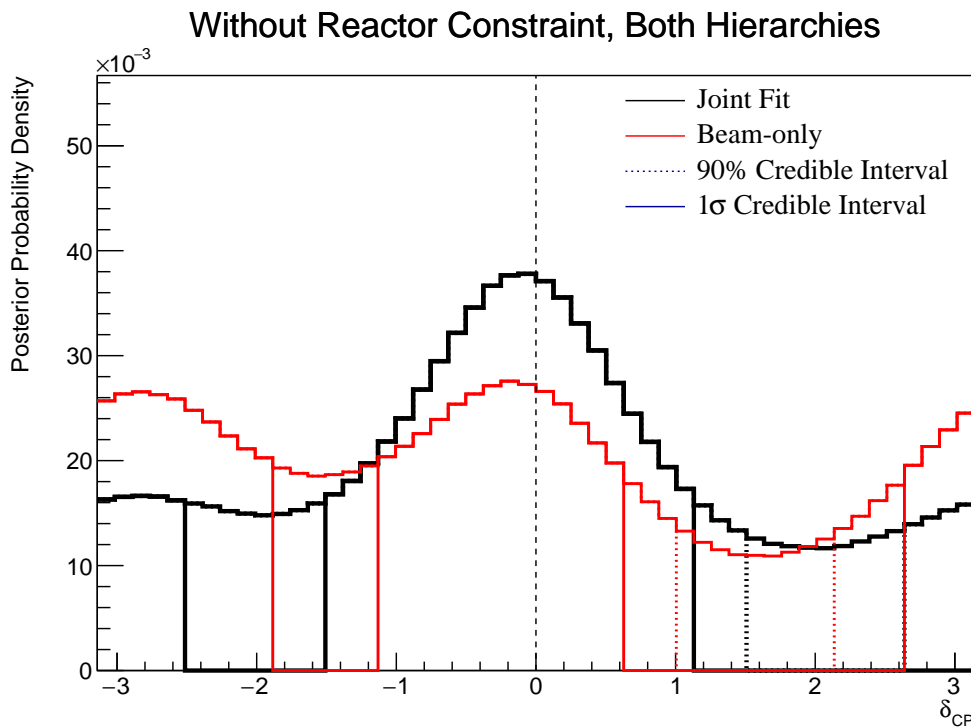


Figure 8.41: The one-dimensional posterior probability density distribution in δ_{CP} compared between the joint beam-atmospheric fit (Black) and the latest T2K sensitivities (Red) [72, 214]. The reactor constraint is not applied in either fit. The distributions are marginalised over both hierarchies.

3372 The sensitivity to δ_{CP} for the joint beam-atmospheric fit is presented in
 3373 Figure 8.41. The results are compared to those from the beam-only analysis
 3374 in [72, 214]. The reactor constraint is not applied in either of the fits. The
 3375 shape of the posterior distribution from the joint analysis is more peaked at

the known oscillation parameter value compared to the beam-only analysis, which has approximately the same posterior probability density at $\delta_{CP} = 0$ and $\delta_{CP} = \pm\pi$. This shows the ability of the joint analysis to better determine the correct phase of δ_{CP} if the true value were CP-conserving. The 1σ credible intervals and the position of the highest posterior probability density are given in Table 8.9. The highest posterior density for the joint beam-atmospheric analysis is $\delta_{CP} = -0.06 \pm 0.06$ which is consistent with the known value.

Parameter	Interval	HPD
δ_{CP} , (BH)	$[-\pi, -2.51], [-1.51, 1.13]$	-0.06 ± 0.06
δ_{CP} , (NH)	$[-1.13, 1.63]$	0.06 ± 0.06
δ_{CP} , (IH)	$[-3.02, -1.88], [-1.76, 0.13]$	-0.44 ± 0.06
Δm_{32}^2 (BH) [$\times 10^{-3}\text{eV}^2$]	$[-2.60, -2.52], [2.46, 2.56]$	2.51 ± 0.01
Δm_{32}^2 (NH) [$\times 10^{-3}\text{eV}^2$]	$[2.47, 2.56]$	2.52 ± 0.01
Δm_{32}^2 (IH) [$\times 10^{-3}\text{eV}^2$]	$[-2.61, -2.52]$	-2.57 ± 0.01
$\sin^2(\theta_{23})$ (BH)	$[0.430, 0.480], [0.545, 0.585]$	0.453 ± 0.003
$\sin^2(\theta_{23})$ (NH)	$[0.430, 0.485], [0.550, 0.580]$	0.453 ± 0.003
$\sin^2(\theta_{23})$ (IH)	$[0.435, 0.480], [0.540, 0.585]$	0.568 ± 0.003

Table 8.9: The position of the highest posterior probability density (HPD) and width of the 1σ credible interval for the joint beam-atmospheric fit. The reactor constraint is not applied. The values are presented by which hierarchy hypothesis is assumed: marginalised over both hierarchies (BH), normal hierarchy only (NH) and inverted hierarchy only (IH).

Naively, if just the 1σ credible interval were considered without observing the shape of the distribution, it would appear that the joint analysis would have a worse sensitivity to δ_{CP} due to the larger interval around $\delta_{CP} = 0$. The 1σ credible interval for the beam-only analysis is given as the range $\delta_{CP} = [-\pi, -1.88], [-1.13, 0.63]$ and $[2.64, \pi]$ which contains 56% of all values of δ_{CP} . Whereas, the joint beam-atmospheric analysis contains 52% of all δ_{CP} values within the 1σ credible interval. Therefore, if the area within the 1σ credible interval were to be compared between the two fits, the joint analysis would be shown to have better precision.

This apparent contradiction stems from the methodology in which the credible interval is calculated. The technique used in this analysis (documented in subsection 4.3.2) fills the credible interval by selecting bins in order of probability density until 68% of the posterior density is contained. If instead, the credible interval were calculated by expanding around the highest posterior probability, the benefits of the joint fit would be more obvious. In the case where the shape of the posterior were uni-modal, these two techniques would be equivalent up to statistical fluctuations.

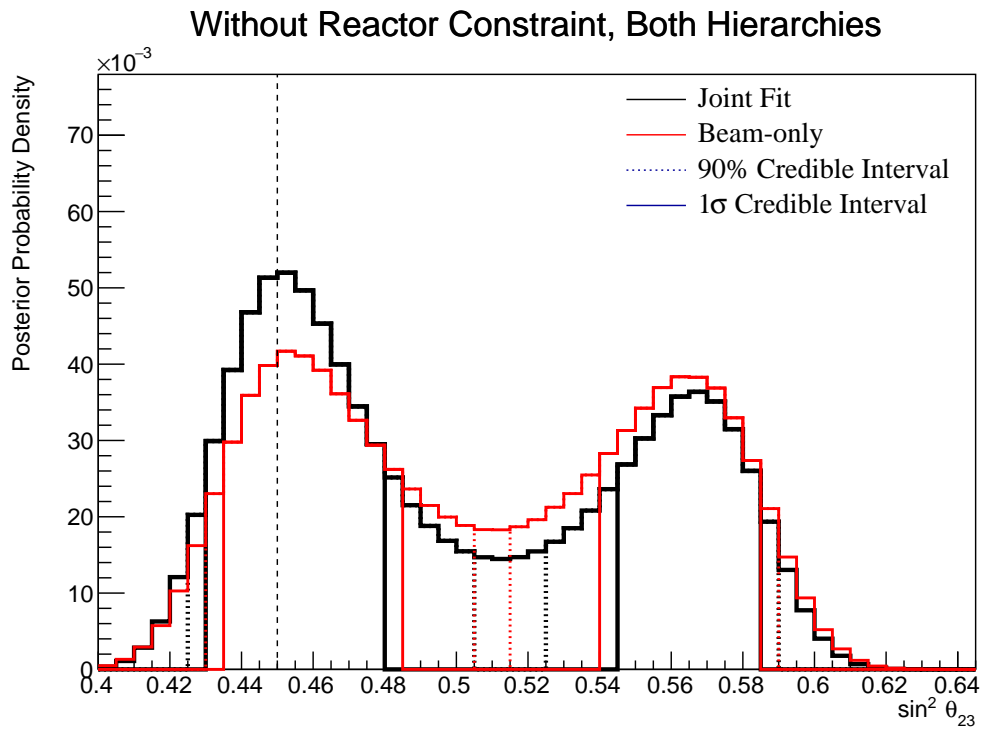


Figure 8.42: The one-dimensional posterior probability density distribution in $\sin^2(\theta_{23})$ compared between the joint beam-atmospheric fit (Black) and the latest T2K sensitivities (Red) [72, 214]. The reactor constraint is not applied in either fit. The distributions are marginalised over both hierarchies.

The sensitivity of the joint beam-atmospheric fit to $\sin^2(\theta_{23})$ is presented in Figure 8.42. The sensitivity is compared to that of the beam-only analysis in [72, 214]. The reactor constraint is not applied in either of the fits being compared. The joint beam-atmospheric fit has a much larger probability density in the region surrounding the known oscillation parameter, $\sin^2(\theta_{23}) = 0.45$.

3405 This shows the better octant determination of the joint analysis compared to
 3406 the beam-only fit. The ratio of the posterior density at the peak of the lower
 3407 octant to the peak of the upper octant from the joint fit is 1.43 compared to
 3408 1.09 from the beam-only analysis.

	LO ($\sin^2 \theta_{23} < 0.5$)	UO ($\sin^2 \theta_{23} > 0.5$)	Sum
NH ($\Delta m_{32}^2 > 0$)	0.35	0.24	0.59
IH ($\Delta m_{32}^2 < 0$)	0.19	0.22	0.41
Sum	0.54	0.46	1.00

Table 8.10: The distribution of steps in a joint beam-atmospheric fit, presented as the fraction of steps in the upper (UO) and lower (LO) octants and the normal (NH) and inverted (IH) hierarchies. The reactor constraint is not applied. The Bayes factors are calculated as $B(\text{NH}/\text{IH}) = 1.43$ and $B(\text{LO}/\text{UO}) = 1.19$.

3409 The distribution of steps, split by hierarchy and octant hypothesis, is presented
 3410 in Table 8.10. The Bayes factor for hierarchy and octant determination are
 3411 $B(\text{NH}/\text{IH}) = 1.43$ and $B(\text{LO}/\text{UO}) = 1.19$, respectively. These values compare
 3412 to $B(\text{NH}/\text{IH}) = 1.08$ and $B(\text{LO}/\text{UO}) = 0.91$ from the beam-only analysis. This
 3413 evidences the joint analysis's ability to select the correct octant and hierarchy
 3414 hypothesis. Comparisons to the AsimovA Bayes factors presented in Table 8.6
 3415 show how the preferences for the correct octant and hierarchy depend on the
 3416 true value of δ_{CP} and $\sin^2(\theta_{23})$.

3417 The sensitivity of the beam-only and joint beam-atmospheric analysis to
 3418 Δm_{32}^2 is given in Figure 8.43. The joint analysis has a stronger preference for the
 3419 correct hierarchy (NH) which is shown by the higher Bayes factor compared
 3420 to the beam-only analysis. This is further evidence by the width of the 90%
 3421 credible interval in the IH region being tigher in the joint analysis compared
 3422 to the beam-only analysis.

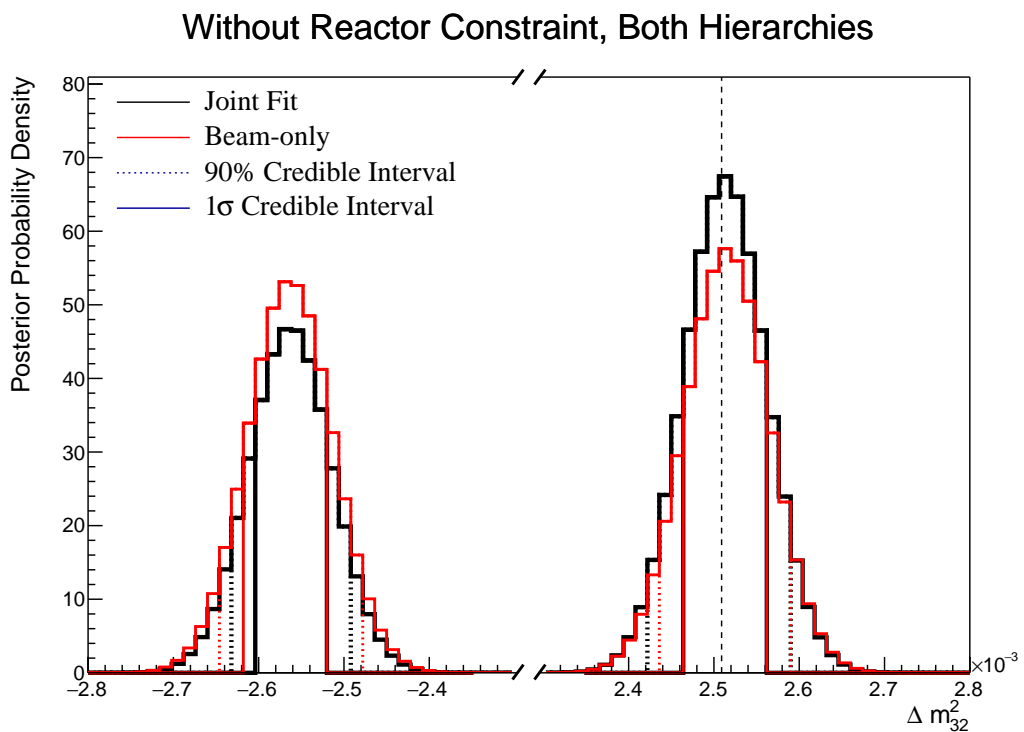


Figure 8.43: The one-dimensional posterior probability density distribution in Δm_{32}^2 compared between the joint beam-atmospheric fit (Black) and the latest T2K sensitivities (Red) [72, 214]. The reactor constraint is not applied in either fit. The distributions are marginalised over both hierarchies.

3423 8.2.9 Effect of Systematics

3424 Using the posterior predictive method documented in subsection 4.3.4, the
 3425 distribution of each sample's spectrum has been generated by sampling 2000 steps
 3426 from the posterior distribution of the joint beam-atmospheric fit. This technique
 3427 reweights the Monte Carlo prediction using the systematic values given by a
 3428 particular step, stores the sample spectra and repeats until the full distribution is
 3429 built. The oscillation parameters are always fixed at Asimov A values. Figure 8.44
 3430 illustrates the distribution for the SubGeV-*elike*-0dcy atmospheric sample. The
 3431 fit being sampled uses an Asimov data set which is created using Asimov A
 3432 oscillation parameters and the post-BANFF tune, as detailed in subsection 8.2.4.
 3433 The distribution closely resembles the Asimov data spectrum (denoted 'Post
 3434 BANFF Spectra'). This would be expected from an Asimov fit where the Monte
 3435 Carlo is fit to itself but gives more credibility to the results of the fit.

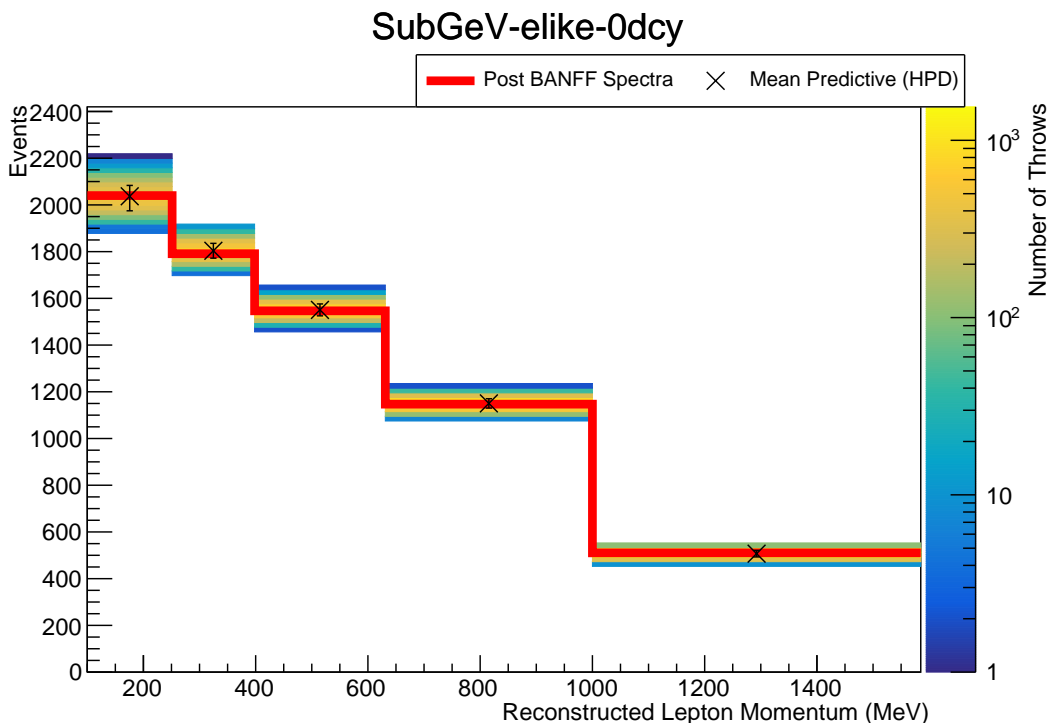


Figure 8.44: Result of the posterior predictive method for the SubGeV_elike_0dcy sample after sampling 2000 steps from the joint beam-atmospheric chain detailed in subsection 8.2.4 (Coloured histogram). The mean and uncertainty is presented for each bin. The Asimov data prediction (Red) assumes the post-BANFF tune and Asimov A oscillation parameters.

The total event rate for each sample from each of the sampled steps is calculated and the fractional uncertainty, $\Delta N_i / N_i$ where N_i is the event rate of the i^{th} sample, is calculated. These values are presented in Table 8.11. In general, the impact of the systematics have an $\sim 3\%$ uncertainty on the event rate of atmospheric samples, where CC1 π targeting samples have slightly larger uncertainties than the CCQE-like samples. The fractional uncertainties on the beam samples are compared to those from the beam-only analysis presented in [72, 214]. The uncertainties on the one-ring muon samples are mostly unchanged, whereas the uncertainties on the one-ring electron samples are different. As discussed in subsection 8.1.1, the atmospheric samples should be able to add constraints on the NC background events present in the FHC1Re and RHC1Re samples. The uncertainty reduction seen in those samples is due to those additional constraints. The reason why the FHC1Re1de has a higher uncertainty in this analysis is due to the addition of the ad-hoc systematic introduce for CC1 π interactions (see subsection 6.4.3).

Beyond the impact on the uncertainty of each sample's event rate, the post-fit constraint on each systematic parameter should checked. Figure 8.45 illustrates the central value and uncertainty on a select group of interaction systematics, for both the joint beam-atmospheric (from subsection 8.2.4) and the beam-only analysis. From the discussion in subsection 8.1.1, the uncertainty on systematics which are strongly constrained by the near detector should not significantly change when adding the atmospheric analysis. This behaviour is evidenced by the fact that the ratio of constraints between the two fits are very similar (within a few %) for almost all systematics. The only systematic which is more constrained in the joint beam-atmospheric analysis is the *NCOtherSK* normalisation parameter, which has a $O(10\%)$ tighter constraint. As expected, the atmospheric samples have been able to constrain this systematic which leads to the reduction in uncertainty for the beam electron-like samples.

Sample	Joint Analysis	Beam-only Analysis
SubGeV- <i>elike</i> -0dcy	2.53	-
SubGeV- <i>elike</i> -1dcy	3.28	-
SubGeV- <i>mulike</i> -0dcy	2.62	-
SubGeV- <i>mulike</i> -1dcy	2.23	-
SubGeV- <i>mulike</i> -2dcy	3.96	-
SubGeV- <i>pi0like</i>	2.84	-
MultiGeV- <i>elike</i> -nue	5.14	-
MultiGeV- <i>elike</i> -nuebar	2.79	-
MultiGeV- <i>mulike</i>	2.99	-
MultiRing- <i>elike</i> -nue	2.94	-
MultiRing- <i>elike</i> -nuebar	2.83	-
MultiRing- <i>mulike</i>	2.89	-
MultiRingOther-1	2.70	-
PCStop	3.22	-
PCThru	2.99	-
UpStop-mu	2.95	-
UpThruNonShower-mu	2.70	-
UpThruShower-mu	3.19	-
FHC1Rmu	2.49	2.33
RHC1Rmu	2.89	2.93
FHC1Re	4.12	4.57
RHC1Re	5.15	5.65
FHC1Re1de	13.38	11.51

Table 8.11: The fractional uncertainty, $\Delta N / N$, as calculated from sampling 2000 throws from a joint beam-atmospheric chain. The same values for the beam samples are provided from the beam-only analysis [72, 214]. These uncertainties consider all systematic parameters to be sampled from the fit whilst the oscillation parameters are fixed at the Asimov A oscillation set.

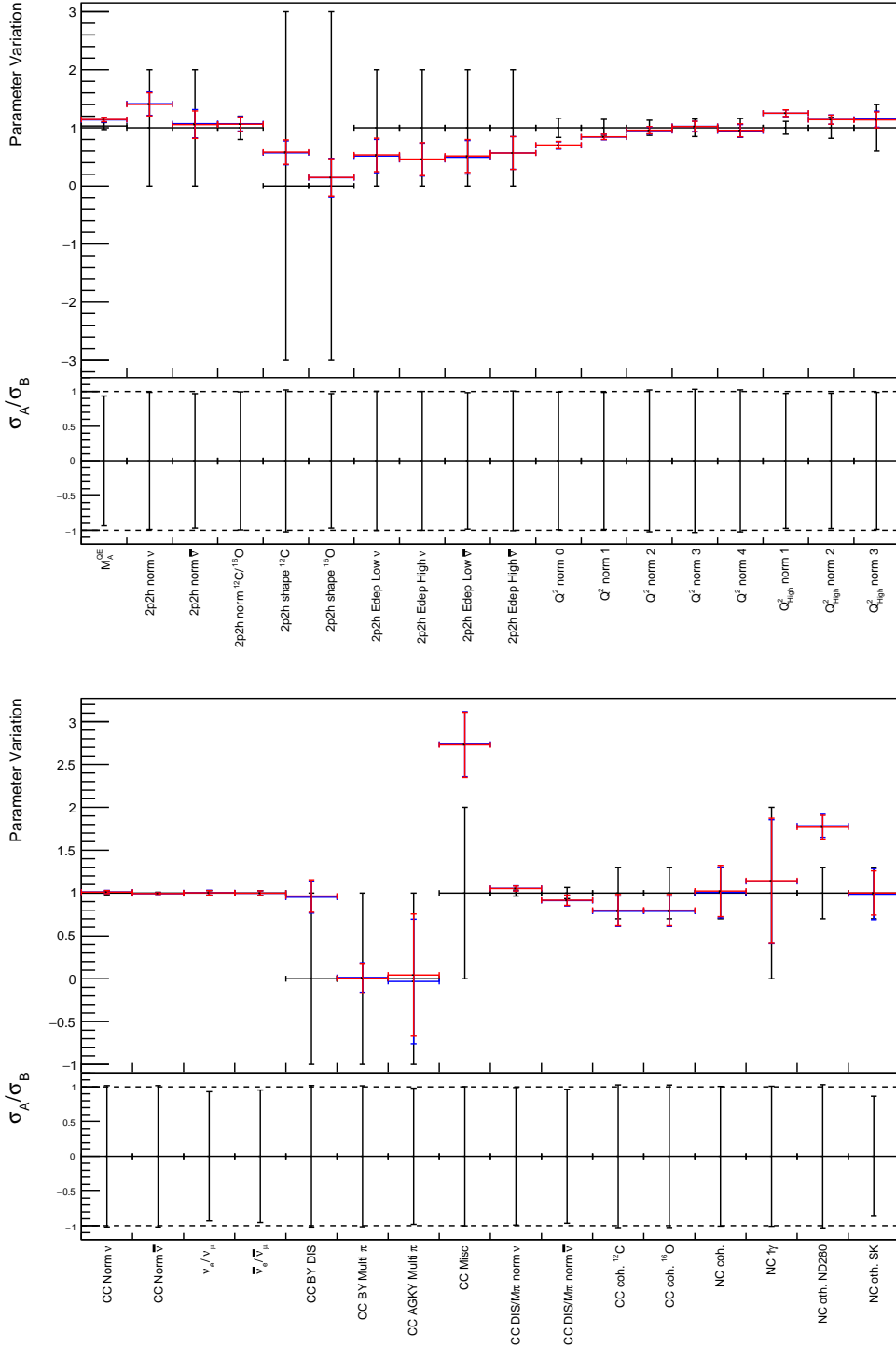


Figure 8.45: Central values and 1σ uncertainties for a select group of interaction systematics. The constraints from the prior uncertainty (Black), joint atmospheric-beam fit given in subsection 8.2.4 (Red) and beam-only analysis [72, 214] (Blue) are presented. The top pad of each plot presents the parameter variation and the bottom pad represents the ratio of the uncertainty between the joint beam-atmospheric and beam-only fits, where a value below 1.0 means the joint fit has a tighter constraint than the beam-only analysis.

9

3464

3465

Conclusions and Outlook

3466 This thesis has presented the sensitivites of the first offcial joint beam and
3467 atmospheric neutrino oscillation parameter measurements from the Tokai-to-
3468 Kamioka (T2K) and Super-Kamiokande (SK) collaborations. It combines the
3469 two independent analyses presented by the two independent collaborations DB:
3470 citations. This equates to a combined 3244.4 days equivalent of SK-IV livetime and
3471 1.97×10^{21} (1.63×10^{21}) POT in the neutrino(antineutrino) beam operating mode.

3472 The ND280 near detector is used to constrain the flux and cross-section
3473 systematics envoked within this oscillation analysis. It uses 1.15×10^{21} POT
3474 and 8.34×10^{20} POT in the neutrino and antineutrino running modes, respectively.
3475 These constraints are applied to both the beam far detector and low energy
3476 atmospheric samples through a correlated neutrino interaction model. This
3477 ensures that a consistent interaction model is used throughout the analysis.
3478 This is the first example of applying the T2K near detector constraints onto
3479 the SK atmospheric samples inside an oscillation analysis. DB: More physics
3480 developments

3481 This analysis implements a Bayesian Markov Chain Monte Carlo (MCMC)
3482 fitting technique built within the MaCh3 framework. This analysis has signifi-
3483 cantly developed the fitting framework, both in terms of technical features and
3484 performance. As a requirement for this analysis, the predominanately T2K fitting

3485 framework was required to simultaneously support and reweight alternative
3486 Monte Carlo samples. These developments include supporting new systematics,
3487 new oscillation probability calculations and previously unconsidered oscillation
3488 channels that saw the first tau events incorporated into the fitter. The devel-
3489 opments required to realise this analysis have been the building blocks of the
3490 frameworks expansion into other experiments.

3491 Due to the MCMC techniques used within the fit, a novel technique of
3492 calculating the atmospheric neutrino oscillation probabilities has been developed.
3493 This calculation uses a sub-sampling linear-averaging approach to ensure that
3494 the sensitivities being calculated are not biased due to insufficient Monte Carlo
3495 statistics in a region of fast varying probability. It illustrates a computationally
3496 feasible method of reliably calculating oscillation probabilities which can be
3497 utilised within any fitting framework. Further techniques, which consider
3498 uncertainties related to modelling the interaction height of the primary cosmic
3499 rays and the density of the Earth have also been implemented. Whilst of critical
3500 importance to this analysis, these techniques are a stand-alone technique and can
3501 be used in any other atmospheric oscillation analysis. Alongside these physics
3502 considerations, an alternative oscillation calculation engine has been interfaced
3503 with the framework to significantly reduce the resources required to perform
3504 this analysis. Current developments, based on the benefits illustrated within this
3505 analysis, are being considered within the T2K analysis.

3506 **DB: Physics results here**

3507 Whilst this analysis provides the first sensitivity measurement of a joint beam
3508 and atmospheric analysis, there are more improvements to be made. Since this
3509 analysis began, T2K has released an updated oscillation analysis with additional
3510 near and far detector samples alongside a more sophisticated interaction model.
3511 The overall change in oscillation parameter measurement observed by T2K
3512 was relatively minor DB: Bronner Nu2022 but the stronger constraints on the
3513 systematics could impact this joint analysis to a larger extent. This, or a particular
3514 focus on CCRES interaction modelling, could lead to a better understanding of

3515 the CC1 π samples from a physics-driven perspective rather than invoking the
3516 ad-hoc systematic used in this analysis. Further developments should consider
3517 the effect of correlating the beam and atmospheric flux uncertainties, where
3518 updates of the Bartol and Honda models are being made to realise this. The
3519 next goal for this analysis would be moving to a data fit. This would require
3520 performing studies which aim to understand the effect of the model choice on
3521 the oscillation parameter measurements. This tests whether there is freedom in
3522 the systematics model to allow alternative models to be fit therefore resulting
3523 in more reliable measurements.

3524 Beyond these model improvements, more data is available than what is
3525 assumed for this analysis. The T2K experiment has ran an additional period of
3526 two months, corresponding to an additional 1.78×10^{20} POT in neutrino mode.
3527 Similarly, there are several SK periods which have not been considered within this
3528 analysis. SK-I to SK-III contained approximately the same number of statistics as
3529 the SK-IV period used within this analysis but were neglected as the `fitQun`
3530 reconstruction algorithm has not validated for those periods. Furthermore,
3531 the SK-V era provides an additional 583 days of data-taking which could also
3532 be included within this analysis. This would require updating the detector
3533 systematics to reflect the changes brought about by the detector refurbishment.

3534 The T2K and SK experiments are continually developing. The near detector
3535 of the T2K experiment is currently undergoing development work to include
3536 new components. This lowers the required energy thresholds and improves
3537 vertex resolution. This may lead to stronger constraints on the flux and cross-
3538 section systematics used within the beam analysis, which could strengthen the
3539 sensitivities provided within this analysis. The SK-Gd era will also continue
3540 to accumulate statistics. Developments in the atmospheric sample selections
3541 may also benefit from the Gadolinium dopants as neutron capture will aid
3542 in neutrino/antineutrino separation leading to better mass hierarchy sensitiv-
3543 ity. This would require including interaction systematics for neutron capture

³⁵⁴⁴ of Gadolinium which has already started DB: Citation to SK neutron paper:
³⁵⁴⁵ Arxiv - 2209.08609.

³⁵⁴⁶ This analysis presents the sensitivities of the first joint beam and atmospheric
³⁵⁴⁷ analysis. This analysis and the supporting framework has the potential to become
³⁵⁴⁸ the basis of the oscillation analysis for future Hyper-Kamiokande experiment.

- ³⁵⁴⁹ • Predicted number of events at the FD
- ³⁵⁵⁰ • SK only results - w/wo RC
- ³⁵⁵¹ • Bayes factor
- ³⁵⁵² • Joint fit has significant preference for correct hierarchy without external
constraints - T2K doesn't have that sensitivity
- ³⁵⁵³ • Summary table
- ³⁵⁵⁴ • Published at Nu2022
- ³⁵⁵⁵ • Further development of correlated detector model
- ³⁵⁵⁶

Bibliography

- 3558 [1] J. Chadwick. "Intensitätsverteilung im magnetischen Spectrum der β -Strahlen
3559 von radium B + C". In: *Verhandl. Dtsc. Phys. Ges.* 16 (1914), p. 383. URL:
3560 <http://cds.cern.ch/record/262756>.
- 3561 [2] C. D. Ellis and W. A. Wooster. "The average energy of disintegration of radium
3562 E". en. In: *Proc. R. Soc. Lond. A Math. Phys. Sci.* 117.776 (Dec. 1927), pp. 109–123.
- 3563 [3] W. Pauli. "Dear radioactive ladies and gentlemen". In: *Phys. Today* 31N9 (1978),
3564 p. 27.
- 3565 [4] E. Fermi. "An attempt of a theory of beta radiation. 1." In: *Z. Phys.* 88 (1934),
3566 pp. 161–177.
- 3567 [5] F. Reines and C. L. Cowan. "Detection of the Free Neutrino". In: *Phys. Rev.* 92 (3
3568 1953), pp. 830–831. URL:
3569 <https://link.aps.org/doi/10.1103/PhysRev.92.830>.
- 3570 [6] C. L. Cowan et al. "Detection of the Free Neutrino: a Confirmation". In: *Science*
3571 124.3212 (1956), pp. 103–104. URL:
3572 <http://science.sciencemag.org/content/124/3212/103>.
- 3573 [7] G. Danby et al. "Observation of High-Energy Neutrino Reactions and the
3574 Existence of Two Kinds of Neutrinos". In: *Phys. Rev. Lett.* 9 (1 1962), pp. 36–44.
3575 URL: <https://link.aps.org/doi/10.1103/PhysRevLett.9.36>.
- 3576 [8] K. Kodama et al. "Observation of tau neutrino interactions". In: *Physics Letters B*
3577 504.3 (2001), pp. 218 –224. URL:
3578 <http://www.sciencedirect.com/science/article/pii/S0370269301003070>.
- 3579 [9] A. Aguilar-Arevalo et al. "Evidence for neutrino oscillations from the observation
3580 of anti-neutrino(electron) appearance in a anti-neutrino(muon) beam". In: *Phys.*
3581 *Rev.* D64 (2001), p. 112007. arXiv: [hep-ex/0104049](https://arxiv.org/abs/hep-ex/0104049) [hep-ex].
- 3582 [10] A. A. Aguilar-Arevalo et al. "Improved Search for $\bar{\nu}_\mu \rightarrow \bar{\nu}_e$ Oscillations in the
3583 MiniBooNE Experiment". In: *Phys. Rev. Lett.* 110 (16 2013), p. 161801. URL:
3584 <https://link.aps.org/doi/10.1103/PhysRevLett.110.161801>.
- 3585 [11] Planck Collaboration. "Planck 2018 results. VI. Cosmological parameters". In: *aap*
3586 641 (Sept. 2020).
- 3587 [12] J. A. Bagger et al. "Precision electroweak measurements on the Z resonance". In:
3588 *Physics Reports* 427.5 (2006), pp. 257 –454. URL:
3589 <http://www.sciencedirect.com/science/article/pii/S0370157305005119>.
- 3590 [13] B. Pontecorvo. "Neutrino Experiments and the Problem of Conservation of
3591 Leptonic Charge". In: *Sov. Phys. JETP* 26 (1968). [Zh. Eksp. Teor.
3592 Fiz.53,1717(1967)], pp. 984–988.

- 3593 [14] B. Pontecorvo. "Inverse beta processes and nonconservation of lepton charge". In: Sov. Phys. JETP 7 (1958). [Zh. Eksp. Teor. Fiz.34,247(1957)], pp. 172–173.
- 3594
- 3595 [15] M. Kobayashi and T. Maskawa. "CP-Violation in the Renormalizable Theory of Weak Interaction". In: Progress of Theoretical Physics 49.2 (1973), pp. 652–657. URL: <http://dx.doi.org/10.1143/PTP.49.652>.
- 3596
- 3597
- 3598 [16] N. Cabibbo. "Unitary Symmetry and Leptonic Decays". In: Phys. Rev. Lett. 10 (12 1963), pp. 531–533. URL: <https://link.aps.org/doi/10.1103/PhysRevLett.10.531>.
- 3599
- 3600
- 3601 [17] A. Maio et al. "Search for Majorana neutrinos with the SNO+ detector at SNOLAB". In: Journal of Physics: Conference Series 587 (2015), p. 012030. URL: <https://doi.org/10.1088/1742-6596/587/1/012030>.
- 3602
- 3603
- 3604 [18] A. Y. Smirnov. "The MSW effect and Solar Neutrinos". In: Arxiv (2003). URL: <https://arxiv.org/abs/hep-ph/0305106>.
- 3605
- 3606 [19] S. P. Mikheyev and A. Y. Smirnov. "Resonance enhancement of oscillations in matter and solar neutrino spectroscopy". In: Soviet Journal of Nuclear Physics 42 (6 1985), pp. 913–917.
- 3607
- 3608
- 3609 [20] L. Wolfenstein. "Neutrino oscillations in matter". In: Phys. Rev. D 17 (9 1978), pp. 2369–2374. URL: <https://link.aps.org/doi/10.1103/PhysRevD.17.2369>.
- 3610
- 3611 [21] V. D. Barger et al. "Matter Effects on Three-Neutrino Oscillations". In: Phys. Rev. D 22 (1980), p. 2718.
- 3612
- 3613 [22] Y. Ashie et al. "Evidence for an Oscillatory Signature in Atmospheric Neutrino Oscillations". In: Phys. Rev. Lett. 93 (10 2004), p. 101801. URL: <https://link.aps.org/doi/10.1103/PhysRevLett.93.101801>.
- 3614
- 3615
- 3616 [23] Q. R. Ahmad et al. "Direct Evidence for Neutrino Flavor Transformation from Neutral-Current Interactions in the Sudbury Neutrino Observatory". In: Phys. Rev. Lett. 89 (1 2002), p. 011301. URL: <https://link.aps.org/doi/10.1103/PhysRevLett.89.011301>.
- 3617
- 3618
- 3619
- 3620 [24] Nobel Prize. 2015 Nobel prize in Physics as listed by Nobelprize.org. https://www.nobelprize.org/nobel_prizes/physics/laureates/2015/. Accessed: 22-06-2022.
- 3621
- 3622
- 3623 [25] J. A. Formaggio and G. P. Zeller. "From eV to EeV: Neutrino Cross Sections Across Energy Scales". In: Rev. Mod. Phys. 84 (2012), pp. 1307–1341. arXiv: 1305.7513 [hep-ex].
- 3624
- 3625
- 3626 [26] A. Oralbaev, M. Skorokhvatov, and O. Titov. "The inverse beta decay: a study of cross section". In: Journal of Physics: Conference Series 675.1 (2016), p. 012003. URL: <https://doi.org/10.1088/1742-6596/675/1/012003>.
- 3627
- 3628
- 3629 [27] A. Bellerive. "Review of solar neutrino experiments". en. In: Int. J. Mod. Phys. A 19.08 (Mar. 2004), pp. 1167–1179.
- 3630
- 3631 [28] R. Davis, D. S. Harmer, and K. C. Hoffman. "Search for Neutrinos from the Sun". In: Phys. Rev. Lett. 20 (21 1968), pp. 1205–1209. URL: <https://link.aps.org/doi/10.1103/PhysRevLett.20.1205>.
- 3632
- 3633
- 3634 [29] N. Vinyoles et al. "A new generation of standard solar models". In: Astrophys. J. 835.2 (Jan. 2017), p. 202.
- 3635

- 3636 [30] V. Gribov and B. Pontecorvo. "Neutrino astronomy and lepton charge". en. In: *Phys. Lett. B* 28.7 (Jan. 1969), pp. 493–496.
- 3638 [31] K. S. Hirata et al. "Observation of ${}^8\text{B}$ solar neutrinos in the Kamiokande-II
3639 detector". In: *Phys. Rev. Lett.* 63 (1 1989), pp. 16–19. URL:
3640 <https://link.aps.org/doi/10.1103/PhysRevLett.63.16>.
- 3641 [32] W. Hampel et al. "GALLEX solar neutrino observations: results for GALLEX IV".
3642 en. In: *Phys. Lett. B* 447.1-2 (Feb. 1999), pp. 127–133.
- 3643 [33] J. N. Abdurashitov et al. "Measurement of the solar neutrino capture rate with
3644 gallium metal". In: *Phys. Rev. C* 60 (5 1999), p. 055801. URL:
3645 <https://link.aps.org/doi/10.1103/PhysRevC.60.055801>.
- 3646 [34] Borexino Collaboration. "Comprehensive measurement of pp-chain solar
3647 neutrinos". en. In: *Nature* 562.7728 (Oct. 2018), pp. 505–510.
- 3648 [35] B. Aharmim et al. "A search for neutrinos from the SolarhepReaction and the
3649 diffuse supernova neutrino background with the Sudbury neutrino observatory".
3650 en. In: *Astrophys. J.* 653.2 (Dec. 2006), pp. 1545–1551.
- 3651 [36] Borexino Collaboration. "Experimental evidence of neutrinos produced in the
3652 CNO fusion cycle in the Sun". In: *Nature* 587.7835 (2020), pp. 577–582. URL:
3653 <https://doi.org/10.1038%2Fs41586-020-2934-0>.
- 3654 [37] K. Abe et al. "T2K neutrino flux prediction". In: *Phys. Rev. D* 87 (1 2013),
3655 p. 012001. URL: <https://link.aps.org/doi/10.1103/PhysRevD.87.012001>.
- 3656 [38] D. G. Michael et al. "Observation of Muon Neutrino Disappearance with the
3657 MINOS Detectors in the NuMI Neutrino Beam". In: *Phys. Rev. Lett.* 97 (19 2006),
3658 p. 191801. URL:
3659 <https://link.aps.org/doi/10.1103/PhysRevLett.97.191801>.
- 3660 [39] M. H. Ahn et al. "Measurement of neutrino oscillation by the K2K experiment".
3661 In: *Phys. Rev. D* 74 (7 2006), p. 072003. eprint:
3662 <https://link.aps.org/doi/10.1103/PhysRevD.74.072003>.
- 3663 [40] M. A. Acero et al. "First measurement of neutrino oscillation parameters using
3664 neutrinos and antineutrinos by NOvA". In: *Phys. Rev. Lett.* 123 (15 2019),
3665 p. 151803. URL:
3666 <https://link.aps.org/doi/10.1103/PhysRevLett.123.151803>.
- 3667 [41] K. Abe et al. "The T2K experiment". In: *Nuclear Instruments and Methods in Physics
3668 Research Section A* 659.1 (2011), pp. 106 –135. eprint:
3669 <http://www.sciencedirect.com/science/article/pii/S0168900211011910>.
- 3670 [42] B. Abi et al. "Long-baseline neutrino oscillation physics potential of the DUNE
3671 experiment". en. In: *Eur. Phys. J. C Part. Fields* 80.10 (Oct. 2020).
- 3672 [43] Hyper-Kamiokande Proto-Collaboration. "Physics potential of a long-baseline
3673 neutrino oscillation experiment using a J-PARC neutrino beam and
3674 Hyper-Kamiokande". In: *Prog. Theor. Exp. Phys.* 2015.5 (May 2015), pp. 53C02–0.
- 3675 [44] C. Blanco, D. Hooper, and P. Machado. "Constraining sterile neutrino
3676 interpretations of the LSND and MiniBooNE anomalies with coherent neutrino
3677 scattering experiments". In: *Phys. Rev. D* 101.7 (2020). URL:
3678 <https://doi.org/10.1103%2Fphysrevd.101.075051>.

- 3679 [45] MicroBooNE Collaboration. "Search for an Excess of Electron Neutrino
3680 Interactions in MicroBooNE Using Multiple Final State Topologies". In: *arXiv*
3681 (2021). URL: <https://arxiv.org/abs/2110.14054>.
- 3682 [46] B. Armbruster et al. "Upper limits for neutrino oscillations $\bar{\nu}_\mu \rightarrow \bar{\nu}_e$ from muon
3683 decay at rest". In: *Phys. Rev. D* 65 (11 2002), p. 112001. URL:
3684 <https://link.aps.org/doi/10.1103/PhysRevD.65.112001>.
- 3685 [47] T. K. Gaisser and M. Honda. "Flux of Atmospheric Neutrinos". In: *Annual Review
3686 of Nuclear and Particle Science* 52.1 (2002), pp. 153–199. URL:
3687 <https://doi.org/10.1146%2Fannurev.nucl.52.050102.090645>.
- 3688 [48] G. D. Barr et al. "Three-dimensional calculation of atmospheric neutrinos". In:
3689 *Phys. Rev. D* 70.2 (2004). URL: <https://doi.org/10.1103/physrevd.70.023006>.
- 3690 [49] M. Honda et al. "Calculation of atmospheric neutrino flux using the interaction
3691 model calibrated with atmospheric muon data". In: *Phys. Rev. D* 75.4 (2007). URL:
3692 <https://doi.org/10.1103/physrevd.75.043006>.
- 3693 [50] M. Honda et al. "New calculation of the atmospheric neutrino flux in a
3694 three-dimensional scheme". In: *Phys. Rev. D* 70 (4 2004), p. 043008. URL:
3695 <https://link.aps.org/doi/10.1103/PhysRevD.70.043008>.
- 3696 [51] M. Honda et al. "Improvement of low energy atmospheric neutrino flux
3697 calculation using the JAM nuclear interaction model". In: *Phys. Rev. D* 83 (12
3698 2011), p. 123001. URL:
3699 <https://link.aps.org/doi/10.1103/PhysRevD.83.123001>.
- 3700 [52] A. Fassò et al. *FLUKA: Status and Prospects for Hadronic Applications*. Ed. by
3701 Andreas Kling et al. Berlin, Heidelberg: Springer Berlin Heidelberg, 2001,
3702 pp. 955–960.
- 3703 [53] Y. Ashie et al. "Measurement of atmospheric neutrino oscillation parameters by
3704 Super-Kamiokande I". In: *Phys. Rev. D* 71.11 (2005). URL:
3705 <https://doi.org/10.1103/physrevd.71.112005>.
- 3706 [54] F. Reines et al. "Evidence for high-energy cosmic-ray neutrino interactions". In:
3707 *Phys. Rev. Lett.* 15.9 (Aug. 1965), pp. 429–433.
- 3708 [55] D. Casper et al. "Measurement of atmospheric neutrino composition with the
3709 IMB-3 detector". In: *Phys. Rev. Lett.* 66 (20 1991), pp. 2561–2564. URL:
3710 <https://link.aps.org/doi/10.1103/PhysRevLett.66.2561>.
- 3711 [56] K. S. Hirata et al. "Observation of a small atmospheric ν_μ/ν_e ratio in
3712 Kamiokande". en. In: *Phys. Lett. B* 280.1-2 (Apr. 1992), pp. 146–152.
- 3713 [57] Z. Li et al. "Measurement of the tau neutrino cross section in atmospheric
3714 neutrino oscillations with Super-Kamiokande". In: *Phys. Rev. D* 98.5 (2018). URL:
3715 <https://doi.org/10.1103/physrevd.98.052006>.
- 3716 [58] K. Abe et al. "Atmospheric neutrino oscillation analysis with external constraints
3717 in Super-Kamiokande I-IV". In: *Phys. Rev. D* 97 (7 2018), p. 072001. URL:
3718 <https://link.aps.org/doi/10.1103/PhysRevD.97.072001>.
- 3719 [59] T2K Collaboration. "Constraint on the matter-antimatter symmetry-violating
3720 phase in neutrino oscillations". en. In: *Nature* 580.7803 (Apr. 2020), pp. 339–344.

- [60] M. A. Acero et al. "First measurement of neutrino oscillation parameters using neutrinos and antineutrinos by NOvA". en. In: *Phys. Rev. Lett.* 123.15 (Oct. 2019), p. 151803.
- [61] M. G. Aartsen et al. "Measurement of atmospheric neutrino oscillations at 6–56 GeV with IceCube DeepCore". In: *Phys. Rev. Lett.* 120.7 (Feb. 2018).
- [62] P. Adamson et al. "Combined analysis of $\nu\mu$ Disappearance and $\nu\mu \rightarrow \nu e$ Appearance in MINOS using accelerator and atmospheric neutrinos". In: *Phys. Rev. Lett.* 112.19 (May 2014).
- [63] M. Sajjad Athar et al. "Status and perspectives of neutrino physics". In: *Progress in Particle and Nuclear Physics* 124 (2022), p. 103947. URL: <https://doi.org/10.1016/Fj.pnpp.2022.103947>.
- [64] S. B. Kim, T. Lasserre, and Y. Wang. "Reactor Neutrinos". In: *Adv. High Energy Phys.* 2013 (2013), pp. 1–34.
- [65] K Abe et al. "First gadolinium loading to Super-Kamiokande". en. In: *Nucl. Instrum. Methods Phys. Res. A* 1027.166248 (Mar. 2022), p. 166248.
- [66] F. P. An et al. "Observation of Electron-Antineutrino Disappearance at Daya Bay". In: *Phys. Rev. Lett.* 108 (17 2012), p. 171803. URL: <https://link.aps.org/doi/10.1103/PhysRevLett.108.171803>.
- [67] J. K. Ahn et al. "Observation of Reactor Electron Antineutrinos Disappearance in the RENO Experiment". In: *Phys. Rev. Lett.* 108 (19 2012), p. 191802. URL: <https://link.aps.org/doi/10.1103/PhysRevLett.108.191802>.
- [68] Y. Abe et al. "Indication of Reactor $\bar{\nu}_e$ Disappearance in the Double Chooz Experiment". In: *Phys. Rev. Lett.* 108 (13 2012), p. 131801. URL: <https://link.aps.org/doi/10.1103/PhysRevLett.108.131801>.
- [69] JUNO Collaboration. "TAO Conceptual Design Report: A Precision Measurement of the Reactor Antineutrino Spectrum with Sub-percent Energy Resolution". In: *arXiv* (2020). arXiv: 2005.08745 [physics.ins-det].
- [70] M. P. Decowski. "KamLAND's precision neutrino oscillation measurements". en. In: *Nucl. Phys. B*. 908 (July 2016), pp. 52–61.
- [71] A. Gando et al. "Constraints on θ_{13} from a three-flavor oscillation analysis of reactor antineutrinos at KamLAND". In: *Phys. Rev. D* 83 (5 2011), p. 052002. URL: <https://link.aps.org/doi/10.1103/PhysRevD.83.052002>.
- [72] P. Dunne. "Latest Neutrino Oscillation Results from T2K". In: *Neutrino 2020* (2020). URL: <https://zenodo.org/record/3959557>.
- [73] Particle Data Group. "Review of particle physics". en. In: *Prog. Theor. Exp. Phys.* 2020.8 (Aug. 2020).
- [74] R. L. Workman et al. "Review of Particle Physics". In: *PTEP* 2022 (2022), p. 083C01.
- [75] K. Abe et al. "Precise Measurement of the Neutrino Mixing Parameter θ_{23} from Muon Neutrino Disappearance in an Off-Axis Beam". In: *Phys. Rev. Lett.* 112 (18 2014), p. 181801. URL: <https://link.aps.org/doi/10.1103/PhysRevLett.112.181801>.

- 3763 [76] R. Wendell. "Three Flavor Oscillation Analysis of Atmospheric Neutrinos in
3764 Super-Kamiokande". PhD thesis. University of North Carolina, 2008.
- 3765 [77] A. M. Dziewonski and D. L. Anderson. "Preliminary reference Earth model". en.
3766 In: *Phys. Earth Planet. Inter.* 25.4 (June 1981), pp. 297–356.
- 3767 [78] Y. Fukuda et al. "Evidence for oscillation of atmospheric neutrinos". In: *Phys. Rev.*
3768 *Lett.* 81.8 (Aug. 1998), pp. 1562–1567.
- 3769 [79] K. Abe et al. "Calibration of the Super-Kamiokande detector". In: *Nuclear*
3770 *Instruments and Methods in Physics Research Section A* 737 (2014), pp. 253–272. URL:
3771 <https://doi.org/10.1016/j.nima.2013.11.081>.
- 3772 [80] L. Wan. "Atmospheric Neutrino Super-K". In: *Neutrino 2022* (2022). URL:
3773 <https://zenodo.org/record/6694761>.
- 3774 [81] M. Jiang. "Study of the neutrino mass hierarchy with the atmospheric neutrino
3775 data collected in Super-Kamiokande IV". PhD thesis. Kyoto University, 2019.
- 3776 [82] S. Fukuda et al. "The super-kamiokande detector". en. In: *Nucl. Instrum. Methods*
3777 *Phys. Res. A* 501.2-3 (Apr. 2003), pp. 418–462. eprint:
3778 <http://www.sciencedirect.com/science/article/pii/S016890020300425X>.
- 3779 [83] Y. Itow et al. "The JHF-Kamioka neutrino project". In: *arXiv* (2001).
- 3780 [84] M. Jiang et al. "Atmospheric neutrino oscillation analysis with improved event
3781 reconstruction in Super-Kamiokande IV". en. In: *Prog. Theor. Exp. Phys.* 2019.5
3782 (May 2019).
- 3783 [85] H. Kume et al. "20 inch diameter photomultiplier". In: *Nuclear Instruments and*
3784 *Methods in Physics Research* 205.3 (1983), pp. 443–449. URL:
3785 <https://www.sciencedirect.com/science/article/pii/0167508783900078>.
- 3786 [86] A. Suzuki et al. "Improvement of 20 in. diameter photomultiplier tubes". In:
3787 *Nuclear Instruments and Methods in Physics Research Section A: Accelerators,*
3788 *Spectrometers, Detectors and Associated Equipment* 329.1-2 (May 1993), pp. 299–313.
3789 URL: [https://doi.org/10.1016/0168-9002\(93\)90949-i](https://doi.org/10.1016/0168-9002(93)90949-i).
- 3790 [87] Y. Nakano et al. "Measurement of the radon concentration in purified water in
3791 the Super-Kamiokande IV detector". en. In: *Nucl. Instrum. Methods Phys. Res. A*
3792 977.164297 (Oct. 2020), p. 164297.
- 3793 [88] Hamamatsu. *Hamamatsu Photonics Photomultiplier Tubes Handbook*. URL:
3794 https://www.hamamatsu.com/content/dam/hamamatsu-photonics/sites/documents/99_SALES_LIBRARY/etd/PMT_handbook_v4E.pdf.
- 3796 [89] J. F. Beacom and M. R. Vagins. "Antineutrino Spectroscopy with Large Water
3797 Čerenkov Detectors". In: *Phys. Rev. Lett.* 93 (17 2004), p. 171101. URL:
3798 <https://link.aps.org/doi/10.1103/PhysRevLett.93.171101>.
- 3799 [90] L. Marti et al. "Evaluation of gadolinium's action on water Cherenkov detector
3800 systems with EGADS". en. In: *Nucl. Instrum. Methods Phys. Res. A* 959.163549
3801 (Apr. 2020), p. 163549.
- 3802 [91] M. Vagins. "Solar/DSNB Neutrino SK-Gd". In: *Neutrino 2022* (2022). URL:
3803 <https://zenodo.org/record/6696210>.
- 3804 [92] J. Focht. "Dark Noise Calibration of the Super-Kamiokande Outer Detector".
3805 PhD thesis. Massachusetts Institute of Technology, 2004.

- 3806 [93] T. Tanimori et al. "Design and performance of semi-custom analog IC including
3807 two TACs and two current integrators for 'Super-Kamiokande'". In: *IEEE*
3808 *Transactions on Nuclear Science* 36.1 (1989), pp. 497–501.
- 3809 [94] J. Hosaka et al. "Solar neutrino measurements in Super-Kamiokande-I". In: *Phys.*
3810 *Rev. D* 73 (11 2006), p. 112001.
- 3811 [95] H. Nishino et al. "High-speed charge-to-time converter ASIC for the
3812 Super-Kamiokande detector". en. In: *Nucl. Instrum. Methods Phys. Res. A* 610.3
3813 (Nov. 2009), pp. 710–717.
- 3814 [96] S. Yamada et al. "Commissioning of the New Electronics and Online System for
3815 the Super-Kamiokande Experiment". In: *IEEE Transactions on Nuclear Science* 57.2
3816 (2010), pp. 428–432.
- 3817 [97] S. Yamada et al. "New online system without hardware trigger for the
3818 Super-Kamiokande experiment". In: *2007 IEEE Nuclear Science Symposium*
3819 *Conference Record*. Honolulu, HI, USA: IEEE, Oct. 2007.
- 3820 [98] G. Carminati. "The new wide-band solar neutrino trigger for super-kamiokande".
3821 In: *Phys. Procedia* 61 (2015), pp. 666–672.
- 3822 [99] P. A. Čerenkov. "Visible radiation produced by electrons moving in a medium
3823 with velocities exceeding that of light". In: *Phys. Rev.* 52.4 (Aug. 1937),
3824 pp. 378–379.
- 3825 [100] I. Frank and I. Tamm. "Coherent visible radiation of fast electrons passing
3826 through matter". In: *Selected Papers*. Berlin, Heidelberg: Springer Berlin
3827 Heidelberg, 1991, pp. 29–35.
- 3828 [101] The T2K Collaboration. "Letter of Intent: Neutrino Oscillation Experiment at
3829 JHF". In: *KEK Proposal* (2001). eprint:
3830 <http://neutrino.kek.jp/jhfnu/loi/loi.v2.030528.pdf>.
- 3831 [102] The K2K Collaboration and S. H. Ahn. "Detection of Accelerator-Produced
3832 Neutrinos at a Distance of 250 km". In: (Feb. 2001). arXiv: [hep-ex/0103001](https://arxiv.org/abs/hep-ex/0103001)
3833 [hep-ex].
- 3834 [103] The T2K Collaboration. "Tokai-to-Kamioka (T2K) Long Baseline Neutrino
3835 Oscillation Experiment Proposal". In: *KEK Proposal* (2006). eprint: [http://j-](http://j-parc.jp/researcher/Hadron/en/pac\0606/pdf/p11-Nishikawa.pdf)
3836 [parc.jp/researcher/Hadron/en/pac\0606/pdf/p11-Nishikawa.pdf](http://j-parc.jp/researcher/Hadron/en/pac\0606/pdf/p11-Nishikawa.pdf).
- 3837 [104] C. Bronner. "Accelerator Neutrino I Recent results from T2K". In: *Neutrino 2022*
3838 (2022). URL: <https://zenodo.org/record/6683821>.
- 3839 [105] K. Abe et al. "Observation of Electron Neutrino Appearance in a Muon Neutrino
3840 Beam". In: *Phys. Rev. Lett.* 112 (6 2014), p. 061802. eprint:
3841 <https://link.aps.org/doi/10.1103/PhysRevLett.112.061802>.
- 3842 [106] T. Fukuda et al. "Proposal for precise measurement of neutrino-water
3843 cross-section in NINJA physics run". Proposal for J-PARC and KEK. 2017.
- 3844 [107] T. Ovsiannikova et al. "New experiment WAGASCI to measure cross sections of
3845 neutrino interactions in water and hydrocarbon using J-PARC beam". In: *Physics*
3846 *of Particles and Nuclei* 48.6 (2017), pp. 1014–1017. eprint:
3847 <https://doi.org/10.1134/S1063779617060478>.

- 3848 [108] M. Antonova et al. "Baby MIND: a magnetized segmented neutrino detector for
3849 the WAGASCI experiment". In: *Journal of Instrumentation* 12.07 (2017), p. C07028.
3850 eprint: <http://stacks.iop.org/1748-0221/12/i=07/a=C07028>.
- 3851 [109] K. Abe et al. "First measurement of the charged current $\bar{\nu}_\mu$ double differential
3852 cross section on a water target without pions in the final state". In: *Phys. Rev. D*
3853 102 (1 2020), p. 012007. URL:
3854 <https://link.aps.org/doi/10.1103/PhysRevD.102.012007>.
- 3855 [110] K. Abe et al. "Measurements of $\bar{\nu}_\mu$ and $\bar{\nu}_\mu + \nu_\mu$ charged-current cross-sections
3856 without detected pions or protons on water and hydrocarbon at a mean
3857 anti-neutrino energy of 0.86 GeV". In: *Progress of Theoretical and Experimental*
3858 *Physics* 2021.4 (Mar. 2021). URL: <https://doi.org/10.1093/ptep/ptab014>.
- 3859 [111] K. Matsuoka et al. "Design and performance of the muon monitor for the T2K
3860 neutrino oscillation experiment". In: *Nuclear Instruments and Methods in Physics*
3861 *Research Section A* 624.3 (2010), pp. 591–600. eprint:
3862 <http://www.sciencedirect.com/science/article/pii/S016890021002098X>.
- 3863 [112] K. Abe et al. "Improved constraints on neutrino mixing from the T2K experiment
3864 with 3.13×10^{21} protons on target". en. In: *Phys. Rev. D.* 103.11 (June 2021).
- 3865 [113] T. Vladisavljevic. *Predicting the T2K neutrino flux and measuring oscillation*
3866 *parameters*. 1st ed. Springer theses. Cham, Switzerland: Springer Nature, Sept.
3867 2020.
- 3868 [114] D. Beavis, A. Carroll, and I. Chiang. "Long baseline neutrino oscillation
3869 experiment at the AGS. Physics design report". In: *Office of Scientific and Technical*
3870 *Information (OSTI)* (Apr. 1995).
- 3871 [115] P.-A. Amaudruz et al. "The T2K fine-grained detectors". In: *Nuclear Instruments*
3872 *and Methods in Physics Research Section A: Accelerators, Spectrometers, Detectors and*
3873 *Associated Equipment* 696 (Dec. 2012), pp. 1–31. URL:
3874 <https://doi.org/10.1016/j.nima.2012.08.020>.
- 3875 [116] N. Abgrall et al. "Time projection chambers for the T2K near detectors". In:
3876 *Nuclear Instruments and Methods in Physics Research Section A: Accelerators,*
3877 *Spectrometers, Detectors and Associated Equipment* 637.1 (May 2011), pp. 25–46. URL:
3878 <https://doi.org/10.1016/j.nima.2011.02.036>.
- 3879 [117] S. Assylbekov et al. "The T2K ND280 off-axis pi-zero detector". In: *Nuclear*
3880 *Instruments and Methods in Physics Research Section A: Accelerators, Spectrometers,*
3881 *Detectors and Associated Equipment* 686 (Sept. 2012), pp. 48–63. URL:
3882 <https://doi.org/10.1016/j.nima.2012.05.028>.
- 3883 [118] D. Allan et al. "The electromagnetic calorimeter for the T2K near detector
3884 ND280". In: *Journal of Instrumentation* 8.10 (2013), P10019–P10019. URL:
3885 <https://doi.org/10.1088%2F1748-0221%2F8%2F10%2Fp10019>.
- 3886 [119] CERN Courier. *UA1 magnet sets off for a second new life*. 2008. URL: <https://cerncourier.com/a/ua1-magnet-sets-off-for-a-second-new-life/>.
- 3887 [120] F. Vannucci. "The NOMAD Experiment at CERN". In: *Advances in High Energy*
3888 *Physics* 2014 (2014), pp. 1–20. URL: <https://doi.org/10.1155/2014/129694>.

- 3890 [121] S. Aoki et al. "The T2K Side Muon Range Detector (SMRD)". In: *Nuclear*
3891 *Instruments and Methods in Physics Research Section A: Accelerators, Spectrometers,*
3892 *Detectors and Associated Equipment* 698 (Jan. 2013), pp. 135–146. URL:
3893 <https://doi.org/10.1016/j.nima.2012.10.001>.
- 3894 [122] K. Suzuki et al. "Measurement of the muon beam direction and muon flux for the
3895 T2K neutrino experiment". In: *Progress of Theoretical and Experimental Physics*
3896 2015.5 (2015), pp. 53C01–0. URL: <https://doi.org/10.1093%2Fptep%2Fptv054>.
- 3897 [123] S. Brooks et al. *Handbook of Markov Chain Monte Carlo*. CRC Press, 2011.
- 3898 [124] W. R. Gilks, S. Richardson, and D. J. Spiegelhalter. *Markov Chain Monte Carlo in*
3899 *Practice*. Chapman & Hall/CRC Interdisciplinary Statistics, 1995.
- 3900 [125] C. Wret. "Minimising systematic uncertainties in the T2K experiment using
3901 near-detector and external data". PhD thesis. Imperial College London, 2018.
- 3902 [126] K. E. Duffy. "Measurement of the Neutrino Oscillation Parameters $\sin^2 \theta_{23}$, Δm_{32}^2 ,
3903 $\sin^2 \theta_{13}$, and δ_{CP} in Neutrino and Antineutrino Oscillation at T2K". PhD thesis.
3904 Oriel College, University of Oxford, 2016.
- 3905 [127] C. Bojeckho and A. Kabooth. "Muon neutrino disappearance simultaneous fit of
3906 ND280 and SK with Run 1+2+3 data using Markov Chain Monte Carlo Analysis".
3907 In: *T2K Technical Note* 140 (2013).
- 3908 [128] T. Bayes. "An essay toward solving a problem in the doctrine of chances". In: *Phil.*
3909 *Trans. Roy. Soc. Lond.* 53 (1764), pp. 370–418.
- 3910 [129] A. Sztuc. "Standard and Non-Standard Neutrino-Antineutrino Oscillation
3911 Analyses and Event Reconstruction Studies using Markov Chain Monte Carlo
3912 Methods at T2K". PhD thesis. Imperial College London, 2021.
- 3913 [130] N. Metropolis et al. "Equation of State Calculations by Fast Computing
3914 Machines". In: *Journal of Chemical Physics* 21.6 (1970).
- 3915 [131] W. K. Hastings. "Monte Carlo Sampling Methods Using Markov Chains and
3916 Their Applications". In: *Biometrika* 57.1 (1970).
- 3917 [132] J. Dunkley et al. "Fast and reliable Markov chain Monte Carlo technique for
3918 cosmological parameter estimation". en. In: *Mon. Not. R. Astron. Soc.* 356.3 (Jan.
3919 2005), pp. 925–936.
- 3920 [133] H. Jeffreys. *The Theory of Probability*. Oxford Classic Texts in the Physical Sciences.
3921 1939.
- 3922 [134] R. E. Kass and A. E. Raftery. "Bayes factors". en. In: *J. Am. Stat. Assoc.* 90.430
3923 (June 1995), pp. 773–795.
- 3924 [135] T.T. Böhlen et al. "The FLUKA Code: Developments and Challenges for High
3925 Energy and Medical Applications". In: *Nuclear Data Sheets* 120 (2014), pp. 211
3926 –214. eprint:
3927 <http://www.sciencedirect.com/science/article/pii/S0090375214005018>.
- 3928 [136] R. Brun et al. *GEANT: Detector Description and Simulation Tool; Oct 1994*. CERN
3929 Program Library. Long Writeup W5013. Geneva: CERN, 1993. eprint:
3930 <http://cds.cern.ch/record/1082634>.

- 3931 [137] C. Zeitnitz and T.A. Gabriel. "The GEANT-CALOR interface and benchmark
3932 calculations of ZEUS test calorimeters". In: *Nuclear Instruments and Methods in*
3933 *Physics Research Section A* 349.1 (1994), pp. 106–111. eprint:
3934 <http://www.sciencedirect.com/science/article/pii/0168900294906130>.
- 3935 [138] A. Fiorentini et al. "Flux Prediction and Uncertainty Updates with NA61 2009
3936 Thin Target Data and Negative Focussing Mode Predictions". In: *T2K Technical*
3937 *Note* 217 (2017).
- 3938 [139] N. Abgrall et al. "Measurements of cross sections and charged pion spectra in
3939 proton-carbon interactions at 31 GeV". In: *Phys. Rev. C* 84.3 (2011). URL:
3940 <https://doi.org/10.1103%2Fphysrevc.84.034604>.
- 3941 [140] N. Abgrall et al. "Measurement of production properties of positively charged
3942 kaons in proton-carbon interactions at 31 GeV". In: *Phys. Rev. C* 85.3 (2012). URL:
3943 <https://doi.org/10.1103%2Fphysrevc.85.035210>.
- 3944 [141] N. Abgrall et al. "Pion emission from the T2K replica target: Method, results and
3945 application". In: *Nuclear Instruments and Methods in Physics Research Section A* 701
3946 (2013), pp. 99–114. eprint:
3947 <http://www.sciencedirect.com/science/article/pii/S016890021201234X>.
- 3948 [142] M. Apollonio et al. "Forward production of charged pions with incident protons
3949 on nuclear targets at the CERN Proton Synchrotron". In: *Phys. Rev. C* 80 (3 2009),
3950 p. 035208. eprint: <https://link.aps.org/doi/10.1103/PhysRevC.80.035208>.
- 3951 [143] B. Blau et al. "The superconducting magnet of AMS-02". In: *Nuclear Physics B -*
3952 *Proceedings Supplements* 113.1-3 (Dec. 2002), pp. 125–132. URL:
3953 [https://doi.org/10.1016/s0920-5632\(02\)01831-5](https://doi.org/10.1016/s0920-5632(02)01831-5).
- 3954 [144] S. Haino et al. "Measurements of primary and atmospheric cosmic-ray spectra
3955 with the BESS-TeV spectrometer". In: *Physics Letters B* 594.1-2 (July 2004),
3956 pp. 35–46. URL: <https://doi.org/10.1016/j.physletb.2004.05.019>.
- 3957 [145] NASA. *U.S. Standard Atmosphere, 1976.* 1976. URL: <https://ntrs.nasa.gov/api/citations/19770009539/downloads/19770009539.pdf>.
- 3959 [146] S. Roesler, R. Engel, and J. Ranft. "The Monte Carlo Event Generator
3960 DPMJET-III". In: *Advanced Monte Carlo for Radiation Physics, Particle Transport*
3961 *Simulation and Applications*. Springer Berlin Heidelberg, 2001, pp. 1033–1038. URL:
3962 https://doi.org/10.1007/978-3-642-18211-2_166.
- 3963 [147] K. Niita et al. "PHITS—a particle and heavy ion transport code system". In:
3964 *Radiation Measurements* 41.9-10 (Oct. 2006), pp. 1080–1090. URL:
3965 <https://doi.org/10.1016/j.radmeas.2006.07.013>.
- 3966 [148] T. Sanuki et al. "Measurements of atmospheric muon spectra at mountain
3967 altitude". In: *Physics Letters B* 541.3-4 (2002), pp. 234–242. URL:
3968 <https://doi.org/10.1016%2Fs0370-2693%2802%2902265-7>.
- 3969 [149] P. Achard et al. "Measurement of the atmospheric muon spectrum from 20 to
3970 3000 GeV". In: *Physics Letters B* 598.1-2 (2004), pp. 15–32. URL:
3971 <https://doi.org/10.1016%2Fj.physletb.2004.08.003>.
- 3972 [150] K. Sato. "Atmospheric Neutrino Reviews on neutrino fluxes (low E atm nu)". In:
3973 *Neutrino 2022* (2022). URL: <https://zenodo.org/record/6695711>.

- 3974 [151] Y. Hayato and L. Pickering. "The NEUT neutrino interaction simulation program
3975 library". In: *The European Physical Journal Special Topics* 230.24 (Oct. 2021),
3976 pp. 4469–4481. URL: <https://doi.org/10.1140/epjs/s11734-021-00287-7>.
- 3977 [152] Y. Hayato. "A Neutrino Interaction Simulation Program Library NEUT". In: *Acta
3978 Physica Polonica B* 40.9 (2009).
- 3979 [153] C. H. Llewellyn Smith. "Neutrino reactions at accelerator energies". In: *Physics
3980 Reports* 3.5 (1972), pp. 261 –379. eprint:
3981 <http://www.sciencedirect.com/science/article/pii/0370157372900105>.
- 3982 [154] O. Benhar, A. Fabrocini, and S. Fantoni. "The nucleon spectral function in infinite
3983 nuclear matter". In: *Nuclear Physics A* 497 (June 1989), pp. 423–430. URL:
3984 [https://doi.org/10.1016/0375-9474\(89\)90484-3](https://doi.org/10.1016/0375-9474(89)90484-3).
- 3985 [155] R. Bradford et al. "A New Parameterization of the Nucleon Elastic Form Factors".
3986 In: *Nuclear Physics B - Proceedings Supplements* 159 (2006). Proceedings of the 4th
3987 International Workshop on Neutrino-Nucleus Interactions in the Few-GeV
3988 Region, pp. 127 –132. eprint:
3989 <http://www.sciencedirect.com/science/article/pii/S0920563206005184>.
- 3990 [156] A. A. Aguilar-Arevalo et al. "First measurement of the muon neutrino charged
3991 current quasielastic double differential cross section". In: *Phys. Rev. D* 81.9 (2010).
3992 URL: <https://doi.org/10.1103/2Fphysrevd.81.092005>.
- 3993 [157] R. Gran et al. "Neutrino-nucleus quasi-elastic and 2p2h interactions up to 10
3994 GeV". In: *Phys. Rev. D* 88 (11 2013), p. 113007. eprint:
3995 <https://link.aps.org/doi/10.1103/PhysRevD.88.113007>.
- 3996 [158] C. Berger and L. M. Sehgal. "Lepton mass effects in single pion production by
3997 neutrinos". In: *Phys. Rev. D* 76 (11 2007), p. 113004. URL:
3998 <https://link.aps.org/doi/10.1103/PhysRevD.76.113004>.
- 3999 [159] C. Berger and L. M. Sehgal. "Partially conserved axial vector current and
4000 coherent pion production by low energy neutrinos". In: *Phys. Rev. D* 79 (5 2009),
4001 p. 053003. eprint: <https://link.aps.org/doi/10.1103/PhysRevD.79.053003>.
- 4002 [160] T. Sjöstrand. "High-energy-physics event generation with PYTHIA 5.7 and
4003 JETSET 7.4". In: *Computer Physics Communications* 82.1 (Aug. 1994), pp. 74–89.
4004 URL: [https://doi.org/10.1016/0010-4655\(94\)90132-5](https://doi.org/10.1016/0010-4655(94)90132-5).
- 4005 [161] C. Bronner and M. Hartz. "Tuning of the Charged Hadrons Multiplicities for
4006 Deep Inelastic Interactions in NEUT". In: *Proceedings of the 10th International
4007 Workshop on Neutrino-Nucleus Interactions in Few-GeV Region (NuInt15)*. Journal of
4008 the Physical Society of Japan, Dec. 2016. URL:
4009 <https://doi.org/10.7566/jpscp.12.010041>.
- 4010 [162] M. Glück, E. Reya, and A. Vogt. "Dynamical parton distributions revisited". In:
4011 *The European Physical Journal C* 5.3 (1998), pp. 461–470. URL:
4012 <https://doi.org/10.1007%2Fs100529800978>.
- 4013 [163] A. Bodek and U. Yang. "Axial and Vector Structure Functions for Electron- and
4014 Neutrino- Nucleon Scattering Cross Sections at all Q^2 using Effective Leading
4015 order Parton Distribution Functions". In: *arXiv* (2010). URL:
4016 <https://arxiv.org/abs/1011.6592>.

- 4017 [164] A. Bodek and U. Yang. "Update to the Bodek-Yang Unified Model for Electron-
4018 and Neutrino- Nucleon Scattering Cross Sections". In: *arXiv* (2010). URL:
4019 <https://arxiv.org/abs/1012.0261>.
- 4020 [165] S. Gollapinni. "Neutrino Cross section Future". In: *arXiv* (2016). URL:
4021 <https://arxiv.org/abs/1602.05299>.
- 4022 [166] E. S. Pinzon Guerra et al. "Using world π^\pm -nucleus scattering data to constrain
4023 an intranuclear cascade model". In: *Phys. Rev. D* 99 (5 2019), p. 052007. URL:
4024 <https://link.aps.org/doi/10.1103/PhysRevD.99.052007>.
- 4025 [167] S. Agostinelli et al. "GEANT4: A Simulation toolkit". In: *Nucl. Instrum. Meth.*
4026 A506 (2003), pp. 250–303.
- 4027 [168] R. Brun et al. "GEANT3". In: *Cern Document Server* (Sept. 1987).
- 4028 [169] A. Himmel et al. "Super-Kamiokande events and data quality studies for T2K
4029 Runs 5 and 6". In: *T2K Technical Note* 219 (2015).
- 4030 [170] S. Berkman et al. "fiTQun: A New Reconstruction Algorithm for Super-K". In:
4031 *T2K Technical Note* 146 (2013).
- 4032 [171] R.B. Patterson et al. "The extended-track event reconstruction for MiniBooNE".
4033 In: *Nuclear Instruments and Methods in Physics Research Section A* 608.1 (2009),
4034 pp. 206–224. URL: <https://doi.org/10.1016/j.nima.2009.06.064>.
- 4035 [172] M. Shiozawa. "Reconstruction algorithms in the Super-Kamiokande large water
4036 Cherenkov detector". In: *Nuclear Instruments and Methods in Physics Research
4037 Section A: Accelerators, Spectrometers, Detectors and Associated Equipment* 433.1-2
4038 (Aug. 1999), pp. 240–246. URL:
4039 [https://doi.org/10.1016/s0168-9002\(99\)00359-9](https://doi.org/10.1016/s0168-9002(99)00359-9).
- 4040 [173] K. Abe et al. "Search for CP Violation in Neutrino and Antineutrino Oscillations
4041 by the T2K Experiment with 2.2×10^{21} Protons on Target". In: *Phys. Rev. Lett.*
4042 121.17 (Oct. 2018). URL: <https://doi.org/10.1103/physrevlett.121.171802>.
- 4043 [174] K. Abe et al. "Measurements of neutrino oscillation in appearance and
4044 disappearance channels by the T2K experiment with 6.6×10^{20} protons on
4045 target". In: *Phys. Rev. D* 91.7 (Apr. 2015). URL:
4046 <https://doi.org/10.1103/physrevd.91.072010>.
- 4047 [175] F. James. "MINUIT Function Minimization and Error Analysis". In: *Reference
4048 Manual, Version 94.1, CERN Program Library Long Writeup D506 D.506* (1994).
4049 eprint:
4050 <https://root.cern.ch/sites/d35c7d8c.web.cern.ch/files/minuit.pdf>.
- 4051 [176] X. Li and M. Wilking. "FiTQun Event Selection Optimization". In: *T2K Technical
4052 Note* 319 (2017).
- 4053 [177] S. Tobayama. "An Analysis of the Oscillation of Atmospheric Neutrinos".
4054 PhD thesis. British Columbia U., 2016.
- 4055 [178] D. Barrow et al. "Super-Kamiokande Data Quality, MC, and Systematics in Run
4056 10". In: *T2K Technical Note* 399 (2020).
- 4057 [179] A. Maghrabi, A. Aldosari, and M. Almutairi. "Correlation analyses between solar
4058 activity parameters and cosmic ray muons between 2002 and 2012 at high cutoff
4059 rigidity". In: *Advances in Space Research* 68.7 (Oct. 2021), pp. 2941–2952.

- 4060 [180] J. Beringer et al. "Review of Particle Physics". In: *Phys. Rev. D* 86 (1 2012),
4061 p. 010001. URL: <https://link.aps.org/doi/10.1103/PhysRevD.86.010001>.
- 4062 [181] S. Nakayama K. Iyogi and Y. Obayashi. "T2K data acquisition and FC event
4063 selection at Super-Kamiokande". In: *T2K Technical Note* 027 (2011).
- 4064 [182] L. K. Pik. "Study of the neutrino mass hierarchy with the atmospheric neutrino
4065 data observed in Super-Kamiokande". PhD thesis. Tokyo University, 2012.
- 4066 [183] R. Wendell et al. "Atmospheric neutrino oscillation analysis with subleading
4067 effects in Super-Kamiokande I, II, and III". In: *Phys. Rev. D* 81 (9 2010), p. 092004.
- 4068 [184] J. Hosaka et al. "Three flavor neutrino oscillation analysis of atmospheric
4069 neutrinos in Super-Kamiokande". In: *Phys. Rev. D* 74 (3 2006), p. 032002. URL:
4070 <https://link.aps.org/doi/10.1103/PhysRevD.74.032002>.
- 4071 [185] D. Barrow et al. "Flux and interaction models for the initial T2K-SK atmospheric
4072 joint fit studies". In: *T2K Technical Note* 422 (2022).
- 4073 [186] L. Munteanu et al. "Constraining the Flux and Cross Section Models with Data
4074 from ND280 using FGD1 and FGD2 for the 2020 Oscillation Analysis". In: *T2K*
4075 *Technical Note* 395 (2020).
- 4076 [187] P. Bartet et al. " ν_μ CC event selections in the ND280 tracker using Run 2+3+4
4077 data". In: *T2K Technical Note* 212 (2015).
- 4078 [188] W. Parker. "Constraining Systematic Uncertainties at T2K using Near Detector
4079 Data". PhD thesis. Royal Holloway University of London, 2020.
- 4080 [189] V. Berardi et al. " $\bar{\nu}_\mu$ event selection in the ND280 tracker using Run 5c and Run 6
4081 anti-neutrino beam data". In: *T2K Technical Note* 246 (2015).
- 4082 [190] B. Kirby J. Kim and M. Wilking. "Michel Electron Tagging in FGD1". In: *T2K*
4083 *Technical Note* 104 (2012).
- 4084 [191] J. Missert. "TN-318: Fit to Super-K Atmospheric Neutrino Data for Optimization
4085 of the fiTQun Fiducial Volume Cuts and Estimation of Detector Uncertainties".
4086 In: *T2K Technical Note* 318 (2017).
- 4087 [192] J. Chakrani et al. "NIWG model and uncertainties for 2021 oscillation analysis".
4088 In: *T2K Technical Note* 414 (2022).
- 4089 [193] M. Wascko. "T2K Status, Results, And Plans". In: *Neutrino 2018* (2018). URL:
4090 <https://zenodo.org/record/1286752>.
- 4091 [194] T. Vladislavljevic et al. "Flux Prediction and Uncertainty with NA61/SHINE 2009
4092 Replica-Target Data (TN354 version 3.3)". In: *T2K Technical Note* 354 (2020).
- 4093 [195] G. Ambrosini et al. "K/ π production ratios from 450 GeV/c protons on
4094 beryllium". en. In: *Phys. Lett. B* 420.1-2 (Feb. 1998), pp. 225–232.
- 4095 [196] E. Atkin et al. "NIWG model and uncertainties for 2019-2020 oscillation analysis".
4096 In: *T2K Technical Note* 344 (2019).
- 4097 [197] D. Barrow et al. "SK atmospheric T2K beam joint fit technical note, MaCh3
4098 details". In: *T2K Technical Note* 426 (2022).
- 4099 [198] A. A. Aguilar-Arevalo et al. "Measurement of ν_μ and $\bar{\nu}_\mu$ induced neutral current
4100 single π^0 production cross sections on mineral oil at $E_\nu \sim \mathcal{O} (1 \text{ GeV})$ ". In: *Phys.*
4101 *Rev. D* 81 (1 2010), p. 013005. eprint:
4102 <https://link.aps.org/doi/10.1103/PhysRevD.81.013005>.

- 4103 [199] P. Perio and J. Imber. "Super-K Systematic Uncertainties for RUN1-4 Joint ν_e and
4104 ν_μ Analyses". In: *T2K Technical Note* 186 (2014).
- 4105 [200] P. Perio and J. Imber. "Update of SK ν_e systematic error for 2012a oscillation
4106 analysis". In: *T2K Technical Note* 107 (2012).
- 4107 [201] D. Barrow and C. Vilela. *T2K-SK Detector Matrix Uncertainties - MaCh3 Integration*.
4108 <https://git.t2k.org/t2k-sk/t2ksk-detcovmat/-/tree/feature/MaCh3Integration>. Accessed: 22-06-2022.
- 4110 [202] R. Barlow and C. Beeston. "Fitting using finite Monte Carlo samples". en. In:
4111 *Comput. Phys. Commun.* 77.2 (Oct. 1993), pp. 219–228.
- 4112 [203] J. S. Conway. "Incorporating Nuisance Parameters in Likelihoods for Multisource
4113 Spectra". In: *arXiv* (2011). URL: <https://arxiv.org/abs/1103.0354>.
- 4114 [204] D. Barrow et al. "Oscillation probability calculation for the T2K+SK atmospheric
4115 joint fit". In: *T2K Technical Note* 425 (2022).
- 4116 [205] R. G. Calland, A. C. Kaboth, and D. Payne. "Accelerated event-by-event neutrino
4117 oscillation reweighting with matter effects on a GPU". In: *IOP Journal of
4118 Instrumentation* 9.04 (Apr. 2014), P04016–P04016.
- 4119 [206] R. Wendell. *Prob3++ Oscillation Probability Calculation*. URL:
4120 <http://www.phy.duke.edu/~raw22/public/Prob3++/>.
- 4121 [207] F. Kallenborn et al. "Massively parallel computation of atmospheric neutrino
4122 oscillations on CUDA-enabled accelerators". In: *Computer Physics Communications*
4123 234 (2019), pp. 235–244.
- 4124 [208] L. Warsame. *MaCh3 Analysis Progress*. Implementation of CUDAProb3 in MaCh3
4125 for DUNE. URL: https://indico.fnal.gov/event/50217/contributions/241232/attachments/155318/202209/MaCh3ProgressforDUNELBL_May17%20%282%29.pdf.
- 4128 [209] S. Bourret et al. "Neutrino oscillation tomography of the Earth with
4129 KM3NeT-ORCA". In: *Journal of Physics: Conference Series* 888 (2017), p. 012114.
- 4130 [210] C. Rott, A. Taketa, and D. Bose. "Spectrometry of the Earth using Neutrino
4131 Oscillations". In: *Scientific Reports* 5.1 (Oct. 2015). URL:
4132 <https://doi.org/10.1038/srep15225>.
- 4133 [211] K. Hagiwara, N. Okamura, and K. Senda. "The earth matter effects in neutrino
4134 oscillation experiments from Tokai to Kamioka and Korea". In: *Journal of High
4135 Energy Physics* 2011.9 (Sept. 2011).
- 4136 [212] D. Typinski. *Earth Gravity*.
4137 <http://www.typnet.net/Essays/EarthGravGraphics/EarthGrav.pdf>.
4138 Accessed: 24-06-2022.
- 4139 [213] D. Barrow. *T2K Beam + SK Atmospheric Joint Fit*. Plenary Slides for May 2022 T2K
4140 Collaboration Meeting. 2022. URL:
4141 https://t2k.org/meet/collab/CM_May_2022/Talks/Friday/T2KSKPlenary.
- 4142 [214] E. Atkin et al. "Measuring PMNS parameters in a joint ND280-SK analysis using
4143 MCMC". In: *T2K Technical Note* 393 (2020).